Frequency combs in the extreme ultraviolet

Akira Ozawa

München 2009

Frequency combs in the extreme ultraviolet

Akira Ozawa

Dissertation
an der Fakultät für Physik
der Ludwig–Maximilians–Universität
München

vorgelegt von
Akira Ozawa
aus Ibaraki, Japan

München, den 13. 11. 2009

Erstgutachter: Prof. Dr. Theodor W. Hänsch
Zweitgutachter: Prof. Dr. Ferenc Krausz
Tag der mündlichen Prüfung: 21. 12. 2009

Zusammenfassung

Optische Frequenzkämme sind zu unverzichtbaren Werkzeugen für die Metrologie und für die Hochfeld-Physik geworden, da sie in einzigartiger Weise hohe spektrale Auflösung und die hohen Spitzenintensitäten der erzeugenden Pulszüge verbinden. Letztere können benutzt werden, um die üblicherweise im Infraroten erzeugten Frequenzkämme mit Hilfe von nichtlinearen Prozessen wie der Erzeugung hoher Harmonischer (HHG) in den extrem-ultravioletten (XUV) Spektralbereich zu erweitern, in dem eine direkte Erzeugung bisher nicht möglich ist.

Die hochpräzise Spektroskopie des 1s-2s-Übergangs in He^+ bei 61 nm ist eine besonders interessante Anwendungsmöglichkeit für einen leistungsstarken XUV-Frequenzkamm. Dieser Übergang verspricht Tests der Quantenelektrodynamik gebundener Systeme (QED) mit noch nie dagewesener Genauigkeit, da Beiträge theoretisch schwer zu behandelnder Korrekturen höherer Ordnung hier zugänglicher sind als z.B. bei der (wohlbekannten) Spektroskopie des 1s-2s-Übergangs in Wasserstoff. Da die ersten XUV-Frequenzkämme mit der nötigen hohen Repetitionsrate nicht leistungsstark genug für ein Spektroskopieexperiment waren, ist die Entwicklung von leistungsstärkeren XUV-Frequenzkämmen von größter Bedeutung.

Im Rahmen dieser Arbeit wurde ein Frequenzkamm gebaut, der durch Leistungsüberhöhung in einem externen Resonator die Erzeugung hoher Harmonischer bei Wellenlängen bis hinab zu 40 nm ermöglicht. Die mittlere Leistung bei 61 nm (entsprechend der 13 ten Harmonischen) betrug knapp 1 μW. Diese 100'000-fache Verbesserung gegenüber der ersten Generation von XUV-Frequenzkämmen hoher Repetitionsrate macht dieses System zum bis dato leistungsfähigsten seiner Art. Ermöglicht wurde dies zum einen durch die Erhöhung der Pulsenergie durch das Absenken der Repetitionsrate auf 10 MHz und zum anderen durch eine äußerst sorgfältige Kompensation der Dispersion.

Trotz der großen Fortschritte befinden sich spektroskopische Anwendungen weiterhin an der Grenze der Machbarkeit, so dass weitere Anstrengungen unternommen wurden, um die beiden wichtigsten Einschränkungen bei der Skalierung zu höheren Leistungen zu bewältigen. Deren erste ist die Verfügbarkeit von geeigneten Lasern mit hoher Leistung, die zweite die niedrige Effizienz und die Nichtlinearitäten der üblicherweise als XUV-Auskoppler eingesetzten Brewsterplättchen.

Dem Bedarf an höherer Leistung wurde durch den Aufbau eines kryogenen optischen Verstärkers begegnet. Damit konnte die mittlere Leistung um den Faktor 4 verstärkt werden, ohne dabei das Strahlprofil zu verzerren oder nennenswertes Phasenrauschen zu erzeugen. Ein solcher Verstärker ist vielseitig einsetzbar und hat zahlreiche Anwendungen jenseits der resonatorgestützten Erzeugung hoher Harmonischer.

Als eine mögliche Lösung des zweiten Problems wurde die Erzeugung von nicht-kollinearen hohen Harmonischen demonstriert. Bei diesem Auskoppelmechanismus kreuzen sich die erzeugenden Strahlen unter einem Winkel, so dass das XUV-Licht entlang der Winkelhalbierenden abgestrahlt wird, was einen Auskoppler unnötig macht. Wir konnten zum ersten Mal die effiziente und zuverlässige Erzeugung kollimierter nicht-kollinearer Harmonischer in einer experimentellen Anordnung zeigen, die direkt auf Resonatoren übertragbar ist. Dieser Ansatz ist Größenordnungen weniger verlustbehaftet als das übliche Brewsterplättchen.

Die im Rahmen dieser Arbeit erzielten Ergebnisse stellen enorme Fortschritte in Richtung eines zuverlässigen XUV-Frequenzkamms dar, der ausreichend Leistung für anspruchsvolle Anwendungen wie die Spektroskopie oder die Laserkühlung bereitstellt.

Abstract

Optical frequency combs have become an indispensable tool for both optical frequency metrology and high-field phyiscs, as they uniquely combine the extremely high spectral resolution and the large peak intensities of their generating pulse trains. By nonlinear processes such as high harmonic generation (HHG), the latter can be exploited to extend frequency combs from the infrared, where they are usually generated, to shorter wavelengths down to the extreme ultraviolet (XUV) spectral region where direct synthesis is not possible.

Among the possible applications of a high-power XUV frequency comb, high precision spectroscopy of the 1s-2s transition in He^+ at 61 nm is a particularly interesting example. Such an experiment promises tests of bound-state quantum electrodynamics (QED) with unprecedented precision by being more sensitive to theoretically challenging higher-order corrections than e.g. hydrogen 1s-2s spectroscopy. However, the first demonstrations of high repetition rate XUV frequency combs generated in external enhancement cavities did not generate sufficient power for spectroscopy. Therefore, the development of high power XUV frequency combs is of utmost importance for applications.

In this work the generation of a high power frequency comb in wavelength regions down to 40 nm via intracavity HHG was demonstrated. The average power around 61 nm (13^{th} harmonic) was close to 1μW (a 10^5 fold improvement over first generation sources) which made it the most powerful XUV frequency comb demonstrated so far. The improvement was achieved by lowering the repetition rate to obtain higher pulse energies and by elaborate dispersion management.

Even with 1μW of average power spectroscopy experiments are still on the verge of feasibility. Thus further efforts were made to overcome the two most important limitations that impede progress. Those are the limited available seed power and the low efficiency and high nonlinearities of the employed Brewster's plate outcoupling method.

The first limitation was mitigated by the demonstration of a cryogenic high repetition rate single pass amplifier. We obtained a 4-fold improvement in average power without deforming the beam and with negligible phase noise. Such an amplifier is a versatile tool and not limited to cavity-enhanced HHG applications.

The second limitation was addressed by a study of non-collinear high harmonic generation. In this outcoupling method, two infrared driving beams that cross at an angle generate an XUV frequency comb which propagates along their bisectrix. This renders the use of any output coupler unneccessary. We demonstrated efficient, stable, and well-collimated non-collinear high-harmonic emission in a setup applicable to an enhancement cavity for the first time. The estimated loss is orders of magnitude lower than with the conventional Brewter's plate method.

The results obtained in the course of this work are important milestones towards reliable high-power XUV frequency combs that make high precision spectroscopy or laser cooling in this wavelength region possible.

Contents

Chapter 1

Introduction

1.1 Short pulses and frequency combs

In this section, we review the basics of ultrashort pulses and frequency combs for future reference. Consider a time dependent electric field $\boldsymbol{E}(\boldsymbol{r}, t)$. For simplicity, we assume that the field is linearly polarized and focus on the time dependence of the field at a fixed position. In this case, it is sufficient to describe the field as $E(t)$. The power spectrum $P(\omega)$ denotes the power density of the field component that is oscillating at an angular frequency of ω. If the field $E(t)$ is non-negligible only within a very short time period, that is, $E(t)$ is pulse-like, a large number of sinusoidal oscillations with different angular frequencies have to be overlapped to compose a rapid change of $E(t)$ in time. Thus, broadband radiation is a prerequisite for the generation of short pulses. However, as we notice in daily life, the continuous broadband radiation (for example, from a light bulb) does not necessarily produce short pulses. To obtain a high field amplitude within a short time period, each wavelength component of the broadband radiation has to constructively interfere at a fixed time. [1] Perfect constructive interference can be obtained when the phases of all spectral components are the same at that time. These handwaving arguments describe the two important conditions for the generation of short pulses:

- Broadband emission
- Spectral phase coherence

The previous discussions are immediately refined when the spectrum $P(\omega)$ is described as the Fourier transform of the electric field $E(t)$:

$$P(\omega) \equiv |\mathcal{FT}\left[E(t)\right]|^2 \equiv \left| \int E(t) e^{-i\omega t} dt \right|^2 . \tag{1.1}$$

Fig. 1.1 shows the correspondence between the pulsed electric field and its spectrum resulting from Eqn. (1.1). Assuming Gaussian spectral and pulse envelopes, it is easy to derive the following relation between the pulse duration (FWHM $\Delta\tau$) and the spectral bandwidth (FWHM in angular frequency, $\Delta\omega$) from Eqn. (1.1).

$$\Delta\tau \times \Delta\omega \geq 2\pi \cdot 0.441. \tag{1.2}$$

[1] See Sec. 1.2 for the detailed definition of the spectral phase.

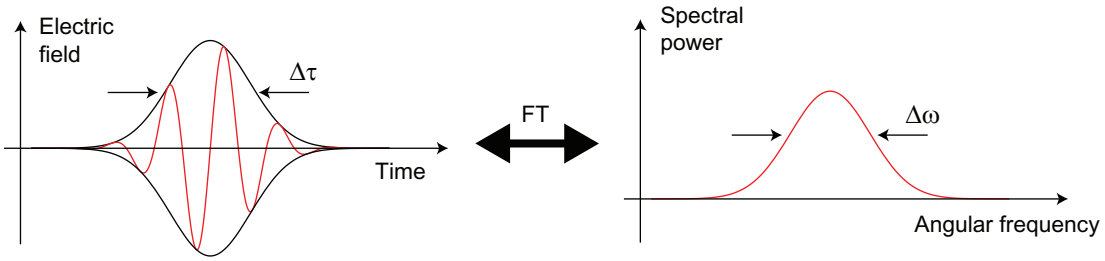

Figure 1.1: *Temporal and spectral representation of a short pulse. The (complex) spectrum can be obtained by applying a Fourier transform to the electric field in the time domain. A large spectral bandwidth with a linear spectral phase is required to generate short pulses. There is a minimum time-bandwidth product which reflects the uncertainty principle of energy and time.*

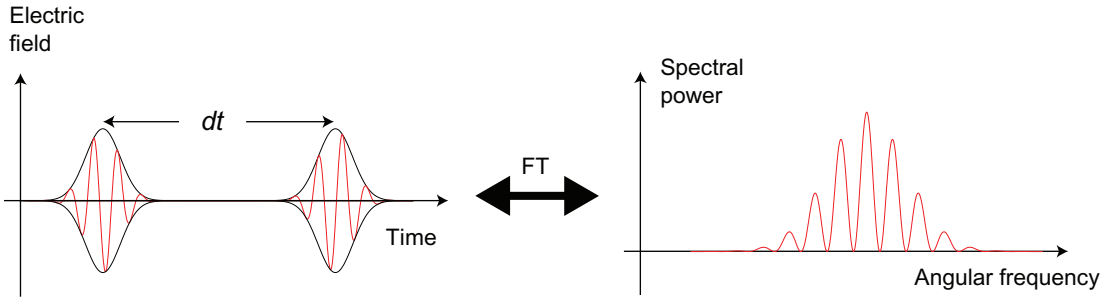

Figure 1.2: *Two pulses delayed in time and their spectrum. The spectrum is modulated due to interference between the two pulses. The spectral fringe structure depends on the phase delay and the envelope delay of the pulses.*

Here, the equation is satisfied when the pulse has a linear spectral phase (Fourier-limited or bandwidth-limited or chirp-free pulse).

Next, consider two Fourier-limited pulses that are delayed in time. In this case, each single wavelength component of one pulse is overlapped with the same wavelength component of the other pulse. These two waves may destructively or constructively interfere depending on the delay between the pulses. Since for a fixed delay, the condition for constructive (or destructive) interference depends on the wavelength, the resulting spectrum is expected to be modulated with full modulation-depth. Fig. 1.2 illustrates the modulated spectrum of two delayed pulses.

If the delay between the two pulses is large, it can be seen that the difference between constructive and destructive interference between the pulses corresponds to a very tiny difference in wavelength. Therefore, the distance between the fringes in the spectral modulation is determined by the delay between the two pulses. The wavelengths that satisfy the condition for constructive interference between the two pulses depends on their phase relation. Thus, by introducing a tailored phase shift, the spectral modulation can be shifted in a controlled manner. This can be applied to high precision spectroscopy. For a narrow absorption line located within the spectral bandwidth, the transition probability will be modulated when a phase shift between the two pulses is introduced. When both the phase shift and the pulse delay are precisely calibrated, the transition frequency can be identified with the precision of the spectral modulation frequency. The latter can be adjusted such that it is small enough by increasing the delay time between the pulses. This is the frequency description of Ramsey

spectroscopy [1–3].

The following calculation summarizes and refines the discussion given above.

The electric field consists of two Fourier-limited pulses that are delayed by dt:

$$E(t) = e^{-\frac{t^2}{\delta^2}} e^{-i\omega_c t} e^{-i\psi_{\mathrm{CE1}}} + e^{-\frac{(t-dt)^2}{\delta^2}} e^{-i\omega_c (t-dt)} e^{-i\psi_{\mathrm{CE2}}}. \tag{1.3}$$

Here, the pulse duration and the center frequnecy are denoted by δ and ω_c, respectively. Note that ψ_{CE1} and ψ_{CE2} are the phases of the fields measured from the peak of their pulse envelopes (Carrier Envelope Phase: CEP).

The power spectrum of the field ($P(\omega)$) is given by:

$$P(\omega) = |\mathcal{FT}[E(t)]|^2 = e^{-\frac{1}{2}\delta^2(\omega-\omega_c)^2} \delta^2 \left(1 + \cos\left(\Delta\psi_{\mathrm{CE}} - \omega dt\right)\right). \tag{1.4}$$

Here, $\Delta\psi_{\mathrm{CE}}$ is defined to be $\Delta\psi_{\mathrm{CE}} = \psi_{\mathrm{CE2}} - \psi_{\mathrm{CE1}}$ (carrier envelope phase slip, or carrier envelope offset phase). From Eqn. (1.4), the angular frequency of the spectral peaks ω_{peak} can be obtained:

$$\omega_{\mathrm{peak}} = N\frac{2\pi}{dt} + \frac{\Delta\psi_{\mathrm{CE}}}{dt}. \tag{1.5}$$

Here, N is the integer number that counts the spectral peaks from zero frequency. The separation between the spectral peaks (ω_{rep}) and the overall shift of the spectral modulation (ω_{CEO}) are given by:

$$\omega_{\mathrm{rep}} = \frac{2\pi}{dt} \tag{1.6}$$

$$\omega_{\mathrm{CEO}} = \frac{\Delta\psi_{\mathrm{CE}}}{dt}. \tag{1.7}$$

Finally, consider the spectrum of multiple pulses, extending the double pulse picture given above. Suppose that there are an infinite number of Fourier limited pulses. In the most general case, the delay and the phase shift between the pulses could exhibit an arbitrary behavior as a function of time. Such pulse trains would produce a complicated spectral structure, which might be also interesting to investigate. However, here we limit ourselves to the simplest case in which the delays (dt_n) and the change of carrier envelope phase between consecutive pulses ($\psi_{\mathrm{CE},n+1} - \psi_{\mathrm{CE},n}$) are all constant ($dt_n = dt, \psi_{\mathrm{CE},n+1} - \psi_{\mathrm{CE},n} = \Delta\psi_{\mathrm{CE}}$).

In this case, the spectrum of two arbitrary consecutive pulses shows a spectral modulation with identical modulation frequency and offset, as illustrated in Fig. 1.3. Thus, the resulting total spectrum is also expected to be modulated in the same way. However, in the case of multiple pulses, tiny deviations from the peak frequency (ω_{peak}) will already result in strong destructive interference because of the accumulating phase shifts. Therefore, the widths of the modulation peaks get narrower and finally approach δ-functions for an infinite number of pulses.

This resulting spectral structure is called frequency comb. The structure of the spectral modulation is basically the same as in the case of double pulses except for the width of the modulation peaks. Thus, the positions of the comb peaks are given by

$$\omega_{\mathrm{comb}} = N\frac{2\pi}{dt} + \frac{\Delta\psi_{\mathrm{CE}}}{dt} = N\omega_{\mathrm{rep}} + \omega_{\mathrm{CEO}} \tag{1.8}$$

with an integer number N. From Eqn. (1.6) and (1.7), the Carrier Envelope Offset (CEO) frequency ω_{CEO} can be described as

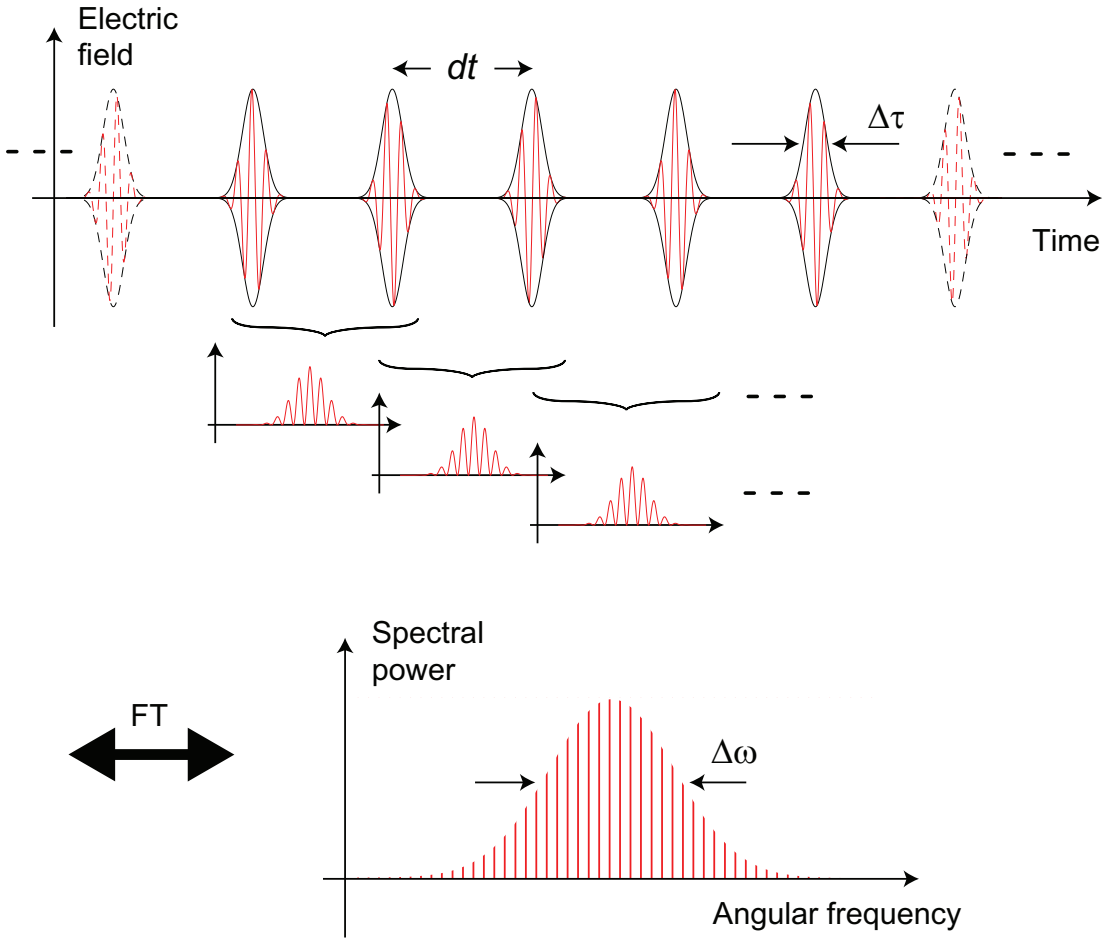

Figure 1.3: *Multiple temporally equidistant pulses with constant phase shifts and their spectrum. Similar to the spectrum of double pulses, the spectrum is modulated due to interference between the pulses. The fringe structure gets narrower and approaches a δ-function for an infinite number of pulses.*

$$\omega_{\mathrm{CEO}} \equiv \frac{\Delta\psi_{\mathrm{CE}}}{2\pi}\omega_{\mathrm{rep}}. \tag{1.9}$$

1.2 Short pulses in dispersive materials

The dispersion properties of a material and their effects on short pulses are important subjects when working with femtosecond enhancement cavities. In this subsection, the propagation of short pulses in dispersive materials is discussed for future reference.

When the electric field of a short pulse ($E(t)$) is expressed by the sum of many sinusoidal optical waves in the follwing way [2]:

$$E(t) = \int E(\omega)e^{-i\omega t+i\phi(\omega)}d\omega \tag{1.10}$$

the phase term $\phi(\omega)$ is often called "spectral phase". Here the spectral envelope function $E(\omega)$ is assumed to be real. When the pulse propagates through a material with the (physical) thickness L, the resulting spectral phase shift can be written as:

$$\phi(\omega) = \frac{n(\omega)L\omega}{c} \tag{1.11}$$

with the frequency-dependent refractive index $n(\omega)$. Eqn. (1.11) can be expanded around the center frequency ω_c:

$$\phi(\omega) = \phi(\omega_c) + \phi'(\omega_c)(\omega-\omega_c) + \frac{1}{2}\phi''(\omega_c)(\omega-\omega_c)^2 + ... \tag{1.12}$$

The constant term ($\phi(\omega_c)$) simply shifts the overall phase of the pulse and does not affect the pulse envelope ($|E(t)|^2$). It can be seen from Eqn. (1.10) that the linear term ($\phi'(\omega_c)(\omega-\omega_c)$) shifts the envelope of the pulse in time ($|E(t)|^2$ is shifted to $|E(t-\phi'(\omega_c))|^2$). The rest of the terms ($\frac{1}{2}\phi''(\omega_c)(\omega-\omega_c)^2+...$) actually change the shape of the pulse envelope and thus cause a frequency chirp of the pulse.

Generally speaking, the word "dispersion" stands for the full ω-dependence of the phase ($\phi(\omega)$). However, it is often used just for the terms equal to or higher than 2$^{\mathrm{nd}}$ order, especially in the field of ultrafast lasers. The 2$^{\mathrm{nd}}$ order term $\phi''(\omega_c)$ is called group delay dispersion (GDD). When the expansion of the phase $\phi(\omega)$ is performed beyond the 2$^{\mathrm{nd}}$ order, the higher order terms are named third order dispersion (TOD), fourth order dispersion (FOD) and so on.

1.3 Generation of frequency combs

How can we experimentally generate radiation which has the frequency comb spectrum discussed in the previous section (Sec. 1.1)? In this section, we will answer this question by describing the most important tool for frequency comb generation, a mode-locked laser. The method can be understood both in the time-domain and the frequency-domain. The following discussion is intended to give an intuitive understanding of frequency comb generation by

[2] This is an inverse Fourier transform of Eqn. (1.1).

mode-locked lasers. For a quantitative study of the mode-locking mechanism, the reader may refer to early theoretical and experimental work on mode-locked lasers [4–10].

Consider a laser in continuous wave (CW) operation. When CW radiation is confined inside the resonator, the field intensity is distributed uniformly inside the cavity. However, it is easy to imagine a second mode of operation in which a single short pulse is traveling around in the resonator. In this mode of operation, the output is a pulse train. To obtain a steady state with a constant pulse duration, the pulse envelope has to reproduce itself, i.e. retain its shape after one round trip. This requires that the dispersion from the intracavity material (e.g. a crystal) has to be compensated. The pulse-to-pulse delay is determined by the group velocity of the pulses and the cavity length. The pulse-to-pulse carrier envelope phase slip ($\Delta\psi_{\mathrm{CE}}$) is affected by the difference between the group and the phase velocity. Thus, when the cavity is mechanically stable without any phase noise in the ideal case, the output is expected to be a phase coherent pulse train as shown in Fig. 1.3.

If the cavity exhibits a high gain (small loss) for high peak intensities and a small gain (high loss) for low peak intensities, a pulse-like structure has a higher probability to be amplified and to survive in the cavity. In other words, if a small peak-like structure is generated from noise, its high-intensity part is more efficiently amplified than its low-intensity part, thus creating a temporally shortened structure with higher peak intensity. This way, the cavity may prefer to store short pulses and not continuous wave radiation.

Any intracavity material or mirror introduces dispersion. Luckily it is found that the nonlinear response (self-phase modulation) of the laser crystal may compensate the residual intracavity dispersion (including negative dispersion from chirped mirrors), if the peak intensity of the pulse is appropriate (see, for example, [9]). This effect helps to obtain a dispersion-free cavity in pulsed operation. When the intracavity peak intensity is adjusted appropriately with sufficient cavity finesse and pump power, a pulse-like structure develops into a short pulse whose width is sustained after one round trip in steady state due to the absence of intracavity dispersion. The complicated interplay of these phenomena results in stable pulsed operation of the laser (mode-locked laser).

The working principles of mode-locked lasers can also be understood in the frequency domain. Consider a laser operating in the continuous wave mode. If the finesse of the cavity is high enough, the cavity only allows the oscillation of frequencies that match the eigenfrequencies of the cavity. If we neglect the cavity dispersion, the frequency modes are equidistant. However, a dispersive cavity (which, without nonlinear response, is also called "cold cavity") has modes whose frequency separation is dependent on the frequency. Without special efforts to obtain single mode operation, the CW spectrum consists of multiple adjacent modes with random phases. Due to nonlinear processes such as four-wave-mixing in the crystal, additional modes tend to be created. If the intracavity dispersion is small enough, such that the additionally created modes overlap with the original eigenmodes of the cavity, the neighbouring eigenmodes are coupled and injection-locked. The more modes contribute to the pulse, the stronger the effect will be, because the peak intensity of the pulse increases with the number of contributing modes. This way, the output spectrum of a laser with a "hot cavity" (i.e. pulsed operation of the laser with nonlinearity) has a broadband comb structure whose tooth are tigthly phase-locked.

In the following, we examine how the mode-locking mechanism described above works in an actual setup. Consider a laser which has Titanium doped sapphire (Ti:sapphire) crystal as a gain medium. Fig. 1.4 describes the typical configuration of a mode-locked Ti:sapphire ring laser. The crystal is pumped with a continuous beam in the green wavelength region.

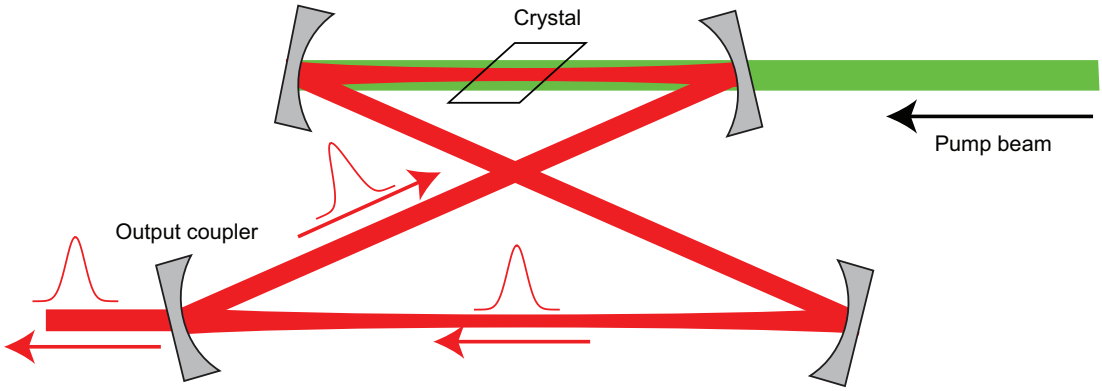

Figure 1.4: *Typical configuration of a mode-locked ring laser*

Typically, frequency doubled Yb or Nd -doped lasers are used to obtain pump beams with high average power at green wavelengths. Several options are at hand to achieve a peak intensity dependent gain in the cavity, such as introducing a saturable absorber into the cavity, taking advantage of the Kerr effect, and active modulation of the gain or cavity loss. In the last two decades, soft-aperture Kerr-lens mode locking (KLM) has been the method of choice for ultrashort pulse generation [4, 11, 12]. This method exploits the fact that - due to the intensity dependence of the refractive index of the crystal ($n = n_0 + n_2 I$, optical Kerr effect) - the laser crystal imposes a spatial phase shift on a traversing beam with high peak intensity. This spatial phase shift acts like a lens (Kerr lens) and focuses the resonating cavity mode tightly. Due to this Kerr-lensing effect, the spatial overlap between the cavity beam and the properly focused pump beam will improve when the intensity of the circulating pulse increases. As described in the previous section, the dispersion introduced by the intracavity material is compensated by the nonlinear reponse of the gain medium. However, to obtain broadband emission, it is crucial to prepare a preliminaly chirp compensated cavity. To this end, chirped mirrors or prism pairs can be employed to introduce negative dispersion. The advent of ultra-broadband chirped mirrors with tailored dispersion properties has been one of the key techniques in ultrashort pulse generation, making the generation of sub-two-cycle pulses (corresponding to spectra spanning an octave) directly from the oscillator possible [12, 13].

1.4 Measurement of carrier envelope offset frequency

As described above, an ideal unperturbed mode-locked laser emits a spectrum whose mode-frequencies read $\omega_{\mathrm{comb}} = N\omega_{\mathrm{rep}} + \omega_{\mathrm{CEO}}$. However, technical noise, e.g. intensity fluctuations of the pump laser and length drifts of the cavity due to thermal effects, lets ω_{rep} and ω_{CEO} drift as well. Therefore, the comb parameters have to be measured and stabilized.

The repetition frequency ω_{rep} can be easily measured by a fast photodiode, and the cavity length can be changed accordingly to keep the repetition frequency ω_{rep} constant. Piezoelectric-transducer (PZT) actuated mirrors that are controlled by an active feedback loop are typically used for this purpose. The offset frequency is less easily accessible. Several methods have been proposed for the measurement and stabilization of the offset frequency ω_{CEO} [14–19]. One commonly used method is to compare the original comb structure with the

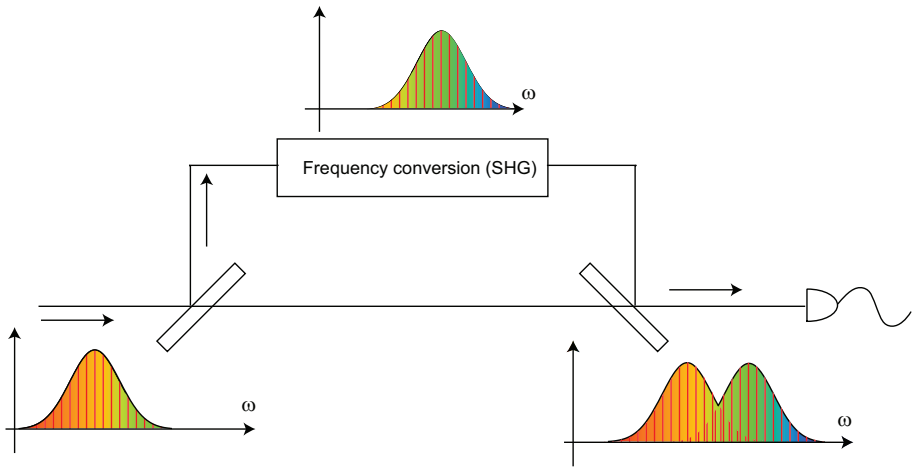

Figure 1.5: *Carrier envelope phase detection by nonlinear frequency conversion*

structure obtained after some nonlinear frequency conversion of the same frequency comb. This way, one can compare the ω_{CEO} before and after the frequency conversion and may obtain information about the original ω_{CEO}(self-referencing method: see Fig. 1.5).

This is particularly easy when the comb spans an octave and frequency-doubling is used as the nonlinear process. The comb structure after frequency-doubling can be described as

$$\omega_{\mathrm{2Hcomb}} = 2N'\omega_{\mathrm{rep}} + 2\omega_{\mathrm{CEO}}. \tag{1.13}$$

The frequency-doubled comb can be overlapped spatially with the original comb onto a photodiode. The two overlapping beams with different frequencies produce an amplitude modulation (beat) at the difference-frequency. The frequency of the beat signal between the two combs can be expressed by taking the difference between two comb modes,

$$\omega_{\mathrm{2Hcomb}} - \omega_{\mathrm{comb}} = (2N' - N)\omega_{\mathrm{rep}} + \omega_{\mathrm{CEO}}. \tag{1.14}$$

If we focus on the spectral region where $2N' - N = 0$, a radio-frequency beat note with a frequency of ω_{CEO} will be observed. This method is called f-to-$2f$ interferometry [15, 17, 20]. A typical setup for the detection of ω_{CEO} based on the f-to-$2f$-method is illustrated in Fig. 1.6. Note that a laser bandwidth larger than one octave is required to be able to overlap spectral regions that satisfy $2N' - N = 0$. A photonic crystal fiber (PCF) is used to broaden incident spectra whose original bandwidth is less than one octave. A small grating spectrometer filters out the required spectral portion to obtain a better signal-to-noise ratio.

The measured ω_{CEO} can be used as an error signal for an active feedback loop controlling ω_{CEO}. For example, the overall frequency can be shifted by introducing an acousto-optic modulator (AOM) into the laser output. Alternatively, ω_{CEO} can also be changed by adjusting the amount of material inserted into the cavity (e.g., by movable wedge plates) [22, 23]. For very fast control of ω_{CEO}, a small change in the intracavity laser power can be introduced by modulating the pump power [21, 24].

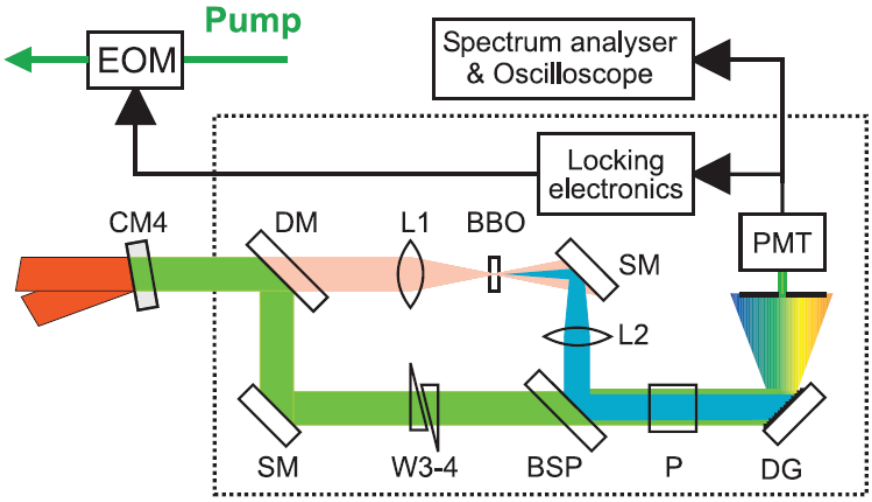

Figure 1.6: *Example of f-to-$2f$ interferometer for the measurement of the carrier envelope offset frequency ω_{CEO} [21]. The frequency-doubled beam is overlapped with the original beam using a Mach-Zehnder interferometer. The delay between the two arms can be adjusted with movable wedge plates (W) so that the two pulses overlap temporally at the detector. The overlapped beams are spectrally dispersed by a grating, and the desired spectral region is detected with a fast and sensitive detector such as an avalanche photodiode or a photo multiplier tube (PMT). SM: silver-coated mirror, L: lens, P: polarizer, DM: dichroic mirror, EOM: electro-optical modulator, DG:diffraction grating, BBO: Beta-Barium Borate crystal, BSP: beam splitter, P:polariser.*

1.5 Applications of frequency combs

1.5.1 A frequency reference for high precision spectroscopy

For spectroscopy, the photon energy of the radiation has to be known precisely. The simplest way to determine the photon energy of light is to measure its wavelength and convert it into photon energy. The measurement of wavelength (or spectral dispersion of multi-colored light) reaches back into the 17^{th} century when the wavelength-dependence of refraction was used. Precise measurements of wavelength in recent days use Fourier spectroscopy methods (wavemeter). In a Michelson interferometer, the interference between its two arms can be measured as a function of time when one arm is scanned. With a calibrated scanning speed, the wavelength of the light can be identified from the modulation frequency of the interference signal. Several variations and improvements of this method have been invented, such as using a stable laser as a reference, or employing a Fizeau-type interferometer without any moving components. The accuracy of these methods is ultimately limited by the wavefront distortion of the measured beams, since the interference profile of two beams critically depends on their wavefront.

The most direct and precise way of characterizing the photon energy of radiation is to measure its frequency. In the radio frequency domain, this can be simply done by counting the oscillation cycles of the radiation. For optical frequencies, however, direct counting of cycles is extremely challenging, if not impossible. In the case of visible light (500 nm), the corresponding optical frequency is 600 THz and has an oscillation period of 1.7 fs. The only possible way currently available to investigate such a short time scale would be a pump-probe

method, such as frequency resolved optical gating (FROG). The fastest realtime detection of optical pulses without using such a pump-probe technique is to use an optoelectronic streak camera, in which the generated photo-electrons are deflected by a fast scanning electric field. Although the method is applicable to detect a fast change in the optical intensity on the timescale of up to a few hundred fs, the detection of single optical cycles is not possible.

Vast efforts have been made to phase-coherently link optical frequencies to a countable frequency region (e.g., the radio frequency domain) [25, 26]. Here, "phase-coherently" means that the phase variations are continuously linked, and thus, the number of cycles of the original laser radiation can be reproduced by counting the cycles of the radio frequency after a sufficiently long measurement time. Fig. 1.7 shows the direct phase link between the calcium line at 456 THz and a cesium frequency standard at 9.2 GHz demonstrated by Schnatz et al. [26]. This method is called frequency chain.

Even though direct frequency measurements improved high precision spectroscopy, as shown in Fig. 1.8, the required experimental effort were enormous as illustrated in Fig. 1.7. A few years later, it was found that the frequency comb can be used to coherentently link the optical and the radio frequency domain. The setup when using a frequency comb is significantly simplified compared with the frequency chain [27]. As can be seen from Eqn. (1.8), the frequency of each comb mode can be uniquely identified by three values: the mode number (N), the repetition rate (ω_{rep}), and the offset frequency (ω_{CEO}). For a conventional frequency comb generated by mode-locked lasers, ω_{rep} typically lies in the MHz to GHz region. The mode number N can be defined such that $\omega_{\mathrm{CEO}} < \omega_{\mathrm{rep}}$. Thus, Eqn. (1.8) shows that the frequency of the comb modes (which is in the optical frequency region) can be determined by measuring two radio frequencies (ω_{rep} and ω_{CEO}).

In practical applications, the frequency comb eliminates the need for the complicated frequency chain setups previously used for frequency measurements. The frequency of a narrow bandwidth laser can be determined by measuring the beat signal between the laser and a frequency comb. For that, the wavefronts and polarizations of the target laser and the frequency comb have to be matched (see Fig. 1.9 and its caption for the details). The beams are then overlapped and detected with a fast photo diode. If the linewidth of the target laser is narrow enough compared with the mode separation of the frequency comb, the obtained signal is expected to be modulated with the beat frequencies. These beat frequencies are determined by the frequency differences between the target laser frequency and the frequencies of the comb modes. Thus, multiple beat frequencies exist that correspond to the beat between the different comb modes. Experimentally, the lowest beat frequencies are often filtered out and measured. Thus, let's define the beat frequency (ω_{beat}) to be the lowest order beat frequency which is given by the frequency difference between the laser and the closest mode.

$$\omega_{\mathrm{beat}} = |\omega_{\mathrm{comb}} - \omega_{\mathrm{laser}}| = |N\omega_{\mathrm{rep}} + \omega_{\mathrm{CEO}} - \omega_{\mathrm{laser}}|. \tag{1.15}$$

The frequency of the target laser ω_{laser} is given by:

$$\omega_{\mathrm{laser}} = N\omega_{\mathrm{rep}} + \omega_{\mathrm{CEO}} \pm \omega_{\mathrm{beat}}. \tag{1.16}$$

If the target laser frequency is already known within the precision of half the spacing of the comb modes, the mode number N can be identified, and the target laser frequency can be measured based on Eqn. (1.16). If the uncertainty of the target laser is too large to identify

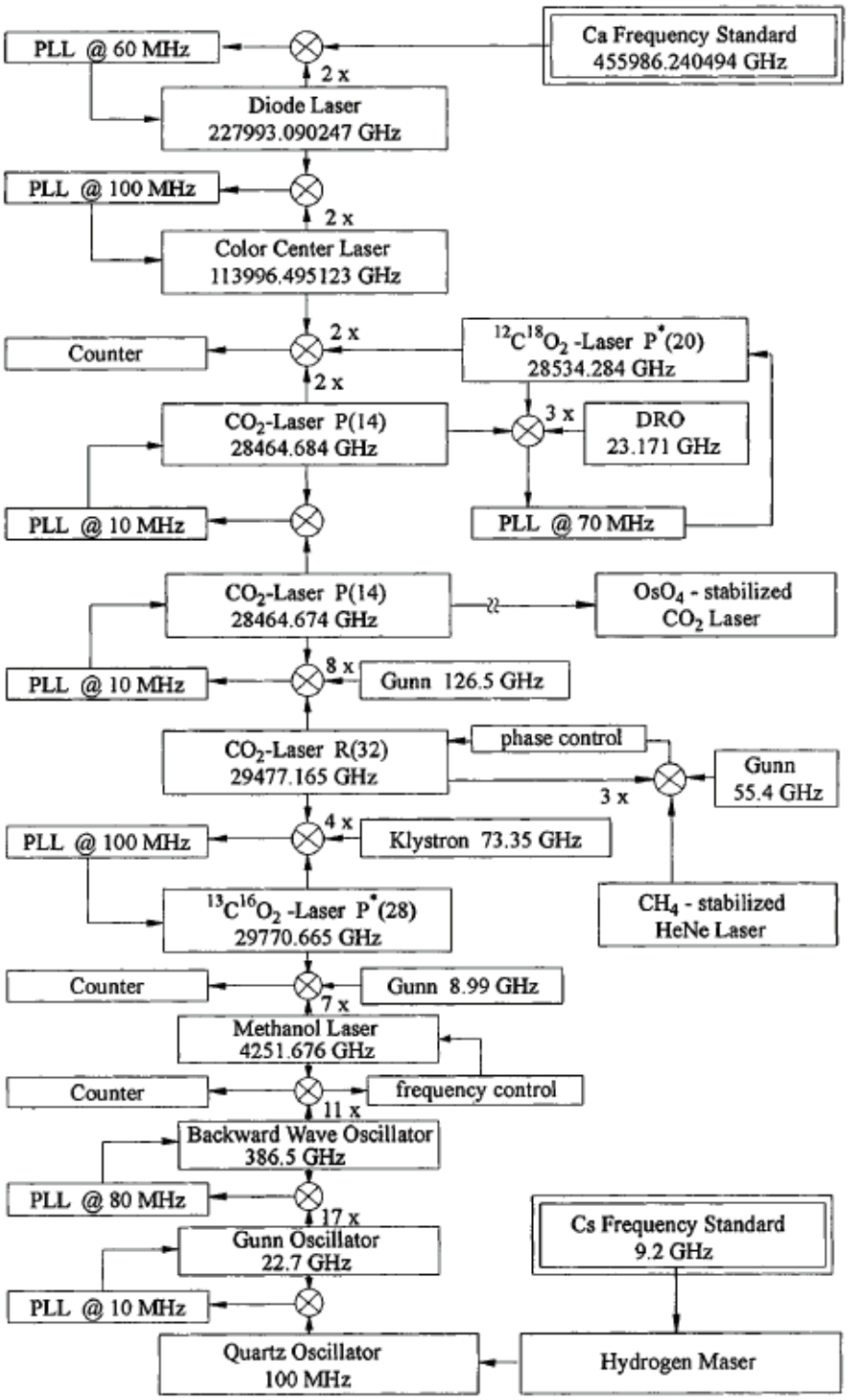

Figure 1.7: *Direct coherent phase link between the calcium line at 456 THz and the cesium frequency standard at 9.2 GHz [26]. Courtesy of Dr. Harald Schnatz.*

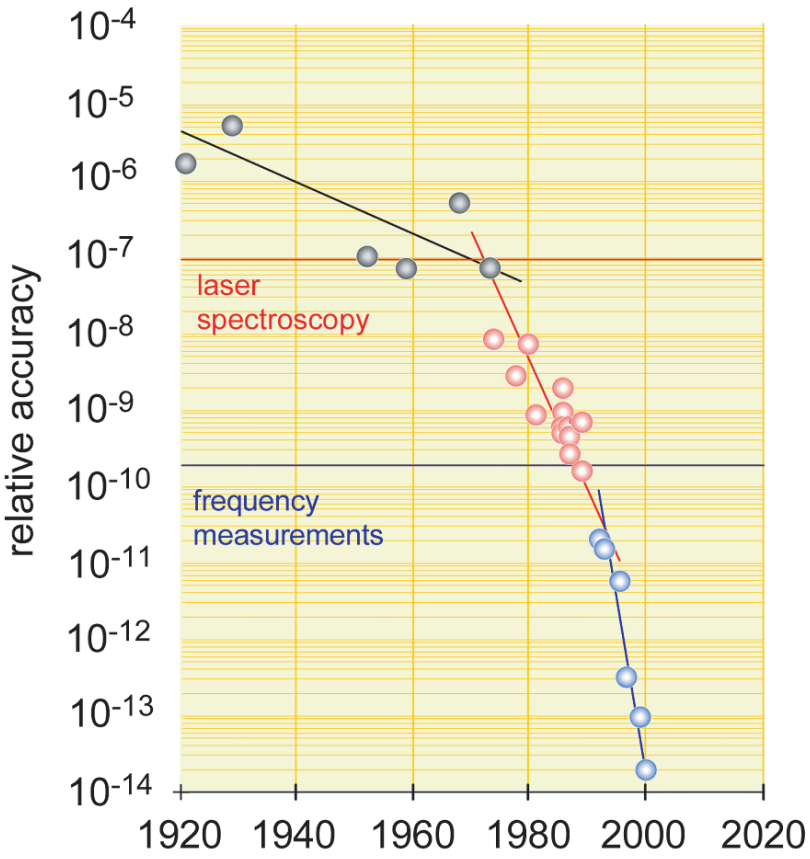

Figure 1.8: *Relative accuracy in the history of hydrogen spectroscopy. Two kinks can be seen corresponding to the invention of laser spectroscopy and direct frequency measurements. (By courtesy of T.W.Hänsch)*

the mode number N, the following method still allows to determine the mode number N unambiguously (see also [28]).

When the beat signal can be measured with two different repetition frequencies (ω_{rep1} and ω_{rep2}), the following relations can be obtained [3]:

$$\omega_{\mathrm{laser}} = N_1\omega_{\mathrm{rep1}} + \omega_{\mathrm{CEO}} \pm \omega_{\mathrm{beat1}} \tag{1.17}$$

$$\omega_{\mathrm{laser}} = N_2\omega_{\mathrm{rep2}} + \omega_{\mathrm{CEO}} \pm \omega_{\mathrm{beat2}}. \tag{1.18}$$

Eqn. (1.17) and Eqn. (1.18) can be reduced to

$$N_1 = N_2\frac{\omega_{\mathrm{rep2}}}{\omega_{\mathrm{rep1}}} + C. \tag{1.19}$$

where the constant C is given by:

$$C = (\pm\omega_{\mathrm{beat1}} \pm \omega_{\mathrm{beat2}})/\omega_{\mathrm{rep1}}. \tag{1.20}$$

[3] The following argument can be easily generalized for two different offset frequencies.

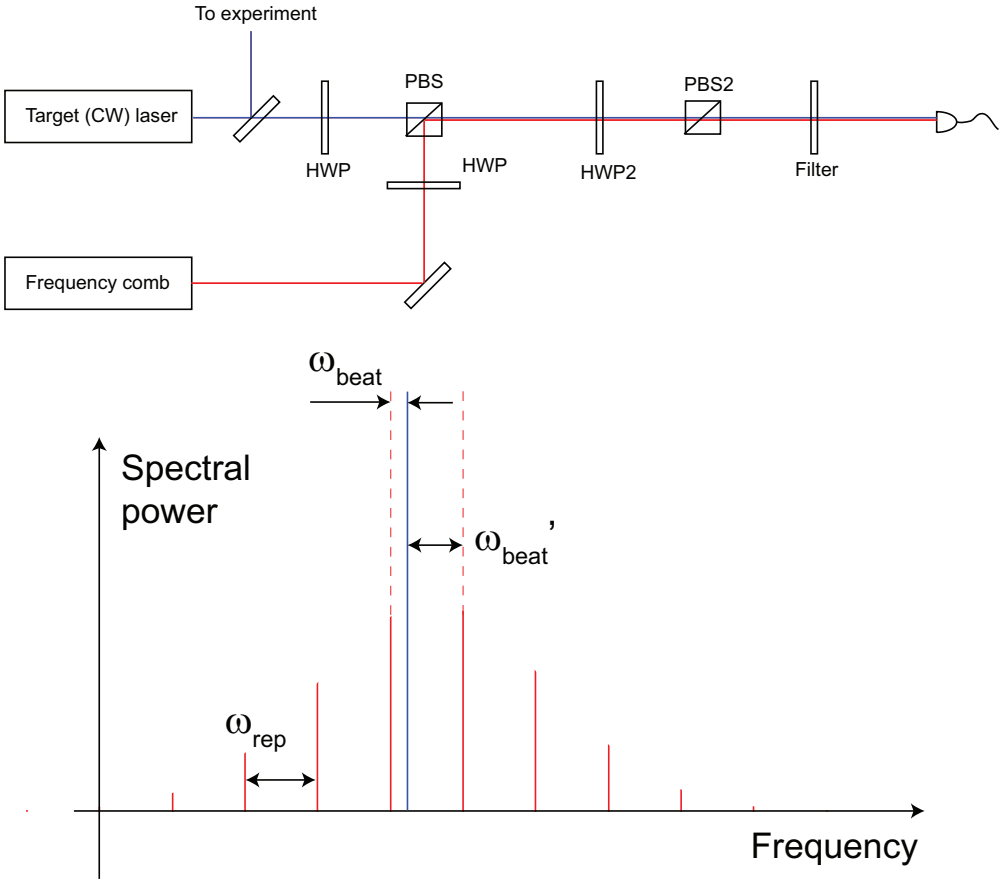

Figure 1.9: *Frequency measurement of a narrow bandwidth laser with a frequency comb. To observe the beat signal between the target laser and the frequency comb, the polarizations and the wavefronts of the two have to be matched. By adjusting the half-wave plates (HWP) installed directly after the lasers, the two beams can be overlapped collinearly with orthogonal polarization after the first polarizing beam splitter (PBS). The next half-wave plate (HWP2) rotates the polarization of both beams by 45 degrees. The rotated polarization is then projected with the next polarizing beam splitter (PBS2) to obtain two overlapping beams with identical polarization. The narrow spectral region around the target laser frequency is filtered out to obtain a beat signal with high signal-to-noise ratio. The beat frequency* ω_{beat} *is determined by the frequency difference between the target laser freqeuncy and the frequency of the adjacent comb mode.*

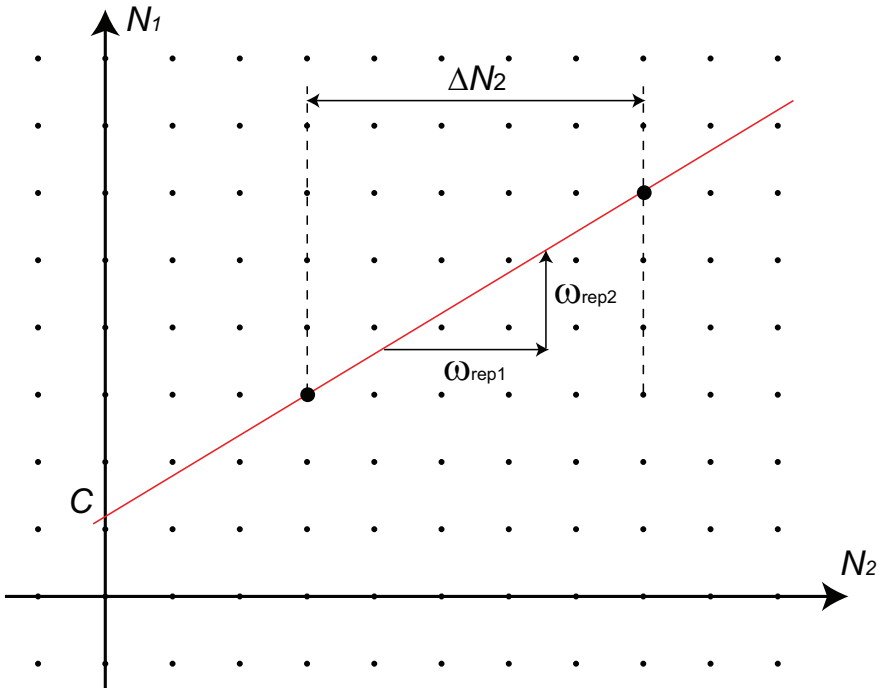

Figure 1.10: *Determination of the mode number (N) when the uncertainty of the target frequency is larger than half the spacing of the comb modes. The problem to find the proper mode numbers in Eqn. (1.17) and Eqn. (1.18) is equivalent to finding the grid points (N_1, N_2) lying on the straight line given by Eqn. (1.19). If the two repetition rates are properly chosen, the distance between the two grid points (ΔN_2) can be large enough to identify the proper mode number without ambiguity.*

Eqn. (1.19) indicates that the problem to identify the mode number is equivalent to finding the grid points (N_1, N_2) lying on the straight line described by Eqn. (1.19) (see Fig. 1.10). The distance ΔN_2 between neighboring grid points satisfying Eqn. (1.19) is equal to the minimum integer number that makes $\Delta N_2 \omega_{\mathrm{rep2}}/\omega_{\mathrm{rep1}}$ an integer value. With properly chosen repetition rates ω_{rep2} and ω_{rep1}, ΔN_2 can be large enough to identify the mode numbers N_1 and N_2 without ambiguity.

As a real-world example for the use of a frequency comb in a spectroscopy experiment, consider high precision spectroscopy of the 1s-2s transition of atomic hydrogen. A typical way to perform high precision spectroscopy is to use a frequency-stabilized laser for the excitation of the target and to then try to measure the frequency of the driving laser. Fig. 1.11 illustrates the setup [29–31].

A frequency-doubled dye laser is stabilized to a stable reference cavity to obtain narrow linewidth. The stabilized laser excites the hydrogen atoms while the frequency of the driving laser is scanned by an acousto-optic modulator (AOM). The frequency of the driving laser is measured by a frequency comb with the method mentioned above. Both repetition rate and offset frequency of the frequency comb are referenced to a 10 MHz frequency standard. The 10 MHz frequency standard is calibrated against the cesium-clock network of the global positioning system (GPS) satellites. The cesium-clock network can be compared with a cesium fountain clock network on the ground. Thus, the frequency of the hydrogen 1s-2s transition can be compared with the cesium fountain clock network, which defines the SI second.

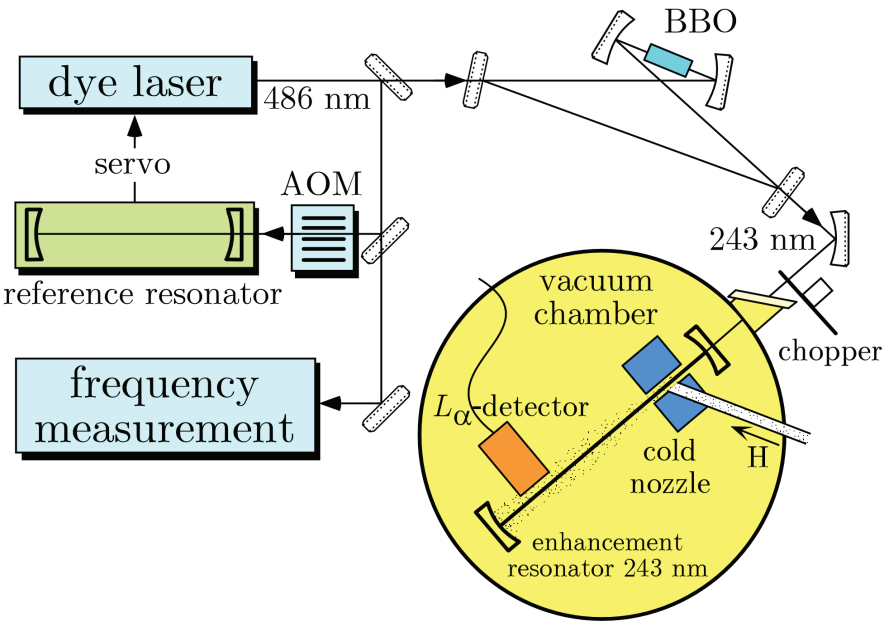

Figure 1.11: *Setup for high precision spectroscopy of the 1s-2s transition in atomic hydrogen*

1.5.2 Direct excitation with frequency comb

In the previous section (Sec. 1.5.1), the frequency comb was employed as a frequency calibration tool for a laser driving a transition.

Alternatively, the frequency comb itself can also be used as a driving laser to excite the target transition. The spectrum of the frequency comb given by Eqn. (1.8) shows that the frequency comb consists of many continuous wave lasers with narrow linewidth. The target transition can be driven with one of the comb mode as demonstrated by Gerginov et al. for the D_1 and D_2 transitions in cesium [32]. The average power of the frequency comb is distributed among all the comb lines. For example, a femtosecond frequency comb with a (Fourier-limited) pulse duration of 100 fs at a wavelength of 800 nm corresponds to a bandwidth of 4.4 THz. Assuming a repetition rate of 100 MHz and an average power of 0.5 W, the power contained in a single comb line is only 11 μW. Thus, for direct frequency comb spectroscopy, both high average power and high repetition rate will be preferable for the investigation of weak transitions.

It is interesting to note that direct frequency comb spectroscopy is an extension of Ramsey spectroscopy. In the case of Ramsey spectroscopy, the first pulse excites the target atom and coherently links its ground state and its excited state. When the second pulse interacts with the pre-excited target, the population of the excited state can increase or decrease, depending on the phase relationship between the second pulse and the atomic state. This can be understood as an interference produced by the coherent interaction of the first and the second pulse with the target atom. Similarly, when more than two pulses were applied, constructive or destructive interference would occur between the contributions from different pulses, but with higher sensitivity to the phase differences. This is the time-domain interpretation of direct frequency comb spectroscopy.

Apart from using only one mode for spectroscopy, the entire combs (and hence all the power) can be used for excitation. A particularly interesting case is a two photon transition

excited by a comb. In the case of a two-photon transition, as illustrated in Fig. 1.12, two independent comb modes can contribute to the excitation [33, 34].

These two modes ω_{comb1} and ω_{comb2} have to satisfy energy conservation

$$\omega_{\text{target}} = \omega_{\text{comb1}} + \omega_{\text{comb2}} \tag{1.21}$$

where ω_{target} is the transition frequency.

Since the modes of the comb are equidistantly distributed, all pairs of comb modes that satisfy Eqn. (1.21), as long as the offset frequency of the comb is adjusted such that the transition frequency either coincides with one of the comb modes or lies exactly between two modes (see Fig. 1.12). For the contributions from all the comb pairs to add up constructively, the contributions have to be phase-matched. This can be obtained if the spectral phase $\phi(\omega)$ satisfies

$$\phi(\omega_{\text{target}} - \omega) + \phi(\omega_{\text{target}} + \omega) = \text{constant}. \tag{1.22}$$

Note that a Fourier-limited pulse is sufficient but not necessary to satisfy Eqn. (1.22). When Eqn. (1.22) is satisfied, the contributions from all the mode pairs add up coherently and efficient excitation of the transition becomes possible, as experimentally demonstrated for the cesium 6s-8s transition by Fendel et al. [35] (see also [33, 36, 37]).

1.6 High precision spectroscopy of He^+

The determination of the 1s-2s transition frequency of atomic hydrogen with high precision has been one of the most accurate tests of the theory of quantum electrodynamics (QED), thus verifying one of the fundamental theories of physics [29, 31, 38, 39]. The energy structure of a simple atom such as hydrogen or helium can be calculated in the framework of bound state QED [40]. In this calculation, the contribution of the self-energy correction of the electron and the vacuum polarization are perturbatively expanded by $(Z\alpha)$ and $\ln(Z\alpha)^{-2}$, with Z and α being the nuclear charge and the fine structure constant, respectively [41, 42]. Vast efforts have been made to numerically calculate the coefficients of each expansion term [43]. Since the interesting higher order corrections scale with high powers of Z, spectroscopy of He^+ promises to be more sensitive to higher-order contributions compared to hydrogen. Moreover, high precision spectroscopy of helium ions is advantageous compared to hydrogen spectroscopy due to following aspects:

- He^+ can be trapped in an ion trap and can be sympathetically cooled, which will significantly reduce the systematic shift of the transition frequency due to the second order Doppler and time-of-flight (TOF) broadening effect.
- The He^+ nucleus is identical to an α-particle and does not have nuclear angular momentum. Thus the energy level structure of He^+ is simpler than that of hydrogen due to the lack of hyperfine structure.
- The nuclear charge radius is known better for the α-particle than for the proton, which enters the QED calculation of hydrogen as one of the biggest uncertainties.

The reader may refer to the literature [44] for further details on He^+ spectroscopy. In this section, we would like to focus on the experimental problems that the development of

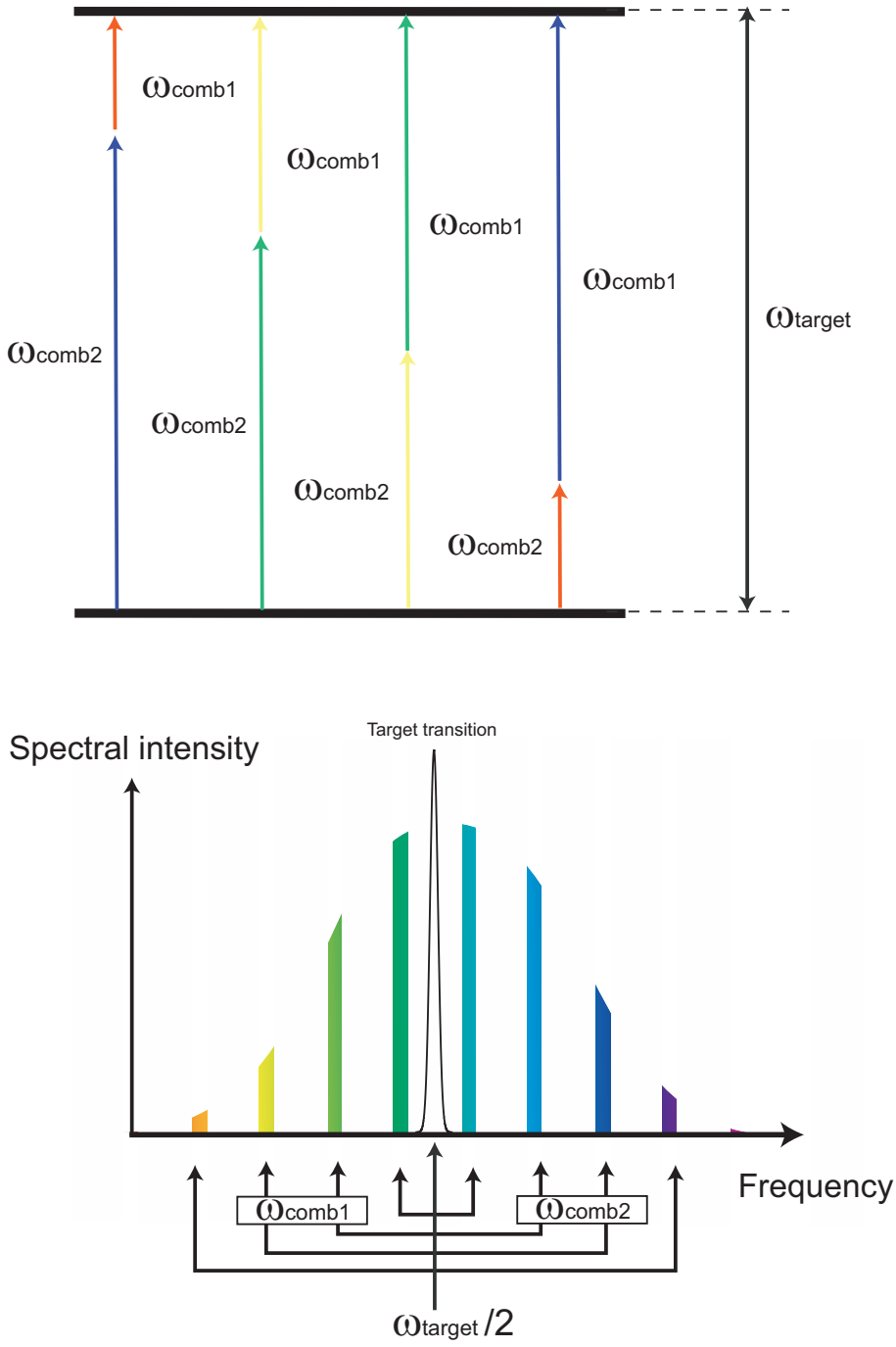

Figure 1.12: *Direct excitation of a two photon transition with a frequency comb. When considering a two photon excitation where either photon originates from a different comb mode, there are many pairs of comb lines that can contribute to the transition, if the transition line lies either exactly between two comb lines or on the comb line.*

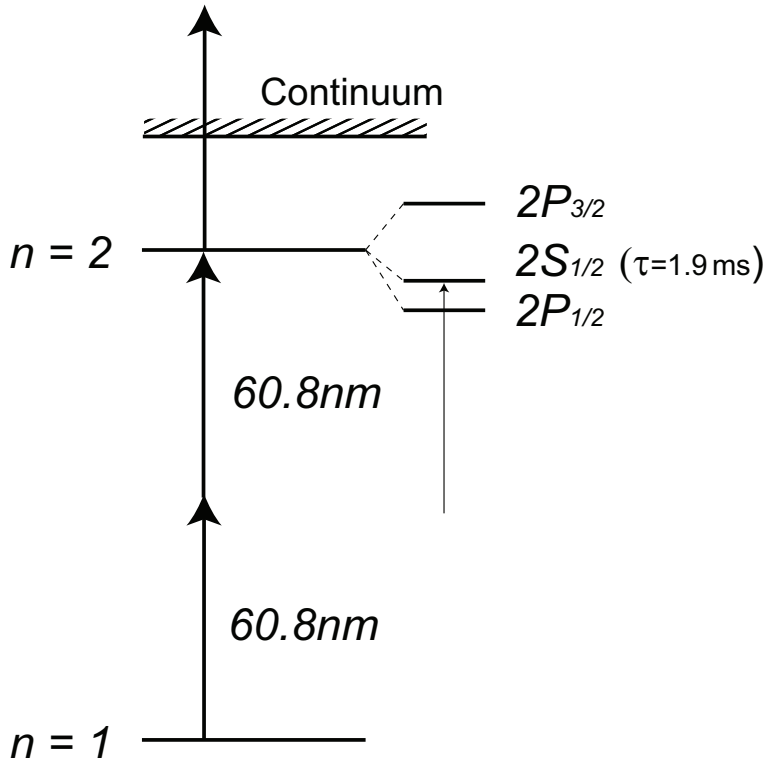

Figure 1.13: *Energy levels of the $^4He^+$ ion. The transition energy between the 1S and the 2S state is 40.8 eV. The excitation of the 2S state from the ground state by two photon abosorption requires 60.8 nm radiation. The lifetime of the 2S state (τ) is 1.9 ms, which is equivalent to a natural linewidth of 84 Hz.*

the driving laser required for high precision spectroscopy of the He^+ 1s-2s transition brings along.

Fig. 1.13 shows the energy levels of the $^4He^+$ ion. To excite the 2S state from the ground state in a two photon absorption process, 60.8 nm radiation is required. Based on the spectroscopic scheme proposed by Herrmann et al. [44], one or more He^+ ion(s) are stored in an ion trap together with coolant ions used for sympathetic cooling of He^+ [4]. The two photon excitation into the 2S state will be driven by an extreme ultraviolet (XUV) frequency comb centered at 60.8 nm, since there is no CW laser available in this wavelength region. The 2S state will then be further excited into the continuum, and the thus created $^4He^{++}$ ions are detected, either outside the trap with an ion-detector (channeltron), or inside the trap by monitoring the fluorescence signal of the coolant ions (secular scan).

In this scheme, an XUV frequency comb at 60.8 nm with sufficient average power is required. An estimation of the required average power of the XUV comb is mandatory for the development of such laser systems. In the work by Herrmann et al. [44], the expected signal count rate of the He^+ spectroscopy is estimated for different excitation geometries. Here, let's compare two possible geometries for the excitation of a single He^+ ion. Fig. 1.14 and Fig. 1.15 illustrate these two schemes of anti-collinear and collinear excitation, respectively.

[4] $^4He^+$ lacks cooling transition accessible with convenient lasers.

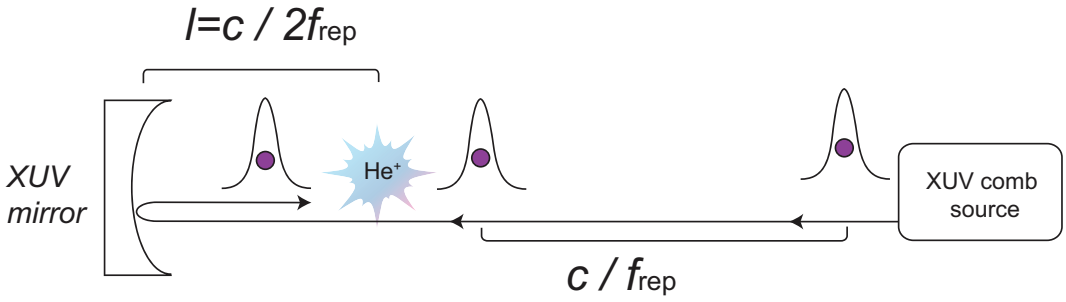

Figure 1.14: *Anti-collinear excitation geometry for* He^+ *spectroscopy. Two counter-propagating pulses produce a standing wave in the interaction region. Each of the two photons for the excitation can be taken from a different pulse.*

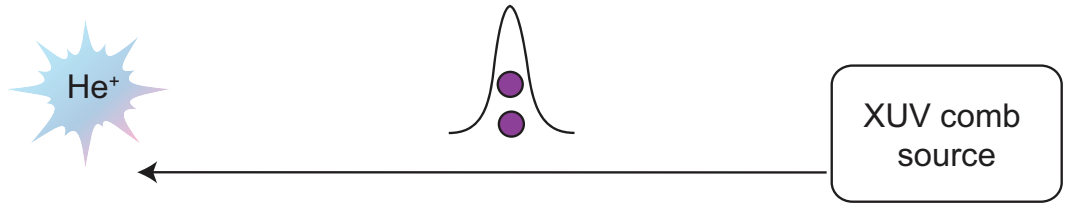

Figure 1.15: *Collinear excitation geometry for* He^+ *spectroscopy. Two photons are taken from a single excitation pulse.*

A Doppler-free transition can be obtained when the two-photon transition is driven with two photons (with similar photon energy) that are propagating anti-collinearly (anti-colliear excitation). The calculated excitation rate is shown in Fig. 1.16.

Experimentally, the simplest method to obtain an anti-collinear geometry is to use an interferometric method to overlap a first pulse with the next incoming pulse in the interaction region. Fig. 1.14 illustrates a single highly reflective XUV mirror to reflect and focus the first pulse onto the He^+ ion. If the distance l between the target ion and the mirror satisfies $l = c/(2f_{rep})$, the next incoming pulse will overlap with the first pulse at the location of the target ion. The alignment of the interferometer required for the anti-collinear excitation might be challenging, since the two pulses have to overlap both temporally and spatially to obtain a signal. The difficulty increases with the size of the interferometer. To realize the anti-collinear excitation geometry, a smaller interferometer, that is, a higher repetition rate of the XUV frequency comb will be preferable. In addition, the limited reflectance of the XUV mirror would limit the power that is available for excitation. In order to simplify the setup and make the experimental realization easier, the transition can also be excited in a collinear geometry as shown in Fig. 1.15. For collinear excitation, the excitation rate is weakened due to the re-distribution of the matrix elements over many motional sidebands in the spectrum. The expected excitation rate for the collinear excitation geometry is shown in Fig. 1.17. It can be seen that the excitation rate deteriorates ~ 2 orders of magnitude compared with the anti-collinear geometry.

The above discussion shows that an appropriate excitation geometry has to be chosen depending on the required signal rate and the available power of the XUV frequency comb.

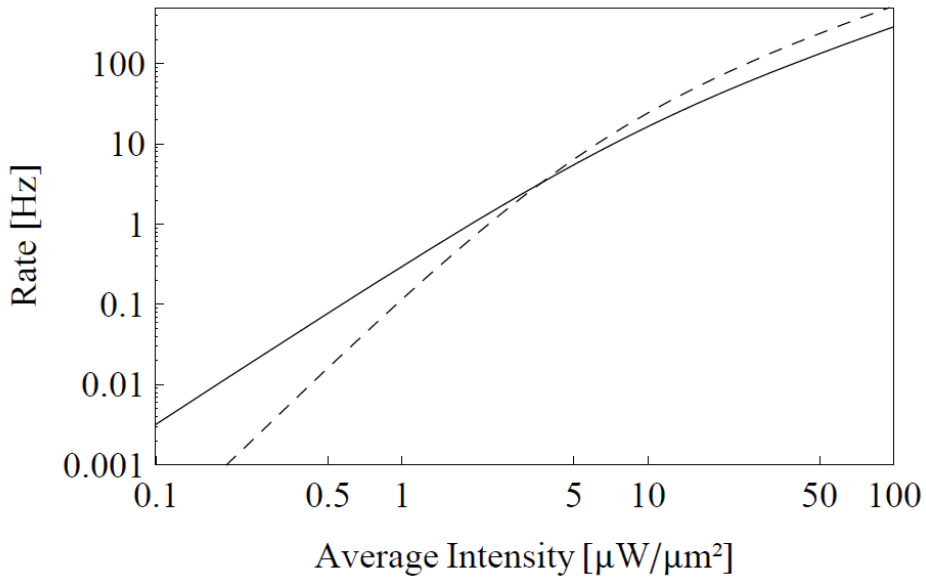

Figure 1.16: *Expected excitation (solid) and ionization rates (dashed) for a single* He^+ *ion, anti-collinear excitation geometry [44].*

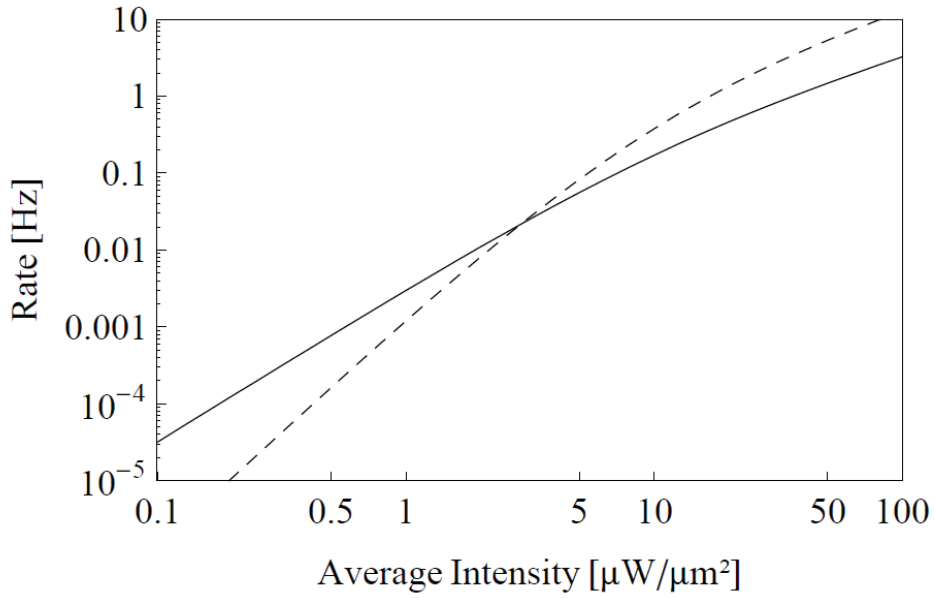

Figure 1.17: *Expected excitation (solid) and ionization rates (dashed) for a single* He^+ *ion, collinear excitation geometry assuming a matrix element reduced to 10% [44].*

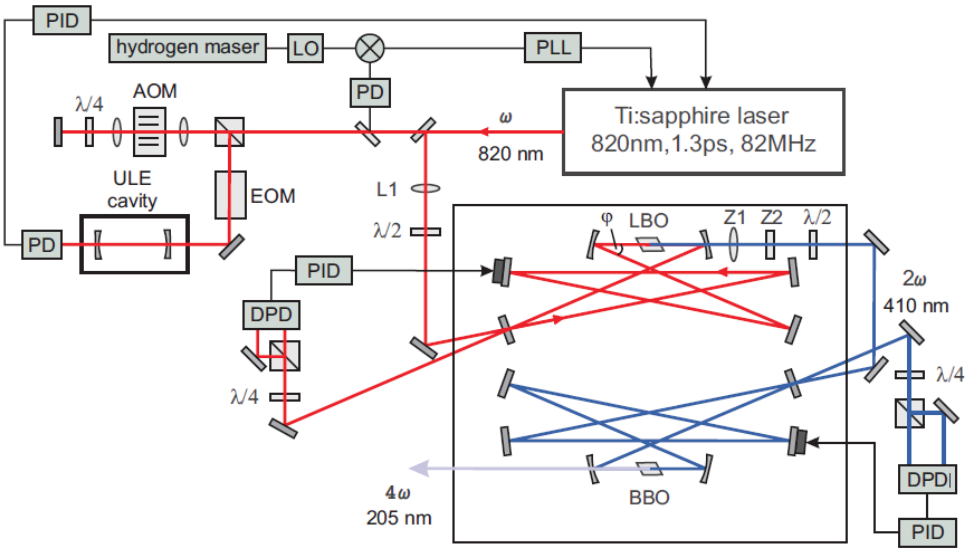

Figure 1.18: *Frequency comb generation in the UV. Two consecutive stages of frequency doubling from 820 nm yield a frequency comb with an average power of 70 mW at 205 nm [45].*

1.7 Frequency conversion into the ultraviolet region

The wavelength region in which frequency combs are available is limited by the wavelength region in which mode-locked lasers and nonlinear frequency conversion are available. Most of the recent mode-locked lasers are available in the near-IR to IR region [5]. For example, a Ti:sapphire based frequency comb is typically centered at 800 nm [6]. Yb- and Er-based frequency combs are available at around 1040 and 1550 nm, respectively. Frequency doubling with nonlinear crystals has been widely used to extend IR frequency combs into the visble and ultra-violet (UV). In the demonstration by Peters et al. [45], a frequency comb with an average power of 70 mW is generated at 205 nm from a frequency comb at 820 nm with two consecutive frequency doubling stages (Fig. 1.18).

The accuracy of the comb structure after frequency conversion in a crystal has been tested to one part in 10^{20} [46]. The shortest wavelength achievable with frequency conversion through a solid state crystal is limited by the transparency and the phase matching condition of the crystal. By adopting a tailored crystal structure such as $KBe_2BO_3F_2$ (KBBF), the generation of UV frequencies as short as 156 nm is possible with a μW power level [47] (Fig. 1.19).

To obtain shorter wavelengths, four-wave-mixing in gaseous media has been demonstrated [48–50]. In this method, 20 nW of continuous wave (CW) radiation is obtained at 122 nm (Lyman-α) by utilizing mercury vapour.

For the generation of frequency combs at even shorter wavelengths, high order harmonic generation (HHG) has been used [51–53]. The details of extreme ultraviolet (XUV) frequency comb generation by means of HHG will be the major topic of the next chapter.

[5] Mode-locked dye lasers could be operated at visible wavelengths.
[6] A Ti:sapphire lasers can be octave spanning.

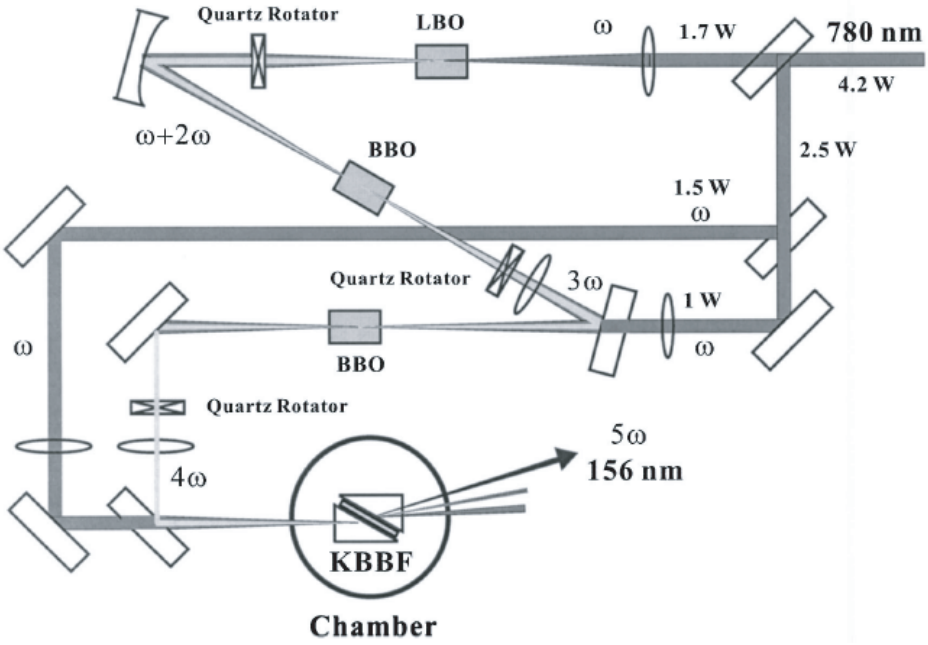

Figure 1.19: *Setup for fifth harmonic generation at 156 nm starting from 780 nm radiation from a Ti:sapphire laser [47].*

Chapter 2

XUV frequency comb generation with a femtosecond enhancement cavity

2.1 Introduction

In this section, extreme-ultra-violet (XUV) frequency comb generation by means of cavity assisted high harmonic generation (HHG) will be discussed. In order to utilize the HHG process for frequency conversion from infrared (IR) to the XUV wavelength region, a sufficiently high peak intensity has to be obtained to drive the HHG process efficiently. In conventional HHG experiments, amplifiers that boost the pulse energy by sacrificing repetition rate have been widely used. Such a low repetition-rate amplifier can be phase stabilized [54], however, the dense comb structure (due to the low repetition rate) makes it hard to use the amplifier for spectroscopic applications. For example, if we take a frequency comb with 1 kHz repetition rate for direct frequency comb spectroscopy, the spectral structure of the target transition should not exceed a width of half of the repetition rate (500 Hz). In addition, the identification of the exact mode number of the comb line would be tricky with such a dense comb structure. Moreover, the power contained in a single comb line is significantly reduced due to the large number of comb lines within the laser bandwidth. For application in He^+ 1s-2s spectroscopy, due to the reason discussed in Sec. 1.6, a repetition rate as high as in the GHz range is preferable. In order to obtain the high pulse energies and peak intensities necessary for HHG at a very high repetition rate, cavity assisted high harmonic generation has been invented [51, 52]. In this method, passively enhanced *intra-cavity* pulses drive HHG at the full repetition rate of the mode-locked oscillator, enabling XUV frequency comb generation at MHz to GHz repetition rates.

In this chapter, firstly, the theoretical aspects of the HHG process will be introduced (Sec. 2.2). The theoretical description of femtosecond enhancement cavities will be discussed in Sec. 2.3. The experimental demonstration of a femtosecond enhancement cavity and XUV frequency comb generation at 10 MHz repetition rate will be described in detail in the succeeding sections (Sec. 2.4).

2.2 High harmonic generation (HHG)

High order harmonic generation (HHG) is a strongly nonlinear process that enables frequency conversion of an IR beam down into the XUV and even into the x-ray region [55–57]. The physics of high harmonic generation has been investigated extensively both experimentally and theoretically for more than 20 years [58–61]. The understanding of HHG can be separated into two aspects: single atom response and phase matching. The "single atom response" of HHG describes the microscopic picture of the high harmonic (HH) emission from a single emission element (most often a single atom or a single molecule). "Phase matching" illustrates how weak HH emission from single emission elements adds up constructively to form powerful HH radiation.

Single atom gases, molecular gases and solid-state materials have been utilized as target medium for HHG. HHG from molecular gases is attracting attention in terms of potentially efficient XUV sources, molecular orbital tomography, atto-second electron dynamics, HHG during molecular-vibration or dissociation processes, and investigations on HHG from several (inner) molecular orbitals (see, for examples [62–64]).

Here, let's consider the simplest target: a ground-state single hydrogen atom, and try to understand the fundamental process of HHG. The single atom response of high harmonic generation can be classified into two regimes: the perturbative and the non-perturbative regime. The perturbative regime stands for high harmonic generation with a rather low driving intensity or low orders of HHG. Here,"low field intensity" means that the additional potential due to an applied field is weaker than the nuclear potential that the electron is exhibited to in the atom. First, let's take a close look at this perturbative regime.

2.2.1 Single atom response of HHG: perturbative regime

A single electron in the ground state of the hydrogen atom is described by the electron wavefunction of the 1s state. The simplest view of HHG is to ascribe the photon emission to a perturbative motion of the electron wavefunction. When a static electric field is applied onto the electron wavefuntion, the wavefunction is expected to be shifted in space and deformed due to Coulomb interaction. When a sinusoidally changing electric field (like an electric field of optical radiation) is applied, the wavefunction is expected to move periodically, as shown in Fig. 2.1. When the field strength is not too strong, the movement of the wavefunction is expected to follow the sinusoidal change of electric field, thus, the dipole moment of the system will also oscillate accordingly.

When the driving field is weak enough the effective potential that the electron feels from the nucleus is approximated to be constant over the displacement of electron, and the response of the dipole moment will be proportional to the driving field. On the other hand, if the field strength of the optical field is stronger, the wavefunction deforms rather strongly and the response of the dipole moment starts to deviate from a linear response to the driving field, resulting in a non-sinusoidal oscillation of the dipole moment. Therefore, high harmonic frequency components of the driving field will be included. When the driving field is not too intense, the high harmonic frequency shows up as modulation sidebands that decay exponentially for higher orders. This picture can be illustrated with a very simple model. Let us consider a 2-dimensional motion of a classical particle (electron) in the potential ($V(r)$) described by

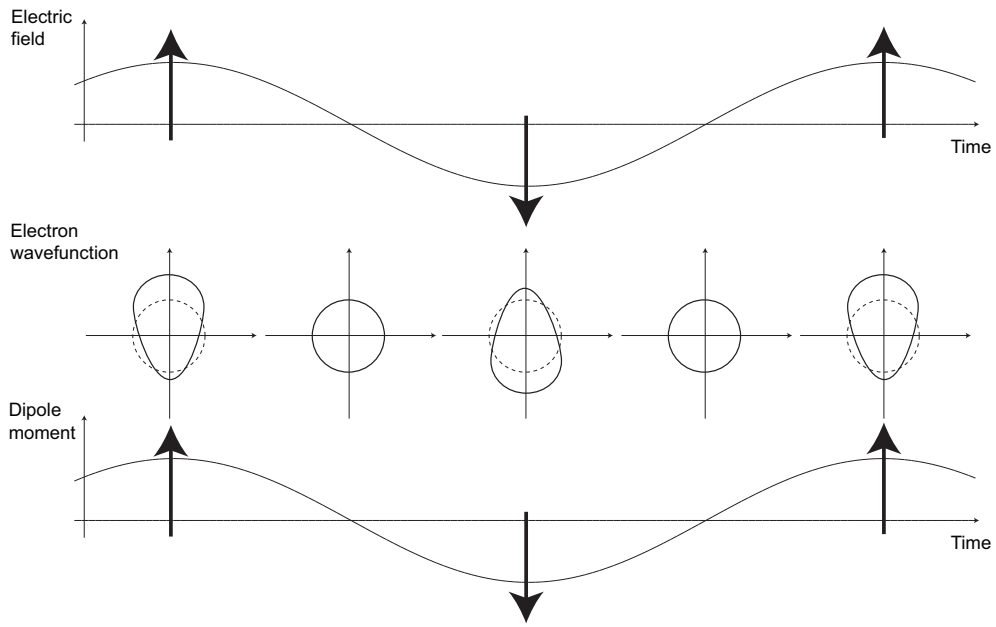

Figure 2.1: *Illustration of high harmonic generation in the perturbative regime.The ground state electron wavefunction is modulated periodically by the optical field. The dipole moment of the system is also modulated with the same frequency. When the field strength is strong enough, the movement of the wavefunction is no more sinusoidal and produces high harmonic components of the driving optical field in the dipole moment.*

$$V(r) = -\frac{\alpha}{r}. \tag{2.1}$$

The shape of the potential is illustrated in Fig. 2.2(a). With appropriately set initial conditions the particle traces the stable trajectory that rotates around the center with angular frequency $\omega_{\text{resonance}}$, as shown in Fig. 2.2(b).

In a simple approach, we imitate the driving laser field by modulating the potential periodically with angular frequency of ω_{mod} as expressed by Eqn. (2.2) and the trajectory of the particle is calculated with the same initial conditions.

$$V(r) = -\frac{\alpha}{r} + \delta\alpha y \cos(\omega_{\text{mod}} t). \tag{2.2}$$

Fig. 2.2 (c) and (e) show the power spectrum of the dipole moment calculated by taking the Fourier transform of the y-coordinate of the particle. It can be seen that odd-order side bands appear in the spectrum of the modulated potential. The exponential decay of the modulation side bands is also observed as shown in pink triangles in (e). In this simple model the nonlinearity originates from the radially dependent potential ($V(r)$), which pulls the particle differently towards the center depending on the radial position of the particle.

2.2.2 Single atom response of HHG: non-perturbative regime

When the driving field is stronger than discusssed in the previous section, the electron wavefunction deforms significantly and the high harmonic generation process cannot be understood in terms of a perturbative deformation of the bound state wavefunction.

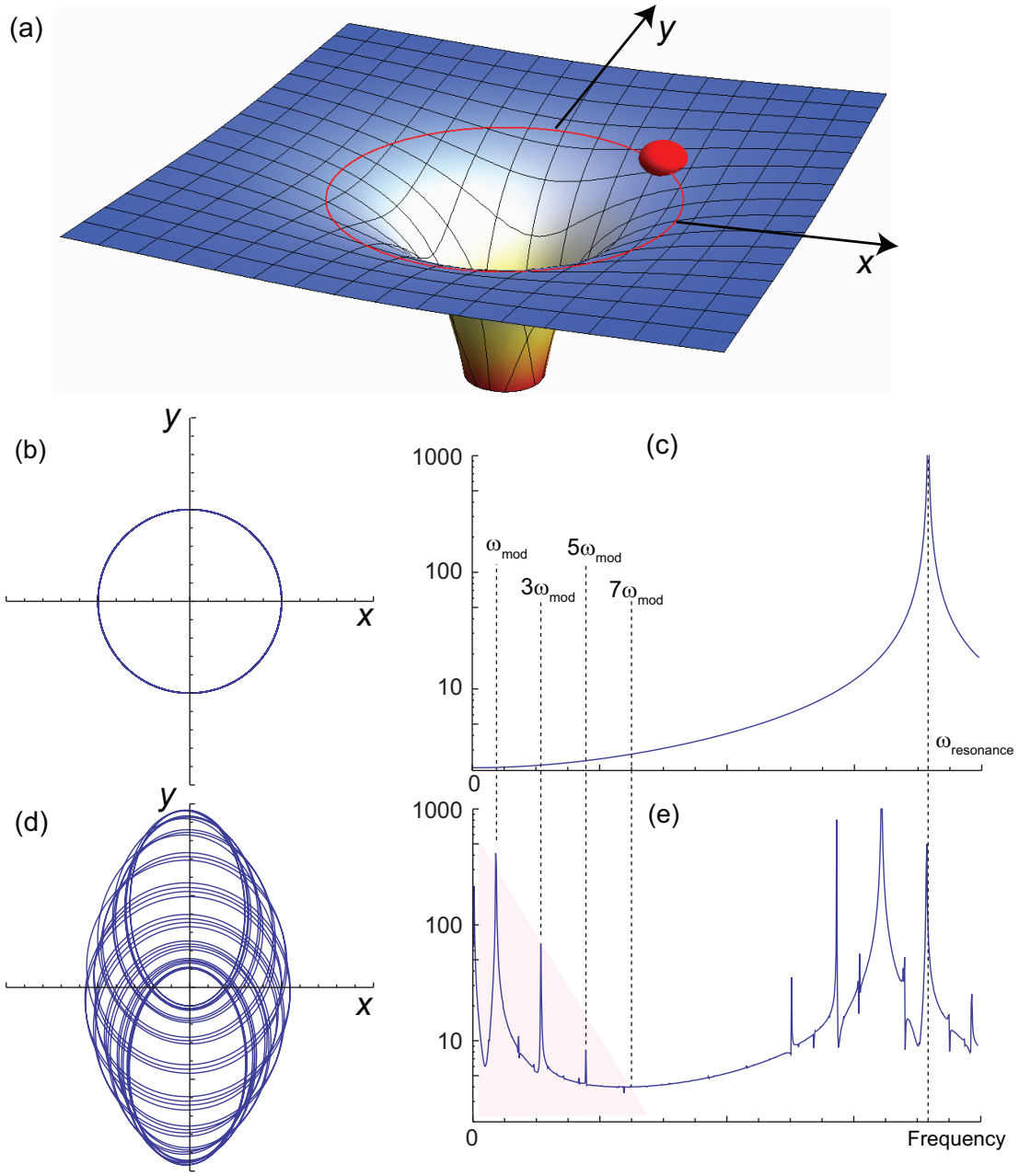

Figure 2.2: *The classical 2-dimensional model of perturbative high harmonic generation. With certain initial conditions the particle stored in the potential that is described by $V(r) = -\alpha/r$ (a) displays the stable trajectory that goes around the center (b). When the potential is modulated periodically as expressed by Eqn. (2.2), the trajectory of the particle is jolt (d). The y-coordinate of the particle is Fourier transformed and shown in (c) and (e) for un-modulated and modulated potential, respectively. $\omega_{\text{resonance}}$ stands for the rotation frequency with un-perturbed potential. When the potential is modulated with modulation frequency of ω_{mod} high harmonic peaks appear at odd multiple frequencies of ω_{mod} (e).*

The dynamics of the electron of a hydrogen atom is described by the 3-dimensional Schrödinger equation with the heavy (immovable) nucleus approximation

$$i\frac{\partial}{\partial t}\left|\psi(\boldsymbol{r},t)\right\rangle = \left[\hat{\boldsymbol{H}}_0 + \hat{\boldsymbol{V}}\right]\left|\psi(\boldsymbol{r},t)\right\rangle \tag{2.3}$$

with unperturbed Hamiltonian $\hat{\boldsymbol{H}}_0$ and interaction Hamiltonian $\hat{\boldsymbol{V}}$. The Hamiltonians $\hat{\boldsymbol{H}}_0$ and $\hat{\boldsymbol{V}}$ are given by:

$$\begin{aligned}\hat{\boldsymbol{H}}_0 &= -\frac{1}{2}\frac{\partial^2}{\partial r^2} + \frac{\hat{L}^2}{2r^2} - \frac{1}{r} \\ \hat{\boldsymbol{V}} &= -\boldsymbol{F}\cdot\boldsymbol{r}f(t)\end{aligned} \tag{2.4}$$

where $\boldsymbol{F}f(t)$ is the optical electric-field vector. Here, linearly polarized light is assumed.

All of the physics of (the single atom response of) HHG (from a single hydrogen atom) is included in the Schrödinger equation described above[1]. The investigations of the single atom response of HHG is equivalent to the understanding of Eqn. (2.3). Several ways have been found to give a physical interpretation of Eqn. (2.3). Here I would like to pick up a few popular treatments classified as follows:

- 1: Numerical simulation of Eqn. (2.3)
- 2: Quantitative Re-scattering theory (QRS)
- 3: Strong Field Approximation (SFA)
- 4: Classical approximation

Going from number 1 to 4, stronger approximations are applied, however, they also become more intuitively understandable. The purpose of this section is to give an overview and a basic understanding of the theoretical aspects of HHG. Thus, the interested reader may be referred to the original work for details.

- *3:Strong Field Approximation (SFA)*

  For simplicity of discussions, let's start with 3: Strong Field Approximation (SFA). The following arguments are based on the literature [65–68]. Let us assume that the solution of the electron's wavefunction is given by the following form,

  $$\left|\psi(\boldsymbol{r},t)\right\rangle = \left|0\right\rangle + \int d^3\boldsymbol{v}\, b(\boldsymbol{v},t)\left|\boldsymbol{v}\right\rangle \tag{2.5}$$

  with $\left|\boldsymbol{v}\right\rangle$ as a wavefunction of the *un-bound electron* with momentum labeled by $\boldsymbol{v}$. $\left|0\right\rangle$ stands for the ground state wavefunction.

  Eqn. (2.5) is based on the following approximations or assumptions.

  - The electron wavepacket consists of the ground state and un-bound states. The contribution from excited bound states is negligible.
  - The un-bound state wave function is labeled only by momentum and not affected by the nuclear potential.

[1] Note that Eqn. (2.3) includes the perturbative behavior of HHG.

– The total population is dominated by the ground state and its contribution is time independent.

The time dependent dipole moment ($d(t)$) is defined as

$$d(t) \equiv e \langle \psi(\boldsymbol{r}, t) | x | \psi(\boldsymbol{r}, t) \rangle . \tag{2.6}$$

When the optical field is expressed as $\boldsymbol{F}f(t) = -\boldsymbol{E}\cos(\omega t)$, the time dependent dipole moment $d(t)$ is calculated from Eqn. (2.3), (2.5) and (2.6), to be

$$d(t) = e \int_0^t dt_I \int d\boldsymbol{p} E \cos(t_I) d_x(\boldsymbol{v}(t_I)) \exp(-iS) d_x^*(\boldsymbol{v}(t)) \tag{2.7}$$

with $d_x(\boldsymbol{v}) = \langle \boldsymbol{v} | x | 0 \rangle$ [2]. S is the action of the electron to propagate under the optical potential. d_x is the transition probability between the ground state and the un-bound state. Thus, Eqn. (2.7) can be interpreted as follows, a simple picture of HHG that has been named Three Step Model:

1. The part of the electron is excited to a un-bound state at t_I
2. The un-bound part of electron is affected by the laser field only (without being affected by the atomic potential)
3. The electron is de-excited to the ground state at t

The steps are often denoted as "ionization", "acceleration" and "recombination" stages, based on the interpretation that the electron is ionized assisted by the high optical field strength, accelerated by the optical field and recombined to a bound-state emitting excess energy as high harmonic radiation.

- *4: Classical approximation*

  The following classical simplification of the three step model gives useful explanations on some of the properties of HHG. Assuming the three step model we add the following simplifications:

  – Right after the ionization the momentum of the electron is negligible.
  – The electron can be treated as a classical charged particle and obeys the classical equation of motion during the acceleration stage.
  – The entire kinetic energy of the electron is converted into a HHG photon in the recombination stage.

  During the acceleration stage, the classical equation of motion for the electron can be given by

$$m \frac{d^2}{dt^2} x(t) = -eE(t) \tag{2.8}$$

with the optical field amplitude given by $E(t)$ and the position of the electron $x(t)$. e and m stand for the electron charge and mass. Here we assumed that the field is linearly polarized along the x-axis, with optical frequency ω and (peak) field amplitude E_0:

[2] Here, $\boldsymbol{v}(t)$ is defined as $\boldsymbol{v}(t) = \boldsymbol{p} - \boldsymbol{A}(t)$ with canonical momentum $\boldsymbol{p}$ and vector potential $\boldsymbol{A}$

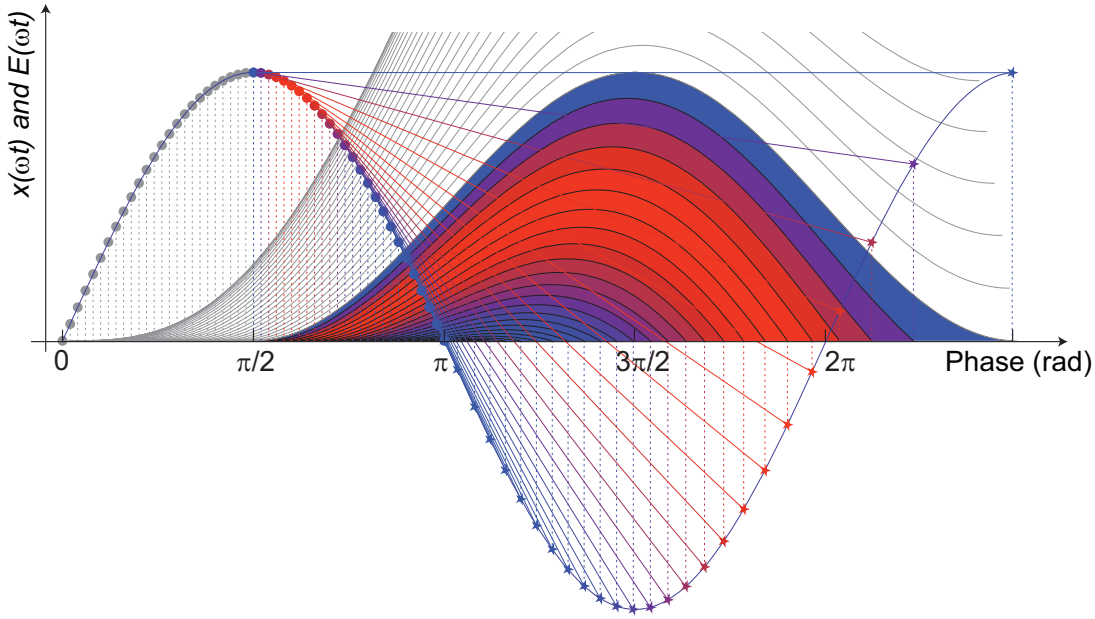

Figure 2.3: *Classical description of HHG. The sinusoidal curve shows the optical field. The x-axis is time shown by the phase of driving field ωt. The vertical axis is the position of the electron ($x(t)$). The electron trajectories are calculated for different ionization phases of ωt_I from 0 to π rad. The color of the electron trajectory stands for the kinetic energy of the electron (red: high energy, blue: low energy) when the electron returns to the origin (recombination energy). The dots and stars on the optical field stand for the ionization and recombination time of each trajectory, respectively. The corresponding dots and stars are connected by lines. The electron trajectories that do not return to the nucleus are shown in gray color.*

$$E(t) = E_0 \sin(\omega t). \tag{2.9}$$

Eqns. (2.8) and (2.9) can be solved analytically for the initial conditions $x(t_I) = 0, x'(t_I) = 0$. Here, t_I stands for the time of ionization.

$$x(t) = \frac{eE_0}{\omega m}\Big[\frac{\sin(\omega t) - \sin(\omega t_I)}{\omega} - (t - t_I)\cos(\omega t_I)\Big]. \tag{2.10}$$

Fig. 2.3 shows the driving field and the electron trajectories calculated for different ionization phases ωt_I. Here, "ionization phase" stands for the phase of the driving field when the electron is ionized. Due to the symmetry of the driving field it is sufficient to investigate the ionization phase from 0 to π rad. It can be seen that the electron trajectory diverges and never returns to the nucleus if the ionization phase is smaller than 0.5π rad. Thus, only the trajectories ionized from $0.5\,\pi$ to π rad contribute to the HHG. The electron returns to the nucleus with some kinetic energy due to the acceleration from the optical field. The energy is dependent on the ionization time t_I. In Fig. 2.3 the color of the electron trajectory shows the kinetic energy of the electron at recombination. The red and blue color correspond to high and low kinetic energy, respectively. The dots and stars on the optical field in Fig. 2.3 stand for the ionization

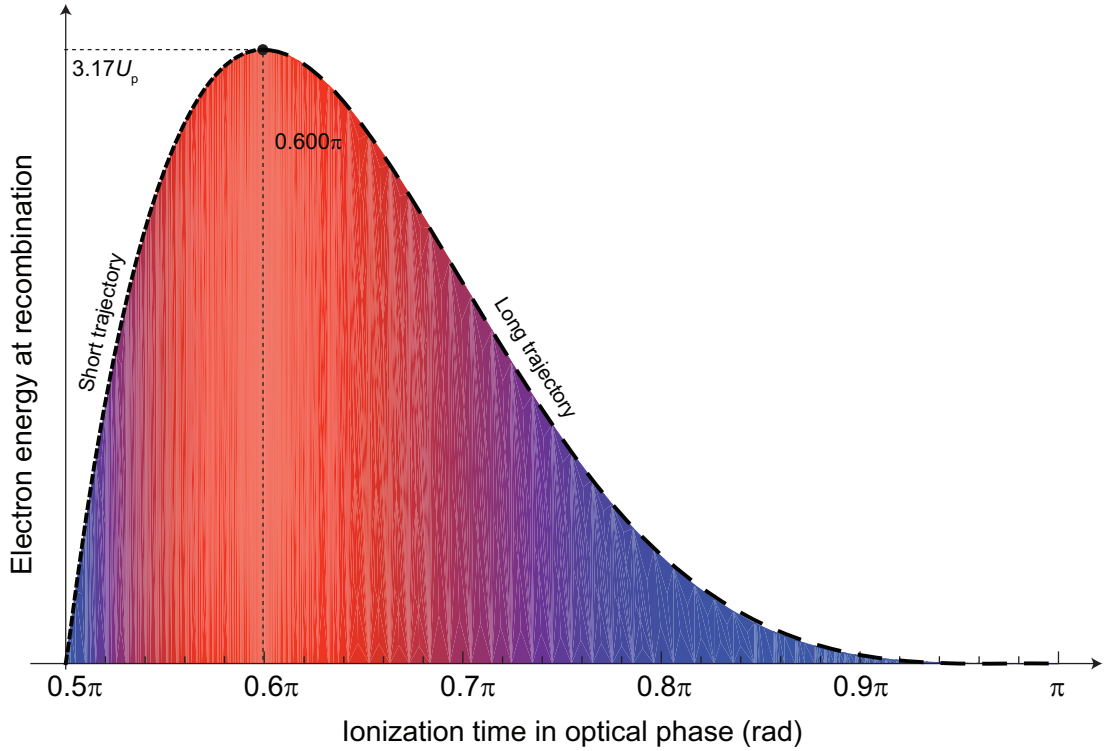

Figure 2.4: *The kinetic energy of the electron at the recombination time. The inside of the plot is painted by a color identical to Fig. 2.3.*

and recombination time of each trajectory, respectively. The corresponding dots and stars are connected by a line. It is interesting to see that these lines are tangential with the electric field at the ionization time[3]. This can be seen in the following way: The condition for recombination at time $t = t_R$ is $x(t_R) = 0$. This is equivalent to

$$\begin{aligned} x(t_R) &= 0 \\ \Leftrightarrow \sin(\omega t_R) - \sin(\omega t_I) &= (t_R - t_I)\big[\frac{d}{dt}\sin(\omega t)\big]_{t=t_I}. \end{aligned} \tag{2.11}$$

The last equation is nothing but the formula for the line connecting ionization and recombination points, which is tangential to the field at the ionization point. It can be seen that there are two electron trajectories that yields identical electron energy at recombination. To investigate this further, the electron energy at recombination is plotted as a function of ionization time (t_I). The result is shown in Fig. 2.4. It can be seen that the energy has a finite maximum. The electron (kinetic) energy ($U(t_I)$) at the recombination time (as a function of ionization time) is given by:

$$U(t_I) = \frac{1}{2}m\dot{x}(t_R)^2 = 2U_p\big(\cos(\omega t_R) - \cos(\omega t_I)\big)^2. \tag{2.12}$$

[3]This gives a simple geometrical method to find the recombination time from the ionization time: one can draw a tangential line at the ionization time and try to find where the line crosses with the sinusoidal curve.

Here, the pondermotive energy U_p is introduced as:

$$U_\mathrm{p} = \frac{e^2 E_0^2}{4\omega^2 m}. \tag{2.13}$$

Numerical evaluation of Eqn. (2.12) shows that $U(t_I)$ takes a maximum value of $3.17U_\mathrm{p}$ when the ionization phase ωt_I is 0.600 rad. For a given energy $E < 3.17U_\mathrm{p}$, there are two ionization times that give the identical electron energy at recombination (E). It can be seen from Fig. 2.3 that the trajectory with earlier(later) ionization time takes shorter(longer) periods until it recombines. Those two are often denoted as "short" and "long" trajectories.

In the simplest model, the photon energy (E_HHG) that is emitted during the recombination process is determined by the sum of ionization energy (I) and the kinetic energy of the electron.

$$E_\mathrm{HHG} = I + U(t_I). \tag{2.14}$$

This classical model predicts the maximum electron energy that can be gained from the optical field as described above, thus, the maximum photon energy that could be emitted (E_cutoff) is given by:

$$E_\mathrm{cutoff} = I + 3.17U_\mathrm{p} \tag{2.15}$$

which is often denoted as "cut-off photon energy".

- *2:Quantitative Re-Scattering theory (QRS)*

  To calculate the HHG spectrum with the SFA-model, the transition dipole d_x is calculated based on the plane wave approximation of continuum electrons [65]. The agreement of the high harmonic spectrum between the SFA-model and reality (or full numerical simulation of Eqn. (2.3) is good for cut-off HHG, however, a significant deviation can often be observed for below cut-off high harmonics. This is due to the fact that the electron wave packet is no longer a plane wave when the recombination energy is low, and the recombination probability cannot be properly evaluated by utilizing the plane wave approximation. On the other hand, it was demonstrated recently that the returning electron wave packet itself obtained from SFA agrees quite well with the numerical simulation of Eqn. (2.3) [69–72]. This investigation indicates that the validity of SFA is limited by the evaluation of the recombination process, not by the ionization and acceleration stages. In the SFA model, the ionization energy (I_p) and the laser field are only parameters to calculate the returning electron wave packet. Thus, the returning electron wavepacket is insensitive to atomic species if the ionization energy is identical, and only determined by the driving field. This results in an interesting factorization of the HHG yield $S(\omega)$ [69–72]:

  $$S(\omega) = W(\hbar\omega - I_\mathrm{p})|d_x(\omega)|^2 \tag{2.16}$$

  with recombination probability $|d_x(\omega)|^2$ and flux of the returning electron wave packet $W(E)$ with electron energy $E = \hbar\omega - I_\mathrm{p}$. $W(E)$ is affected only by the laser parameters

and the ionization energy, while $|d(\omega)|^2$ is a property of the target atom. This way, the properties of HHG can be separated into target dependent and laser field dependent contributions. This will be useful in comparing the behavior of HHG with different targets (including molecular targets). When the recombination probability $|d(\omega)|^2$ is calculated without utilizing the plane wave approximation but with exact scattering wave it is demonstrated that Eqn. 2.16 gives a significant improvement over SFA in agreement with the numerical simulation of Eqn. (2.3), especially in low order of HHG. Conceptually, the factorization in Eqn. (2.16) is interesting since it shows the validity of the three step model with the complete isolation of recombination process, and thus it shows that the unique response of HHG for different targets (including molecules) originates mainly from the recombination process.

- *1:Numerical simulation of Eqn. (2.3)*

  One straightforward but computationally demanding way to investigate Eqn. (2.3) would be to numerically solve the equation as a function of time. Our efforts to do so are discussed in the following section. (Sec. 2.2.3)

2.2.3 Single atom response of HHG: numerical simulations

Entire process of (the single atom response of) HHG (for a single hydrogen atom) can be described by 3-dimensional Schrödinger equation (Eqn. (2.3)). Several numerical methods have been invented to efficiently and precisely solve the equation [73–76]. Remember that the typical efficiency of HHG around the cut-off region would be far below 10^{-6}. Therefore Eqn. (2.3) has to be evaluated within an accuracy better than 10^{-6} for a detailed discussion of the cut-off region. We developed a code to fully numerically solve the HHG process based on the Time-Dependent Generalized Pseudo-Spectral (TDGPS) method invented by Chu et al. [73]. Here we briefly outline the method. The hydrogen potential is modified to be confined in a finite-size box with an infinitely high potential barrier in order to obtain discretized energy levels for ionized states. The electron wave function is expanded with energy eigenfunctions of the potential that consist of bound and ionized states. The time-evolution of the wavefunction is calculated with the split-operator method where each time-step contains the time-evolution due to an interaction free Hamiltonian and the interaction Hamiltonian. The dipole moment is calculated from so obtained wavefunctions for each time step. The high harmonic spectrum is obtained by taking the Fourier transform of the dipole moment. Fig. 2.5 shows the obtained high harmonic spectrum. For this example the following parameters are used in the simulation:

peak intensity	$1 \times 10^{14}\,\mathrm{W/cm^2}$
wavelength of driving beam	1064 nm
pulse duration	210 fs
pulse shape	$\sin^2$

The appearance of odd order high harmonics is visible. Also, the perturbative, plateau and cut-off region can be identified. The noisy structures between the harmonic peaks reflect the real electron dynamics of the process and are not due to computational noise. The contrast of the harmonic peaks against the noise structures decreases for shorter pulses, since less optical cycles contribute to the HH emission (see following section (Sec.2.2.4)).

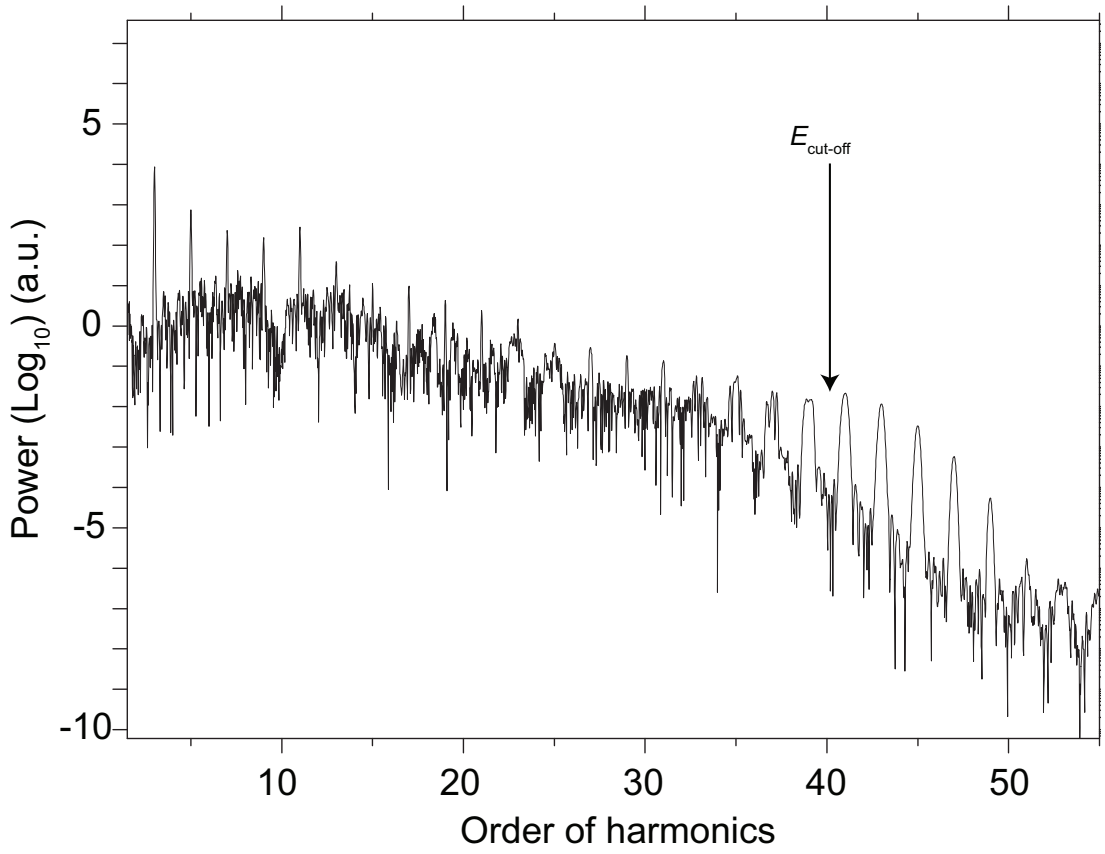

Figure 2.5: *High harmonic spectrum calculated based on a full quantum 3-dimensional simulation. The paremteres of the driving field are in the text.*

2.2.4 Other important remarks of high harmonic generation

In this subsection, a few additional important features of HHG are discussed for future reference.

- Odd harmonics

  The three step model introduced in Sec. 2.2.2 describes the microscopic process of HHG within an optical half-cycle. In fact the spectrum of HH radiation from a single optical half-cycle does not show a peak-like structure, but is rather continuous. However, in reality, the process repeats itself every optical half-cycle and all the contributions interfere. It is easy to see that full destructive (constructive) interference can be obtained for even (odd) order harmonics. Thus, HHG driven with many optical cycles shows a peak-like spectrum that consists of only odd orders of harmonics. When few-cycle pulses are used for driving HHG, the resulting spectrum tends to show a rather continuous structure for the high order harmonics due to the lower number of cycles that contribute to the HH emission. This feature is exploited to generate single attosecond pulses for which a (less structured) extremely broad bandwidth is required.

- Polarization

As can be expected from the three step model, if the driving field is not linearly polarized, the emission of HH is strongly supressed due to the lack of an electron trajectory that returns to the nucleus. The effect is used for single attosecond pulse generation where quasi-mono-cycle pulses are required to drive HHG (polarization gating, see e.g. [68] for the details.). When HHG is driven with linearly polarized pulses, the resulting HH emission is also linearly polarized, because the dipole moment is mainly induced along the axis of the driving electric field (for an intuitive picture see Fig. 2.1). This feature eliminates the possibility to use a polarization-dependent outcoupling method for HH radiation in cavity-enhanced HHG experiments.

- Coherence of high harmonic radiation

  The frequency comb structure originates from spectral interference between multiple pulses (see Sec. 1.1.). This means that the pulse-to-pulse phase coherence has to be preserved in the HHG process for XUV frequency comb generation. Yet, there are several reasons why the comb structure might be disturbed during the HHG process: If the driving laser exhibits phase noise, the noise will be transfered to the XUV. The power spectral density of the phase noise normalized by its carrier scales with q^2 for the qth order of harmonics. Thus, for really high order harmonics, the comb structure will be disturbed (carrier collaps). The question is up to which order the comb structure is clean enough for applications. Other important contributions will be the amplitude-phase coupling during the HHG process. As will be shown in Fig. 3.18, the atomic phase of the single atom response depends on the intensity of the driving beam (and the electron trajectory). Thus, when the driving laser shows amplitude fluctuations, the phase of the single atom response will fluctuate as well. In a typical HHG experiment, a gaseous medium is used as a target. If there is a fluctuation of the target gas density within the time scale of the pulse-to-pulse time separation (the inverse of the repetition rate), the pulse-to-pulse phase shift of both the driving beam and the HH beam will be affected. Additionaly, the plasma density fluctuations also introduce phase noise into the driving and the HH beams, since the refractive index of the plasma is different from that of the target gas. Since the plasma density is intensity-dependent, this effect introduces additional amplitude-phase coupling. When the intensities of the driving beam and the XUV beam are high, nonlinear processes such as self-phase modulation from the plasma and the target gas will introduce uncontrollable phase shifts which also depend on the intensity of the beams. These effects originating from the plasma density will be even more significant when the driving peak intensity is high, because the plasma density can rapidly change within the pulse duration. The hope to generate coherent XUV combs is based on the expectation that some of these nasty effects will reach a steady state after a large number of pulses. This (potentially) is the biggest advantage of XUV frequency comb spectroscopy compared with Ramsey-type spectroscopy where the precision of the method relies on a precise calibration of the phase shift between only two (or a few) pulses [4]. Experimentally, the comb structure has been confirmed for the 3rd order of HH [51]. An experimental demonstration of the coherent comb structure in the XUV region will be one of the important milestones in the field. The following literature summarizes the efforts made so far made to confirm the coherence of HH radiation [1, 51, 52, 77–87].

[4] However, even in the case of XUV frequency comb generation with multiple pulses, the possibility of chaotic noise dynamics that may not reach a steady state is not ruled out.

2.3 Femtosecond enhancement cavity

As outlined in the introduction, it is the aim of this work to produce a high-power XUV frequency comb at high repetition rates. The previous section showed that this requires high peak intensities (typically $\sim 10^{14}\mathrm{W/cm^2}$). Our approach to achieve these peak intensities is to passively enhance the power of an infrared frequency comb in a resonator, similar to intracavity second harmonic generation (SHG) which is commonly used for frequency doubling of CW lasers [88, 89]. Since the intracavity average power is higher than that of the driving laser, nonlinear frequency conversion works more efficiently inside the cavity. In this subsection, theoretical aspects of femtosecond optical cavities are discussed. The theory of optical cavities is simple but often could be confusing, partially because of varying assumptions and definitions, and partially because of the counter-intuitive behavior of cavities. This subsection intends to summarize the important basics.

2.3.1 Femtosecond and continuous wave optical cavities

An optical cavity consists of mirrors to provide a closed beam path in the cavity. When one of the mirrors is partially transmissive (input coupler), the beam from the driving laser can be coupled into the cavity. Steady state operation of the cavity is obtained when the power loss in the cavity is exactly compensated by the seeding power from the driving laser. For a proper choice of the cavity parameters, the intracavity pulse energy can be more than a factor of 1000 higher than the one of the pulsed driving laser. Here we denote a cavity, which is intended and designed to achieve high intracavity pulse energies (or average power), as an "enhancement cavity" [5].

The cavity allows certain frequencies and spatial modes of the laser to be stored, which are denoted as longitudinal and transversal modes of the cavity, respectively. Only when the optical frequency is matched to the cavity eigenmodes, the circulating beam constructively interferes with the incoming beam from the driving laser. Thus, laser frequencies and cavity eigenfrequencies have to be matched to obtain passive enhancement (frequency resonance condition). The frequency modes of the cavity are determined by their round-trip phase-shift, which is proportional to the round-trip optical path-length. Thus, when the cavity is built under typical experimental conditions, the frequency modes of the cavity fluctuate due to, for example, mechanical vibration of the cavity mirrors. This is also the case for the laser cavity. Therefore, the frequency of the laser has to be actively controlled to match the eigenfrequencies of the cavity. Contrary, it is also possible to control the frequency modes of the cavity to match the laser frequency. In both cases active feedback is required. The details of the feedback method will be discussed in Sec. 2.4. Fig. 2.6 illustrates the CW operation of the cavity in the frequency domain.

The situation becomes a little more complicated for pulsed operation of the cavity. Experimentally, passive enhancement of pulsed lasers inside cavities has been demonstrated with picosecond and also femtosecond pulses [51, 90, 91]. To obtain passive enhancement, that is, to obtain constructive interference between the circulating pulses and the seeding pulses, the pulse train from the driving laser has to be pulse-to-pulse phase coherent. A mode-locked

[5] A high finesse cavity does not necessarily lead to high intracavity power due to impedance matching issues. For some of the applications of the cavity (e.g. as an ultrastable reference cavity), a high cavity finesse with low intracavity power is required.

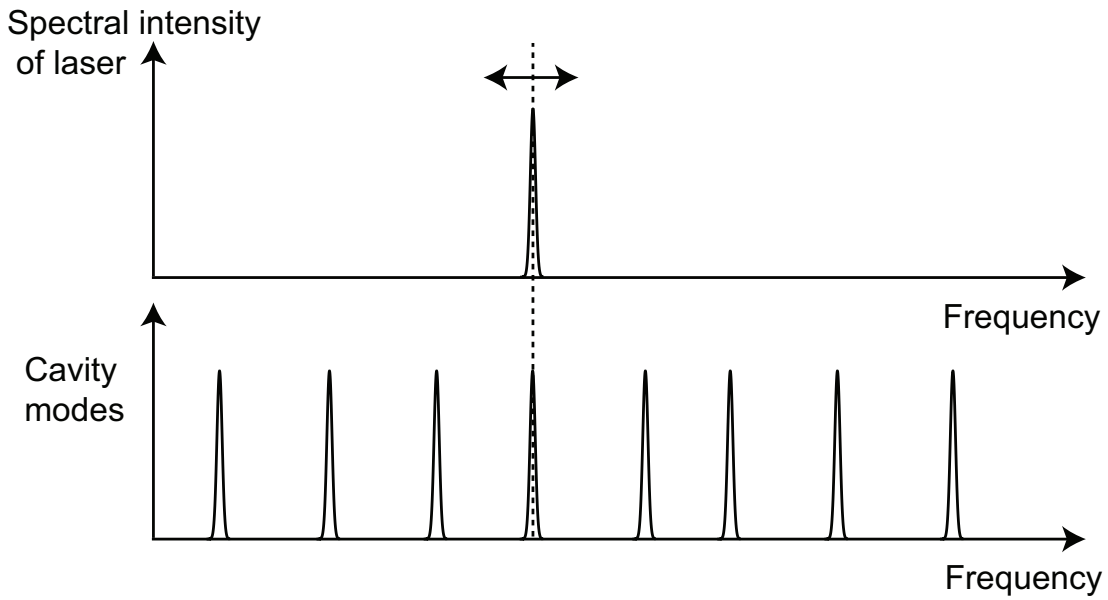

Figure 2.6: *The frequency modes of a cavity and a cw seeding laser. The frequencies of either cavity modes or the laser have to be controlled to maintain the resonance condition.*

laser with a frequency comb structure provides such a coherence [6]. Here, let us consider the coupling of a broadband frequency comb into the enhancement cavity.

As described above, the laser frequencies have to be matched to the eigenfrequencies of the cavity to be coupled into the cavity. In the case of a frequency comb as seed laser, all (or most) comb lines have to sit on a resonance frequency of the cavity to obtain the desired broadband resonance. Fig. 2.7 illustrates the frequency coupling between the frequency comb and the cavity.

From Fig. 2.7 it can be seen that the following three conditions have to be met in order to locate all the the comb modes onto the cavity eigenmodes.

1. The cavity has to exhibit equidistant frequency eigenmodes.

2. The comb mode separation has to be matched to cavity mode separations.

3. The entire comb mode has to be shifted properly.

The comb mode separation is determined by the repetition frequency ω_{rep} of the laser. The cavity mode separation is given by the inverse of the round trip time $2\pi/t_{\mathrm{r}}$. The shift of the comb modes is expressed by the offset frequency (ω_{CEO}) of the laser. Equidistance of cavity modes indicates that the round trip time of the cavity is independent of the laser frequency, corresponding to zero intra-cavity dispersion. Therefore, the three conditions listed above, can be re-phrased as follows:

1. The intra-cavity dispersion has to be compensated.

[6] On the other hand, broadband radiation that can be coupled into the cavity does not necessarily have to be a frequency comb. A comb-like spectrum with (incoherent) random spectral phases can also be coupled into the cavity.

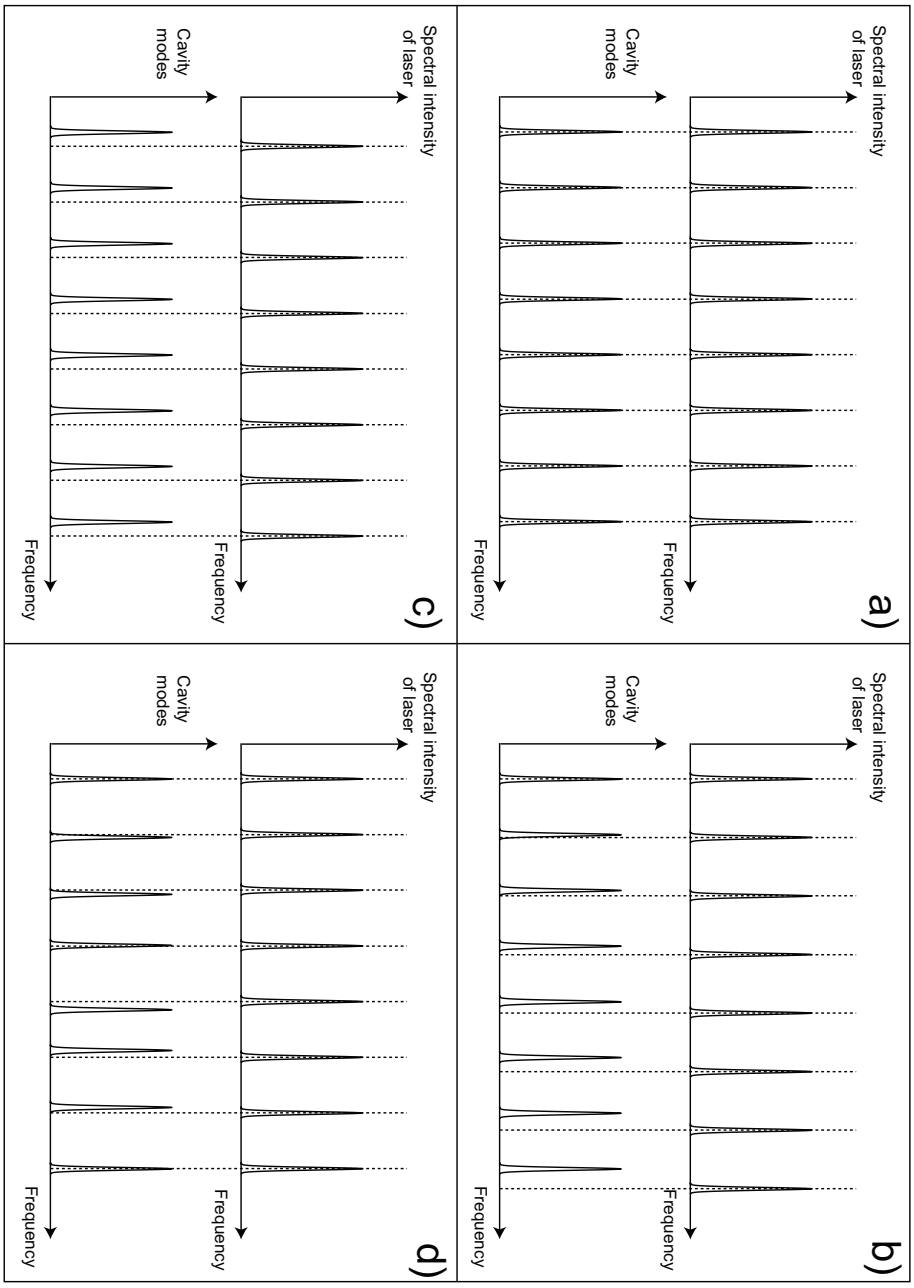

Figure 2.7: *Frequency modes of the cavity and of the mode-locked laser that seeds the cavity. The three parameters repetition frequency, offset frequency and dispersion of the cavity have to be controlled to obtain broadband resonance. a): All three conditions in the list (p. 44) are satisfied. All comb modes sit on the cavity eigenfrequencies to obtain broadband resonance. b) The repetition frequency of the comb is not properly set (Condition 1 in the list is missing.). c) The offset frequency of the comb is not properly set (Condition 2 in the list is missing.). d) Intra-cavity dispersion is not compensated (Condition 3 in the list is missing).*

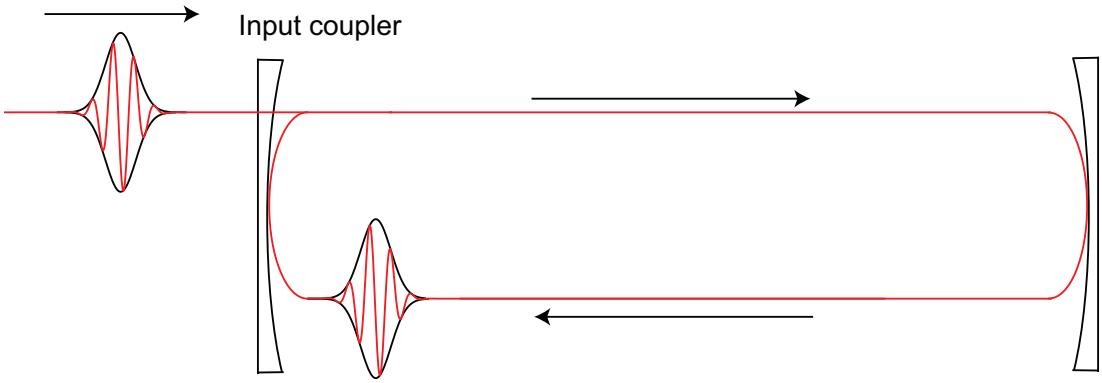

Figure 2.8: *Time domain illustration of the enhancement cavity for a pulse train. The circulating pulses overlap with incoming pulses and so passive enhancement takes place.*

2. The repetition frequency ω_{rep} has to be matched to the inverse of the cavity round trip time $2\pi/t_{\mathrm{r}}$.

3. The offset frequency (ω_{CEO}) has to be adjusted.

When these conditions are satisfied all of the comb modes can be coupled into the cavity and the pulse train can be amplified.

It is interesting to describe these conditions in the time domain. When one of the pulses is coupled into the cavity and returns to the input coupler after one round trip, the succeeding pulse is coupled into the cavity and interferes with the circulating pulse (see Fig. 2.8). If the interference is sufficiently constructive passive enhancement will be realized and the intra-cavity power will be enhanced. The conditions for constructive interference in time-domain can be listed as follows:

1. The envelope of the circulating pulse has to be identical to that of seeding laser. (The pulse envelope should retain its shape after the round trip.)

2. The intra-cavity pulse has to arrive exactly when the next seeding pulse arrives at the input coupler.

3. The phase of the electric field inside the envelope has to be identical for the circulating and the seeding pulse.

It is easy to see that the these three conditions correspond to the ones listed previously for the frequency domain.

For a quantitative discussion of the enhancement cavity in the following subsection we describe the basic model of a (femtosecond) cavity and summarize the cavity response for several conditions.

2.3.2 A basic model of a femtosecond cavity

Consider the simple three-mirror cavity shown in Fig. 2.9 [7] The input coupler is assumed to have the following properties:

[7] Actually, a two-mirror (Fabry-Perot) cavity is even simpler, but we want to avoid the confusion originating from the fact that the beam passes intracavity objects twice within a single round trip for a Fabry-Perot cavity.

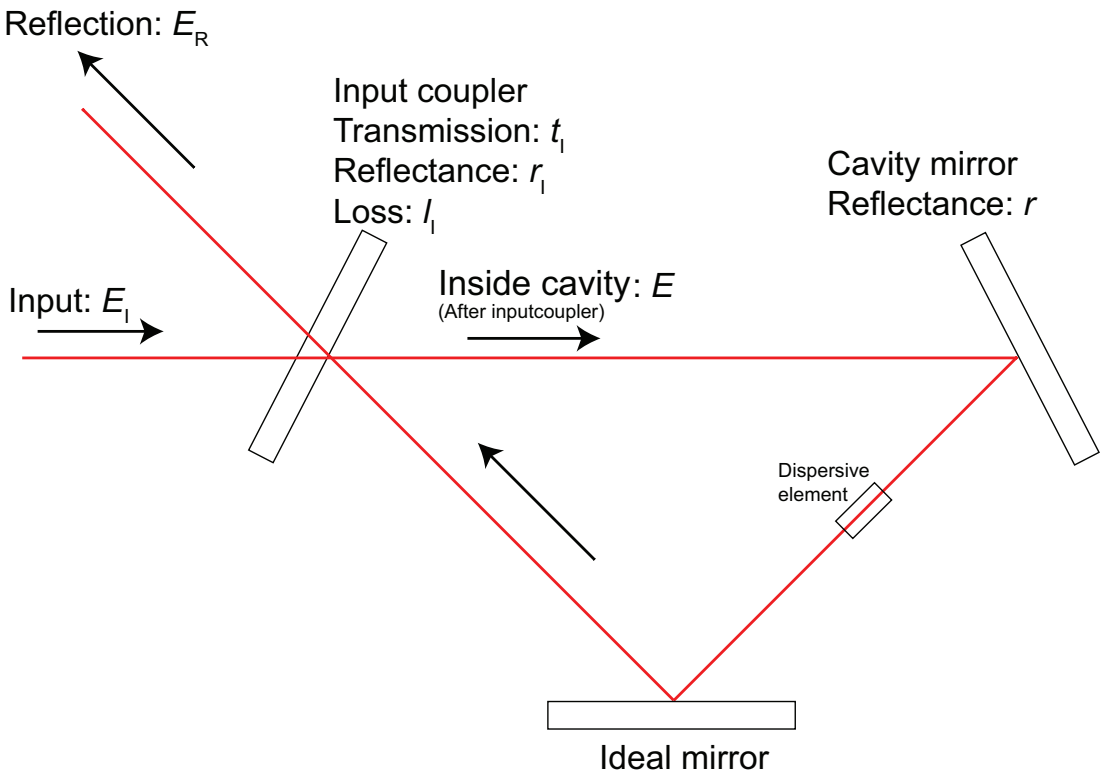

Figure 2.9: *Model cavity consisting of three mirrors. The field amplitude of the seeding beam and the intracavity field amplitude directly behind the input coupler are denoted E_I and E, respectively. The total round trip loss is represented by a single parameter, the "cavity round trip amplitude factor" r. When the cavity is aligned, the reflection from the cavity (E_R) consists of the simple reflection of the input beam and the transmitted intracavity beam.*

- field transmission of input coupler: t_{I}
- field reflection of input coupler: r_{I}
- field loss of input coupler: l_{I}

Due to energy conservation at the input coupler, the following equation holds:

$$ {t_{\mathrm{I}}}^2 + {r_{\mathrm{I}}}^2 + {l_{\mathrm{I}}}^2 = 1. \tag{2.17} $$

The amplitude of the field incident on the cavity is denoted E_{I}. The field amplitude inside the cavity directly behind the input coupler is expressed by E. The amplitude of the field that is reflected from the cavity is denoted E_{R}.

The field E behind the input coupler experiences losses inside the cavity and its amplitude is decreased to $rr_{\mathrm{I}}E$ after a single round trip. Here, we lump all losses of the cavity except the input coupler into the reflectivity of one of the cavity mirror (r) [8]. We call r the "round trip amplitude factor".

In addition, the phase of the field is affected by any dispersive element inside the cavity and simply just by free space propagation. The round trip phase shift ($\phi(\omega)$) is expressed by

$$ \phi(\omega) = \frac{L\omega}{c} + \delta\phi(\omega). \tag{2.18} $$

Here, the cavity length and the angular frequency of the radiation are denoted by L and ω, respectively. In Eqn. (2.18), $\phi(\omega)$ is separated into the obvious phase shift term due to free space propagation ($\frac{L\omega}{c}$) and an additional term $\delta\phi(\omega)$.

The field after a single round trip can be written as $rr_{\mathrm{I}} \exp(i\phi)E$. For the steady state, the condition: "(field after one round trip)+(seeding field)=(field before round trip)" has to hold:

$$ rr_{\mathrm{I}} \exp(i\phi)E + E_{\mathrm{I}}t_{\mathrm{I}} = E. \tag{2.19} $$

The reflected field from input coupler E_{R} is given by the sum of the reflected seeding field and the transmitted cavity field:

$$ E_{\mathrm{R}} = -E_{\mathrm{I}}r_{\mathrm{I}} + Ert_{\mathrm{I}} \exp(i\phi). \tag{2.20} $$

Here, the first minus sign originates from the phase shift of π for the reflected light.

The power enhancement P is defined as the ratio between the intracavity power and the incident power:

- Power enhancement :

$$ P \equiv \frac{|E|^2}{|E_{\mathrm{I}}|^2} \tag{2.21} $$

[8] For example, in the case of a typical cavity for frequency doubling (SHG), r can be expressed as:

$$ r = (r_{\mathrm{mirror}})^N \sqrt{(1 - {l_{\mathrm{crystal}}}^2)(1 - {l_{\mathrm{air}}}^2)(1 - {l_{\mathrm{SHG}}}^2)...} $$

with the field reflectance of the mirror r_{mirror}, the field losses of the crystal l_{crystal} and air l_{air}, and the field loss due to the frequency conversion l_{SHG}. N stands for the number of mirrors.

The normalized reflection R is defined to be the ratio between the reflected power and incident power:

- Normalized reflection :

$$R \equiv \frac{|E_{\mathrm{R}}|^2}{|E_{\mathrm{I}}|^2} \tag{2.22}$$

With the help of Eqns. (2.19), (2.20), (2.21), and (2.22), the power enhancement P and the normalized reflection R can be described as:

$$P = \left| \frac{t_{\mathrm{I}}}{1 - r_{\mathrm{I}} r \exp(i\phi)} \right|^2 = \frac{{t_{\mathrm{I}}}^2}{1 + r^2 {r_{\mathrm{I}}}^2 - 2 r r_{\mathrm{I}} \cos(\phi(\omega))} \tag{2.23}$$

$$R = \left| -r_{\mathrm{I}} + \frac{r {t_{\mathrm{I}}}^2 \exp(i\phi)}{1 - r_{\mathrm{I}} r \exp(i\phi)} \right|^2 = ({t_{\mathrm{I}}}^2 + {r_{\mathrm{I}}}^2) + \frac{{t_{\mathrm{I}}}^2(-1 + r^2({t_{\mathrm{I}}}^2 + {r_{\mathrm{I}}}^2))}{1 + r^2 {r_{\mathrm{I}}}^2 - 2 r r_{\mathrm{I}} \cos(\phi(\omega))}. \tag{2.24}$$

The power enhancement P and the normalized reflection R are plotted as a function of the phase shift (ϕ) in Fig. 2.10. The values used in the calculation are ${t_{\mathrm{I}}}^2 = 0.015, {r_{\mathrm{I}}}^2 = 0.985$, and ${l_{\mathrm{I}}}^2 = 0, r^2 = 0.99$. As obvious from Eqn. (2.18), the phase shift ϕ is proportional to the angular frequency ω when the dispersion of the cavity is neglected. Thus, the plots can be understood to be showing the spectral response of the cavity. As can be seen from the plots, the power enhancement is periodically modulated and maximized when the phase shift is an integer multiple of 2π, indicating that a high power enhancement can only be obtained when the cavity is operated in the vicinity of a resonance. The normalized reflection is also modulated with the same period, and minimized when the cavity is on resonance. This indicates that the seeding power can be coupled into the cavity efficiently only when the resonance condition is satisfied. When the cavity is "impedance matched" (as will be discussed below), the full seed power will be coupled into the cavity and the normalized reflection on resonance condition will be zero [9].

Fig. 2.11 shows a magnified plot of both power enhancement (P) and normalized reflection (R). The Airy-shaped resonance spectra are observed for power enhancement. The phase response of the cavity field (ϕ_{P}) and the reflection field (ϕ_{R}) are also calculated based on the following expressions and shown in Fig. 2.11.

$$\phi_{\mathrm{P}} = \arg\left(\frac{E}{E_{\mathrm{I}}}\right) = \arg\left(\frac{t_{\mathrm{I}}}{1 - r_{\mathrm{I}} r \exp(i\phi)}\right) \tag{2.25}$$

$$\phi_{\mathrm{R}} = \arg\left(\frac{E_{\mathrm{R}}}{E_{\mathrm{I}}}\right) = \arg\left(-r_{\mathrm{I}} + \frac{r {t_{\mathrm{I}}}^2 \exp(i\phi)}{1 - r_{\mathrm{I}} r \exp(i\phi)}\right). \tag{2.26}$$

In order to investigate the response of the cavity for several typical conditions, we introduce the following four cases:

- On resonance

  As shown in Fig. 2.10, the cavity is on resonance when the round trip phase shift is an integer multiple of 2π.

[9] Under the assumption that the other parameters such as spatial mode and polarization do not deteriorate the coupling.

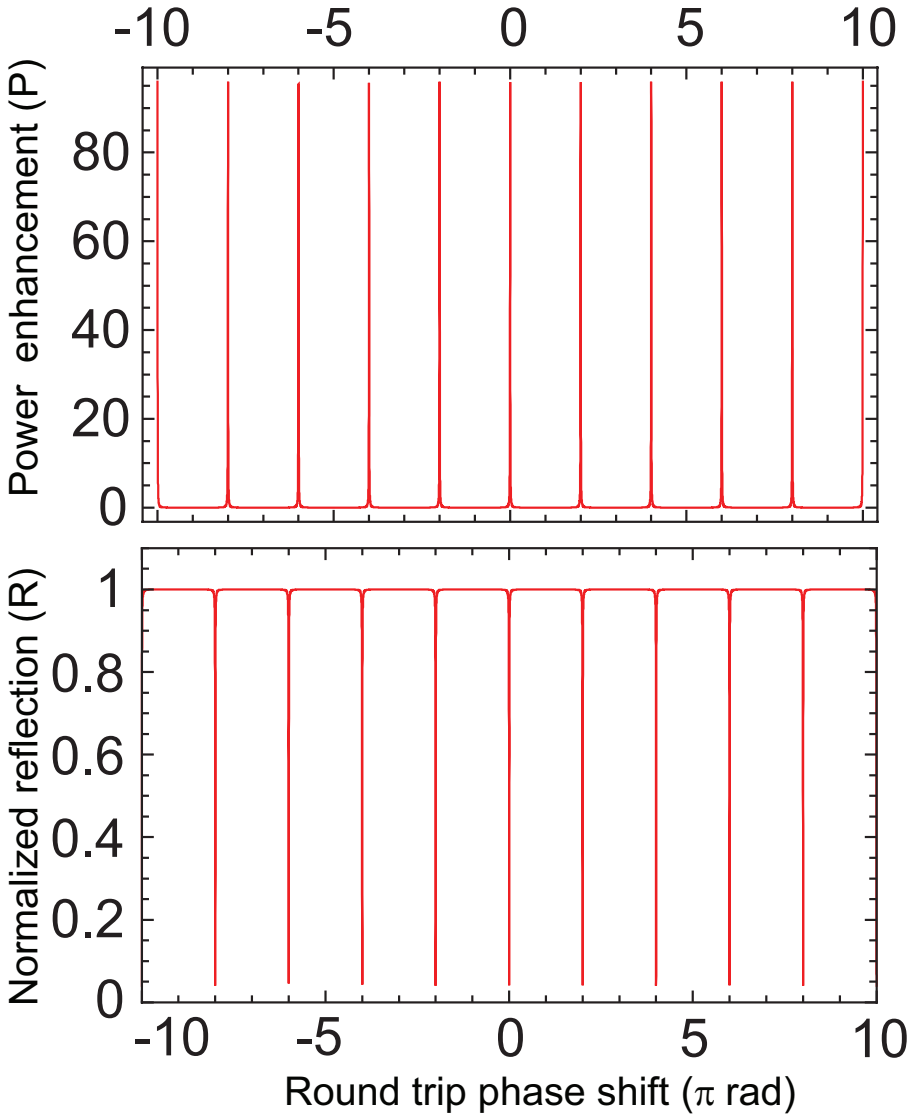

Figure 2.10: *Power enhancement P and normalized reflection R as a function of cavity round trip phase shift. The periodic modulations correspond to the periodic cavity resonance condition, which is satisfied when the cavity round trip phase shift is an integer multiple of 2π. The field transmission and the reflection of the input coupler are set to be ${t_1}^2 = 0.015$ and ${r_1}^2 = 0.985$, respectively. The loss of the input coupler is assumed to be zero ${l_1}^2 = 0$. 99 % of cavity round trip power factor is assumed ($r^2 = 0.99$). Note that the cavity is not impedance matched, and thus, the dips of the normalized reflection do not reach zero in this example.*

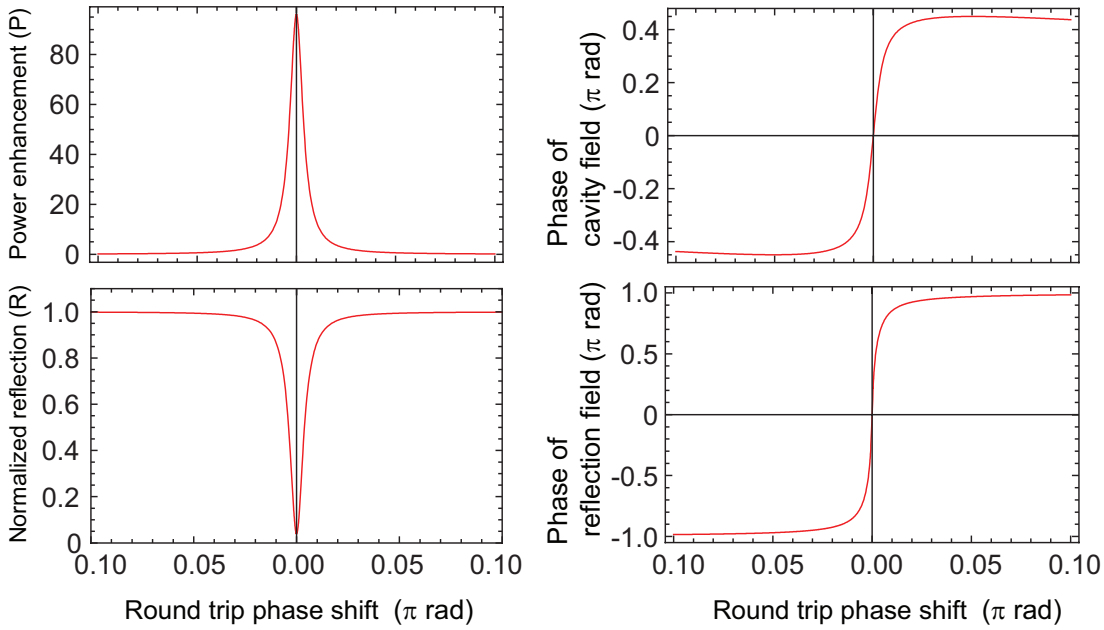

Figure 2.11: *Power enhancement P and normalized reflection R as a function of the round trip phase shift. The phase response of the intracavity field and the reflected field are also shown. The parameters for the calculation are the same as those used for Fig. 2.10.*

- Impedance matched

  Eqn. (2.23) shows that the power enhancement P is a function of the round trip amplitude factor r and of both the transmission t_I and the reflection r_I of the input coupler, respectively. Let's consider the question which input coupler maximizes the power enhancement. The input coupler is characterized by two parameter values out of t_I, r_I and l_I [10]. Since there are two parameters characterizing the input coupler, "the optimization of the input coupler" is an ambiguous statement because the optimization method will differ depending on how the loss l_I is dependent on the reflectance t_I and the transmission r_I. Here, let's consider the simplest case in which the loss l_I is constant and independent of reflectance t_I and transmission r_I [11]. With Eqn. (2.17), the power enhancement can be described by:

$$P = \frac{1 - {l_\mathrm{I}}^2 - {r_\mathrm{I}}^2}{1 + r^2{r_\mathrm{I}}^2 - 2r r_\mathrm{I}\cos\left(\phi(\omega)\right)}. \tag{2.27}$$

  Assuming constant loss l_I, the maximum power enhancement on rosonance ($\phi(\omega) = 0$) is obtained when

$$r_\mathrm{I} = r(1 - {l_\mathrm{I}}^2). \tag{2.28}$$

  When Eqn. (2.28) is satisfied, we call the cavity "impedance matched".

[10] Note the condition described by Eqn. (2.17).

[11] In this case, the change in t_I is associated with the change of r_I, so that Eqn. (2.17) is always satisfied.

- Lossless input coupler

  When the input coupler is lossless,

  $$l_{\mathrm{I}} = 0 \tag{2.29}$$

  is satisfied. In this case, impedance matching is fullfilled if the (field) reflectance of inputcoupler is identical to cavity round trip amplitude factor ($r_{\mathrm{I}} = r$).

- Lossless cavity

  A better enhancement is always obtained when the cavity losses are smaller. In the extreme case, we can consider a unity round trip amplitude factor r.

  $$r = 1. \tag{2.30}$$

For each combination of those conditions, the power enhancement given by Eqn. (2.23) can be simplified. The results can be obtained after simple arithmetics and are summerized in Fig. 2.12.

It is interesting to compare the power enhancements of the lossless cavity and the impedance matched cavity. Consider a cavity with a lossless input coupler ($l_{\mathrm{I}} = 0$). As shown in a) and b) in Fig. 2.12, the power enhancement in a lossless cavity ($r = 1$) is four times higher compared with the impedance matched ($r_{\mathrm{I}} = r$) cavity. However, this is not contradictory to the definition of "impedance matching" which describes the optimum input coupler to maximize the power enhancement for a given intracavity loss. A smaller intracavity loss always yields a higher power enhancement for any input coupler. The situation becomes quite clear looking at Fig. 2.13, where the power enhancement is plotted as a function of the round trip power factor r^2 and the power reflectance ${r_{\mathrm{I}}}^2$ of the input coupler. It can be seen that the power enhancement is maximized for the impedance-matched input coupler if the cavity loss is constant. However, there is no "optimum cavity loss" and a smaller cavity loss always results in a better power enhancement.

The normalized reflection given by Eqn. (2.24) is calculated for several combinations of cavity conditions and summarized in Fig. 2.14. Again, the simple derivations have been skipped.

Although the expression for the normalized reflectance is derived for the most general case (see Eqn. (2.24)), it is not straightforward to apply it to a cavity with an input coupler of finite loss. When the input coupler is lossy, the losses of the two surfaces could differ depending on the actual cause of loss. In the expression for the normalized reflectance in Eqn. (2.20), it is implicitly assumed that the reflectance is the same for both surfaces of the input coupler which is usually not the case. Therefore, to precisely model the input coupler, we have to increase the number of parameters to adequately describe both surfaces. Here, we limit ourselves and just apply the expression for the normalized reflectance (Eqn. (2.24)) to lossless input couplers. The calculation of the power enhancement is not affected because only the reflectance of one input coupler surface contributes to the calculation.

There are a few additional parameters that quantify the performance of the cavity. Here we describe the definitions and expressions for the finesse ($\mathcal{F}$), the quality factor (Q) and the lifetime (τ):

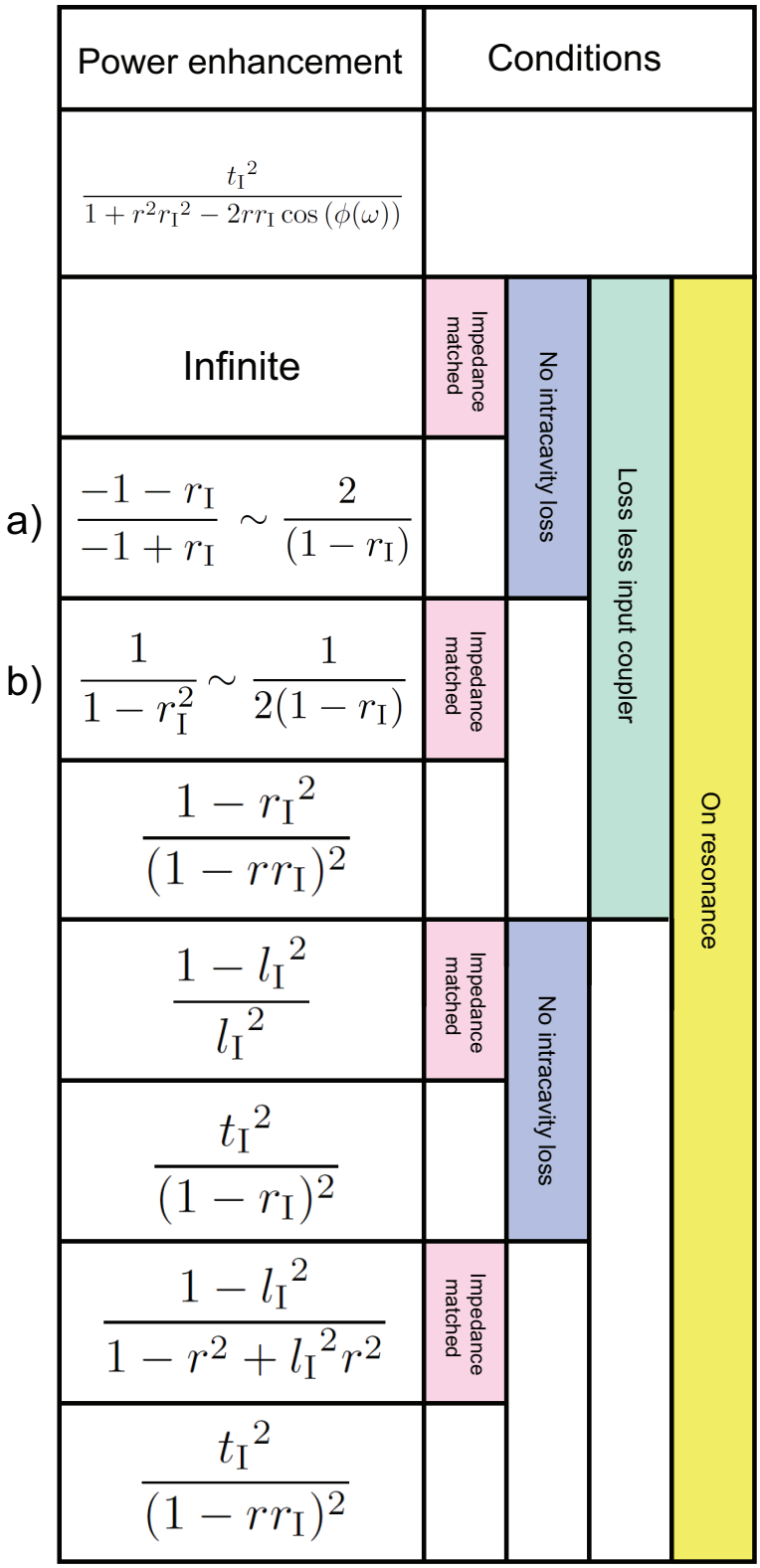

Figure 2.12: *Power enhancement P for different combinations of cavity conditions. The approximation ($\sim$) is valid for high finesse ($rr_I \sim 1$).*

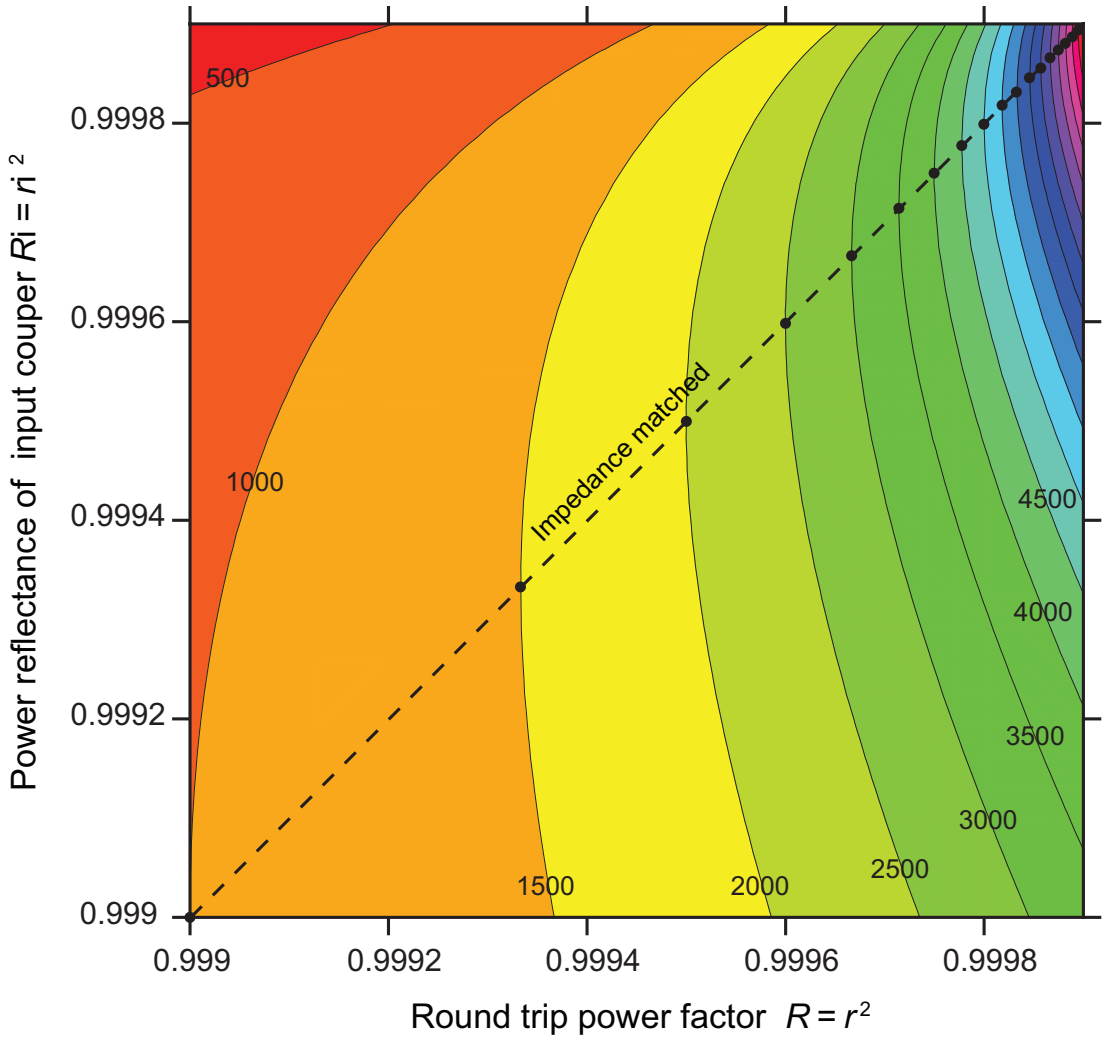

Figure 2.13: *Power enhancement P as a function of the round trip power factor (r^2) and the power reflectance of the input coupler ($r_\mathrm{I}{}^2$). A lossless input coupler is assumed ($l_\mathrm{I} = 0$). The dashed line indicates the impedance-matched case ($r_\mathrm{I} = r$). It can be seen that the impedance-matched cavity does not yield the highest power enhancement for a given input coupler. As intuitively known, smaller losses always result in a better power enhancement for any input coupler.*

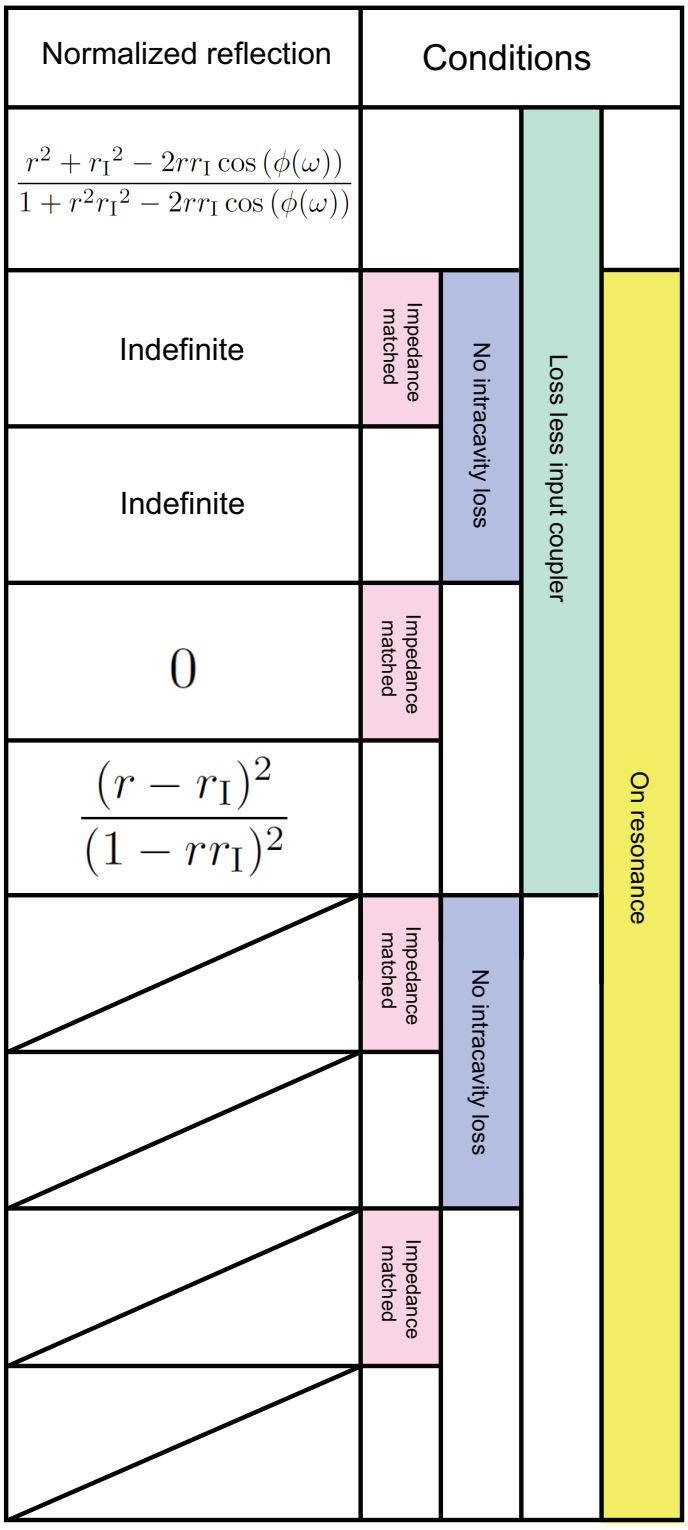

Figure 2.14: *Normalized reflectance R for different combinations of cavity conditions. The normalized reflectance is not calculated for a cavity with a lossy input coupler due to the reasons discussed in the text.*

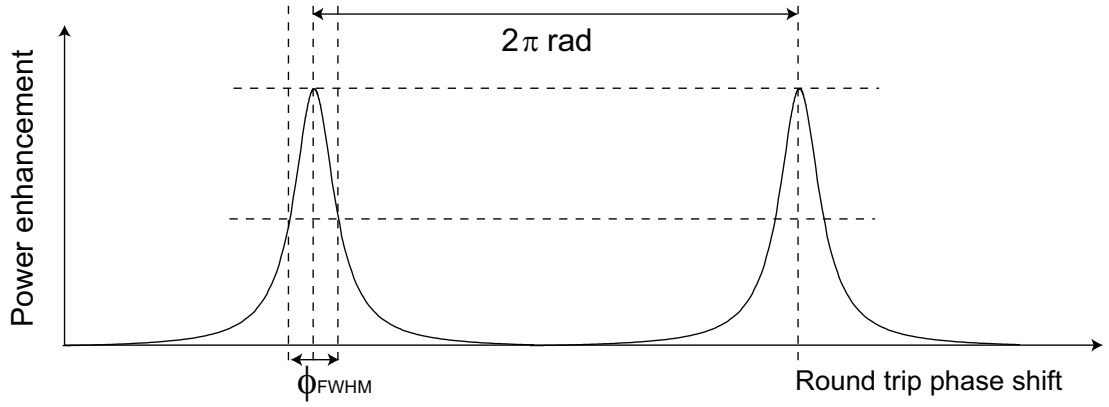

Figure 2.15: *The cavity finesse ($\mathcal{F}$) is defined to be the ratio between the resonance separation and the resonance width.*

- Finesse : $\mathcal{F}$

  The cavity finesse ($\mathcal{F}$) is defined as

  $$\mathcal{F} \equiv \frac{\omega_{\mathrm{FSR}}}{\omega_{\mathrm{FWHM}}}. \tag{2.31}$$

  Here, ω_{FSR} stands for the frequency separation between two adjacent resonances (Free Spectral Range: FSR) and ω_{FWHM} is the FWHM of the resonance peak.

  The same quantity can also be expressed in terms of the round trip phase shift

  $$\mathcal{F} = \frac{2\pi}{\phi_{\mathrm{FWHM}}} \tag{2.32}$$

  where ϕ_{FWHM} is the FWHM of a resonance in the phase shift (see Fig. 2.15). With Eqn. (2.23), ϕ_{FWHM} can be evaluated by solving

  $$P(\phi = \frac{\phi_{\mathrm{FWHM}}}{2}) = \frac{P(\phi = 0)}{2}. \tag{2.33}$$

  Eqns. (2.33) and (2.32) yield

  $$\begin{aligned} \mathcal{F} &= \frac{\pi}{\arccos\left[\frac{1}{2}(4 - \frac{1}{rr_{\mathrm{I}}} - rr_{\mathrm{I}})\right]} \\ &\approx \frac{\pi}{1 - rr_{\mathrm{I}}}. \end{aligned} \tag{2.34}$$

  Here, the last approximation is valid for high finesse ($rr_{\mathrm{I}} \approx 1$). It is interesting to note that the finesse ($\mathcal{F}$) is equivalent to $\pi\times$ (the impedance-matched power enhancement).

- Quality factor (Q)

The quality factor of the cavity (Q) is defined as

$$Q \equiv -\frac{P_{\mathrm{cav}}}{\delta P_{\mathrm{cav}}} 2\pi \tag{2.35}$$

with the intracavity power P_{cav} and the dissipated power within one optical period δP_{cav}. After one round trip ($\Delta t = \frac{L}{c}$), the power dissipation is given by $-\Delta P_{\mathrm{cav}} = P_{\mathrm{cav}} - P_{\mathrm{cav}} r^2 {r_{\mathrm{I}}}^2$. Thus, the Q factor can be written as

$$\begin{aligned} Q &= -\frac{P_{\mathrm{cav}}}{\delta P_{\mathrm{cav}}} 2\pi = \frac{P_{\mathrm{cav}}}{-\frac{\Delta P_{\mathrm{cav}}}{f \Delta t}} 2\pi \\ &= \frac{Lf}{c} \frac{2\pi}{1 - r^2 {r_{\mathrm{I}}}^2} \sim \frac{Lf}{c} \frac{\pi}{1 - r r_{\mathrm{I}}} \\ &= \frac{\omega}{\omega_{\mathrm{FSR}}} \mathcal{F}. \end{aligned} \tag{2.36}$$

Here, f stands for the optical frequency. The approximation is valid for high finesse ($r r_{\mathrm{I}} \sim 1$).

- Lifetime (τ)

  Suppose the cavity is seeded with pulsed or CW radiation. When the seeding is stopped, the power stored in the cavity starts decreasing. The cavity lifetime τ is defined to be the $1/e$ decay time of the intracavity power. Thus, the lifetime τ can be related to the round trip time Δt and the round trip power dissipation ΔP_{cav}.

$$\frac{\Delta P_{\mathrm{cav}}}{\Delta t} = -\frac{P_{\mathrm{cav}}}{\tau}. \tag{2.37}$$

  Eqn. (2.37) can be simplified as:

$$\tau = -\Delta t \frac{P_{\mathrm{cav}}}{\Delta P_{\mathrm{cav}}} = \frac{L}{c} \frac{1}{1 - r^2 {r_{\mathrm{I}}}^2} \sim \frac{Q}{\omega}. \tag{2.38}$$

  The last approximation is valid for high finesse ($r r_{\mathrm{I}} \sim 1$).

2.3.3 The effect of intracavity dispersion

An intracavity dispersion close to zero is one of the important prerequisites for a femtosecond enhancement cavity, as discussed in Sec. 2.3.1. In this subsection, the effect of intracavity dispersion will be considered in a more quantitative way based on the expressions derived in the previous section (Sec. 2.3.2). The term intracavity dispersion stands for the nonlinear dependence of the cavity round trip phase on the optical frequency. Thus, it can be represented by the term $\delta\phi(\omega)$ in Eqn. (2.18). Here, let's consider the Taylor expansion of Eqn. (2.18) up to second order around an angular center frequency of ω_{c}:

$$\phi(\omega) = \phi(\omega_{\mathrm{c}}) + \phi'(\omega_{\mathrm{c}})(\omega - \omega_{\mathrm{c}}) + \frac{1}{2}\phi''(\omega_{\mathrm{c}})(\omega - \omega_{\mathrm{c}})^2. \tag{2.39}$$

$\phi'(\omega_c)$ and $\phi''(\omega_c)$ in the above equation are often called group delay (GD) and group delay dispersion (GDD), respectively. The resonance frequencies of the resonator can be obtained by requiring the phase shift $\phi(\omega)$ to be an integer multiple of 2π. Thus,

$$\phi(\omega) = \phi(\omega_c) + \phi'(\omega_c)(\omega - \omega_c) + \frac{1}{2}\phi''(\omega_c)(\omega - \omega_c)^2 = 2\pi n \tag{2.40}$$

holds with integer n. To obtain the resonance frequency, Eqn. (2.40) can be reduced to

$$\omega = \frac{2\pi}{\phi'(\omega_c)}n + \left(\omega_c - \frac{\phi(\omega_c)}{\phi'(\omega_c)}\right) - \frac{1}{2}\frac{\phi''(\omega_c)}{\phi'(\omega_c)}(\omega - \omega_c)^2. \tag{2.41}$$

When the intracavity dispersion is zero ($\phi''(\omega_c) = 0$), it can be seen that the resonance frequencies of the cavity form a comb of equisitant modes with a constant offset. Thus, when the repetition frequency and the offset frequency of the frequency comb that seeds the cavity are set to

$$\begin{aligned} \omega_{rep} &= \frac{2\pi}{\phi'(\omega_c)}, \\ \omega_{CEO} &= \omega_c - \frac{\phi(\omega_c)}{\phi'(\omega_c)}, \end{aligned} \tag{2.42}$$

all the modes of the seeding frequency comb will be resonant with the cavity modes.

However, this is not the case anymore for non-zero intracavity GDD ($\phi''(\omega_c) \neq 0$). In that case, when the repetition rate and the offset frequency are set according to Eqn. (2.42), the round trip phase shift becomes

$$\phi(\omega) = 2\pi n + \frac{1}{2}\phi''(\omega_c)(\omega - \omega_c)^2. \tag{2.43}$$

For a comb with a broad bandwidth, the round trip phase can thus differ from an integer multiple of 2π at the edge of the spectrum so that the power enhancement drops. This way, the remaining intracavity GDD limits the bandwidth of the pulse that can be coupled into the cavity. Here we define the maximum enhanced bandwidth $\Delta\omega$ such that the power enhancement drops to half of its maximum value at $\omega = \omega_c \pm \frac{\Delta\omega}{2}$. The phase detuning from the resonance peak that yields half of the peak enhancement factor is nothing but $\frac{\phi_{FWHM}}{2}$, as introduced in Sec. 2.3.2. Thus, from the following set of equations

$$\begin{aligned} \frac{2\pi}{\phi_{FWHM}} &= \mathcal{F} \\ \frac{1}{2}\phi''(\omega_c)(\frac{\Delta\omega}{2})^2 &= \frac{\phi_{FWHM}}{2}, \end{aligned} \tag{2.44}$$

we obtain

$$\phi''(\omega_c) = \frac{8\pi}{\mathcal{F}\Delta\omega^2}. \tag{2.45}$$

This expression indicates that in order to couple 20 THz of bandwidth into a cavity with a finesse of $\mathcal{F} = 100\pi$, the intracavity dispersion has to be compensated to below 5 fs^2.

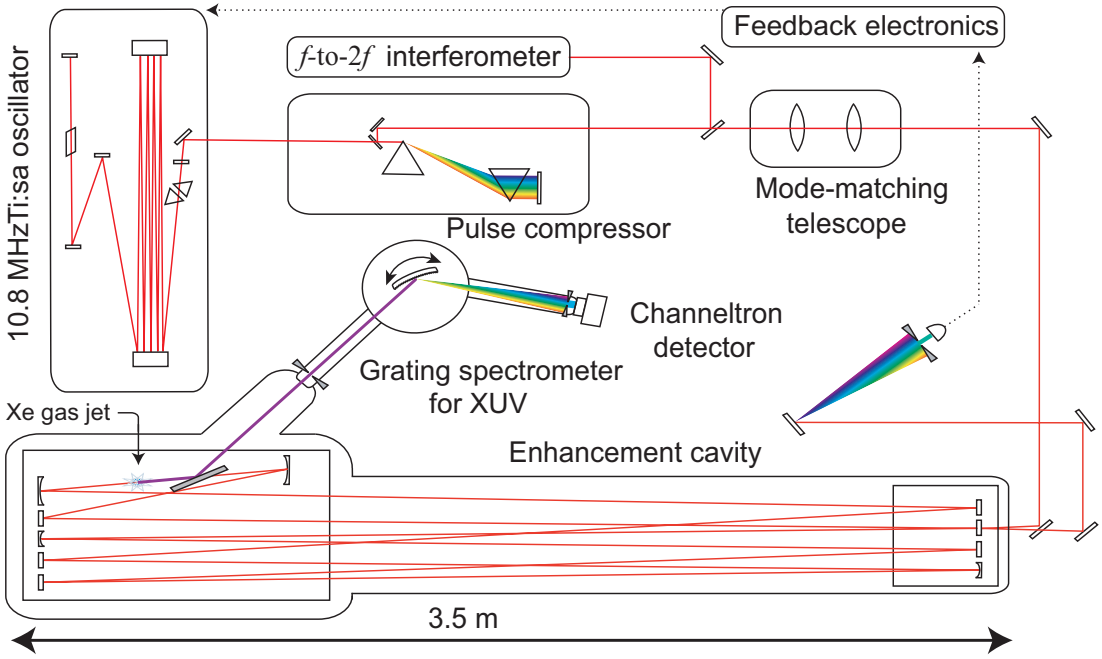

Figure 2.16: *Setup of the femtosecond enhancement cavity for intracavity high harmonic generation at a repetition rate of 10 MHz. Details are discussed in the text.*

2.4 Experiments and results

In this subsection, the experimental details of XUV frequency comb generation with a 10 MHz enhancement cavity are discussed. Fig. 2.16 shows the entire experimental setup.

2.4.1 Positively chirped oscillator at 10 MHz repetition rate

First, let us focus on the driving oscillator for the enhancement cavity. Fig. 2.17 shows the setup of our mode-locked Ti:sapphire oscillator at a repetition rate of 10.8 MHz. This oscillator was developed in collaboration with the group of Prof. Krausz and more detailed information on it can be found in [92–94].

Here we give a brief summary of the oscillator setup. A repetition rate of 10.8 MHz corresponds to 28 m of round-trip path-length. Since the oscillator operates in a linear geometry, a cavity length of 14 m is required. To produce such a long beam path in a rather compact setup, a Herriott-type multi-pass cell is introduced into the cavity. The beam bounces off each Herriott-cell mirror 8 times, thus covering an additional 12 m of path length. In order to facilitate finding the optimum alignment of such a long cavity, it is first aligned without the Herriott-cell. Then the Herriott-cell which is designed such that it does not influence the q-parameter of the cavity mode at the position of the crystal is introduced. Specially designed chirped mirrors and intracavity prism pairs are used to set the intracavity dispersion to be positive (GDD of $\sim$55 fs^2). The oscillator thus works in the positively chirped pulse regime (chirped pulsed oscillator: CPO). Further details about the CPO will be discussed in Sec. 4.1.1 of this thesis. In order to control the offset frequency and the repetition rate, several piezo-electric actuators are installed to adjust the positions of mirrors and prisms. The details of this active control will be discussed in Sec. 2.4.3. The entire oscillator cavity is

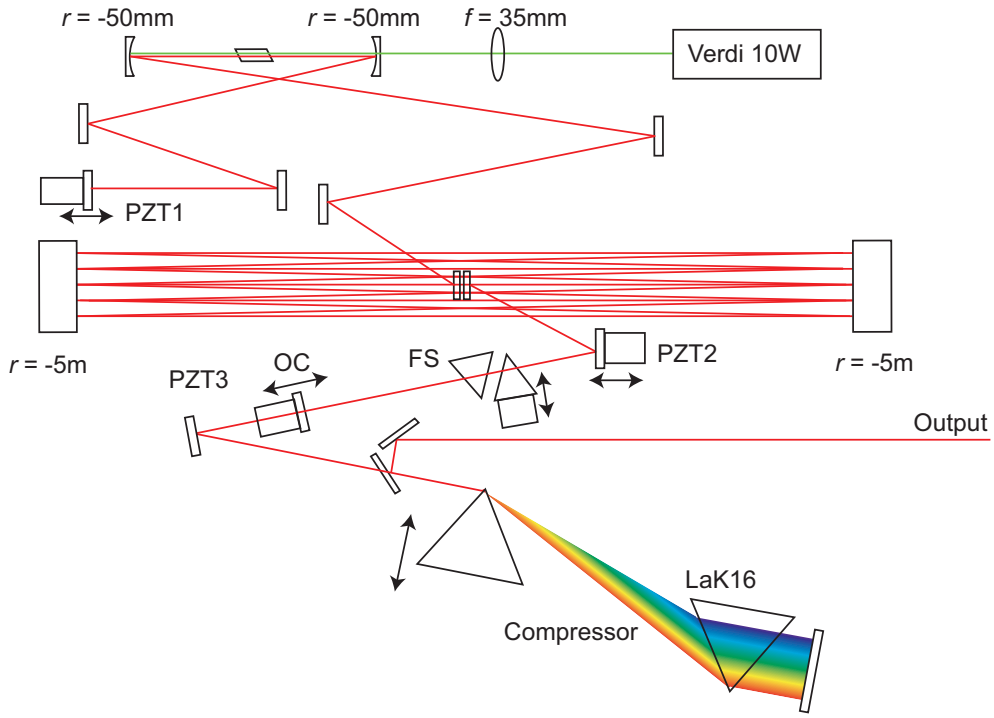

Figure 2.17: *Setup of the positively chirped oscillator [92, 93].*

covered with a virtually air-tight box to obtain an acoustically stable atmosphere around the cavity, which turns out to be indeed necessary for stable active locking of the comb modes to the enhancement cavity. The output of the oscillator is chirp-compensated by two LaK16 prism pairs. Fig. 2.18 shows a typical spectrum and a typical autocorrelation trace of the oscillator after the pulse compression. Typically, the oscillator operates with the following paramters:

- repetition rate: 10.8 MHz
- pulse duration (after the pulse compression): 38 fs
- average power: 1.5 W
- pulse energy: 140 nJ

2.4.2 Enhancement cavity

The enhancement cavity has the same repetition rate as the oscillator (10.8 MHz) and is therefore also 28 m long. The entire cavity is placed in a vacuum chamber and evacuated to a pressure of 10^{-2} mbar. This is vital because the generated XUV frequency comb would otherwise be absorbed by the air. In addition, evacuating the chamber eliminates both the dispersion of and the scattering loss from air. The enhancement cavity consists of 10 mirrors: 7 quarter-wave-stack mirrors, 4 of which are curved, 2 chirped mirrors, and one input coupler. The conventional ABCD matrix method is used to calculate the spatial cavity mode that results from the stability condition and allows to determine the focal radius and the beam

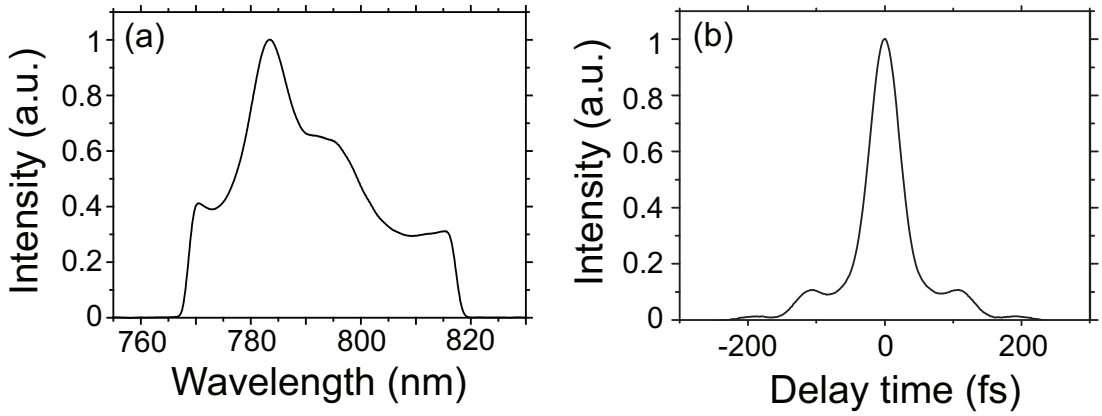

Figure 2.18: *Typical spectrum (a) and autocorrelation trace (b) of the oscillator. The pulse duration after the pulse compression is 38 fs.*

diameter at the mirrors [95]. As shown in Fig. 2.16, two separate breadboards are used to support six and four mirrors, respectively. The original plan was to make the distance between the two boards insensitive to temperature fluctuations by connecting them through a long tube made of invar. However, it turned out that mechanical vibrations of the invar tube corrupted the short term stability of the cavity. Thus, the invar tube was removed and the two boards were firmly fixed onto the optical table. The vacuum chamber is vibrationally isolated from the breadboards. The spatial profile of the seeding beam is shaped after the pulse compressor with two lenses to match the spatial mode of the enhancement cavity (see Fig. 2.16).

The cavity uses two different curved mirrors (radii of curvature 0.1 m and 0.24 m, respectively) to asymmetrically focus the beam to a waist size of $w_0 = 13\,\mu$m. Fig. 2.19 shows pictures of parts of the enhancement cavity and the vacuum chamber.

2.4.3 Locking of the cavity

As described in detail in Sec. 2.3.3 and Sec. 2.3.1, the repetition frequency (ω_{rep}) and the offset frequency (ω_{CEO}) have to be controlled actively to maintain the broadband resonance condition between the cavity and the seeding laser. We call this "locking the cavity". Active control of the experimental parameters can be realized with a Proportional-Integral-Derivative (PID) controller which embodies one of the control-loop feedback mechanisms that have been widely used [96]. The detailed theory of the PID control loop is described elsewhere [96], and here we limit ourselves to a brief description of the method. A feedback loop requires an "error signal" which becomes zero when the value of the controlled parameter and the target value are equal. When the parameter differs from its target value, the error signal should have opposite sign depending on whether the parameter value is larger or smaller than the the target value. The error signal is multiplied, integrated and/or differentiated to yield a feedback signal for the controlled parameter. There are several methods to obtain an error signal to lock an enhancement cavity, such as the frequency modulation method (Pound-Drever-Hall method: PDH) [97], the polarization method (Hänsch-Couillaud: HC) [98], and the method based on the spatial mode [99]. Both the PDH and the HC method have been implemented successfully into the 10 MHz enhancement cavity. However, the 10 MHz oscillator tends to

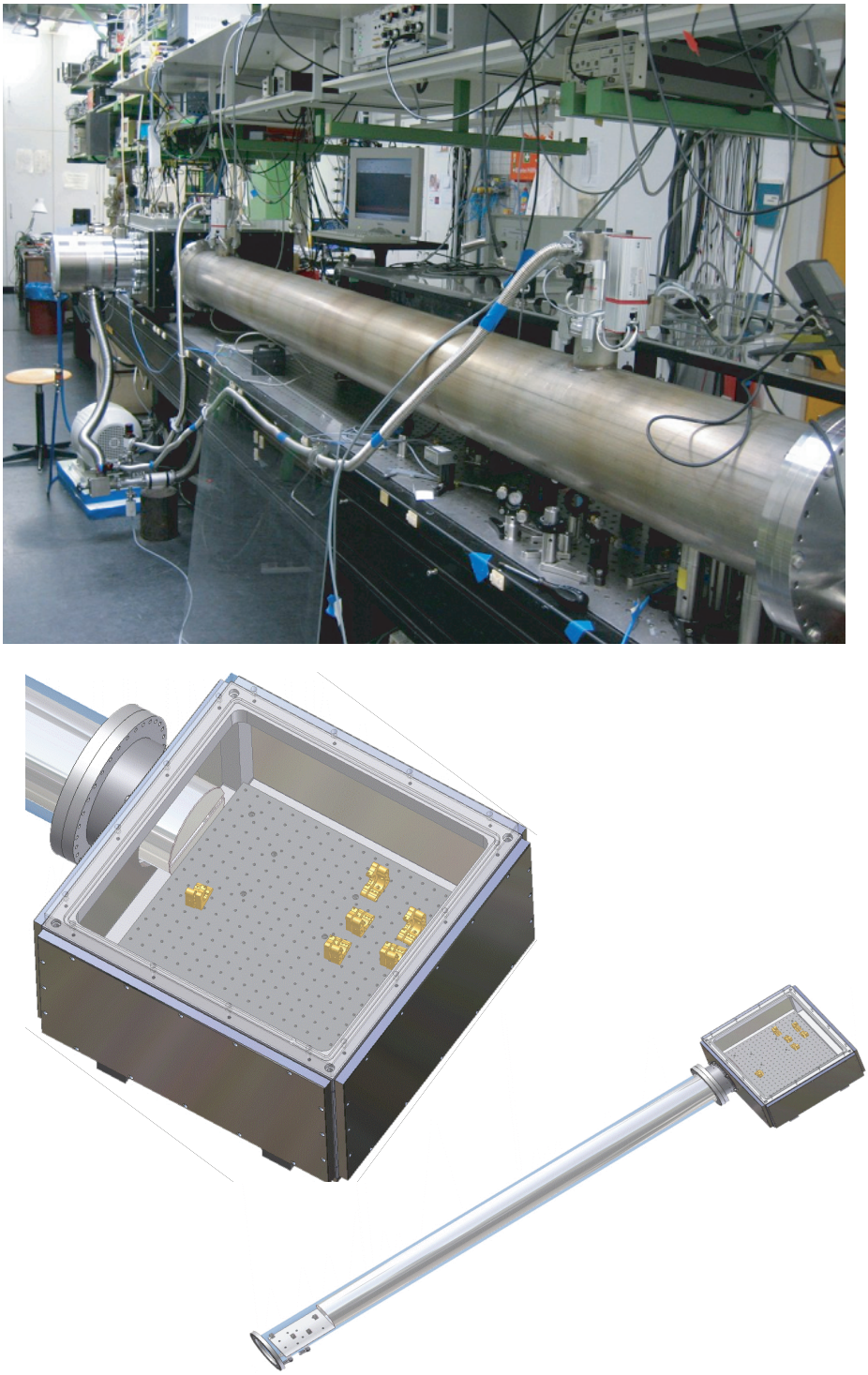

Figure 2.19: *The pictures of experimental setup for enhancement cavity at 10 MHz repetition rate. The enhancement cavity with a length of 28 m is set up in a vacuum chamber with a length of 3.5 m.*

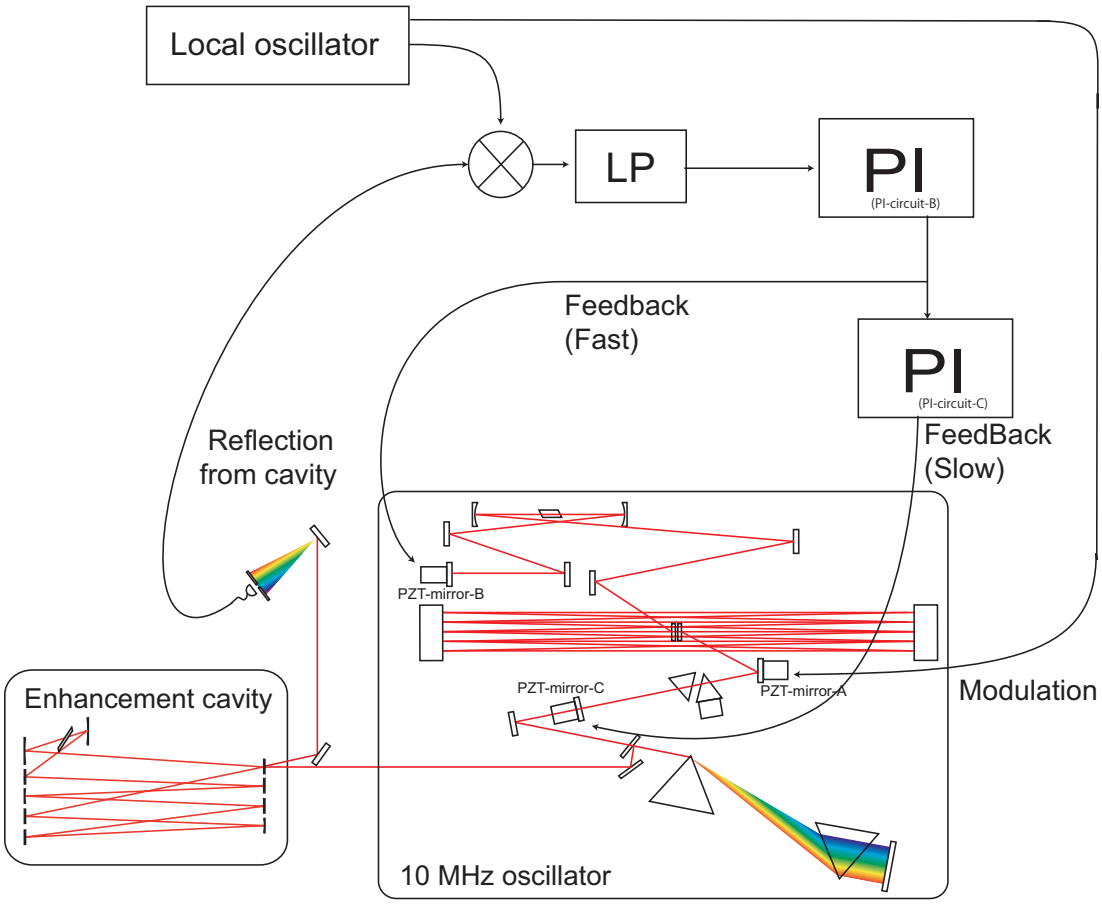

Figure 2.20: *Repetition rate locking of the 10 MHz enhancement cavity. The error signal is produced by the Pound-Drever-Hall (PDH) method [97]. The phase modulation is created by a piezo-actuated mirror in the oscillator cavity. The error signal is processed by a proportional and an integrating (PI) circuit and then applied to the piezo-actuated mirrors in the oscillator cavity. Two separate piezo-actuated mirrors are used for slow and fast feedback. In the fast feedback loop, a maximum bandwidth of 100 kHz is obtained.*

exhibit a weak intensity modulation of its output power. In this case, it is found that the PDH method works in a more reliable manner because of its insensitivity against intensity fluctuations. Fig. 2.20 illustrates the setup of the feedback loop for the repetition rate locking of the 10 MHz cavity.

There are three piezo-actuated mirrors (PZT mirrors) installed inside the oscillator cavity, as illustrated in Fig. 2.17. We denote these actuated mirrors as "PZT-mirror-A,-B and -C", respectively. PZT-mirror-A is driven with a 650 kHz sinusoidal wave. Although the amplitude response of the PZT mirror starts to decay below 650 kHz due to the limited bandwidth, the mirror can still be actuated quite efficiently at this frequency. This is because the frequency corresponds to a mechanical resonance of the system consisting of the piezo-actuator and the mirror. The phase delay between the driving frequency and the actual motion of the PZT mirror can be adjusted precisely by slightly detuning the driving frequency from the mechanical resonance. Thus, no additional radio-frequency phase delay circuit is required to obtain the optimum PDH error signal. The reflection from the cavity is spectrally resolved,

and a tiny portion of the spectral components is used to generate the PDH error signal. The error signal is processed by the proportional-integrating (PI) circuit to obtain an control signal that can be used to tune the cavity length of the oscillator (or to adjust the repetition frequency ω_{rep}). We denote this circuit "PI-circuit-B". The control signal is amplified by a fast high-voltage amplifier and fed into PZT-mirror-B which is composed of a $2 \times 2 \times 2\,\mathrm{mm}$ PZT actuator glued to a $\sim 2 \times 2 \times 1\,\mathrm{mm}$ dielectric high reflective mirror. Before installed in to the enhancement cavity, the mechanical response of PZT-mirror-B is characterized with a Michelson-Interferometer whose one arm is actuated with PZT-mirror-B. By monitoring the interferogram for different driving frequencies, the phase and the amplitude response of PZT-mirror-B are obtained. Due to the small dimensions and the resulting small masses of both PZT actuator and mirror, the lowest resonance frequency lies above 100 kHz. Therefore, when appropriate electronic PI circuit is utilized, a feedback loop with more than 100 kHz of bandwidth is possible. Since the maximum travel range of PZT-actuator-B is limited to 2.2 μm, PZT-actuator-C is installed in addition to obtain a slow but long-range ($32\,\mu$m) control of the cavity length. A fraction of the output of PI-circuit-B is sent into an additional PI circuit (PI-circuit-C) to produce an control signal that can be fed back to PZT-mirror-C after amplification through a high voltage amplifier. The feedback loop for PZT-mirror-C can be understood in both the frequency and the time domain:

- *frequency-domain*
  The original error signal is filtered twice by the response curve of the PI circuit. Thus, the effective amount of low-pass action of the feedback loop is higher for PZT-mirror-C. This way, a higher gain can be obtained for lower frequencies without increasing the gain for higher frequencies. This is necessary when driving PZT-mirror-C to avoid instabilities.

- *time-domain*
  The second PI loop (PI-circuit-C) tries to stabilize the control signal of PZT-mirror-B. PZT-mirror-B is actuated fast to compensate the high frequency motion of the cavity, but its average position is controlled by the slow PZT-mirror-C to keep its position stable on a longer timescale.

The bandwidth of the entire feedback loop is limited by the mechanical resonances of PZT-mirror-B. Recently, a highly reflective coating structure without a substrate has been demonstrated. The coating structure is a very thin film, but it is still free-standing to avoid surface deformations. This highly reflective mirror can be attached to a piezo-actuator, thereby reducing the mass of the mirror-actuator system significantly and thus increasing the bandwidth of the feedback loop. This method may help to improve the stability of the feedback loop and to get rid of the high frequency noise in the cavity.

Since the error signal for the repetition rate is generated from a spectrally dispersed reflection from the cavity, the repetition rate can just be stabilized such that the resonance condition is met for a certain narrow wavelength region. [12]

To obtain a broadband resonance, the offset frequency ω_{CEO} also has to be optimized. Several methods to control the offset frequency of a mode-locked oscillator have been proposed and investigated [91,100]. In the 10 MHz enhancement cavity experiment, the offset frequency

[12] To be precise, the PZT-actuated mirror that supposed to change the repetition rate introduces tiny misalignment of the cavity and thus the offset frequency of the laser also changes accordingly.

of the oscillator is controlled with two intracavity prism pairs. One of the prisms is on a piezo-actuated stage so that its insertion into the beam can be controlled. The stability of the offset frequency of a mode-locked laser strongly depends on the configuration of the cavity. For example, a mode-locked oscillator in which the intracavity dispersion is compensated with prism pairs often needs a long dispersive arm and therefore tends to exhibit rather strong fluctuations of the offset frequency. In contrast, an oscillator which uses chirped mirrors for dispersion-compensation often has a stable offset frequency. In the case of the 10 MHz oscillator, the prism pair is installed in order to introduce positive dispersion into the cavity. Therefore, the dispersive arm is short ($\sim 10\,\mathrm{cm}$) compared to the case in which a prism pair is installed to introduce negative dispersion. Consequently, the offset frequency can be expected to be rather stabele. If the offset frequency drifts away from its optimum value while the repetition rate is locked to the cavity, the intracavity bandwidth starts to decrease due to the limited overlap between the laser comb and the cavity modes. Therefore, the drift of the offset frequency can be monitored by measuring the intracavity power or the intracavity spectrum. The required stability of the offset frequency depends on the cavity finesse and the laser bandwidth. It turns out that the offset frequency of the 10 MHz oscillator is stable enough to keep the enhancement higher than 90 % of the maximum enhancement for more than 5 minutes without any adjustment. Therefore, it is sufficient for the demonstration of XUV frequency comb generation to manually optimize the offset frequency, which eliminates the need for a rather complicated setup to produce an error signal for the offset frequency [91, 100].

2.4.4 Dispersion management of enhancement cavity

As discussed in Fig. 2.3.3, it is crucial to carefully control the intracavity dispersion to obtain a high broadband enhancement. In the 10 MHz enhancement cavity, a significant amount of dispersion is readily eliminated by moving the entire cavity into a vacuum chamber. The GDD from air amounted to $57\,\mathrm{fs}^2$ in our previous setup [51] and would have been $591\,\mathrm{fs}^2$ in our current setup. We used a single sapphire plate of 0.5 mm thickness as an Brewster output coupler for the XUV. In our previous setup, a tiny vacuum chamber which only covered the area around the focus of the cavity was used. In this case, two Brewster sapphire windows thick enough to withstand atmospheric pressure were necessary. Altogether, the GDD contribution of the sapphire plate(s) and air were reduced from $197\,\mathrm{fs}^2$ in the previous 3 m cavity to only $34\,\mathrm{fs}^2$ in our 27.8 m cavity. Besides the sapphire plate and air, dispersion is also introduced by the highly reflective mirrors. The different contributions to the total GDD as a function of wavelength are shown in Fig. 2.21.

The total intracavity GDD is the sum of the contributions from nine highly reflective mirrors, the sapphire plate, and the input coupler. The blue curve in Fig. 2.21 shows the estimated total dispersion of the cavity which amounts to more than $100\,\mathrm{fs}^2$ for the shorter wavelength region. To precisely estimate the expected power enhancement for this amount of intracavity GDD, the spectrally resolved power enhancement has to be calculated based on Eqn. (2.23) assuming that the offset frequency and the repetition rate of the seed laser have been optimized. Here, let us give a rough estimate of the effect of GDD assuming that the averaged GDD amounts to $50\,\mathrm{fs}^2$. Aiming for a bandwidth of 20 THz centered at 800nm, which corresponds to a (Fourier-limited) pulse duration of 22 fs, the cavity finesse $\mathcal{F}$ has to be decreased down to 32, leading to an impedance-matched power enhancement of about 10 (see Eqn. (2.45)). To achieve a better power enhancement with a broad bandwidth, the compensation of the intracavity dispersion is mandatory.

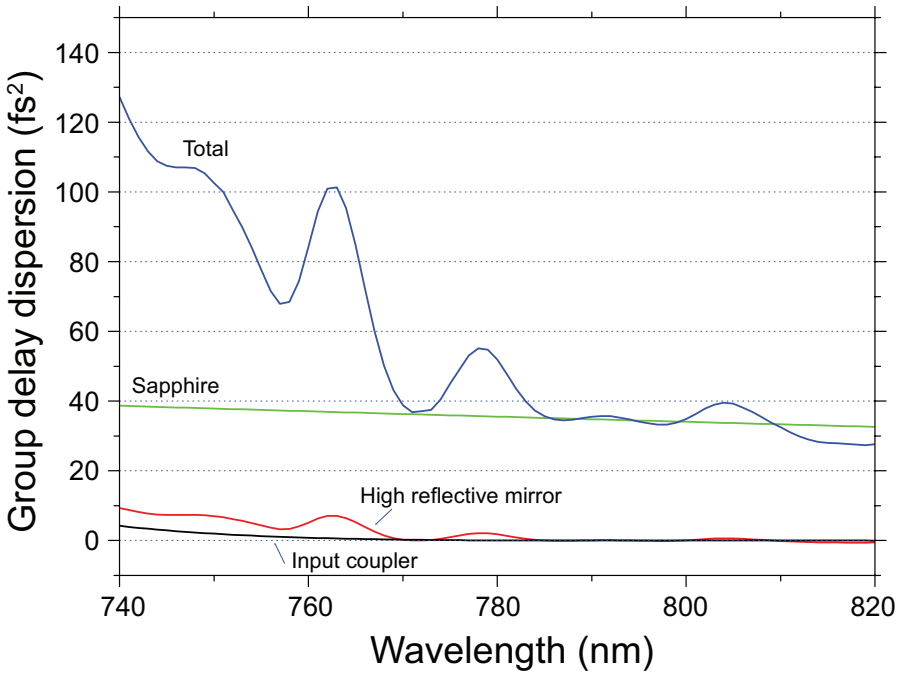

Figure 2.21: *Estimated total intracavity GDD (blue). The total GDD is the sum of the contributions from nine highly reflective mirrors, the sapphire plate and the input coupler. The GDD of individual components is also shown for a sapphire plate of 0.5 mm thickness at Brewster's angle (green), a single highly reflective mirror (red), and a single input coupler (black).*

When the cavity is locked with optimized repetition rate and offset frequency as described in the previous section (Fig. 2.4.3), the intracavity spectrum can be still narrowed by residual intracavity dispersion because in that case the cavity modes are not equidistant which prevents broadband resonance. Fig. 2.22 shows a comparison of the intracavity spectrum and the laser spectrum without the use of chirped mirrors in the cavity. The laser spectrum is measured from the transmitted light of the cavity when the cavity is not locked and detuned in length. When the cavity length is detuned, the transmission spectrum shows strong intensity modulations. In the frequency domain, this is because the resonance condition is periodically satisfied due to the strongly detuned repetition rate. In the time domain, multiple pulses stored in the cavity because of the mismatched cavity length produce a spectral modulation due to pulse-to-pulse interference. The envelope of the modulated transmission spectrum yields the laser spectrum. When the laser spectrum is measured this way, a better comparison between the cavity spectrum and the laser spectrum can be obtained, because both spectra are affected by the transmission spectrum of the highly reflective mirrors and the input coupler in the same manner. From Fig. 2.22, it can be seen that the cavity spectrum is narrowed significantly compared with the laser spectrum. Dispersion mismatch affects the intracavity peak intensity at the focus in two different ways: it reduces the coupling efficiency which limits the intracavity average power and it increases the intracavity pulse duration.

To cancel the positive dispersion introduced by the highly reflective mirrors, the sapphire plate, and the input coupler, one of the highly reflective mirrors is replaced with a negatively chirped mirror (denoted "CM1" here). The layer structure of CM1 is designed to have the dispersion properties shown in Fig. 2.23. Note that the curve resembles the total intracavity

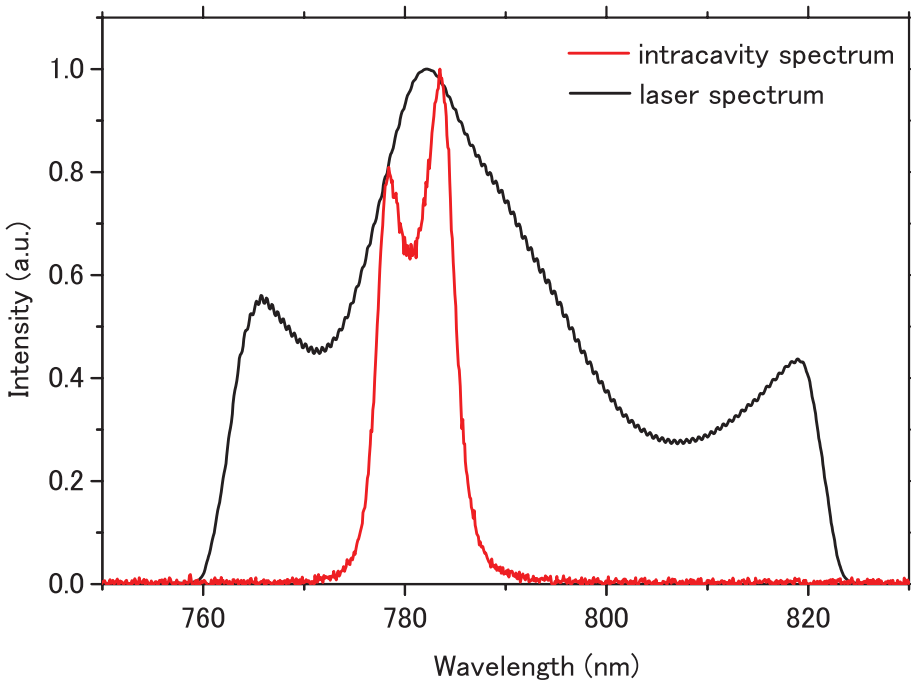

Figure 2.22: *Intracavity spectrum measured without any dispersion compensation (red). The black curve shows the driving laser spectrum for comparison.*

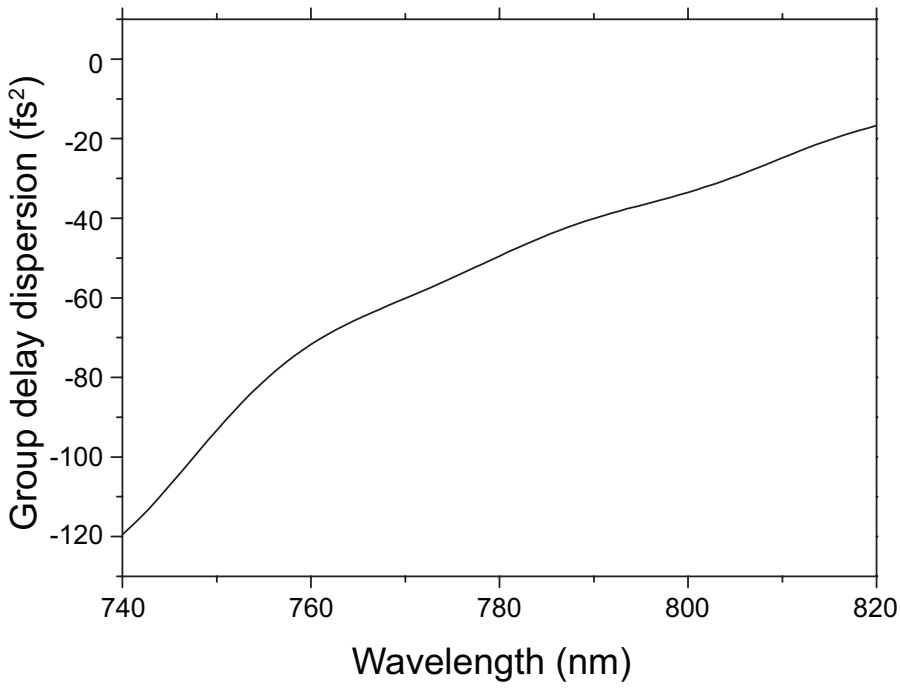

Figure 2.23: *Target curve of negatively chirped mirror (CM1) for intracavity dispersion compensation.*

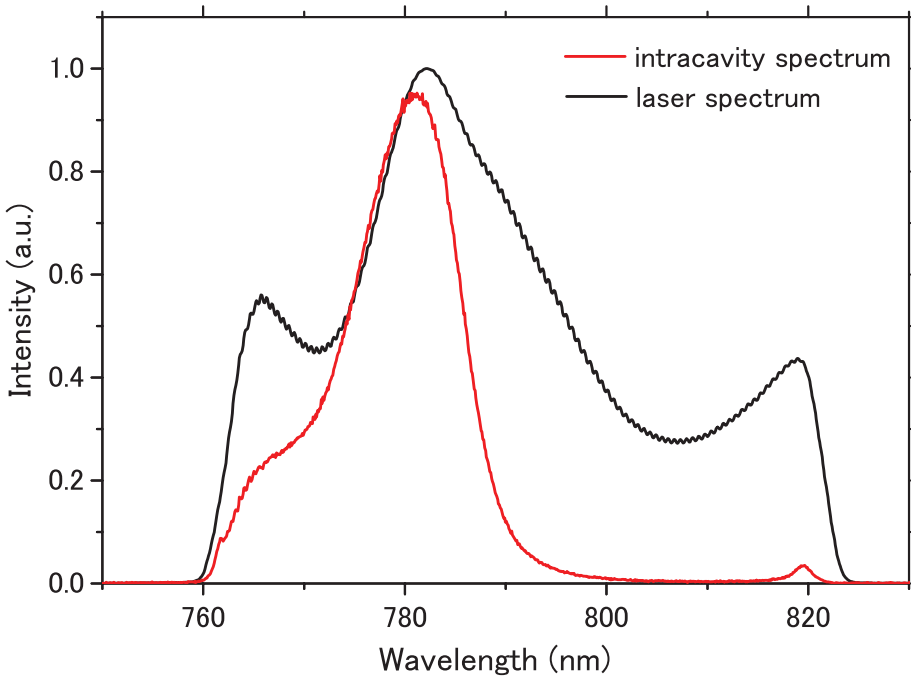

Figure 2.24: *Intracavity spectrum measured with chirped mirror CM1 designed to compensate the dispersion from sapphire plate, highly reflective mirrors, and input coupler. The target GDD for the chirped mirror design is obtained from the GDD of sapphire taken from the literature [101] and the theoretical GDD response of the mirrors.*

GDD curve shown in Fig. 2.21 except for the reversed sign.Fig. 2.24 shows a comparison of the intracavity spectrum with CM1 installed and the laser spectrum. The intracavity spectrum is indeed broader, indicating a somewhat better intracavity dispersion compensation. Yet, more than 60 % of the available laser power is not coupled into the cavity.

The imperfect dispersion compensation could have various origins. One possibility is an imprecise estimation of the target GDD. The dispersion of the highly reflective mirrors and the input coupler critically depends on the angle of incidence which cannot be determined precisely. Also, the material dispersion of the sapphire plate could differ because of the limited manufacturing precision for its thickness or because of imperfect adjustment of Brewster's angle. The other possibility is the error that originates from the mirror manufacturing itself. If the layers are not deposited precisely as designed, the dispersion characteristics of the mirror will deviate from the design. In order to solve these two possible problems, the intracavity dispersion is measured with high precision to obtain a reliable target GDD curve, and a novel optimization method is introduced to improve the coating design such that dispersion properties of the mirrors become insensitive to manufacturing errors. The following sections describe those procedures in more detail.

2.4.5 High precision intracavity dispersion measurement

The intracavity spectrum of the enhancement cavity is strongly dependent on the intracavity dispersion. Thus, by measuring the intracavity spectra for different values of appropriate parameters such as the repetition rate or the offset frequency of the driving beam, it is expected

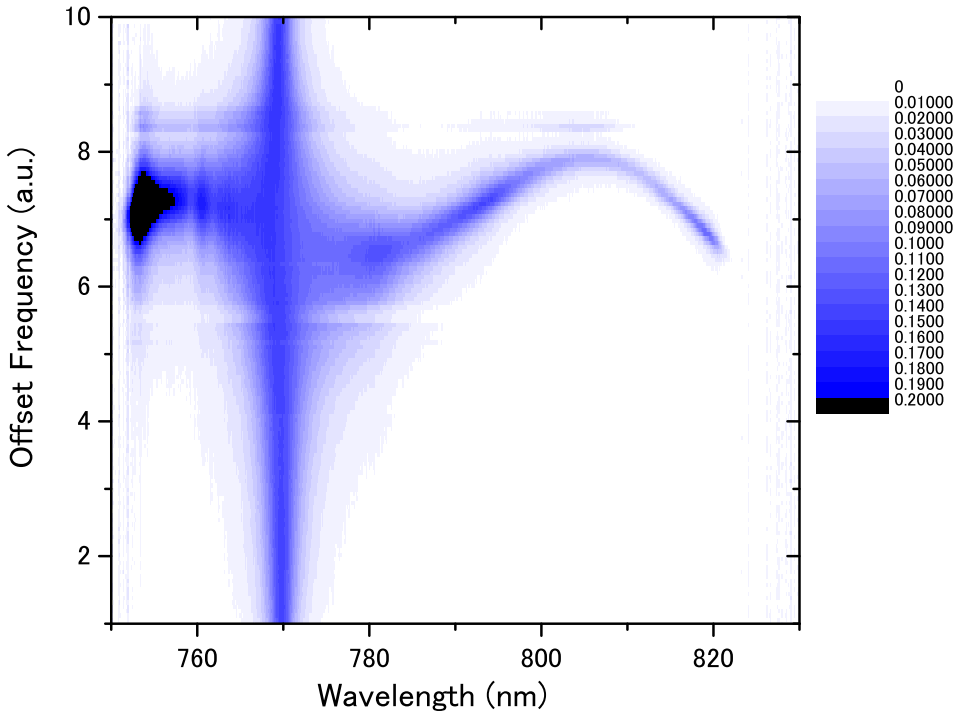

Figure 2.25: *Data obtained from intracavity dispersion measurement. The intracavity spectrum is measured for different offset frequencies. The repetition rate of the laser is controlled to meet the resonance condition at a fixed wavelength. The details of the measurement are described in the text and in the original paper [102].*

that the dispersion can be characterized precisely. Several methods for this application have been proposed and demonstrated [102–104]. For the 10 MHz enhancement cavity experiment, the method reported by Schliesser et al. is used to measure the residual dispersion of the cavity when CM1 is installed [102]. In this method, the repetition rate of the laser is controlled so that it always meets the resonance condition at certain (fixed) wavelength. While actively controlling the repetition rate this way, the offset frequency is scanned, and the intracavity spectrum and the repetition rate are measured. The acquired spectra can be shown in a 2-dimensional plot as a function of wavelength and offset frequency (see Fig. 2.25).

The cuts of the obtained 2D data along fixed wavelength can be always fitted with a Lorentz function to identify the resonant offset frequencies (ω_{CEO}) as shown in Fig. 2.26. Fig. 2.27 illustrates how the intracavity GDD can be determined from the resonance offset frequency $\omega_{\mathrm{CEO}}(\omega)$ as a function of the optical frequency. The following discussions are based on the literature [102, 105]. The blue solid line is given by $\psi(\omega) = 2\pi\frac{\omega}{\omega_{\mathrm{rep}}} + \Delta\psi_{\mathrm{CE}}$. Here, $\Delta\psi_{\mathrm{CE}}$ is a carrier envelope phase slip given by $\Delta\psi_{\mathrm{CE}} = 2\pi\frac{\omega_{\mathrm{CEO}}}{\omega_{\mathrm{rep}}}$ (see Eqn. (1.9)). Note that the frequency of the comb modes ω_{comb} is given by the condition that $\psi(\omega)$ is an integer multiple of 2 π. Thus, the curve $\psi(\omega)$ shows the phase-frequency relation that makes the cavity resonant. The red curve is the round trip phase shift ($\phi(\omega)$) of the cavity, which is

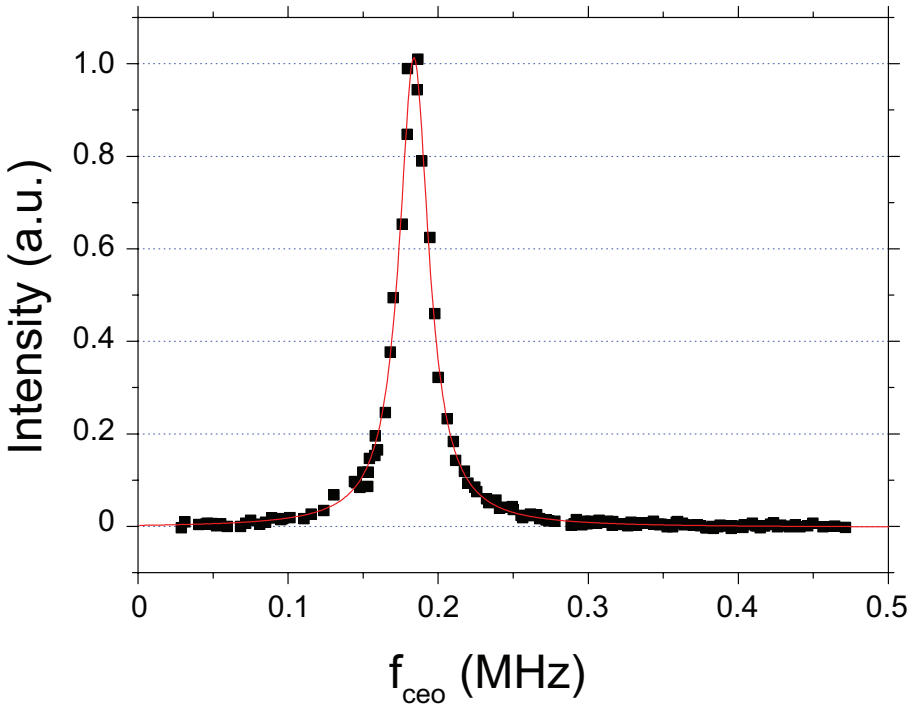

Figure 2.26: *Cross section of Fig. 2.25 at 797 nm. The solid line is a Lorentzian fit to the data to locate the peak ($\omega_{\mathrm{CEO}}(\lambda = 797\,\mathrm{nm})$). The same procedure is repeated for all other wavelengths so that the optical frequency dependence of the resonance offset frequency ($\omega_{\mathrm{CEO}}(\omega)$) is obtained.*

what we want to eventually extract from the measurement. The cavity becomes resonant at the frequency ω where the two curves $\phi(\omega)$ and $\psi(\omega)$ intersect each other [13]. The point L defined in Fig. 2.27 is the locking point of the repetition rate. During the measurement, the repetition rate is controlled to meet the resonance condition at an optical frequency of ω_{L}. Therefore, at this point, which does not move during the measurement, the blue and the red curve overlap. The intersection of the blue line with the y-axis (point C) is given by the carrier-envelope phase slip $\Delta\psi_{\mathrm{CE}} = 2\pi\frac{\omega_{\mathrm{CEO}}}{\omega_{\mathrm{rep}}}$. Point C moves up and down during the measurement in accordance with the respective setting of the offset frequency ω_{CEO}. Thus, the slope of the blue line changes accordingly, and point R where the blue and the red curve intersect moves as well. Point R yields the second optical frequency that satisfies the cavity resonance condition apart from the locking frequency (ω_{L}). Looking at the two geometrically similar triangles shown in pink in Fig. 2.27, it can be seen that the following equation holds:

$$\frac{\phi(\omega_{\mathrm{R}}) - \Delta\psi_{\mathrm{CE}}}{\phi(\omega_{\mathrm{L}}) - \phi(\omega_{\mathrm{R}})} = \frac{\omega_{\mathrm{R}}}{\omega_{\mathrm{L}} - \omega_{\mathrm{R}}}. \tag{2.46}$$

Thus,

[13] To be more precise, one of the curves could be shifted by an interger multiple of 2π rad.

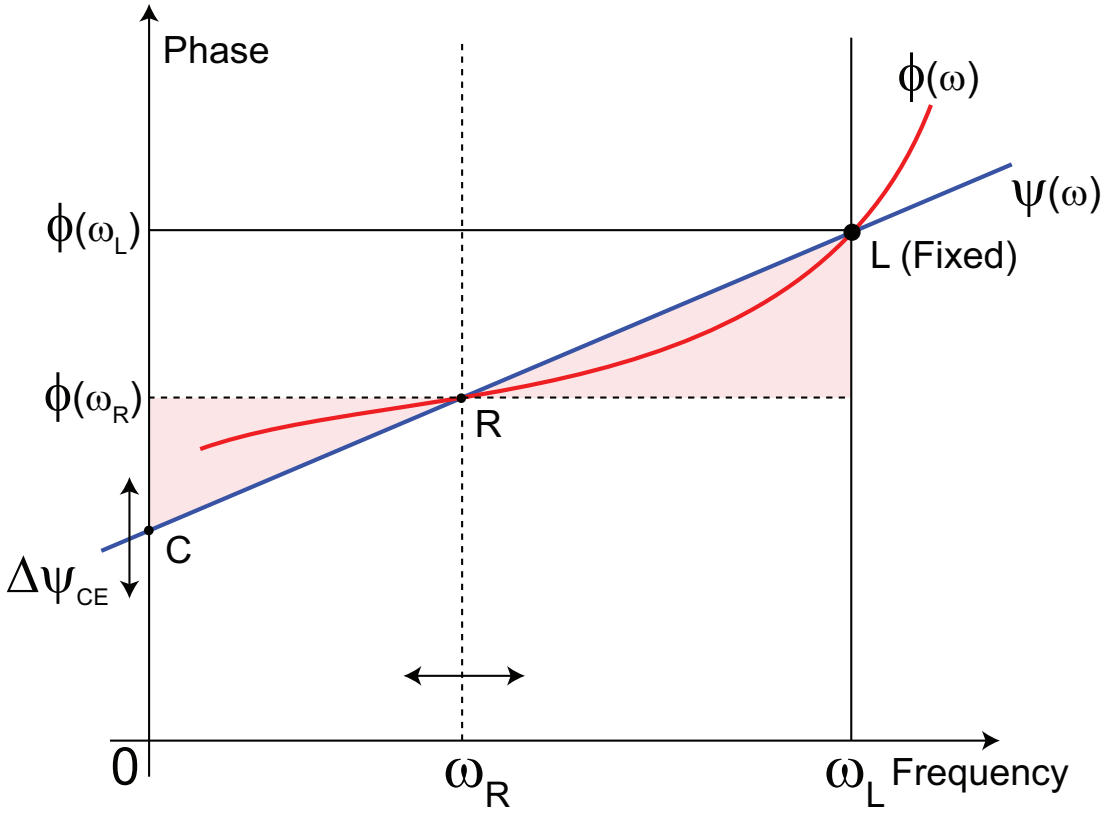

Figure 2.27: *Illustration on how to extract phase information from measured data given in Fig. 2.25. See the text for detailed explanations.*

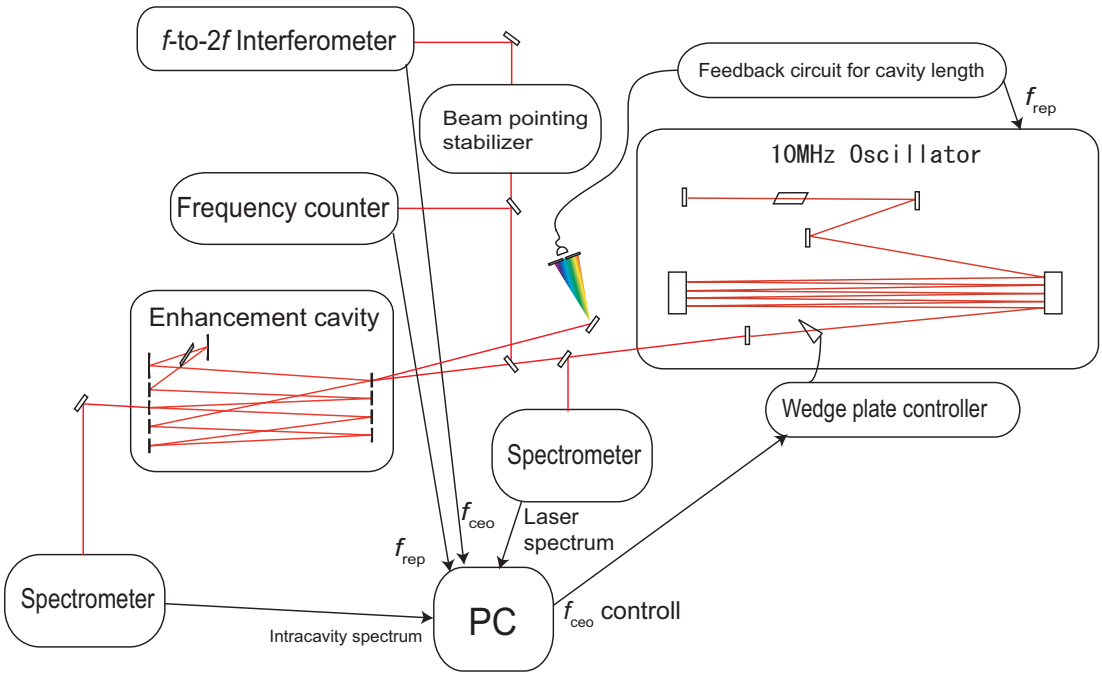

Figure 2.28: *Setup of the intracavity GDD measurement for the 10 MHz enhancement cavity. The offset frequency is controlled by moving the intracavity prism. The resulting change in offset frequency is monitored by an f-to-2f interferometer. The intracavity spectrum, the laser spectrum, and the repetition rate are measured while the offset frequency of the laser is scanned. The active beam pointing stabilization is essential to obtain a stable f-to-2f beat signal.*

$$\begin{aligned}\phi(\omega_{\mathrm{R}}) &= \frac{\omega_{\mathrm{L}}-\omega_{\mathrm{R}}}{\omega_{\mathrm{L}}}\Delta\psi_{\mathrm{CE}}+\frac{\omega_{\mathrm{R}}}{\omega_{\mathrm{L}}}\phi_{\mathrm{L}} \\ &= \frac{\omega_{\mathrm{L}}-\omega_{\mathrm{R}}}{\omega_{\mathrm{L}}}2\pi\frac{\omega_{\mathrm{CEO}}}{\omega_{\mathrm{rep}}}+\frac{\omega_{\mathrm{R}}}{\omega_{\mathrm{L}}}\phi_{\mathrm{L}}.\end{aligned} \tag{2.47}$$

Substituting the measured $\omega_{\mathrm{CEO}}(\omega)$ into Eqn. (2.47), the round trip phase $\phi(\omega)$ can be obtained as a function of ω (within the uncertainty of constant offset and slope, which are not relevant for most of the applications). The intracavity GDD can be immediately obtained by taking the second derivative of the measured phase.

The actual setup of the intracavity dispersion measurement for the 10 MHz enhancement cavity (with CM1) is shown in Fig. 2.28. A fraction of the output power of the oscillator is sent into an *f*-to-*2f* interferometer to monitor the offset frequency. As described and explained in detail in Sec. 1.4, the beam is coupled into a single mode fiber which is connected to a photonic crystal fiber for spectral broadening. The distance between the oscillator and the *f*-to-*2f* interferometer is more than 4 m, including the external pulse compressor. In addition, the 10 MHz oscillator has an intrinsically poor beam pointing stability due to its long cavity. Therefore, the coupling efficiency of the oscillator output into the single mode fiber of the *f*-to-*2f* interferometer is fluctuating and drifting on a time scale of minutes. In order to obtain a stable *f*-to-*2f* beat signal, active stabilization of the beam pointing is necessary. The two steering mirrors that guide the beam into the *f*-to-*2f* interferometer are replaced with PZT

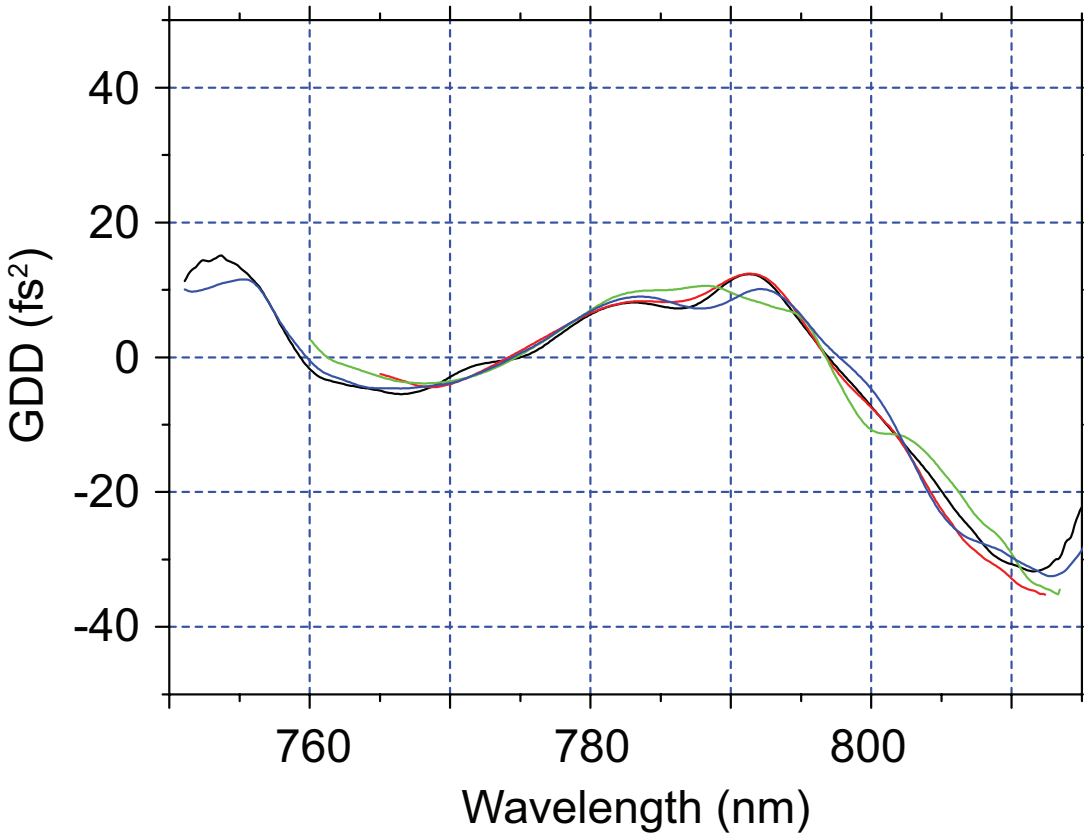

Figure 2.29: *Obtained intracavity GDD as a function of wavelength. Four independent measurements are shown to illustrate the reproducibility and reliability of the measurements. It can be seen that all measurements agree within* $\sim 5\,\mathrm{fs}^2$ *of precision.*

controlled mirrors whose alignment in the x- and y-direction can be controlled independently. Si quadrature photodiodes are installed to detect the horizontal and vertical shift of the beam at the photodiodes. The signals from the two photodiodes are processed with a PI feedback loop and used to control the two piezo-actuated steering mirrors. This way, the displacement and the beam pointing of the oscillator output are stabilized. With this stabilized beam, hours of stable measurement of the offset frequency are possible. The offset frequency is controlled by moving the intracavity prism placed on a piezo-actuated stage. Fig. 2.29 shows the measured intracavity GDD for four independent measurements. The measurements agree within a precision of $\sim 5\,\mathrm{fs}^2$.

2.4.6 Designing chirped mirrors for high precision dispersion compensation

After reliably characterizing the residual intracavity dispersion with the chirped mirror CM1, an additional chirped mirror CM2 was manufactured in order to further optimize the dispersion compensation for the cavity [14]. In this section, we consider the possibilities to improve

[14] To be more precise, the difference between the measured residual dispersion and the dispersion of a single highly reflective mirror would be the real target curve, because CM2 has to be replaced with a single highly reflective mirror. However, the dispersion properties of a single highly reflective mirror are not known precisely. We assumed that the dispersion curve of the highly reflective mirror that can be estimated from

the design of the coating layers to achieve an improved intracavity dispersion compensation.

The dispersion properties of a chirped mirror can be described either in terms of phase or in terms of GDD. Here, we will investigate which description is more appropriate for designing the layer structure of chirped mirrors.

In the field of short-pulsed lasers, the effect of dispersion is typically discussed based on group delay dispersion (GDD) which is the second derivative of the phase. As discussed in Sec. 1.2, the constant phase delay and the first derivative of the phase are not interesting parameters in most of the applications. This is because the former just results in a constant phaseshift for all frequencies and the latter simply displaces the pulse in the time domain. The slope and the offset of the phase are not relevant parameters for the enhancement cavity, either, because they can be compensated by proper adjustment of the offset frequency and the repetition rate of the driving laser as shown in Eqn. (2.42). However, the phase is still a sufficient parameter to describe the dispersion properties. There is an infinite number of phase functions which all yield the same GDD, but when the phase function is given, the GDD is uniquely fixed.

Since the slope and the offset of the phase can be arbitrarily choosen, well-defined additional conditions can be considered to define the slope and the offset of the phase curve in order to yield a one-to-one correspondence between the phase and the GDD. For example, we can assume that the slope and the offset of the phase function are determined such that the phase curve is as close to zero as possible for a given (fixed) bandwidth. Under these additional conditions for the slope and the offset, the phase will be uniquely determined for a given GDD. In this case, the descriptions of dispersion in terms of phase or GDD are totally equivalent. If a mirror is designed to have a certain target GDD exactly, it will exactly reproduce the target phase, and vice versa.

However, the situation will be different if there is a limited precision in the layer coating. Due to the limited control over the layer deposition process, the thickness of the layers may deviate from the design. The error in the layer thickness will produce a deviation of the mirror properties both in phase and GDD. For a given target curve (either in GDD or in phase), there will be an infinite number of layer structures that (almost) exactly reproduce the target curve. However, some of them will be sensitive to coating errors and some will not. When a certain amount of coating errors is inevitable, it is desirable and important to find a design which is insensitive to these errors. Conventionally, efforts have been made to minimize the sensitivity of the GDD against coating errors. Since the GDD is the second derivative of the phase, a small sensitivity of GDD to coating errors does not necessarily mean a small sensitivity of phase to coating errors, and vice versa. For the intracavity dispersion compensation of our enhancement cavity, we want to obtain a small sensitivity of the phase to coating errors, since the power enhancement is directly related to the phase detuning, as shown in Eqn. (2.39) and Eqn. (2.23). *We found that a small sensitiveity of the phase can be obtained when we use the phase instead of the conventionally used GDD as the target curve for the layer design.* This fact can be exemplified by the manufacturing process of a chirped mirror for the 10 MHz enhancement cavity. Our results will be published elsewhere [106].

We first consider the design goal in terms of the wavelength dependence of the GDD (conventional approach). The optimization was performed with the help of the OptiLayer

its layer structure is a good estimate. Even when the estimation turns out to be poor for some reason, the resulting effects are expected to be small since the dispersion introduced by a single higly reflective mirror is tiny.

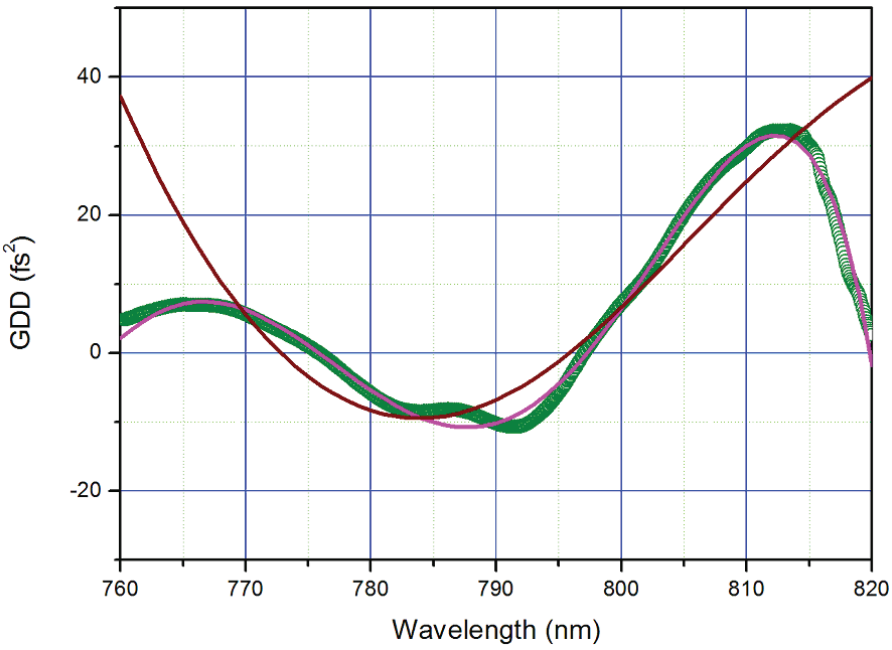

Figure 2.30: *Comparison of GDD-optimized and phase-optimized mirrors. Theoretical GDD wavelength dependences of the designs obtained using phase optimization and conventional approaches using GDD optimization are shown with brown and magenta curves, respectively. The wavelength dependence of the target GDD is also shown with green circles.*

software [107] using conventional needle and gradual evolution optimization algorithms [108, 109]. The designed chirped mirror has a high reflectivity of $> 99.99\,\%$ for normal incidence in the range of 740-830 nm. The theoretical GDD dependence of the obtained design at normal incidence is shown in magenta in Fig. 2.30. The target curve obtained from the intracavity GDD measurement is also shown.

One can see that there is quite a good correspondence between the target and the theoretical GDD curves. Now, let us have a look at the phase property of this (GDD optimized) mirror. The theoretical phase response of a GDD optimized mirror is calculated and compared with the target phase. The result is shown in Fig. 2.31. We applied a statistical error analysis to investigate the influence of potential deviations in the layer thickness on the phase properties of the obtained GDD optimized design. To this end, we used a Monte-Carlo error analysis algorithm that simulates independent randomly distributed deviations in thickness for all layers. The standard deviations of these deviations are equal to 1 nm for all layers. A corridor of standard deviations of the phase curves corresponding to the perturbed designs is shown in Fig. 2.31 (blue error bars).

The obtained theoretical phase curve closely resembles the target phase curve. However, the expected reproducability of the target phase is limited due to its high sensitivity to fluctuations in layer thickness, as can be seen from huge error bar in Fig. 2.31.

Next, let us consider the design goal in terms of the wavelength dependence of the phase.

The obtained theoretical GDD responses are compared with the target curves. In Fig. 2.30, it can be seen that the obtained theoretical curves poorly reproduce the target responses of the GDD. On the other hand, the target phase response given in Fig. 2.32 shows good agreement with the target phase curve. This behaviour is indeed expected for the phase optimization

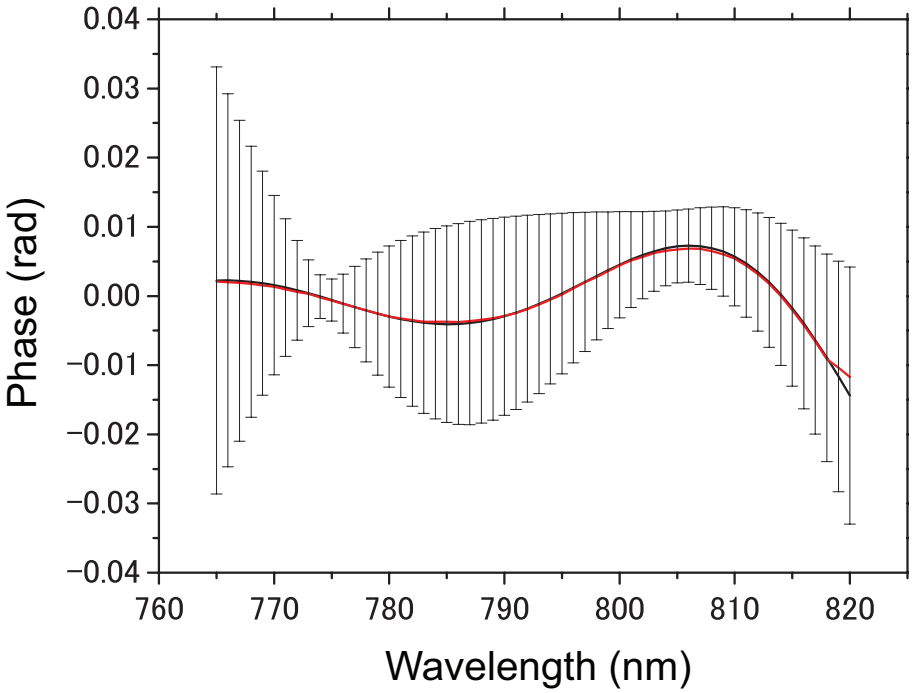

Figure 2.31: *Wavelength dependence of theoretical phase curve for GDD optimized mirror (black). The target phase curve is also shown (red).*

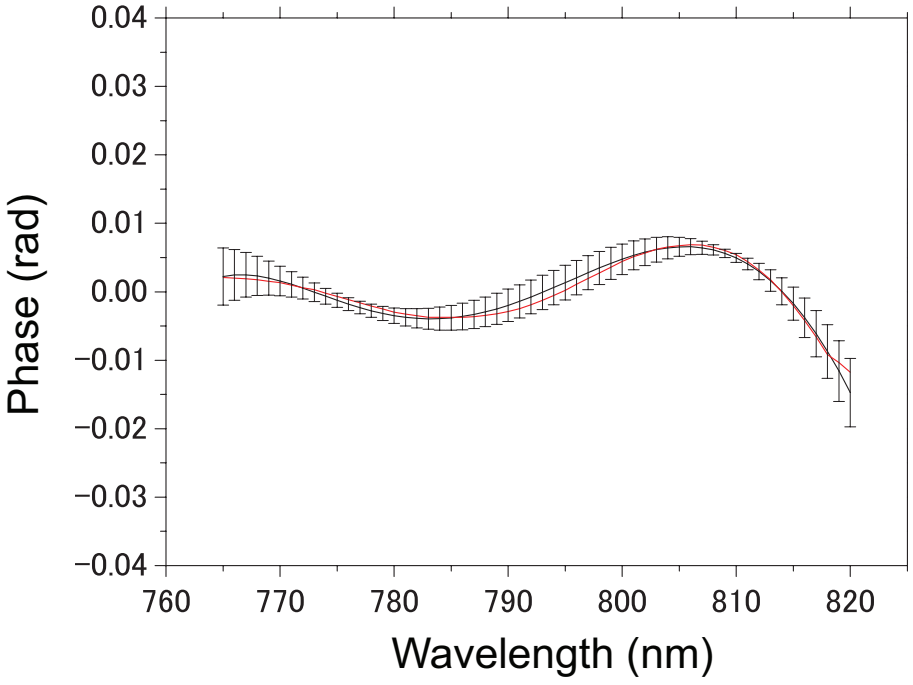

Figure 2.32: *Wavelength dependence of theoretical phase curve for phase optimized mirror (black). The target phase curve is also shown (red).*

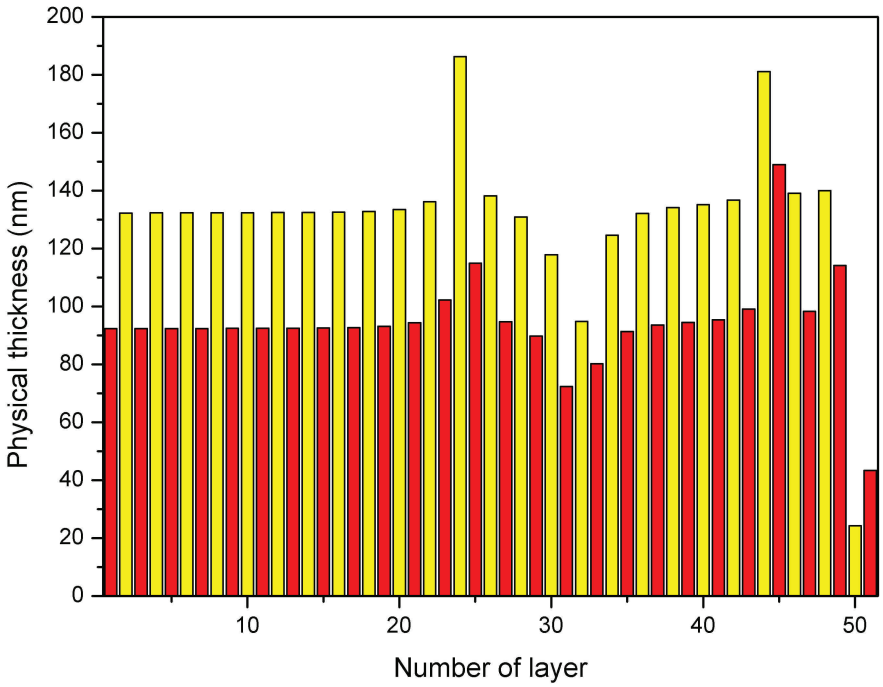

Figure 2.33: *Layer structures of the chirped mirror designed by the conventional GDD optimization approach.*

approach where tiny structures in the GDD which are not relevant for the phase [15] could be neglected and the global structure of the GDD that will strongly affect the phase response is emphasized in order to obtain a good agreement in phase. In addition, the sensitivity of the phase to coating errors is far smaller than the one of GDD optimized mirrors. Because of this smaller sensitivity against fluctuations in layer thickness, a better reproducability of the target curve can be expected for phase-optimized mirrors.

Here we would like to give a qualitative argument why the phase-optimized design is less sensitive to coating errors. When the GDD is used as a target curve, by definition, the layer structure is designed to precisely reproduce the target GDD curve. However, structures in the GDD curves do not affect the phase curves evenly. For example, a very fast oscillatory structure in the GDD will be smoothed out after integrating twice to obtain the phase. Thus, it would have a small effect compared to slower oscillatory structures. The optimization routine may require more complicated layer structures in order to reproduce a GDD structure which is not significantly relevant to the phase curve. On the other hand, if we use the phase as a target curve, a necessary and sufficient optimization will be performed to reproduce the major structures of the phase curve, resulting in a reduced number of required layers. The obtained layer structures for both the GDD and the phase optimization routines are shown in Fig. 2.33 and Fig. 2.34, respectively. Applying the new phase optimization approach, we were able to obtain a design consisting of 40 layers. This is 11 layers less than required in the previously used design that was obtained with the conventional GDD optimization approach. In addition, one can see that the design looks similar to a quarter-wave stack with only a few last layers modified. The design obtained with the phase optimized approach is a lot simpler

[15] due to the two integrations required to obtain the phase from the GDD

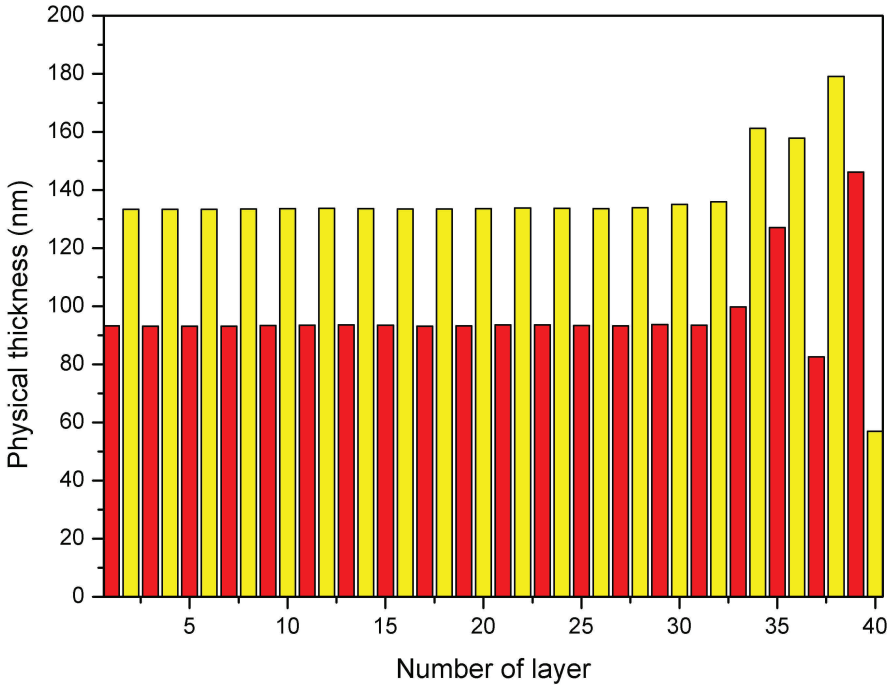

Figure 2.34: *Layer structures of the chirped mirror designed by the phase optimization approach.*

than the GDD optimized design, where complicated irregular variations in thickness are found for a significant number of layers. Typically, designs which are similar to quarter-wave stacks with less irregular structures usually exhibit a relatively small sensitivity to deposition errors. Thus, phase optimized chirped mirrors tend to have a small sensitivity to deposition errors.

Using the phase target curve obtained from the intracavity dispersion measurement described in Sec. 2.4.5, the layer design for the chirped mirror required for intracavity dispersion compensation is obtained. The improved design is significantly less sensitive to coating errors, and a high reproducability of the target phase curve is expected. We denote the chirped mirror manufactured this way as "CM2".

2.4.7 Dispersion compensated broadband enhancement cavity

One of the highly reflective mirrors of the 10 MHz enhancement cavity is replaced with the phase optimized chirped mirror (CM2), and the intracavity spectrum is measured when the cavity is locked. The offset frequency is optimized to obtain the power enhancement with the broadest bandwidth. The intracavity spectrum is shown in Fig. 2.35 together with the laser spectrum for comparison. It can be seen that a broadband power enhancement with more than 40 nm of bandwidth is obtained.

Although the sapphire plate is placed at Brewster's angle for the fundamental cavity mode, a small portion of the intracavity beam is coupled out due to the residual reflectance of the sapphire plate. The auto-correlation trace is measured with this outcoupled beam to characterize the intracavity pulse width. The pulse compressor after the oscillator is optimized to obtain the shortest pulses at the autocorrelator. The measured autocorrelation trace is shown in Fig. 2.36. The FWHM pulse duration is measured to be 57 fs. The increase in

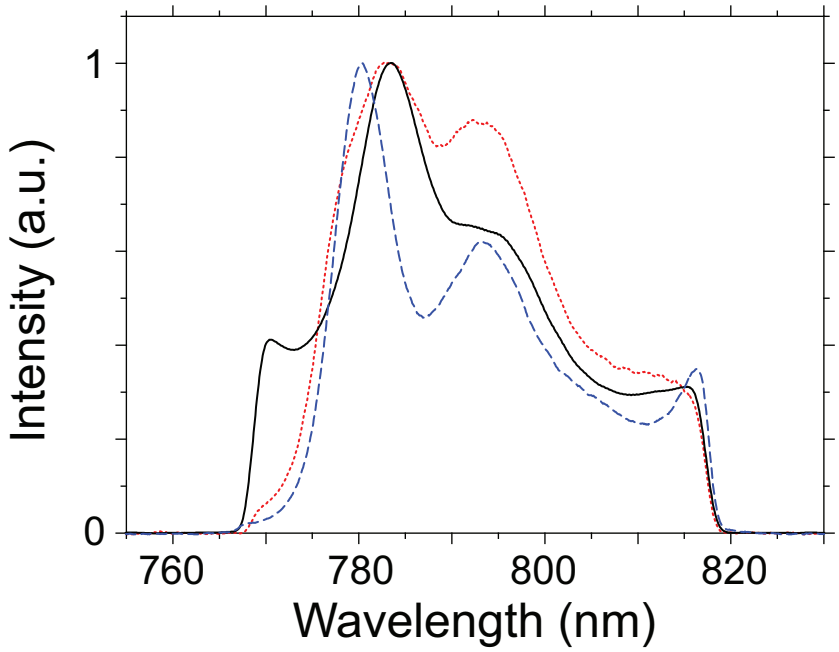

Figure 2.35: *Intracavity spectrum (blue: dashed) of dispersion-compensated cavity and laser spectrum (black: solid). A power enhancement exceeding 40 nm of bandwidth is obtained. The intracavity spectrum is also measured with strongly chirped seed pulses in order to investigate the nonlinear response of the cavity (red: dotted).*

pulse duration compared to the original laser pulse duration of 38 fs is partially due to the narrower intracavity spectrum. Although the dispersion of *extra-cavity* materials such as the telescope lenses and the optical windows of the vacuum chamber is precompensated by the pulse compressor, a still imperfect compensation of the (especially higher order) *extra-cavity* dispersion may also contribute to the increased intracavity pulse duration.

The intracavity average power is characterized by measuring the transmission from one of the highly reflective mirrors. The transmittance of the high-reflector is measured for the entire wavelength region and can then be used to determine the transmitted power from the intracavity power. This way, an average intracavity power of 100 W is obtained when the cavity is seeded with a driving beam of 1 W. The spectral dependence of the enhancement factor can be obtained by normalizing the intracavity spectrum to the laser spectrum. This is shown as a blue curve in Fig. 2.37. The absolute value of the power enhancement in Fig. 2.37 is determined based on the measured power enhancement for the average power.

In Fig. 2.35 and Fig. 2.37, it can be seen that the intracavity spectrum and the power enhancement are rather modulated as a function of wavelength. In addition, the intracavity spectrum does not resemble the laser spectrum. In order to investigate the possibility that this effect originates from the nonlinear response of the intracavity material, the intracavity spectrum is measured with a chirped ($\sim$ 1 ps) seeding laser. The results are shown as a red dots in Fig. 2.35 and Fig. 2.37. A smoother and less modulated power enhancement spectrum is observed for a similar average power enhancement. Comparing the power enhancement spectra for short and chirped pulses, it can be concluded that the nonlinear response of the cavity deforms the intracavity spectrum. Nonlinear effects (including thermal effects) may add an additional roundtrip phase shift which is intensity dependent. If this effect is wavelength

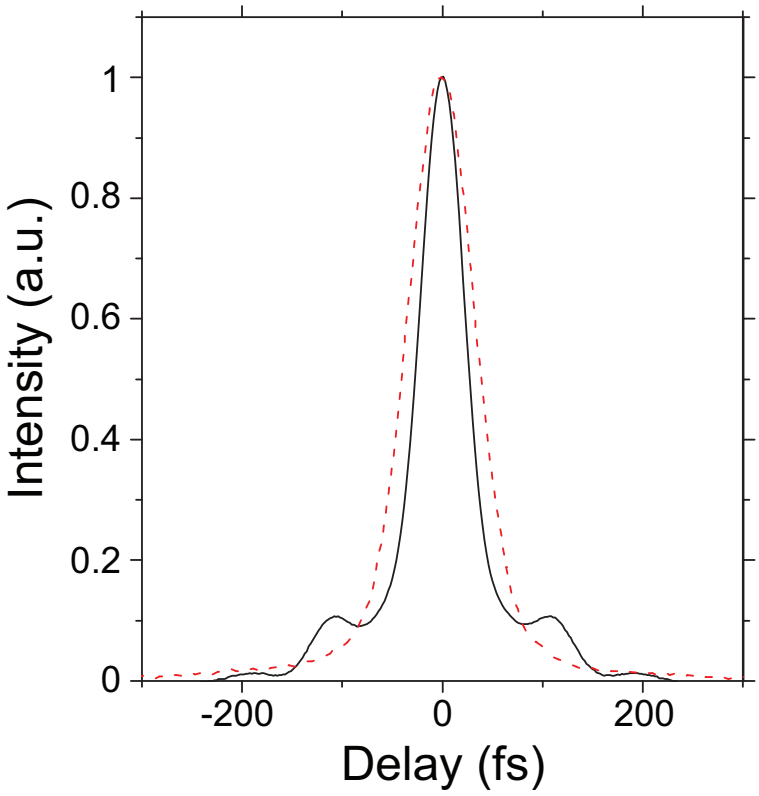

Figure 2.36: *Intracavity pulse duration measurement (red: dashed). The intracavity pulse duration is characterized by measuring the autocorrelation trace of the IR pulse coupled out by the sapphire Brewster's plate. The FWHM pulse width of intracavity pulses is 57 fs. The autocorrelation trace of the laser pulses is also shown for comparison (black: solid)(38fs).*

dependent, it will show up as additional intracavity GDD which can modulate the spectral dependence of the power enhancement. The peak intensity at the Brewster's sapphire plate is indeed high enough to expect such an effect (calculated B integral of 1.8 rad for 100 round trips).

2.4.8 Intracavity high harmonic generation

With the improved intracavity dispersion compensation described in Sec. 2.4.5, Sec. 2.4.6 and Sec. 2.4.7, broadband enhancement is achieved with an average enhancement factor of 100 (as shown in Fig. 2.37), which enables us to keep the pulse duration short (57 fs) inside the cavity to obtain a high peak intensity at the focus.

From the intracavity average power and focal radius of the cavity mode, the peak intensity is estimated to be $> 5 \times 10^{13}\,\mathrm{W/cm^2}$ at the focus. Here, the uncertainty originates from the limited accuracy in estimating the focal diameter of the cavity mode.

For the demonstration of intracavity HHG, a continuous flow of Xe, Ar, or air is introduced into the cavity through the gas nozzle. Typical gas flows are estimated to be $1 \times 10^{-2}\,\mathrm{mbar\,l/s}$. The pressure of the chamber is kept below $1 \times 10^{-1}\,\mathrm{mbar}$. When the gas flow is increased and the chamber pressure exceeds $\sim$1 mbar, the locking of the cavity becomes unstable. We suspect that this is due to the increased acoustic coupling between the turbo-molecular pump

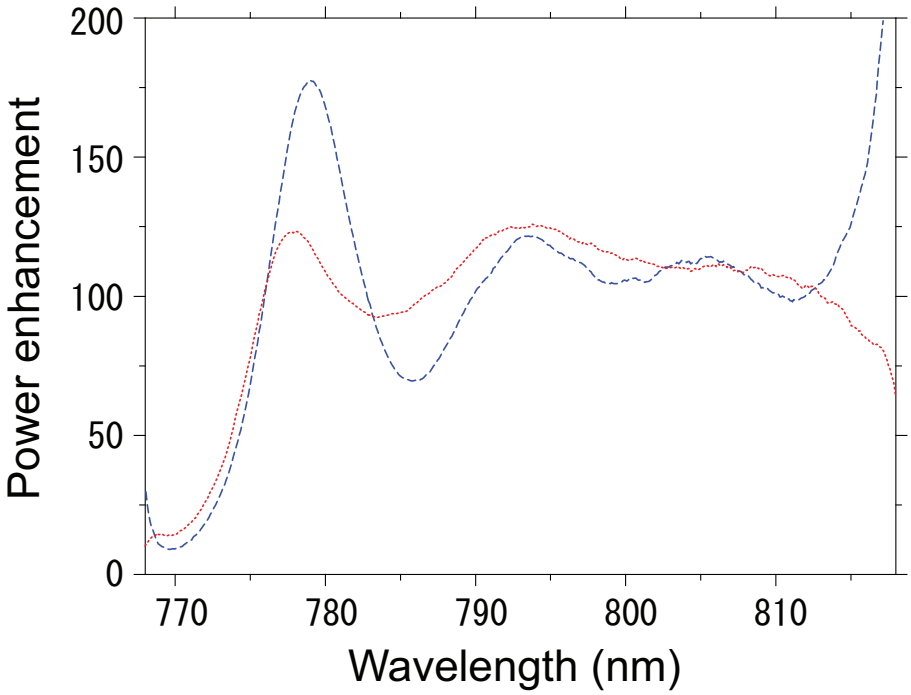

Figure 2.37: *Spectrally dependent power enhancement factor measured by comparing the intracavity spectrum and the laser spectrum (blue). The absolute value of the power enhancement is calibrated based on the measured average power enhancement. The power enhancement spectrum is measured with also strongly chirped seed pulse, in order to investigate the nonlinear response of the cavity (red).*

and the cavity at higher pressure. However, the optimum gas flow which maximizes the high harmonic yield is typically obtained at a gas flow far below this regime ($< 1 \times 10^{-1}$ mbar). The gas nozzle is installed at the focus with a 5-way adjustable mount (x,y,z,rotation and tilt) (see Fig. 2.38). The gas nozzle is a tube with an inner diameter of 0.4 mm which has been pierced with holes of 200 μm diameter to allow the laser beam to enter perpendicularly to its axis. When Xe gas or air was introduced, bright fluorescence was visible at the focus. Although the focal spot cannot be seen because it is inside the gas nozzle, the plasma created from the gas that flows out of the holes is clearly visible. Fig. 2.39 shows a picture of the plasma fluorescence observed at the focus.

The XUV output is analysed by a scanning grating spectrometer (Jobin-Yvon, LHT30) with an estimated resolution of 1.4 nm and a channeltron detector (Burle, CEM4839). An additional turbopump (300 l/s) is installed close to the channeltron detector in order to obtain sufficient differential pumping between the spectrometer chamber and the enhancement cavity chamber. The pressure inside the spectrometer chamber is kept below 5×10^{-6} mbar. This is required to supress the background signal of the channeltron detector. The pulse compressor, the gas flow rate, the nozzle position, and ω_{CEO} are optimized to maximize the XUV signal. In particular, the XUV output power is found to be quite sensitive to the adjustment of the pulse compressor and the nozzle position. In addition, the parameters of the feed-back loop are also optimized to obtain the best XUV output power. The optimization was both performed for the sum of all XUV orders (using the 0 th diffraction from the XUV grating), and the 13 th order HH. The data shown below is all based on the optimization for the 13 th order. It is found that the optimum offset frequency and the locking parameter drift within

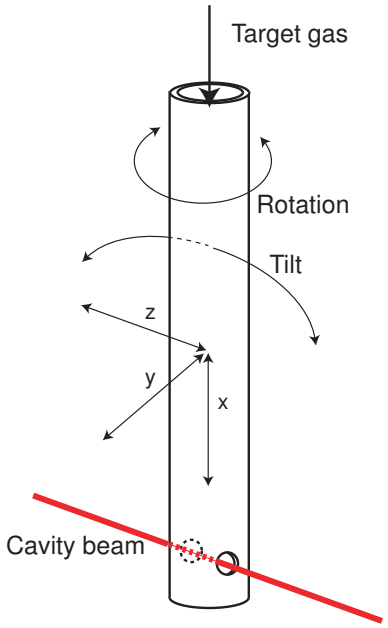

Figure 2.38: *Schematic of the gas nozzle. The gas nozzle is a tube with an inner diameter of 0.4 mm which has been pierced with holes of 200 µm diameter to allow the laser beam to enter perpendicularly to its axis. The position of the nozzle can be adjusted with a 5-way stage. The z-position of the nozzle is optimized to maximize the power of the generated HH.*

the time scale of seconds after locking the cavity. Once it is readjusted, the cavity runs stably for a longer period ($\sim$ 10 min) without any additional adjustment. We suspect that the effect originates from thermal effects at either the cavity mirrors or the sapphire Brewster's plate. After operation with gas for some time ($\sim$ 20 min), it is observed that the intracavity power starts to decay slowly. The power can be recovered fully by opening the chamber and cleaning the sapphire Brewster's plate with acetone. The power just deteriorated when the HHG process in the gas jet was driven. We assume that generated UV radiation causes a recoverable damage or contamination of the sapphire plate which increases the intracavity loss.

In order to independently calibrate the XUV power, the (spectrally unresolved) total power is measured with a calibrated Si photodiode (IRD, AXUV20HS1) placed directly after the Brewster's plate XUV output coupler. The specified quantum efficiency is used for the calibration. For this measurement, an aluminium filter (Lebow, 150 nm thickness) is used to remove the residual reflection of the fundamental laser beam. The transmission of the Al filter is characterized by comparing the XUV spectra with and without the filter. The result is shown in Fig. 2.40.

The tabulated value for the transmission of aluminium deviates significantly from the measured transmission of the Al filter. This is due to a thin aluminium oxide layer which developed on the surface of the filter and shows a strong absorption in the XUV. Since the thickness of the Al oxide is not known precisely, an experimental determination of the filter transmission is mandatory.

The XUV spectrum is measured without the Al filter, because the channeltron detector is insensitive to the residual IR beam. However, the Al filter is used to suppress the scattered IR beam for the measurement of the HH radiation higher than 15th order. Together with the

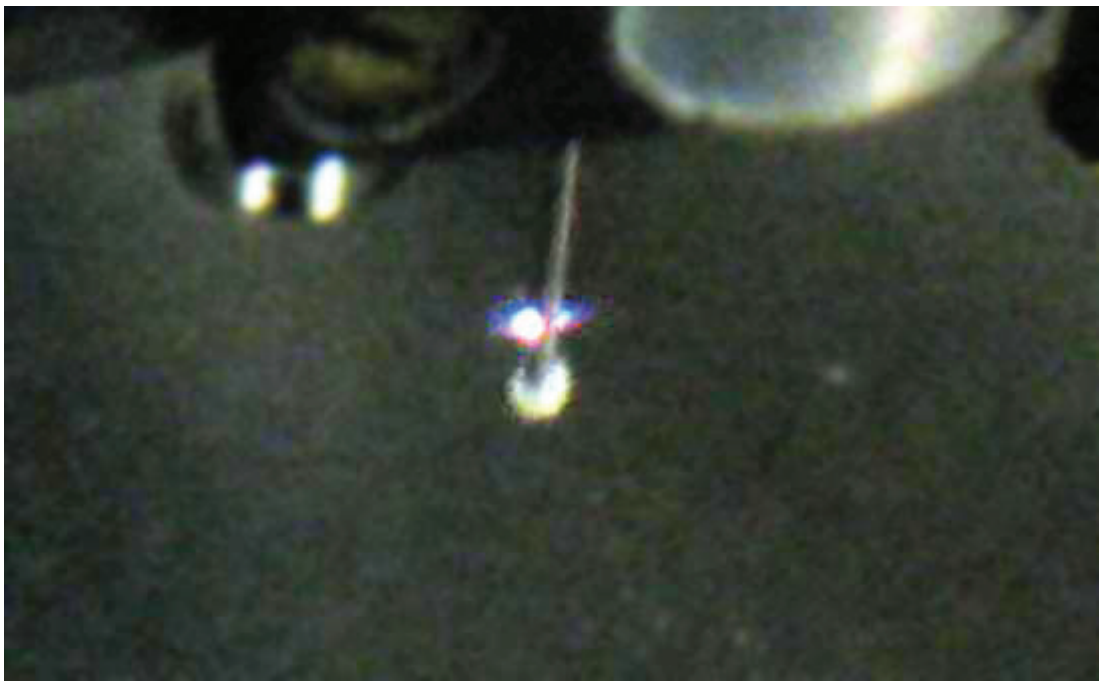

Figure 2.39: *Plasma fluorescence observed at the focus. Xe gas is introduced at a flow of* 1×10^{-2} *mbar l/s. The peak intensity at the focus is estimated to be* $> 5 \times 10^{13}$ W/cm^2.

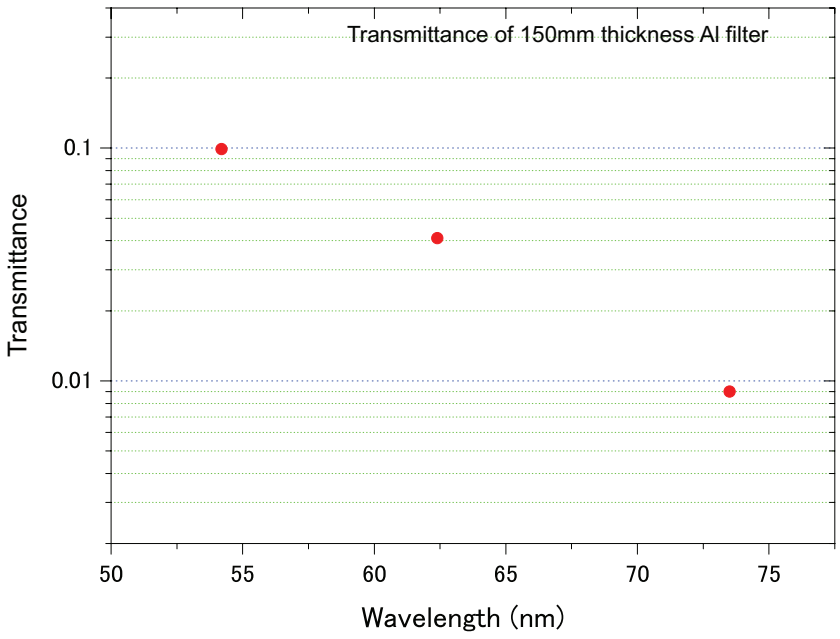

Figure 2.40: *Measured transmittance of Al filter (Lebow, 150 nm thickness). Typically, the Al filter is coated with aluminium oxide. Since the absorbance of Al and Al oxide are significantly different and the thickness of the Al oxide layer is unknown, the transmittance of the Al filter has to be experimentally determined.*

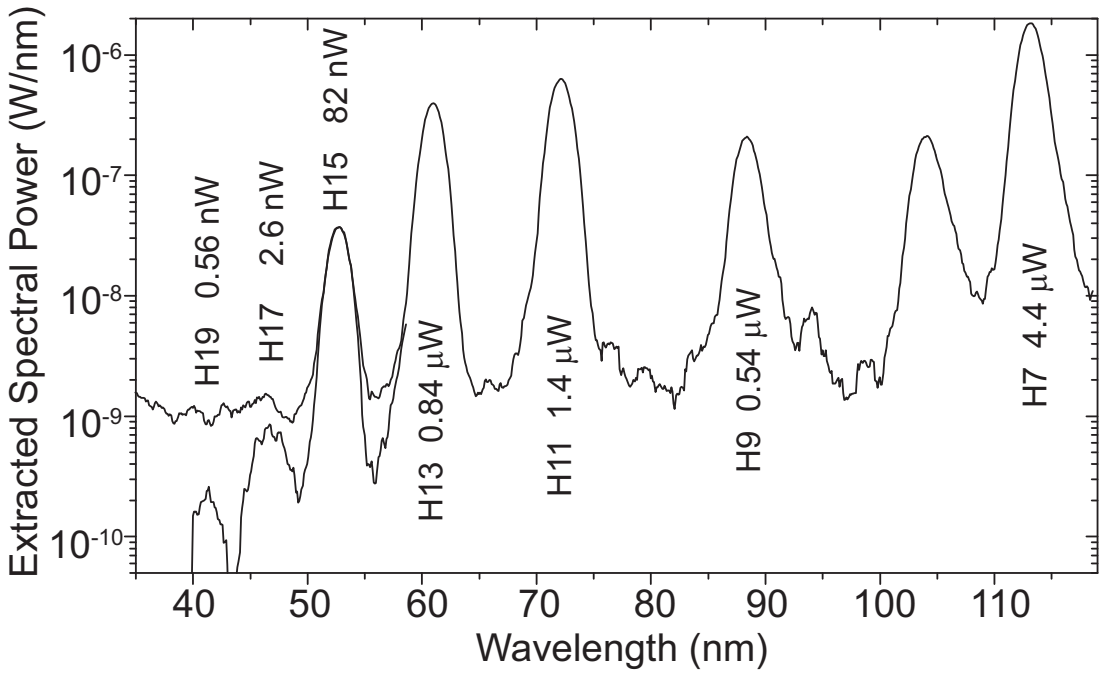

Figure 2.41: *Calibrated XUV spectrum of high harmonic radiation outcoupled from enhancement cavity. The spectrum for higher than 15th high harmonic orders is measured with an aluminium filter (150 nm thickness). High harmonics up to the 19th order are observed. For the details of the calibration of the power, see the text.*

specified wavelength dependence of the diffraction efficiency of the grating, we can determine a calibrated XUV spectrum. After normalization to the total power, the absolute spectral power density of the outcoupled XUV beam is obtained as shown in Fig. 2.41. Due to the limited accuracy in calibration (Al filter transmission measurement and grating diffraction efficiency) the absolute power can only be determined up to a factor of ~ 2.

High harmonics up to the 19th order (41 nm) are clearly observed. The cutoff energy is calculated to be 22 eV based on Eqn. (2.15). This corresponds to 57 nm, which agrees with the measured cutoff which is located between the 13th and the 15th harmonic. The outcoupled power in the plateau region approaches 1 μW for each single order of harmonics. In addition to the odd harmonics, a rather broad peak at 104 nm is observed. Its origin is not yet understood but it appears to be related to the occupancy of excited bound states of the Xe atom [51].

The power of each high harmonic order is normalized to the driving infrared power to obtain the conversion efficiency of the high harmonic generation process. The result is calibrated by taking into account the outcoupling efficiency of the sapphire Brewster's plate (see Fig. 2.42).

Two mechanisms are responsible for the improvement over our previous results [51]: larger focal volume and higher peak intensity. The lower repetition rate and the improved cavity lead to a 30 times higher pulse energy. The XUV output power scales with large powers of the input power (e.g. $\propto I^9$ for H11 [51]), so even a slightly higher peak intensity leads to significantly higher output. When saturation is reached more XUV power is obtained by looser focusing while keeping the peak intensity constant. This lets the interaction volume

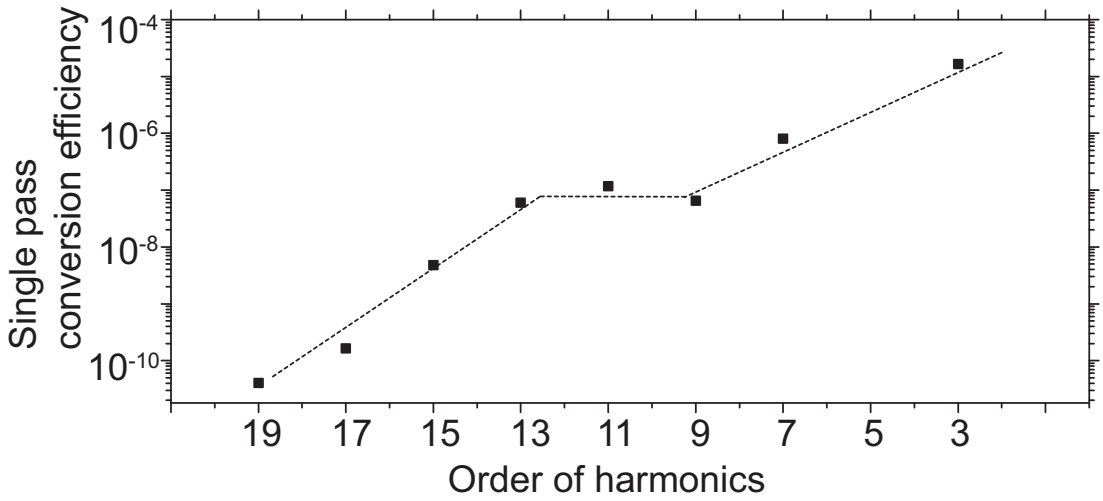

Figure 2.42: *Single pass conversion efficiency of intracavity HHG. The power of each high harmonic order is normalized to the driving power to obtain the conversion efficiency of the high harmonic generation process.*

grow $\propto w_0^4$ and the adverse Guoy phase shift is reduced $\propto w_0^2$. In total, the single pass conversion efficiency for H11 rose from a very low 2×10^{-11} to 10^{-7}. This is a typical value for gas jet HHG without special phase matching measures [57]. We would like to note further that in cavity-assisted HHG the beam quality (due to spatial filtering) is much better than in an amplified system. Therefore, under otherwise identical conditions, we expect higher conversion efficiencies.

2.5 Conclusion

- High harmonic generation is one of the promising nonlinear processes to convert an IR frequency comb into the XUV region. For the application of XUV frequency comb spectroscopy (especially for high precision spectroscopy of the He^+1s-2s transition), a repetition rate on the GHz level is preferable.

- The pulse energy and the peak intensity of an IR frequency comb can be passively amplified with the help of femtosecond enhancement cavities, thus enabling intracavity high harmonic generation at the full repetition rate of the oscillator.

- In order to obtain a higher pulse energy compared with a previous demonstration at the repetition rate of ~ 100 MHz, a femtosecond enhancement cavity is built at a repetition rate of 10 MHz. The entire enhancement cavity is placed in a vacuum chamber of 3.5 m in length which contains the folded 30 m of beam path of the enhancement cavity. Working under vacuum eliminates the dispersion of and the scattering loss from air. A long-cavity Ti:sapphire mode-locked oscillator working in the positively-chirped regime to obtain a high average output power exceeding 1.5 W is used to seed the enhancement cavity.

- A high precision intracavity dispersion measurement was done to obtain a target phase curve for the mirror required to nicely compensate the dispersion of the enhancement

cavity. When designing the layer structure of this chirped mirror, it was demonstrated that the phase target optimization method yields a simpler layer structure than the GDD target optimization method and that it exhibits a smaller sensitivity to coating errors.

- The dispersion-compensated cavity supports a bandwidth of more than 40 nm centered at 780 nm with an average power enhancement of 100. An interacavity pulse energy of 9.3 μJ is obtained at a repetition rate of 10.8 MHz. The intracavity FWHM pulse duration is measured to be 57 fs.

- XUV frequency comb generation is demonstrated with an enhancement cavity at a repetition rate of 10 MHz. Due to the high intracavity pulse energy, XUV radiation down to 42 nm (up to the 19 th harmonic order) is generated with a μW-level average power in the plateau region.

Chapter 3

Non-collinear high harmonic generation (NCHHG)

3.1 Introduction

3.1.1 Current outcoupling methods

One of the biggest challenges so far in cavity-assisted high harmonic generation (HHG) has been to find a way to efficiently extract the generated high harmonics from the enhancement cavity without disturbing the cavity performance. The difficulty of outcoupling comes from various reasons: First, an XUV beam is absorbed by most of the materials, and thus, only reflective optics can be used for outcoupling. Second, the performance of the cavity is sensitive to intracavity dispersion and loss. Therefore, the outcoupling method should neither introduce too much dispersion nor loss. Third, in conventional configurations for HHG, the XUV beam is generated collinearly with respect to the driving IR beam and with identical polarization. This eliminates the possibility to use the spatial or the polarization dependence for outcoupling.

In the first demonstrations of extreme ultraviolet (XUV) frequency comb generation with enhancement cavities, a thin sapphire plate was used as a dichroic mirror to separate the high harmonic radiation from the fundamental beam [51–53]. The outcoupling plate is placed at Brewster's angle for IR, so it introduces only $\sim 10^{-3}$ of cavity loss. Since the refractive index of sapphire is different for infrared (IR) and ultraviolet (UV) radiation, the generated (X)UV frequency comb can be outcoupled using Fresnel reflection from the surface of the plate. When improving the intracavity power and pulse energy, this method encounters several severe problems listed in the following:

- The intracavity plate introduces loss into the cavity due to material absorption, scattering, imperfect alignment of the plate, and imperfect parallelism of the two surfaces. In addition, the curved wavefront of the cavity mode prevents us from aligning the plate at Brewster's angle for the entire beam cross section, which introduces inevitable losses to the cavity. Some of these contributions can be minimized by employing a plate with the highest possible machining precision, yet it still remains the most lossy component in a high finesse enhancement cavity.
- Any intracavity material introduces group delay dispersion (GDD) which has to be compensated with additional chirped mirrors. It is a tedious effort to design and manufacture chirped mirrors to precisely compensate the dispersion of intracavity material. In

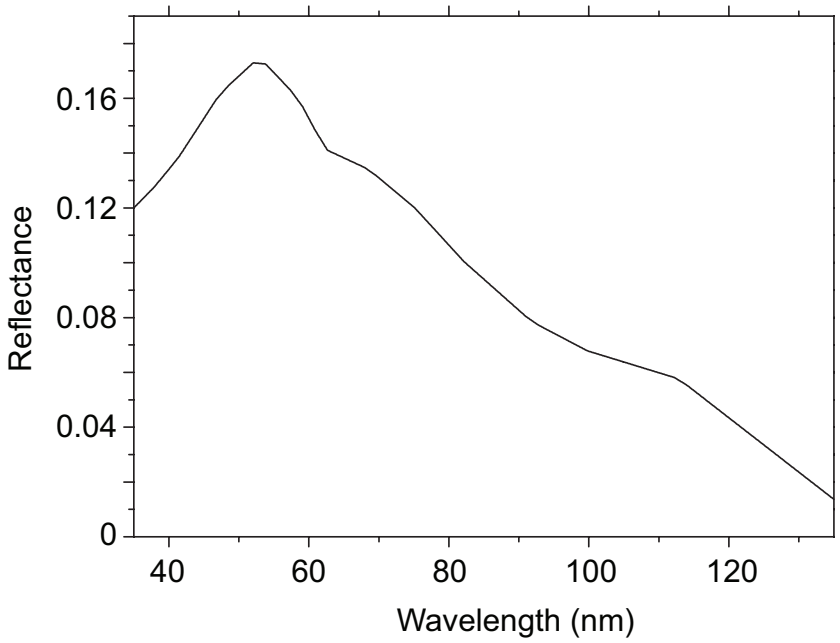

Figure 3.1: *The outcoupling efficiency of a sapphire plate placed at Brewster's angle for IR beam. The data for the complex refractive index is taken from [101].*

addition, for applications where extremely high intracavity finesse is necessary, strongly chirped mirrors show a limited performance in terms of reflectance when compared with high reflective mirrors with a quarter-wave stack coating structure.

- With very high peak intensities incident on the outcoupling plate, the plate shows a nonlinear response to the circulating beams [53, 110]. A frequency dependent phase shift due to this nonlinear response is equivalent to introducing additional GDD into the cavity. In principle, this phase shift can also be compensated with chirped mirrors, however, it would be challenging since the phase shift is strongly intensity-dependent. Once the intracavity dispersion is compensated with chirped mirrors, the resulting higher pulse energy will again change the nonlinear response of the outcoupling plate, which in turn modifies the intracavity dispersion again. As discussed in Chap. 2, a nonlinear response of the outcoupling plate was already observed at the intracavity peak power level obtained in the XUV frequency comb generation experiments at a repetition rate of 10 MHz [53]. Therefore, it is important to eliminate the nonlinearity of the intracavity material to scale up the intracavity pulse energy further.

- Fig. 3.1 shows the reflectance (outcoupling efficiency) of a sapphire outcoupling plate placed at Brewster's angle for the driving infrared beam. The reflectance of the XUV beam is $\sim 15\,\%$ at 60 nm. For future applications in which the available output power of the XUV frequency comb may limit the feasibility of possible experiments [44], a novel outcoupling method with higher efficiency would be beneficial. In addition, the Brewster's plate method does not work for really high order harmonics where no appropriate material exists.

3.1.2 New outcoupling methods

To overcome these problems, several alternative outcoupling methods have been suggested and investigated [111–114].

1. Thin Brewster's plate

The simplest idea is still to use a Brewster plate, but to reduce its thickness significantly. A short optical path length inside the material mitigates both the accumulated nonlinear phase shift (small B-integral) and the loss due to material absorption. However, sapphire is one of the hardest crystalline materials and it is technically hard to manufacture a very thin plate with the required high optical quality. We studied the possibility to use a very thin film of Silicon Nitride (Si_3N_4) as an outcoupling plate. Silicon nitride has a very high melting point of 1900 °C and is chemically very stable. In addition, silicon nitride has a high stiffness and is often used for applications where superior mechanical reliability is required under high temperature conditions, e.g. in bearings, combustion engines and machining tools for metals. A thin film of silicon nitride can be manufacutured by Low Pressure Chemical Vapor Deposition (LPCVD). It is used as a low-background sample mount in scanning electron microscopy and X-ray microscopy. Very thin films (20 nm) with high optical quality are commercially available [115]. Fig. 3.2 shows a picture of a silicon nitride film.

Fig. 3.3 shows the reflectance of the silicon nitride film when the film is placed at Brewster's angle for the infrared cavity beam (63.5 deg at 800 nm). It shows a reflectance (outcoupling efficiency) of $\sim 30\,\%$ at 60 nm, which is twice than that of a sapphire output coupler. The GDD of a silicon nitride film with a thickness of 30 nm is shown in Fig. 3.4[1]. All the data shown here is calculated from the refractive index data obtained from [101].

It can be seen that the GDD introduced by the silicon nitride film is less than $0.01\,\mathrm{fs}^2$ at 800 nm. The other important figure of merit is the loss caused by surface scattering and material absorption. We built a simple Fabry-Perot cavity containing a silicon nitride film at Brewster's angle and characterized the loss introduced by the film by comparing the cavity ringdown signal with and without the film. The result shows that the film with a thickness of 30 nm introduces only 5×10^{-5} of intensity loss in a single pass. This is extremely low compared to a thick (~ 0.5 mm) outcoupling plate made of sapphire. The only remaining concern is potential thermal damage due to the high intracavity power. Experimentally, it is confirmed that the film itself withstands up to 3 kW of intracavity average power [116].

In this demonstration, we are suspicious that the damage of the film at higher intracavity power is due to the heating of the silicon frame. Under vacuum conditions, a very little portion of the beam that is hitting the frame of the film can significantly increase the temperature of the frame and may destroy the film. Proper design of the frame size and cavity beam configuration together with carefull alignment will be necessary.

2. Hole coupling

Another interesting idea for outcoupling is to take advantage of the feature that high harmonic radiation is spatially more collimated than the driving IR beam [111]. A scaling

[1] Here, GDD is calculated for 30 nm path length. Note that when the plate is installed at Brester's angle, the path length is increased to 34 nm.

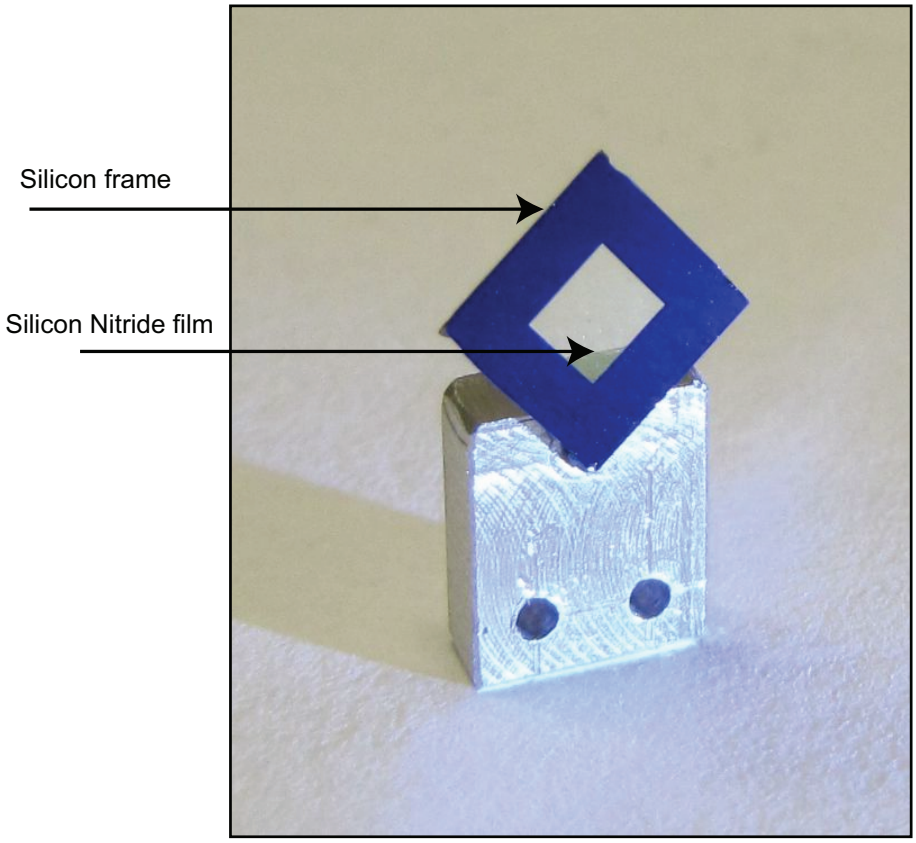

Figure 3.2: *Thin film of silicon nitride (Si_3N_4). The film is supported by a square frame made of silicon which is glued onto an aluminium holder. Films as thin as 20 nm are commercially available [115]. A film with a thickness of 30 nm is used to investigate the transmission loss of a laser beam at 800 nm. The result shows that a film of that thickness introduces only 5×10^{-5} of intensity loss in a single pass.*

law for the collimation of high harmonic radiation of different orders can be obtained through the following simple discussion. Here we assume a simple power scaling law

$$E_{\mathrm{HHG}} = {E_{\mathrm{IR}}}^{p} \tag{3.1}$$

where E_{HHG} and E_{IR} stand for the field amplitude of the high harmonic and the fundamental radiation, respectively. Based on the principles of Fraunhofer diffraction, the emission angle θ depends on both the typical size of the emitter d and the wavelength of the radiation λ:

$$\theta \propto \frac{\lambda}{d}. \tag{3.2}$$

For high order harmonic generation, λ_{HHG} is inversely proportional to the harmonic order q. Eqn. (3.1) indicates that the effective size of an emitter is p times smaller for the high harmonics compared with the fundamental radiation. Thus, the ratio of the emission angles θ_{HHG} and θ_{IR} of the high harmonic and the fundamental radiation are given by:

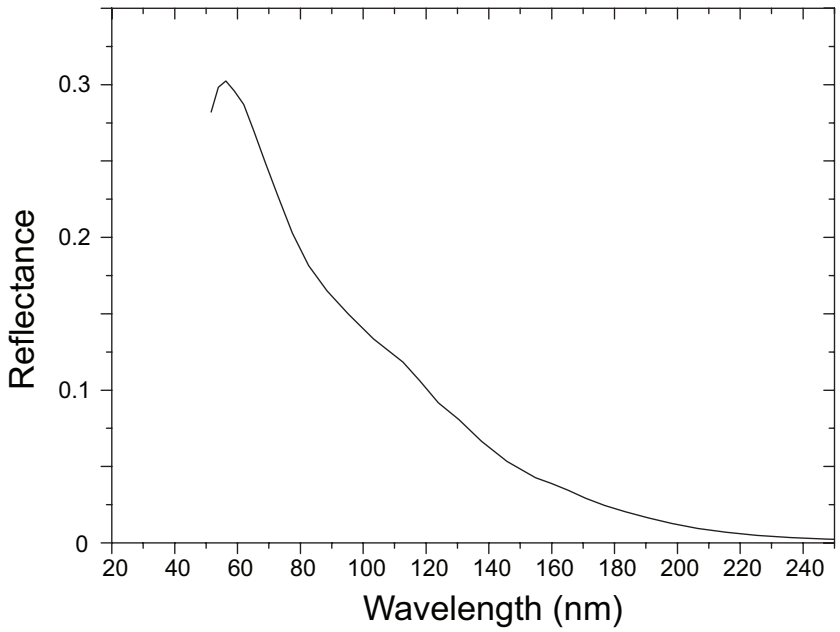

Figure 3.3: *The reflectance (or outcoupling efficiency) of silicon nitride placed at Brewster's angle for 800 nm radiation. The data for the complex refractive index is taken from [101].*

$$\frac{\theta_{\mathrm{HHG}}}{\theta_{\mathrm{IR}}} = \frac{\frac{\lambda}{q}/\frac{d}{p}}{\frac{\lambda}{d}} = \frac{p}{q}. \tag{3.3}$$

Assuming that p is constant, which is the case in the plateau region, Eqn. (3.3) shows that the collimation of the harmonic radiation will get stronger for increasing harmonic order q. If q is large enough and the high harmonic emission is significantly more collimated than the fundamental beam, outcoupling of high harmonic radiation through a tiny hole in one of the cavity mirrors (see Fig. 3.5) seems feasible. If drilling a suitable hole into the mirror is too challenging, a tiny XUV mirror could be glued onto the cavity mirror instead. This method is a trade-off between good outcoupling efficiency and low cavity losses, because the hole (or mirror) introduces additional losses for the fundamental beam. Furthermore, the given description is an approximation based on the assumption that the cavity mode will remain Gaussian despite the hole in the mirror which is not true in general.

In fact, an extension of this outcoupling method would be to use a tailored spatial cavity mode which has a non-Gaussian distribution in order to minimize the infrared intensity incident on the outcoupling hole [111] and thus reduce the intracavity losses. For example, certain higher oder transversal modes (like the TEM_{01} or TEM_{10} modes) have a low intensity node at the center of the beam and thus avoid the outcoupling hole. However, this idea has not been realized experimentaly because of two difficulties. Higher order modes have alternating phases in between the neighboring nodes which introduces a spatially dependent phase onto the dipole moment of the high harmonic radiation. This results in limited phase matching of the high harmonic radiation in the direction of the outcoupling hole. Intracavity phase masks (with very small loss) have to be introduced to modify and fix the phase of the beam to eliminate this effect. The other challenge will be the efficient coupling of the seed beam and the cavity mode. Typically, the seed beam for the cavity is generated from a mode-locked

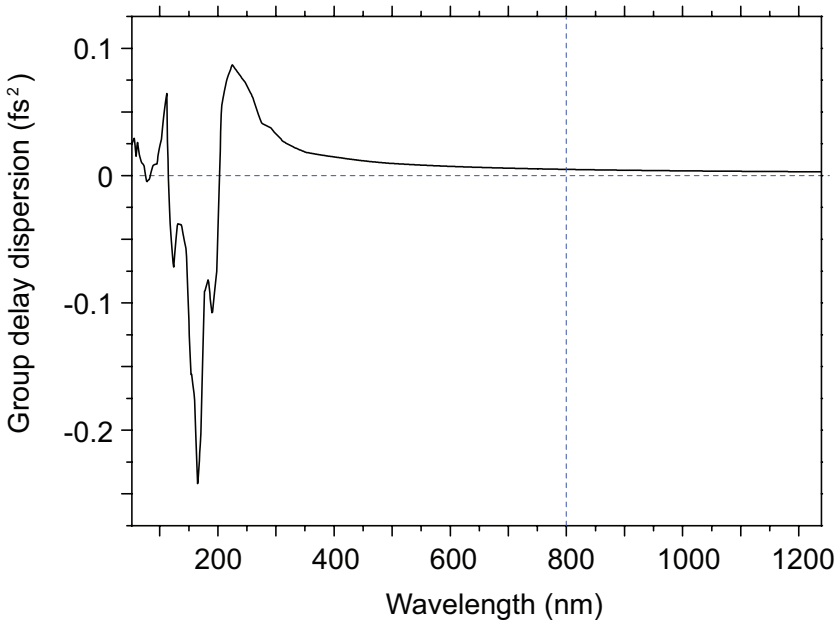

Figure 3.4: *Group delay dispersion (GDD) of a silicon sitride film with a thickness of 30 nm.*

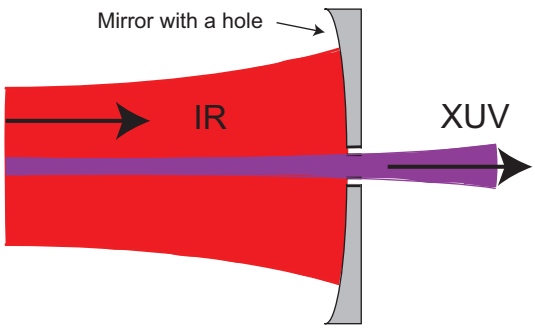

Figure 3.5: *Outcoupling of an XUV frequency comb through a tiny hole in one of the cavity mirrors*

laser and has a fundamental Gaussian beam profile (TEM_{00} mode). Additional optics such as holographic plates will be required for efficient mode-matching of the seed beam and the cavity mode.

3. Grating mirror

Recently, a novel type of output coupler was demonstrated by Yost and co-workers [113]. They etched a fine grid into one of the cavity mirrors so that it acts as an XUV grating for the high harmonic radiation which will be diffracted out of the cavity. Since the typical dimensions of the grating structure on the mirror surface are significantly smaller (40 nm) than the wavelength of the fundamental beam, it still serves as a low loss cavity mirror for the intracavity IR beam. This method eliminates any intracavity material besides a gas jet for harmonic generation such that no additional dispersion compensation will be necessary. However, since the diffraction angle is wavelength dependent, the outcoupled beam will be chromatically dispersed in space (spatial chirp). This effect might be crucial for the application of direct two photon excitation where a small distortion of the spectral phase could ruin the excitation probability. To prevent this, additional optical components with low loss have to be installed behind the grating mirror to compensate for spatial chirp.

4. Outcoupling by non-collinear high harmonic generation (NCHHG)

Another possibility for outcoupling that does not require intracavity material is to generate high harmonics that propagate non-collinearly with respect to the driving beams [111, 112, 114, 117]. To achieve non-collinear emission, two driving beams are overlapped with a small crossing angle at the focus of a gas jet. Non-collinear emission of high order harmonics is expected from the pulse collision volume shared by the two crossing beams. In general, the direction and the efficiency of high harmonic emission crucially depends on phase matching. For example, in the case of conventional high harmonic generation with a single driving beam, the phase matching condition is satisfied only in the collinear direction, resulting in high harmonic radiation propagating collinearly with the driving beam (Fig. 3.6 (a)).

However, for two driving beams crossing at a common focus, numerical calculations suggest that phase matching is also possible non-collinearly depending on the atomic densities, the crossing angle between the fundamental beams, and the intensities of the driving beams [112, 114, 117]. (Fig. 3.6 (b)). High harmonics emitted non-collinearly can be outcoupled without hitting the cavity mirrors, if the non-collinear angle is large enough. Thus, no special outcoupling element will be required so that both the nonlinear response of additional intracavity material and additional dispersion management can be avoided.

Besides a favorable power scaling as compared to the Brewster's plate method, NCHHG also has the advantage of spatially separating the high harmonic radiation from the driving beams [2]. This is of particular interest with regard to spectroscopy in the XUV, because it might render the use of additional filters for the infrared unnecessary. These are required for setups based on Brewster's plate output couplers in order to block the residual IR reflection which is typically orders of magnitude stronger than the XUV output. Therefore, since the filters are only partially transmissive in the XUV as well, NCHHG will result in about one order of magnitude higher absolute XUV power available for applications. In addition,

[2] The lack of spatial chirp has to be still investigated. See also Sec. 3.6.

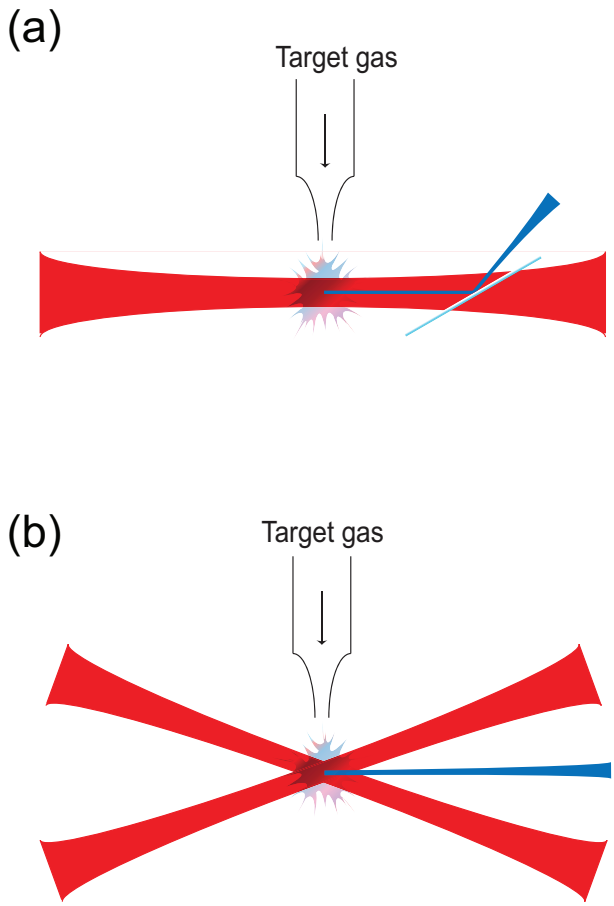

Figure 3.6: *Collinear (a) and non-collinear (b) high harmonic generation.*

the restriction of XUV outcoupling to wavelength regions, where appropriate materials for Brewster's plates exist, is lifted by NCHHG, thus making it a promising outcoupling method in the short wavelength region of higher order harmonics.

So far the investigations of NCHHG have been quite limited both theoretically and experimentally. In our work, we give a proof-of-principle demonstration of NCHHG with amplified pulses and show that the method can be applied as an outcoupling method for cavity-enhanced HHG. We explain the basic principles of NCHHG with a simplified model and investigate the systematic behaviour of NCHHG, e.g. its dependence on the delay between the two driving pulses, for the first time. Additionally, the emission of NCHHG is spectrally resolved and the results are compared with the model. The following sections give a detailed description of these topics.

3.1.3 Previous demonstrations of non-collinear high harmonic generation

Non-collinear high harmonic generation has not been investigated but in a few experiments [117–119]. One of the demonstrations by Fomichev et al. [117] used a single fundamental beam which was spatially filtered with a diaphragm to produce two spatially separated beams.

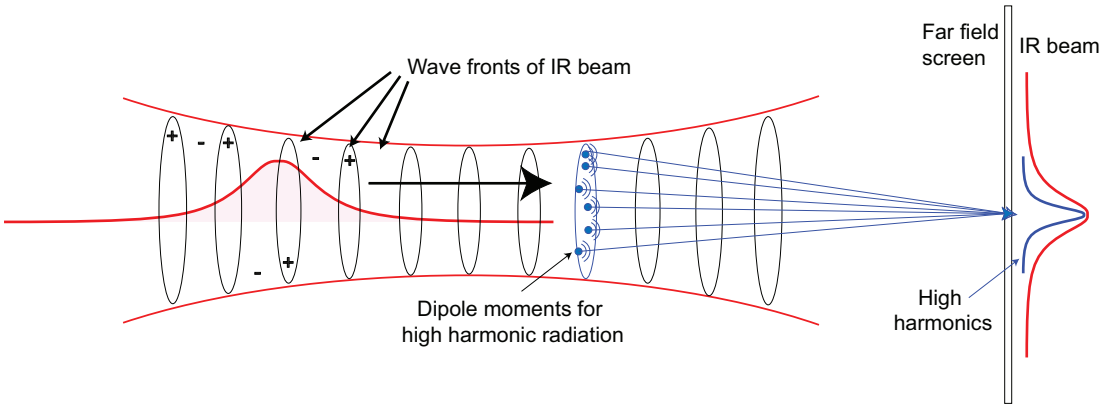

Figure 3.7: *Geometry of collinear high harmonic generation. The periodic change of optical phase is expressed by "+" and "-" sign.*

These were then focused to a common focus in the gas target with a single focusing lens, and the emission profile of the generated high harmonic radiation was measured.

They found that high harmonics were generated in the direction of the bisectrix of the driving beams and that those harmonics were stronger than the ones created collinearly by the individual beams (see Fig. 6 in [117]).

However, in this experiment, the intensity distribution of the non-collinear high harmonic radiation largely overlapped with that of the fundamental beam. Therefore, one crucial prerequisite for a potential application as an outcoupling method, the spatial separation of the non-collinear high harmonics from the driving beams, could not be demonstrated. Moreover, as both driving beams were generated from a single Gaussian beam, they partially share the common wavefront of the original beam. Thus, it still had to be shown that NCHHG was also possible with two separate Gaussian beams.

3.1.4 A simple picture of non-collinear high harmonic generation

In this subsection, a simplified picture of NCHHG is given. A more adequate discussion including a numerical simulation will follow in Sec. 3.4.

On a microscopic level, the dipole moments of single emitters (or atoms) driven by a fundamental laser beam are the sources of high harmonic radiation. Consequently, the high harmonic emission profile of a single atom is expected to be similar to that of dipole radiation. However, this is not the case anymore when considering a number of emitters distributed in three dimensions, because the total high harmonic emission profile is then determined by phase matching, that is, the constructive accumulation of harmonic emission from multiple emitters. In general, phase matching depends on the dispersion of the medium, the dispersion of the generated plasma, the spatial beam profile of the propagating driving beam and the Gouy phase of the driving beam. Here we would like to explain the emission profile of NCHHG by phase matching effects due to the spatial beam profile of the propagating driving beams.

Both in collinear and non-collinear HHG, the intensity profile of the driving beam(s) is typically Gaussian. For conventional HHG from a single fundamental beam, the phase matching condition is satisfied only for the collinear direction. This is exemplified in Fig. 3.7 where the phase fronts of the driving Gaussian beam in the interaction region ($\sim$ Rayleigh

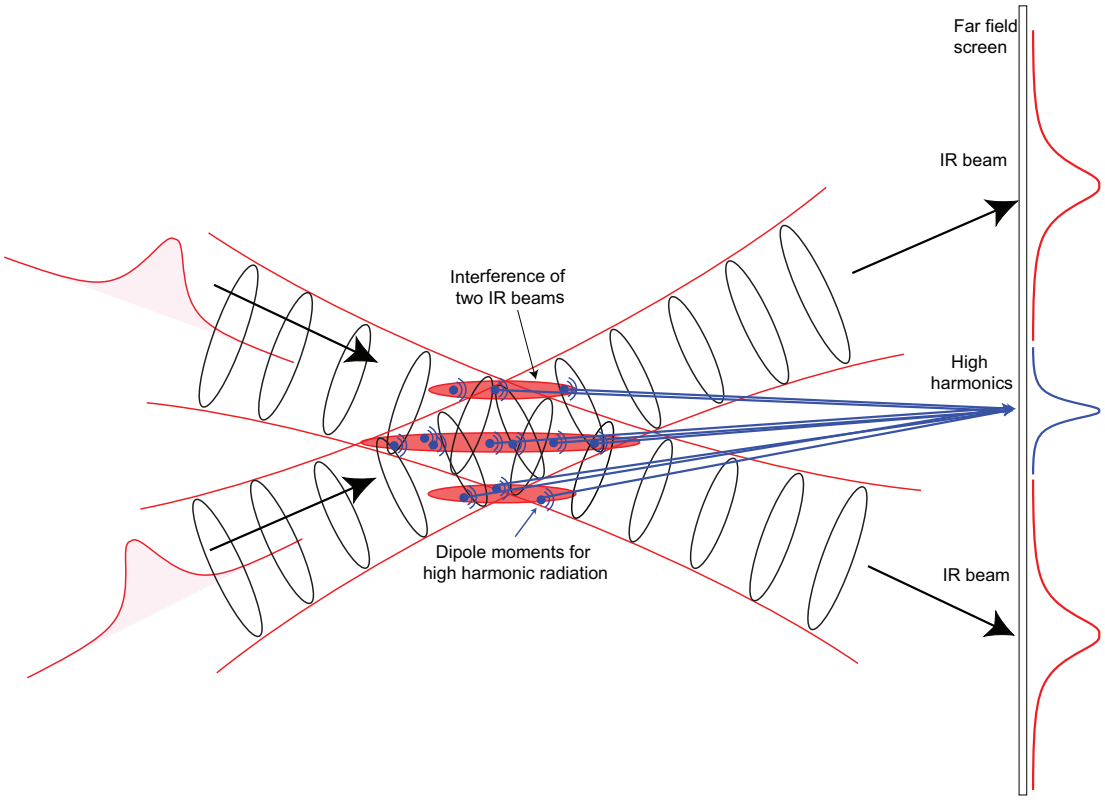

Figure 3.8: *Geometry of non-collinear high harmonic generation.*

range) are shown as lobes (positive phase) and blank space (negative phase) at fixed time. Due to rotational symmetry, these lobes correspond to disks in three dimensions. Each of these disks contains numerous, randomly distributed emitters as shown in Fig. 3.7. As is also the case for the Fraunhofer diffraction, the contributions from those emitters interfere constructively only in the direction of propagation of the driving beam with finite emission angle given by Eqn. (3.2).

The geometry of NCHHG is shown in Fig. 3.8. Two phase-coherent driving beams intersect at a small angle. The intensity distibution in the region of intersection is modulated in the direction perpendicular to the bisector of the crossing angle due to interference. Since the strength of the harmonic emission is directly related to the driving field strength, only the emitters within these interference fringes will contribute significantly to the harmonic emission. Contributions from different fringes will again interfere so that the direction of the high harmonic emission in the far field is determined by the condition for constructive interference between the contribution from those fringes. It is easy to see that, just like in a double- or multi-slit experiment, constructive interference is possible in the direction of the bisectrix of the crossing angle of the two driving beams. The simplified description given above neglects the emission dipole phase which is related to both the phase and the intensity of the driving beam. In Sec. 3.4, we will reformulate the model more precisely taking into account the emission dipole phase. We will show that the numerical simulation of the model is capable of describing most of the experimentally observed features of NCHHG.

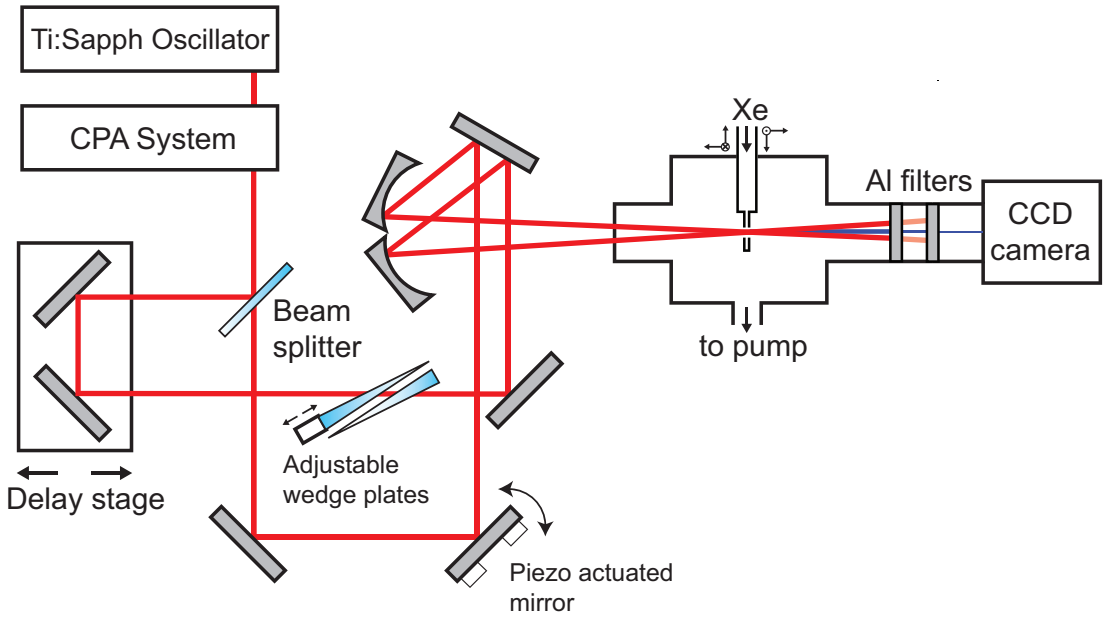

Figure 3.9: *Schematic of the experimental setup.*

3.2 Experimental

Thus far, to our knowledge, there has been no experimental demonstration of NCHHG in a setup that allows to take advantage of all the benefits of the method and that is therefore directly applicable to cavity-enhanced HHG [114,117]. Here we demonstrate that a collimated XUV beam can be emitted to the bisector of the crossing angle of two IR driving beams in such a way that it can be separated from the IR in the farfield. We show that the loss introduced by such a beam separation is low enough to allow the use in a high-Q enhancement resonator without any additional intracavity material besides a gas jet. For this proof of principle demontration, we did not use an enhancement resonator yet but investigate possible geometries with amplified pulses from a chirped pulse amplification system.

The schematic of our setup for non-collinear high harmonic generation is shown in Fig. 3.9. A chirped pulse amplification (CPA) system (Spectra-Physics Spitfire) that is seeded by the output of a mode-locked Ti:Sapphire oscillator (Femtolasers Femtosource 20) provides 150-fs-duration pulses with an average pulse energy of 1 mJ at a repetition rate of 1 kHz and at a wavelength centered about 790 nm. The pulses from the CPA system propagate along two different paths of equal length and are then recombined non-collinearly inside the vacuum chamber with two identical spherical mirrors ($f = 300\,\mathrm{mm}$). Whereas a piezo-actuated mirror is added into one path for precise spatial alignment, the other path contains a pair of wedge plates one of which is mounted on a piezo-actuated stage and a manual delay stage in order to precisely control the delay between the pulses from each path.

The two beams are focused onto a Xe gas target inside a metal tube (inner diameter: 1 mm) through a transverse hole of 200 μm in diameter. During the experiments the gas flow supplied to the nozzle is controlled by a regulating valve (Pfeiffer Vacuum EVR 116) and the nozzle itself can be precisely aligned for maximum non-collinear high harmonic emission with a three-dimensional translation stage. The waists of the driving beams are $w_0 = 24\,\mu\mathrm{m}$

resulting in a peak intensity of $2.6 \times 10^{14}\,\mathrm{W/cm^2}$ at the focus for each beam. A XUV sensitive camera with a back-illuminated charge-coupled device (CCD) without anti-reflection coating (Princeton Instruments PIXIS XO-100B) allows to monitor and record the spatial profile of the high harmonics at a distance of $\sim 750\,\mathrm{mm}$ from the focus. The scattered laser light and high harmonics of orders $q < 11$ are blocked by two aluminum filters ($200\,\mu\mathrm{m}$ thickness, Lebow 0.2Al-0-L3.0).

3.3 Discussion of results

3.3.1 NCHHG beam profiles

Typical images obtained from the CCD camera at a Xe gas flow of $6 \times 10^{-2}\,\mathrm{mbar\,l/s}$ and a backing pressure of about 10^{-2} mbar are presented in Fig. 3.10. The top and bottom pictures show the collinearly generated high harmonics, if only one of the fundamental beam is introduced. When both fundamental beams overlap spatially and temporally at the common focus, collimated XUV harmonic radiation can be observed in the bisection direction. Adjusting the beam overlap, the delay and the nozzle position for maximum non-collinear HHG, the collinear emission vanishes so that the full XUV power becomes available at the bisectrix (center picture in Fig. 3.10).

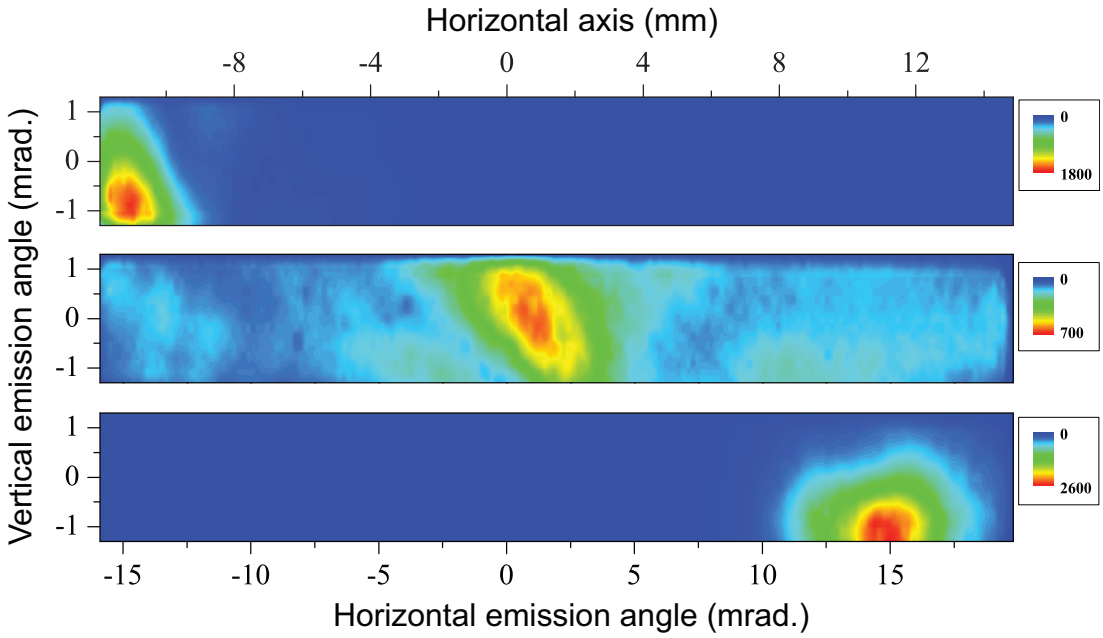

Figure 3.10: *Demonstration of Non-Collinear HHG. Two-dimensional beam profiles of high harmonics obtained with a CCD camera. Top, bottom: Collinear high harmonics observed with only one driving beam, respectively. Center: non-collinear high harmonics observed with both fundamental beams. Note that the collinear harmonics vanish in that case. The scattered laser light and high harmonics of orders $q < 11$ are blocked by two aluminum filters.*

The horizontal beam profiles of both collinear and non-collinear high harmonics shown in Fig. 3.11 (a) are obtained by integrating the images in the vertical direction. For comparison, the estimated beam profiles of the driving IR beams have been added. The full non-collinear

angle is determined to be 30 mrad from the images. The high harmonics generated non-collinearly exhibit a collimation that is comparable to that of the collinear high harmonics and show a broad pedestal.

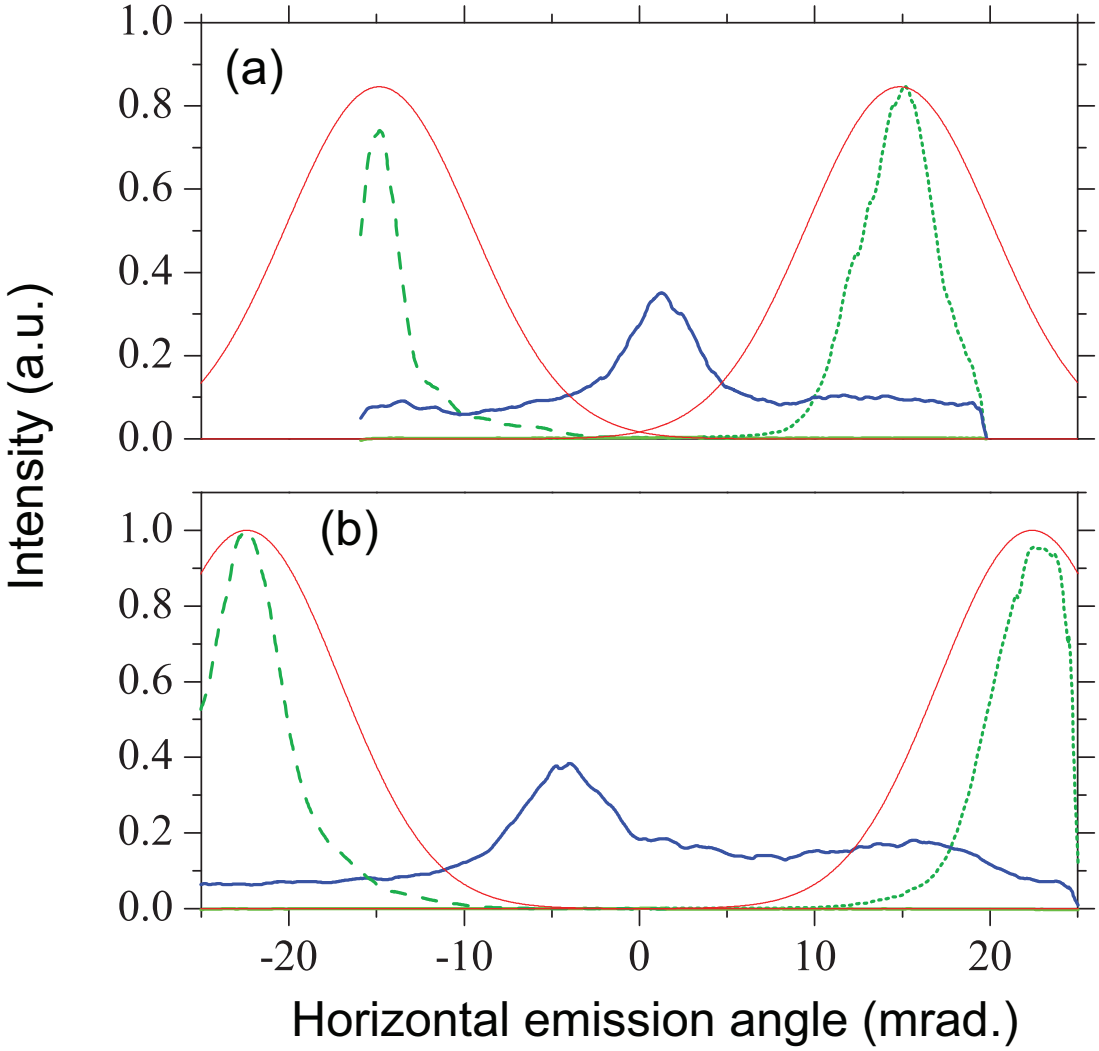

Figure 3.11: *(a) Horizontal beam profiles of collinear (dashed/green, dotted/green) and non-collinear high harmonics (thick solid/blue) obtained from vertical integration of the recorded images. The non-collinear angle is set to 30 mrad. To illustrate the potential as an outcoupling method, the estimated beam profiles of the fundamental infrared beams are also shown (thin solid/red). (b) Same as (a) for a larger non-collinear angle (45 mrad). The same intensity scale is used for both (a) and (b). Note that for this angle, the intensity ratio between collinear and non-collinear high harmonics stays similar.*

The overlap between the driving infrared and the non-collinear high harmonics along the bisector of the two fundamental beams found in Fig. 3.11 (a) suggests an investigation of NCHHG at larger non-collinear angles. Fig. 3.11 (b) shows the results of the same experiment as described above with an increased non-collinear angle of 45 mrad which was the maximum achievable angle in our current experimental apparatus. For this measurement, the distance between the focus and the CCD camera has to be decreased to 525 mm to monitor the full two-dimensional beam profiles. After careful alignment of the two IR beams, collimated non-

collinear high harmonics are observed close to the bisectrix and with a more pronounced pedestal. Fig. 3.11 shows that the intensity ratio between the collinear and non-collinear high harmonics does not deteriorate at 45 mrad. At the same time, however, the spatial overlap between the IR and the high harmonic radiation is reduced. This behavior is of crucial importance for efficient output coupling of the XUV from an enhancement cavity.

3.3.2 Estimation of outcoupling efficiency

One possible implementation of NCHHG as an outcoupling method in femtosecond enhancement cavities is to use two separate Fabry-Perot cavities arranged at a small crossing angle such that they share a common focus (Fig. 3.12(a)) [111].

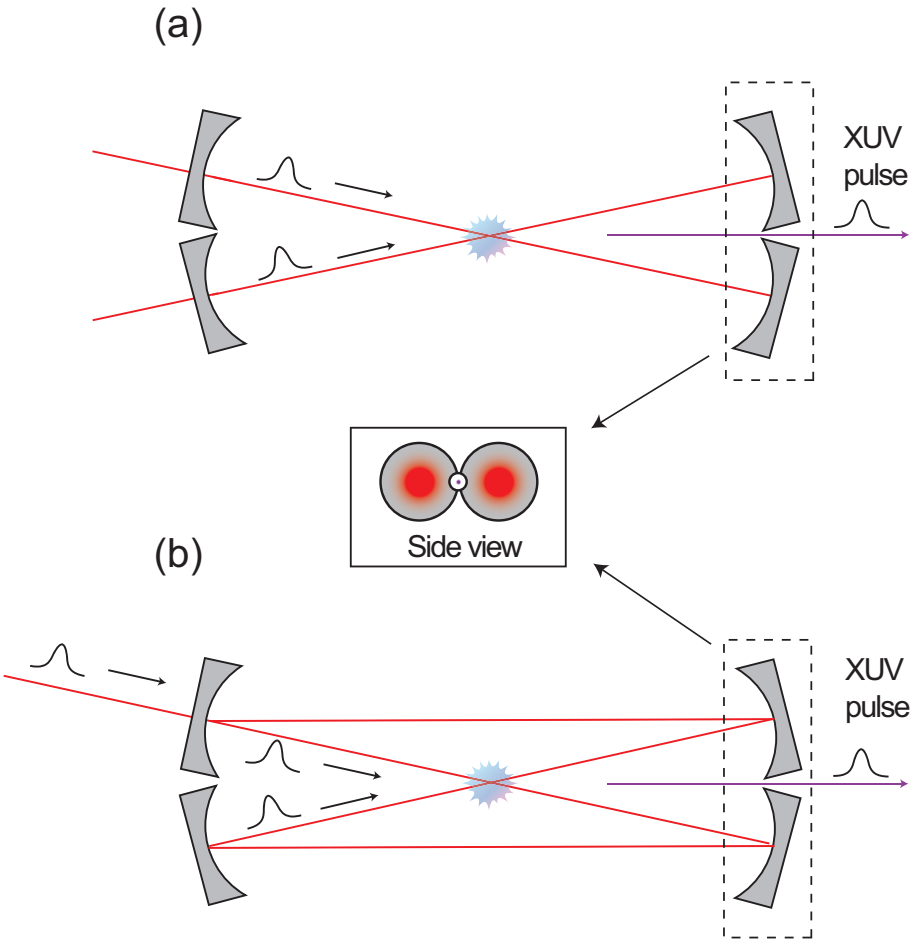

Figure 3.12: *Possible configurations of non-collinear high harmonic generation in an enhancement cavity. With a small outcoupling hole between the folding mirrors (inset), the generated XUV beam can be efficiently outcoupled without introducing any additional material into the cavity (see also [111]).*

In this scheme, the non-collinear harmonics can be outcoupled through an opening (which is assumed to be spherical here) between the two adjacent folding mirrors (see inset of Fig. 3.12). When two independent cavities are used, the overlap between the two non-collinear beams can be optimized without disturbing the alignment of the individual enhancement cavities.

Another possibility is to use a single enhancement cavity which contains two circulating pulses at the same time. When the length of the cavity and its symmetry are adjusted properly, the two pulses collide at the intersection of the two beams (Fig. 3.12(b)). An opening between two neighbouring mirrors can then be used for outcoupling of the non-collinear high harmonics just like in case (a).

In both cases, efficient outcoupling without introducing severe diffraction loss into the cavities requires the size of the hole to be carefully chosen. Since the eigenmode of the buildup cavities will be modified slightly to avoid high intensities at the outcoupling hole, a ray-tracing analysis of a cavity round trip is required to precisely evaluate the diffraction loss introduced by the hole. We estimate the diffraction loss from the intensity of an unmodified Gaussian beam hitting the outcoupling hole. Fig. 3.13 shows the diffraction loss calculated in this way as a function of the outcoupling efficiency. The latter is defined here as the ratio between the outcoupled XUV power and the collinear high harmonic power. At the larger non-collinear angle, more than 20 % of outcoupling efficiency can be obtained by introducing only 4×10^{-5} of loss into the cavity. These values are far superior to those of a sapphire Brewster's plate. For higher order harmonics, which are expected to be more collimated so that the diameter of the outcoupling hole can be reduced, the outcoupling efficiency should be even larger.

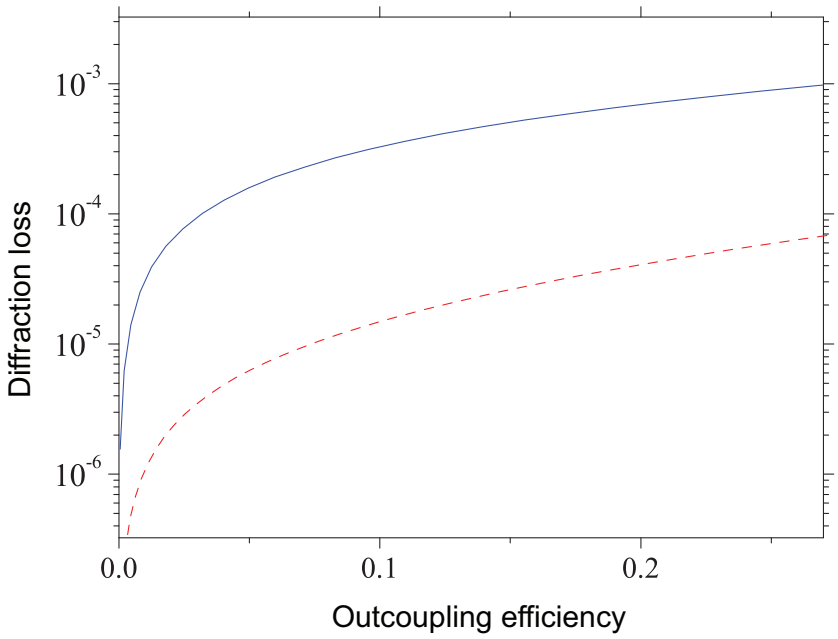

Figure 3.13: *Estimation of intracavity loss as a function of outcoupling efficiency for non-collinear angles of 30 mrad (solid (blue)) and 45 mrad (dashed (red)). Here, the outcoupling efficiency is defined as the power-ratio between the outcoupled XUV and the collinear harmonics.*

3.3.3 Systematic investigation of NCHHG

In the experimental demonstration presented in the previous section, the obtained image contains the contributions of all the different orders of high harmonics that were generated. In order to compare further investigations of NCHHG with a theoretical model that will be

described in more detail in Sec. 3.4, it is essential to spectrally resolve the generated high harmonics. We modified the existing setup (see Fig. 3.9) by incorporating an XUV grating spectrometer (Jobin-Ivon, LHT30) into the beamline after the high harmonic generation stage as illustrated in Fig. 3.14. The two driving infrared beams are oriented in the vertical plane, while the grating disperses the generated harmonic beam in the horizontal plane. The setup used to create the two non-collinearly propagating driving pulse trains is installed on a vertical breadboard. The rest of the experimental setup remains unmodified, but special care is taken to prevent any scattered driving infrared light from reaching the CCD and disturbing the recorded signals. This became necessary, since the small hole in the filter mount (which was used as a pressure bypass) turned out to be still leaking multiply scattered light.

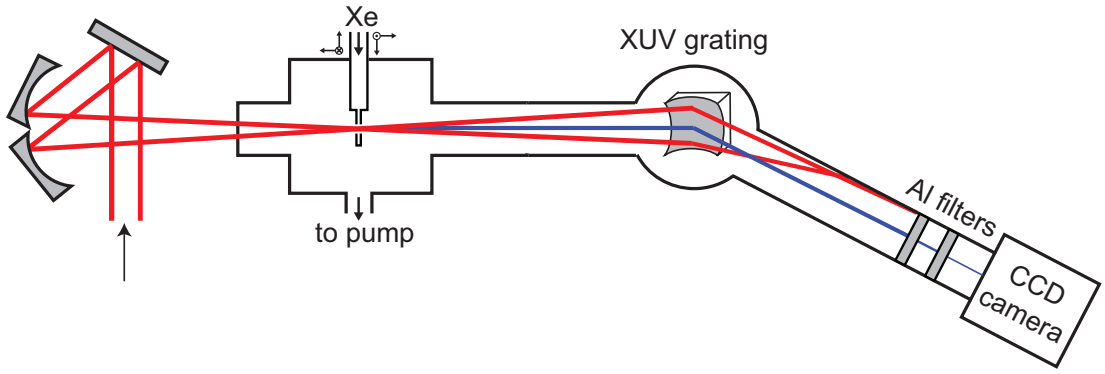

Figure 3.14: *Modified setup for spectrally resolved NCHHG measurements. An XUV grating spectrometer is inserted into the beam line. The two driving infrared beams lie in the vertical plane, while the grating disperses the generated harmonic beam in the horizontal plane. The setup used to create the two non-collinearly propagating driving pulse trains is installed on a vertical breadboard.*

We find that there is no fundamental difference between the far field emission patterns of different harmonic orders and thus will only show results for the 19 th harmonic in the following. The beam profile obtained through integrating the CCD image in the vertical direction is shown in Fig. 3.15. The full non-collinear angle is estimated to be ∼14 mrad.

It can be seen from Fig. 3.15 that the non-collinearly generated single harmonic order radiation is still well collimated. In addition, a clear distinction between the narrow central peak and a broad pedestal structure is observed, similarly to the spectrally unresolved case. Interestingly, at a delay time of 34 fs (Fig. 3.15(a)) the envelope of the profile is modulated. This modulation cannot be observed at all delays (Fig. 3.15(b)) and was not observed clearly in the spectrally unresolved measurements, either.

Fig. 3.16 shows the far field emission pattern of NCHHG as a function of the delay between the two driving pulse trains. When the delay is set to be much larger than the pulse width ($>\sim$ 150 fs), high harmonics are generated by both driving beams in the respective collinear direction, resulting in two harmonic peaks. When the delay is set such that the pulses of the two driving pulse trains overlap temporally at the focus, the high harmonic emission is directed to the bisector of the crossing angle of the two driving beams (NCHHG).

As discussed above and shown in Fig. 3.16, there are quite a number of interesting, yet complicated phenomena observed in the spectrally resolved measurements. Here we would like to focus on the following three major observations and try to illucidate the physics behind them:

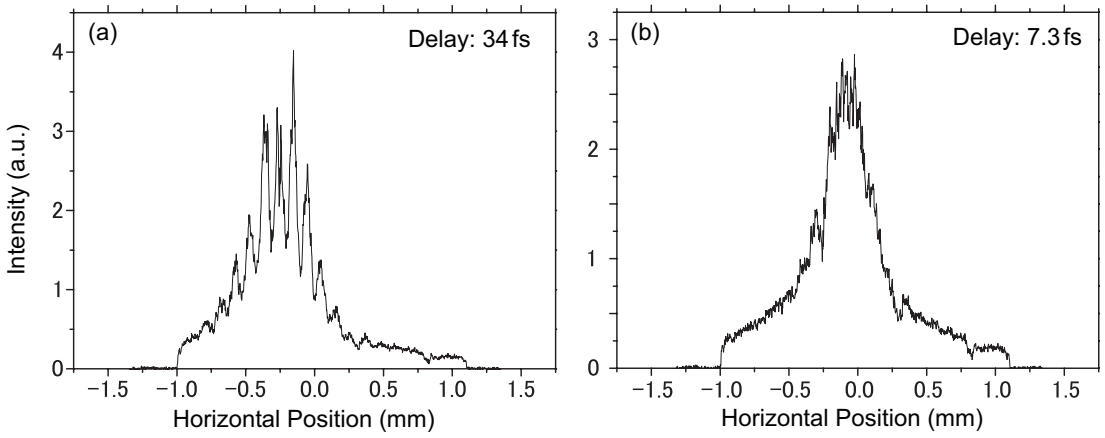

Figure 3.15: *Far field beam profiles of the non-collinearly generated 19 th harmonic. The one dimensional beam profiles are obtained by vertically integrating the two dimensional image recorded with the CCD. The delay between the two pulses is set to be 7.3 fs and 34 fs for (a) and (b), respectively. A fringe-like modulation of the peak is observed in (a) but not in (b). See text for more details.*

A The direction of the generated high harmonic emission varies continuously from collinear to non-collinear when the delay is scanned. However, the behaviour is not symmetric about the bisector of the non-collinear angle. As can be seen in Fig. 3.16, when reducing the delay, the collinear harmonic emission generated by the later driving pulse train is continuously moving towards the center, while the one generated by the earlier suddenly disappears at a certain delay. This results in the "anti-crossing"-like shape of the emission profile which resembles the letter "ℵ" depicted in Fig. 3.17.

B As shown in Fig. 3.15, far field emission profiles both with and without modulation are observed depending on the delay between the two driving pulse trains. This behaviour only appears clearly for spectrally resolved NCHHG.

C As is also the case for the spectrally unresolved measurement, the collinear high harmonic emission from the individual driving beams almost completely disappears, when the two driving pulse trains overlap temporally at the focus such that all the power of the high harmonic radiation is emitted in the direction of the bisector of the crossing angle of the driving beams.

3.4 Numerical Simulation

In order to gain a deeper understanding of the physics of NCHHG and thus find explanations for the observations (*A* – *C*) presented in the previous section, we have set up a code to simulate the non-collinear emission of high harmonics according to our experimental setup. The calculation is based on a simplified model: Our simulation determines the intensity dependent amplitude and phase of the high harmonic dipole moments of the atoms in three dimensions. Similarly to the calculation of Fraunhofer diffraction, the high harmonic intensity at a single point in a arbitrarily chosen far field plane is obtained by coherently adding up the contributions from all the emitters in the interaction region.

A full simulation of high harmonic generation according to the single atom response re-

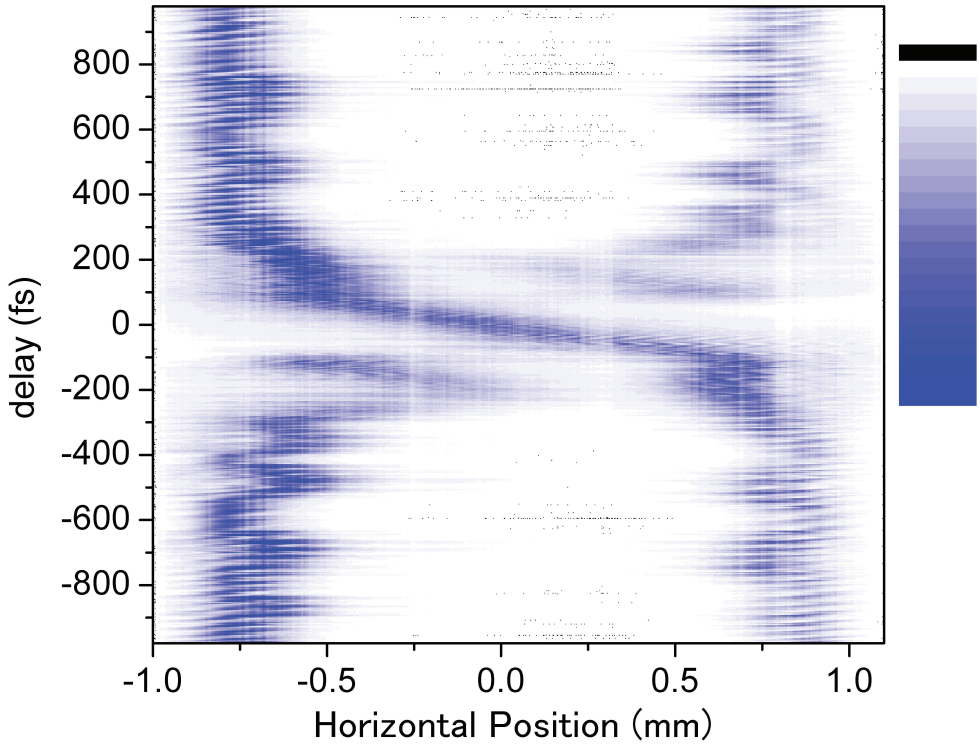

Figure 3.16: *Far field emission pattern of NCHHG as a function of the delay between the two driving pulse trains. Note that the pulse duration is 150 fs.*

quires numerically solve the 3-dimensional Schrödinger equation [73, 75, 120]. This is possible in one- or two-electron systems [121, 122]. For rare gases, an effective potential has been succesfully used to determine the single atom response in the single active electron approximation [123–126]. For a simulation of NCHHG, the single atom response has to be calculated for a large number of target atoms that are distributed in the interaction region. Since this approach is computationally demanding, we decided to aim for a qualitative understanding of NCHHG first. Therefore, in our simplified model for the single atom response, the phase and the amplitude of the q th harmonic radiation from a single emitter are assumed to be given by:

$$D(x, y, z, t) = |E_{\mathrm{IR}}(x, y, z, t)|^p \cdot e^{i\phi_D} \tag{3.4}$$

$$\phi_D = q\,\phi_{\mathrm{IR}} + \Delta\phi_D \cdot |E_{\mathrm{IR}}(x, y, z, t)|^2. \tag{3.5}$$

Here, $E_{\mathrm{IR}}(x, y, z, t)$ stands for the driving field, and ϕ_D and ϕ_{IR} are the phase of dipole moment and the driving beam, respectively. A power scaling law identical to Eqn. (3.4) is employed in [127] in which the power scaling of the harmonics is determined by p. We used $p = 7.8$ for all our simulations, which is the number of photons at 800 nm required for ionization of Xenon atom. $\Delta\phi_D \cdot |E_{\mathrm{IR}}(x, y, z, t)|^2$ represents the phase contribution of the dipole moment which depends on the intensity of the driving field. This phase contribution is evaluated using classical action of electron that correspond to two well-known main contributing trajectories shown in Fig. 3.18, the short and the long trajectory [105].

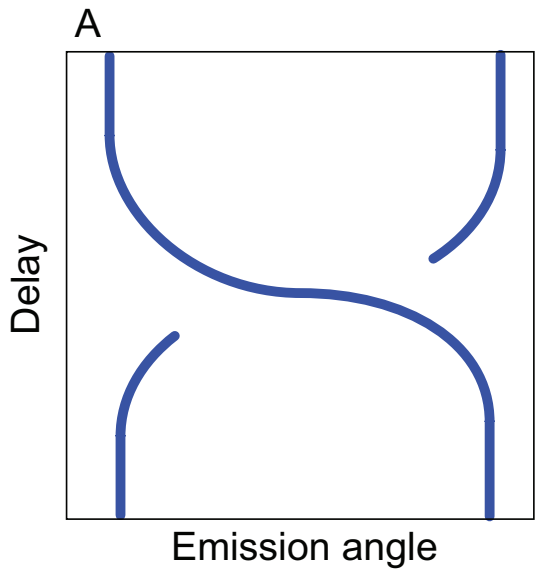

Figure 3.17: *Generic "א – like" shape of NCHHG emission profile corresponding to Fig. 3.16*

The coodinate system used in our simulation is defined according to Fig. 3.19. The fundamental beams propagate towards the z-direction at a small non-collinear angle. Both beams lie in the x-z-plane. A dipole moment located at (x, y, z) in the interaction (or emission) region emits high harmonic radiation. This radiation is propagated to the far field. Since generated high harmonic radiation is linearly polarized, the electric field vector can be treated as a sclar field when the non-collienar angle is small. The far field emission profile is evaluated at every position (X, Y) of a screen which is located at a fixed position Z_0. We assumed that the dipole moment radiates uniformely in all directions. This approximation is justified if the emission angle against the Z-axis is significantly smaller than the divergence of the dipole radiation. The distance l between the emitting dipole and the point (X, Y, Z_0) at the screen is given by

$$l = \sqrt{(X - x)^2 + (Y - y)^2 + (Z_0 - z)^2}. \tag{3.6}$$

The phase shift ϕ due to the propagation from the emission region to the screen is given by

$$\phi = kl = k\sqrt{(X - x)^2 + (Y - y)^2 + (Z_0 - z)^2}. \tag{3.7}$$

Here, k is the wavenumber of the high harmonic radiation. The electric field of the high harmonics ($E_{\mathrm{HHG}}(X, Y, t)$) at time t at the point (X, Y) on the far field screen is given by accumulating all the contributions of the high harmonic dipole moments in the emission region. Note that the phase has to be taken into account for this integration (Fraunhofer diffraction model of NCHHG):

$$E_{\mathrm{HHG}}(X, Y, t) = \int_x \int_y \int_z D\,(x, y, z, t) \cdot e^{-i\phi}. \tag{3.8}$$

Here $D(x, y, z, t)$ stands for the complex high harmonic field emitted from a dipole moment located at (x, y, z) at time t. The absolute value of the phase of the electric field at the screen

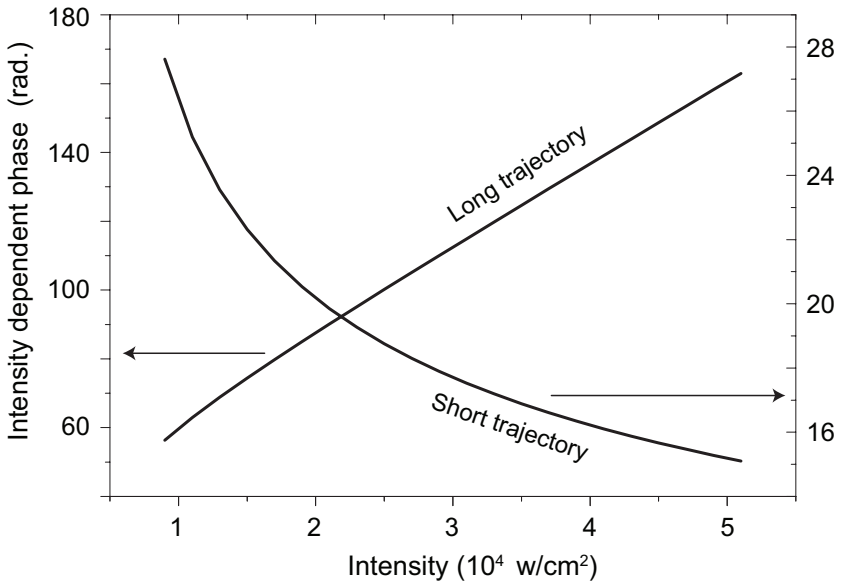

Figure 3.18: *Dipole phase of high harmonic generation used in the simulation, calculated based on classical elctron trajectories for 19^{th} order of harmonics. See text for more details.*

is not important for simulating the high harmonic emission profile in the far field. Thus, it is convenient to introduce the relative phase shift $\Delta\phi$ defined as:

$$\Delta\phi = kl - kl_0 = k\sqrt{(X-x)^2 + (Y-y)^2 + (Z_0-z)^2} - k\sqrt{X^2+Y^2+Z_0^2} \tag{3.9}$$

where the reference distance between the emission point $(x = 0, y = 0, z = 0)$ and the point (X, Y) on the screen is denoted as l_0. In the "far field" approximation $(x, y, z, X, Y \ll Z_0)$, $\Delta\phi$ can be approximated as:

$$\Delta\phi = k\frac{x^2+y^2}{2Z_0} - k(x\theta_x + y\theta_y + z). \tag{3.10}$$

Here, angular coodinates defined as $\theta_x = X/Z_0$ and $\theta_y = Y/Z_0$ have been introduced. Neglecting an overall phase shift, Eqn. (3.8) becomes:

$$E_{\mathrm{HHG}}(X,Y,t) = \int_x\int_y\int_z D\,(x,y,z,t)\cdot e^{-i\Delta\phi} \tag{3.11}$$

$$= \int_x\int_y\int_z D\,(x,y,z,t)\cdot e^{-ik\frac{x^2+y^2}{2Z_0}}\cdot e^{ik(x\theta_x+y\theta_y+z)}. \tag{3.12}$$

It can be seen that the last equation can be evaluated efficiently by using a fast-fourier-transform (FFT):

$$E_{\mathrm{HHG}}(X,Y,t) = \int_x\int_y\int_z D\,(x,y,z,t)\cdot e^{-ik\frac{x^2+y^2}{2Z_0}}\cdot e^{ik(x\theta_x+y\theta_y+z)} \tag{3.13}$$

$$= e^{iwt}\cdot \mathrm{FFT}_{(x,y,z)}\left[D(x,y,z,t)\cdot e^{-ik\frac{x^2+y^2}{2Z_0}}\right] \tag{3.14}$$

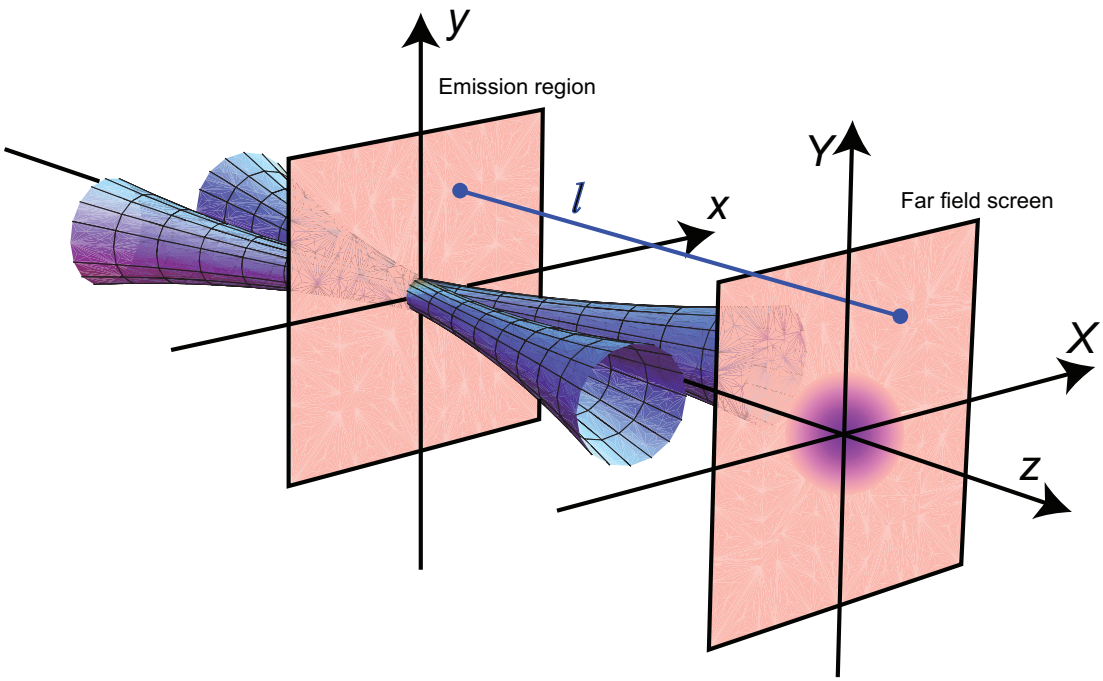

Figure 3.19: *Geometry used for our NCHHG simulation*

Using Eqn. (3.14), the intensity distribution of the high harmonic radiation at the screen $I_{\mathrm{HHG}}(X,Y)$ becomes:

$$I_{\mathrm{HHG}}(X,Y,t) = |E_{\mathrm{HHG}}(X,Y,t)|^2. \tag{3.15}$$

We wrote a C++ program to evaluate Eqn. (3.14). The Fourier transform of Eqn. (3.14) is perfomed with the Fast Fourier Transform (FFT) routine of the FFTW library [128].

3.4.1 Discussion of results

To simulate the driving beam geometry for NCHHG, two Gaussian driving beams are overlapped at a common focus with a (full) non-collinear angle of 2θ so that the total fundamental field is given by

$$\begin{aligned} E_{\mathrm{IR}}(x,y,z,t) = {} & E_{\mathrm{Gaussian}}(x\cos(-\theta) - y\sin(-\theta), x\sin(-\theta) + y\cos(-\theta), z, t) \\ & + E_{\mathrm{Gaussian}}(x\cos(\theta) - y\sin(\theta), x\sin(\theta) + y\cos(\theta), z, t) \end{aligned} \tag{3.16}$$

Here, the first and second term correspond to two Gaussian beams that have been rotated by θ and $-\theta$ with respect to the z axis, respectively. Each single Gaussian beam is expressed by [129]:

$$E_{\mathrm{Gaussian}}(x,y,z,t) = E_0 \frac{\omega_0}{\omega(z)} \cdot e^{i\eta(z) - i\frac{kr^2}{2q(z)}} \cdot e^{i(wt-kz)}. \tag{3.17}$$

Here the Gouy phase shift and q-parameter are represented by $\eta(z)$ and $q(z)$, respectively.

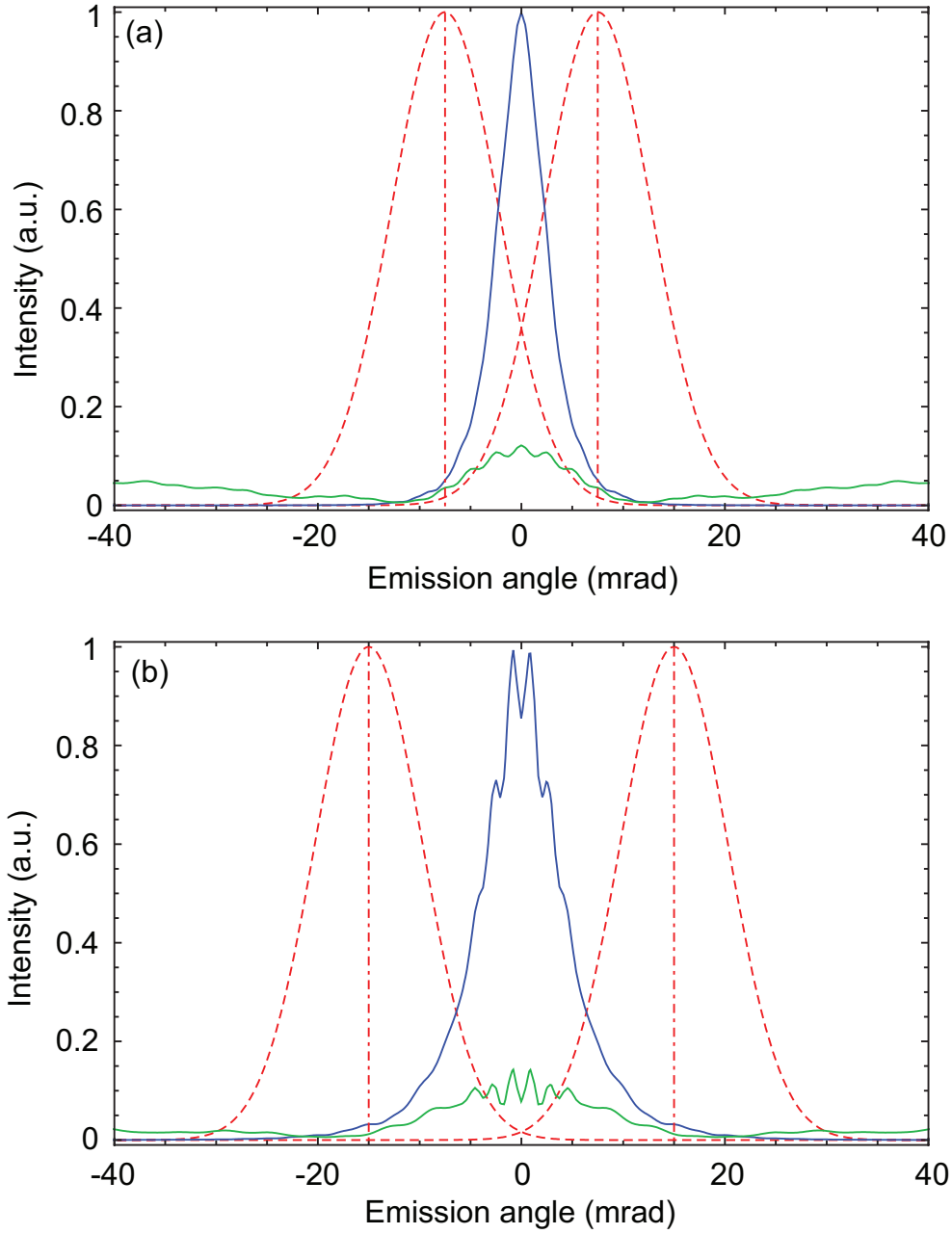

Figure 3.20: *Simulated beam profiles of NCHHG for short (blue) and long (green) electron trajectory. Non-collinear angle of 15 mrad (a) and 30 mrad (b) are used in the simulation. Vertical lines correspond to the two emission directions of driving beams. Dashed lines show beam profiles of driving beams at the screen. Note that the collinear HH-emission is strongly supressed.*

We run the simulation for atomic phases that correspond to the short and to the long trajectory. The obtained 2-dimensional images of NCHHG are integrated in the vertical direction (Y direction) and shown as 1D beam profiles in Fig. 3.20. The parameters used in the simulation are as follows:

peak intensity (single beam)	$2.6 \times 10^{14}\,\mathrm{W/cm^2}$
focal radius	$24\,\mu\mathrm{m}$
order of harmonic	19 th
wavelength of driving beam	790 nm
noncollinear angle	15 and 30 mrad
delay between the two beams	0 fs
dipole phase	short and long trajectory

Note that the peak intensity in the table is given for a single beam. Due to interference between the two beams, the actual driving intensity can be higher. In Fig. 3.20, collimated non-collinear emission centered between the two driving beams is observed for the short trajectory. The emission profiles for the long trajectory exhibit a broad pedestal-like structure. In addition, it can be seen that the collinear emission of high harmonic radiation is strongly suppressed both for the short and the long tragectory, and for both a non-collinear angle of 15 mrad and 30 mrad.

In order to investigate the features A and B described in Sec. 3.3.3, the emission profile of NCHHG is calculated for different delays between the two driving pulse trains. A pulse duration of 150 fs is assumed in the simulation. The 1D beam profiles are calculated with the phase of the short electron trajectory as a function of the delay time and then normalized to their respective peak for each delay. The results are shown in Fig. 3.21.

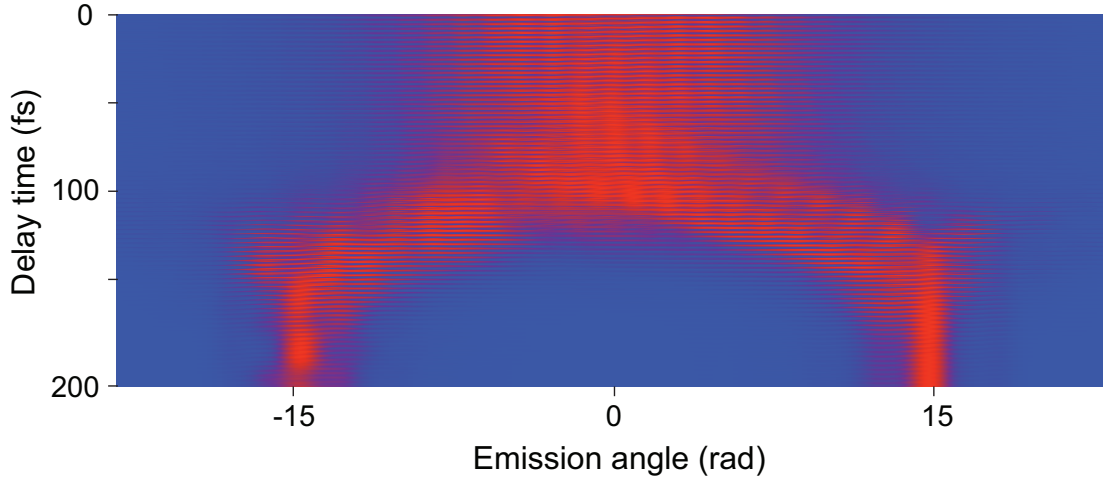

Figure 3.21: *Simulated beam profile of NCHHG as a function of delay.*

It can be seen from Fig. 3.21 that the non-collinear emission appears when the two driving pulse trains are temporally overlapped. In this case, the collinear emission is strongly suppressed, which agrees with experimental observation (feature C in Sec. 3.3.3). When the delay is increased significantly until the overlap between the two pulse trains is negligible,

two isolated beams of high harmonic radiation generated collinearly to the driving beams are obtained. It can be seen that the transition from non-collinear emission to collinear emission is continuous, and that the direction of the non-collinear emission crucially depends on the delay. The simulation results thus reproduce the experimental observations described above. However, as can be immediately seen in Fig. 3.21, the simulation shows a mirror symmetry of NCHHG about center of the emission angle, which is in contrast to the "ℵ-like" feature of the experimental results shown in Fig. 3.16. This discrepancy cannot be explained within the current Fraunhofer diffraction model of NCHHG. One possible explanation would be a transient effect in the target gas. The current model assumes that both pulses from both beams interact with a target medium of an exactly identical response independent of the delay between the pulses. In reality, the earlier pulse may alter the electronic state of the target atom, resulting in a different response of the medium for the second later pulse. For example, if the first pulse excites the target atom into some higher excited state, the second pulse will interact with an atom with an effectively smaller ionization potential. This changes the conversion efficiency of HHG for the second driving pulse due to a shift in the cut-off energy. A similar behaviour has indeed been observed both experimentally and theoretically in traditional (collinear) high harmonic generation from a pre-excited medium [130–134]. In some of these demonstrations, independent double pulses with different wavelengths were applied for the excitation of the medium and for efficient high harmonic generation, respectively. It was found that the conversion efficiency of HHG can be significantly improved due to the effect of pre-excitation of the target medium.

So far, the dependence of NCHHG on the delay between the driving pulse trains has been discussed on a rather large timescale (on the order of a few hundred fs) referring to Fig. 3.21. Now, we would like to focus on the effects that can be observed on a much shorter timescale, that is, when the phase difference between the two driving beams is rather small. Fig. 3.22 shows a series of NCHHG emission profiles simulated with the phase of the short electron trajectory. Here, the phase shifts between the two driving pulses were swept around the case of perfect temporal overlap. The profiles are normalized to their peak intensities for each phase shift. The parameters used in the simulation are the following:

peak intensity (single beam)	$2.6 \times 10^{14}\,\mathrm{W/cm^2}$
focal radius	$24\,\mu\mathrm{m}$
order of harmonic	19 th
wavelength of driving beam	790 nm
non-collinear angle	15 mrad
phase delay between the two beams	$0 - 2\pi$ rad
dipole phase	short trajectory

The simulated delays shown in Fig. 3.22 correspond to a phase shift from $0 \cdot \pi$ to 2π. When the phase delay is set to π, the high harmonic emission profile shows a fringe-like modulation structure with almost full modulation depth. When the phase shift is increased from π to 2π, the visibility of the modulation decreases continuously and finally almost disappears completely. These simulation results nicely agree with the measured NCHHG emission profiles shown in Fig. 3.15. The appearance and disappearance of the fringe structure can be explained based on the interference pattern of the driving beams in the interaction region. Figures 3.23 (a) and (b) illustrate the intensity distribution in the interaction region for different

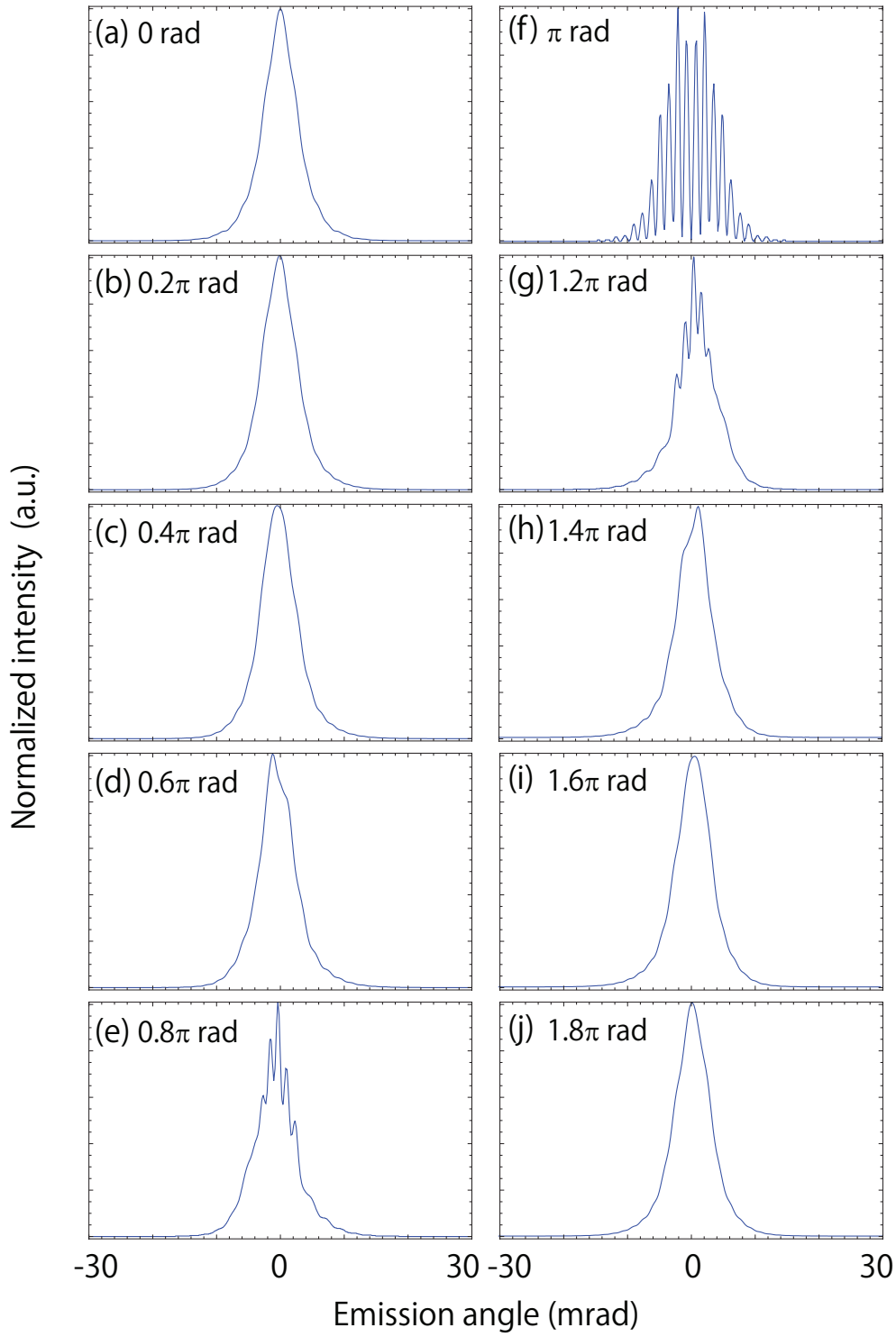

Figure 3.22: *Simulated beam profile of NCHHG for different phase delay between the two driving beams.*

phase delays ϕ between the two driving beams. The fringe pattern in the interaction region depends on the non-collinear angle and the driving wavelength. As shown in Fig. 3.23(a), when the phase delay is adjusted to $\phi = 0$, a single elliptical region with high intensity appears at the center of the two driving beams. The cross-section of the interference profile is shown in Fig. 3.23(b). The profile of the cross-section consists of a central peak with small sidebands. On the other hand, when the phase shift is set to $\phi = \pi$, the intensity profile in the interaction region consists of two separate fringes. Recalling the interference pattern in a double slit experiment, it can be seen that the far field emission profile of NCHHG in this case is modulated because of interference between those two spatially separated emission regions.

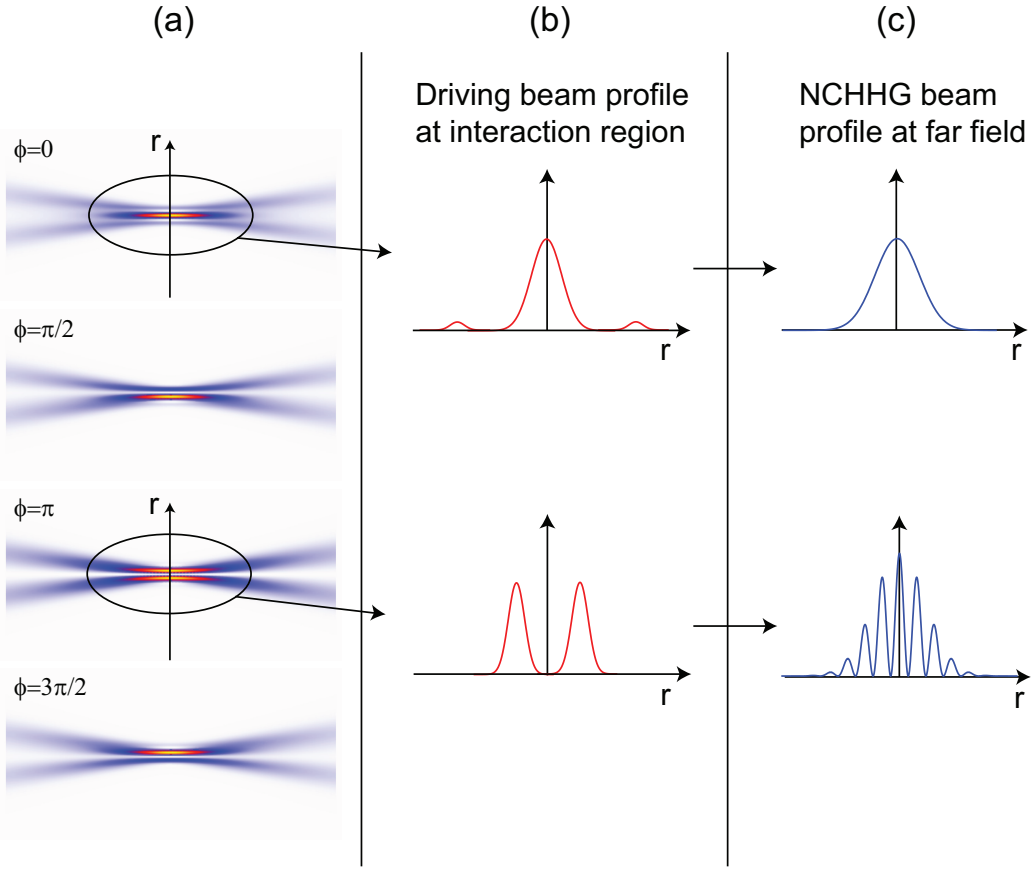

Figure 3.23: *(a) and (b) show the interference profiles of two driving beams for different phase delays between the two beams. (c) shows the expected far field beam profile for non-collinear high harmonic emission.*

The observation that the collinear high harmonic radiation disappears for maximum non-collinear high harmonic emission (feature *C*) can be explained with Fig. 3.24. The interference pattern of the two crossing driving beams shows a modulation perpendicularly to the direction of the bisector of the two beams and is elongated in the bisector direction for any phase delay between the two pulses. If we look at the intensity profile of the driving beams along the axis of one single driving beam (collinear direction, denoted as z' axis in Fig. 3.24), we find a strong variation depending on the phase delay between the two driving pulse trains. However, if the intensity is so strongly modulated along the collinear propagation direction,

the intensity dependent phase of the dipole emitters also varies rapidly. This results in destructive interference of the high harmonic radiation in the collinear direction and explains why the collinear emission is strongly suppressed when non-collinear emission is obtained.

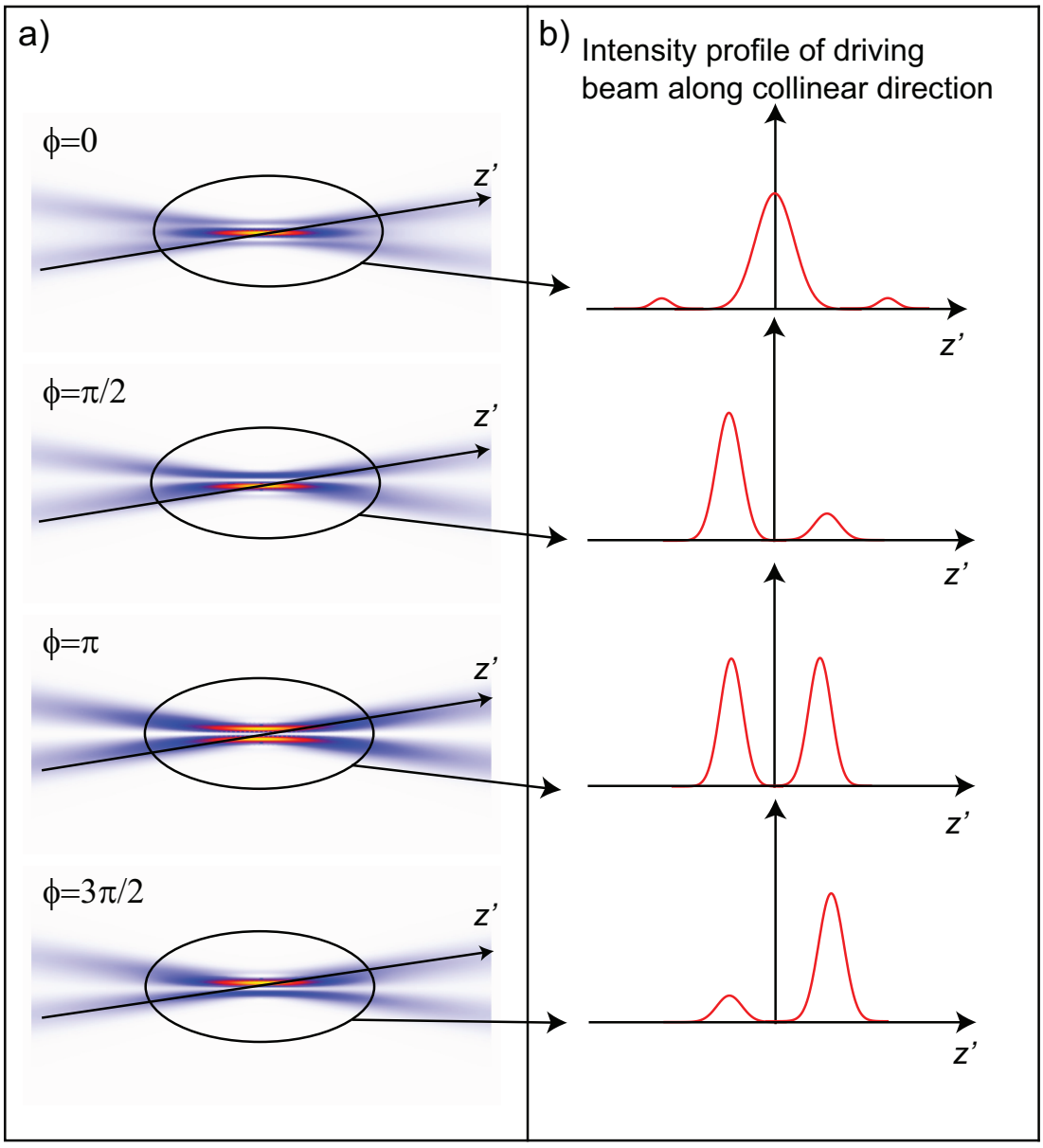

Figure 3.24: *Interference profile of two driving beams for different phase delays between the beams (a). (b) shows the intensity cross section along one of the driving beams*

3.5 Conclusions

- Non-collinear high harmonic generation (NCHHG) has been demonstrated for the first time with two individually controllable beams.

- Based on the observed beam profiles and the expected divergence of the non-collinear high harmonics, the outcoupling efficiency and the introduced losses are estimated for cavity configurations in which NCHHG can be applied as a combined generation and outcoupling method of high harmonic radiation. It is shown that the NCHHG-based outcoupling method introduces a significantly smaller loss than the Brewster's plate approach. Non-collinear high harmonic generation is thus expected to be a promising candidates for the next generation of enhancement cavity experiments.

- In order to investigate the physics of NCHHG, non-collinear emission has been spectrally resolved and its dependence on the delay between the driving pulse trains has been measured. The results of our measurements are nicely reproduced by a simple numerical simulation based on a Fraunhofer diffraction model of NCHHG. The simulation results show that most of the experimentally observed features of NCHHG can be explained by effects of the modified emission profile in the interaction region due to interference between the two driving beams.

3.6 Future prospects

A few technical and fundamental issues have to be investigated and overcome to apply NCHHG as an outcoupling method for cavity-enhanced HHG. One experimental challenge is certainly the alignment of both the cavity and the spatial overlap between the driving beams. Several configurations have been considered to implement NCHHG in an enhancement cavity [111, 114]. In the demonstration of NCHHG described in this chapter, very careful alignment of the spatial overlap of two driving beams was required to obtain strong non-collinear high harmonics. It would be advisable to use a setup in which the degrees of freedom for the alignment of NCHHG are totally decoupled from the alignment of the enhancement cavity. One possible configuration is using two independent cavities as shown in Fig. 3.12. If the two cavities are installed on two independent base plates, NCHHG can be optimized by carefully aligning the relative position of the two base plates. Careful attention will still be required to keep the beam pointing reasonably stable and thus ensure reliable long term operation of NCHHG.

One fundamental issue that has to be looked into further is the angular chromatic dispersion of the NCHHG emission. Here we consider angular chromatic dispersion after isolating a single order of harmonics, which is sufficient for most of the applications. In our simulation, it is always assumed that the driving beam is monochromatic. However, in reality for broadband driving pulses, if two color components of the driving beams experience different phase matching conditions for NCHHG, it may possible to produce non-collinear high harmonic emission with angular chromatic dispersion. Consider two broadband driving pulses with slightly different chirp which could be a result of an imperfectly dispersion-balanced setup to produce the two pulse trains for NCHHG. When NCHHG is driven with these pulses, the phase delay between the two pulses is dependent on the driving wavelength. Since the emission profile is phase-delay dependent as discussed in 3.4.1, this will lead to a spectral distribution that differs for different emission directions. Thus, the chirp of the driving pulses has to be precisely controlled. Even when the two driving beams have no chirp, the following concern still exists: Consider non-collinear second harmonic generation with broadband pulses. When the driving beam is not monochromatic, the process could be better understood as a sum-frequency generation between different spectral components within the broad

bandwidth of the driving beams. In this case, the emission direction for which the phase matching condition is satisfied depends on the two wavelength components of the driving beams. A similar effect could also produce angularly dispersed non-collinear high harmonic emission. The effect would be more pronounced for ultrashort pulses with extremely broad spectral bandwidth. Modelling of NCHHG with multiple wavelengths will be necessary to investigate those effects in detail.

The other concern is the stability of the delay between the two driving pulses. It is demonstrated in this work that the fringe structures of the NCHHG emission profile periodically appear and disappear when the phase delay between the two driving pulses is shifted. The period corresponds to one optical cycle of the driving beam. This demonstration indicates that the delay between the two pulses has to be stabilized to better than one driving wavelength. This can be easily done by applying conventional active feedback to the interferometric setup used to create the two driving pulse trains for NCHHG.

The phenomenon of NCHHG itself is still interesting enough to be investigated further. NCHHG could be useful for the investigation of the single atom response of HHG. In our numerical simulation, we found that the fringe structures which appear in the NCHHG beam profile strongly depends on the intensity-dependent atomic phase. By measuring the fringe shift as a function of the driving beam intensity, it may be possible to determine the intensity dependence of the atomic phase. In our current setup, the stability of the interferometric setup used to create the two driving beams was not good enough to resolve and investigate this effect.

In Fig. 3.16, it can be seen that the non-collinear emission is only possible when the two pulses are both spatially and temporally overlapped. The latter feature can be used to characterize the pulse duration of the original pulses. This is a direct extension of frequency resolved optical gating (FROG) [135], where second harmonic generation is employed for nonlinear frequency conversion. The advantage of a NCHHG-based pulse width measurement is the high sensitivity due to the high order of nonlinearity of the high harmonic generation process. Thus, if the intensity of the driving pulse is properly chosen so that the HHG process does not saturate, the interference between the central peak and a very weak sideband can still be detected. In addition, the method can be used for ultrashort pulses in the short wavelength region where no tranparent nonlinear crystal exists. It will be of interest to investigate the possibility to extract information about the spectral phase of the original pulse from pictures like Fig. 3.16.

Chapter 4

High repetition rate cryogenic amplifier for femtosecond laser pulses

4.1 Introduction

Obtaining high pulse energies to efficiently drive the process of high harmonic generation (HHG) is essential for high power XUV frequency comb generation. For a given pulse duration, higher pulse energies allows higher peak intensities that improve the efficiency of HHG[1]. For XUV frequency comb generation at large repetition rates, high pulse energy implies high average power. Given a constant conversion efficiency, higher average power of the driving beam will scale up the average power of the XUV frequency comb output. As described in detail in Chap. 2, cavity assisted high harmonic generation has been utilized to obtain a sufficiently high pulse energy (and high average power as well) at a comparatively large repetition rate of 10 MHz. Considerable efforts have been made to improve the power enhancement of broadband cavities: careful adjustment of the intra-cavity dispersion, advanced mirror manufacturing (tailored layer design and coating process) to obtain low loss and broadband high reflective cavity mirrors, and the development of efficient outcoupling methods with minimum loss. For a given cavity enhancement further improvement can still be expected by increasing the power of the seed laser that is coupled into the cavity. When the power enhancement is not limited by nonlinearities, the pulse energy and the average power inside the cavity are proportional to the respective parameters of the seed laser. To increase the laser power is sometimes more realistic and rewarding, especially when the efforts to further improve the performance of the enhancement cavity have reached their limits.

4.1.1 Mode-locked oscillator with high average power

There are several ways to obtain a seed beam with high average power. Here we limit ourselves to a Ti:sapphire based laser system. Recent developments of Ytterbium based oscillators and amplifiers will be briefly discussed in Chap. 5.

[1] When ionization leads to saturation with intensity, improvement can still be obtained by increasing the laser focus in order to increase the interaction volume.

One obvious possibility is to try to obtain a large average output power directly from the mode-locked oscillator. For conventional mode-locked short-pulse (fs) Ti:sapphire oscillators[2], the average output power has thus far been limited to about 1 W [136]. For mode-locked lasers, it is known that the intensity at the intra-cavity focus has to be carefully adjusted to obtain an appropriate amount of non-linearity to initiate and sustain mode-locking [9, 92, 137]. For mode-locked operation in the soliton regime, simply increasing the average power by stronger pumping is known to result in formation of a continuous wave (CW) oscillation component and/or pulse-splitting. In the latter case the average power is distributed among several pulses which limits the energy of each individual pulse [9,137,138]. Another solution seems to be to select a larger focus of the laser beam inside the laser crystal to limit the peak intensity with high average power. The method has not been proven successful and, as far as I can see, there is no widely-accepted explanation for this. Several possible hypotheses can be considered:

1. Weaker focusing requires a stronger pump laser to generate the required intensity for inverting the gain medium. Green pump lasers are often made from frequency doubled CW laser (such as Nd:YVO_4 , Nd:YLF and Nd:YAG laser). The power limitation of commercially available lasers sets the limit for the maximum available pump power [136].

2. Higher pump power that is applied to the gain medium results in stronger thermal effects, such as thermal lensing. The distorted cavity mode profile may disturb the Kerr-lens-driven mode-locking process [136].

3. Using weaker focusing to maintain the same peak intensity with higher average power, the Rayleigh length of the cavity mode changes as well. This introduces an un-scalable change to the geometrical cavity configuration: The ratio between the strength of the Kerr-lens and the unbiased focusing will be different. This may make soft-aperture mode-locking un-scalable.

In order to maneuver around these problems and still obtain high average output power, several methods can be considered. The following list summarizes the efforts that were made so far towards high power mode-locked oscillators.

High power mode-locked oscillators

- Large transmission output coupler in combination with large pump power
- Chirped pulse oscillator (CPO)
- Intra-oscillator amplification (double crystal oscillator)

The first option is to use an output coupler with larger transmission to maintain the intracavity power level. With this method, we have obtained an average output power of 2 W from a Ti:sapphire mode-locked laser (Giga optics, 1 GHz repetition rate, ∼30 fs pulse duration). This method will eventually be limited by thermal effects in the crystal.

The second possibility is to utilize a chirped pulses in order to reduce the peak intensity within the crystal. This way, the non-linear response of the gain medium can be reduced even for increased average power. Passive mode-locking has been employed for a long time in the so-called soliton mode-locking regime [9]: Slightly negative or close to zero intra-cavity

[2] i.e. without applying the chirped pulsed oscillator (CPO) method

group delay dispersion (GDD) is balanced by self-phase modulation inside the crystal (and air). A nearly Fourier limited pulse develops and can be sustained. In the negative GDD regime, the pulse duration is insensitive to the amount of intracavity GDD[3]. On the other hand, it is found that mode-locking also works in a cavity with strong positive GDD [139,140]. Contrary to mode-locking in the soliton regime, the resulting pulse is far from the Fourier limit and strongly chirped [94, 141]. It was expected and experimentally demonstrated that a chirped pulse oscillator can supply more than 2 W of average output power [93, 142]. In this demonstration, a pulse energy of 0.5 μJ is reported at a repetition rate of 2 MHz. The disadvantage is the requirement for an extra pulse compression stage outside the cavity, that somewhat reduces the available power of the compressed pulses. However, a chirped mirror pulse compressor with a transmission as high as 98 % has been reported recently [143].

The third possibility is to introduce a second gain medium into the laser cavity for additional amplification. The idea is to amplify the circulating beam just before the outcoupling mirror while maintaining a lower average power at the oscillator crystal that ensures mode-locking. In essence, the transmission of the outcoupler is increased to release the additional power gained from the second (amplifier) crystal. Here "oscillator crystal" stands for the originally installed crystal that provides enough self phase modulation for mode-locking. The extra crystal we denote as "amplifier crystal". The schematic of the set up is shown in Fig. 4.1.

In the case of a conventional laser with a single crystal, the circulating power after the output coupler (P_1) is given by $P(1-T_1)$. T_1 stands for the power transmittance of the output coupler[4]. The power before the output coupler is denoted as P. After installing the second crystal, the circulating power after the output coupler (P_2) is given by $PG(1-T_2)$, where G stands for gain of the amplifier crystal. T_2 stands for the transmission of new output coupler used in the double crystal oscillator. If T_2 is chosen such that $P_1 = P_2$, then the double crystal oscillator can be operated as the single crystal oscillator, i.e. with the same conditions *at the oscillator crystal*. As mentioned previously, this is important for stable oscillator operation.

$$P_1 = P_2 \tag{4.1}$$

$$\leftrightarrow \qquad T_2 = 1 - \frac{(1-T_1)}{G}. \tag{4.2}$$

The output power from the laser P_{out} is given by:

$$P_{\text{out}} = PGT_2 = PT_1 + P(G-1). \tag{4.3}$$

The second term of the last equation expresses the extra power that would be available with this method. The high intra-cavity laser power is used as seed for the amplifier crystal. Thus, amplification in the saturated regime can be obtained without too tight focusing, which prevents additional and unwanted self phase modulation inside the amplifier crystal. Of experimental concern are thermal effects inside the amplifier crystal due to strong pumping. Thermal lensing has to be small enough in order not to disturb the spatial mode of the cavity. When the pump power is significant, i.e. likely more than tens of Watts (see Sec. 4.2.8), active or even cryogenic cooling might be necessary. The double crystal oscillator method is currently under experimental investigations in our group.

[3]This is true compared with the positive GDD regime. For few-cycle ultra-short pulse generation, careful dispersion management is mandatory.

[4]A loss-less output coupler is assumed.

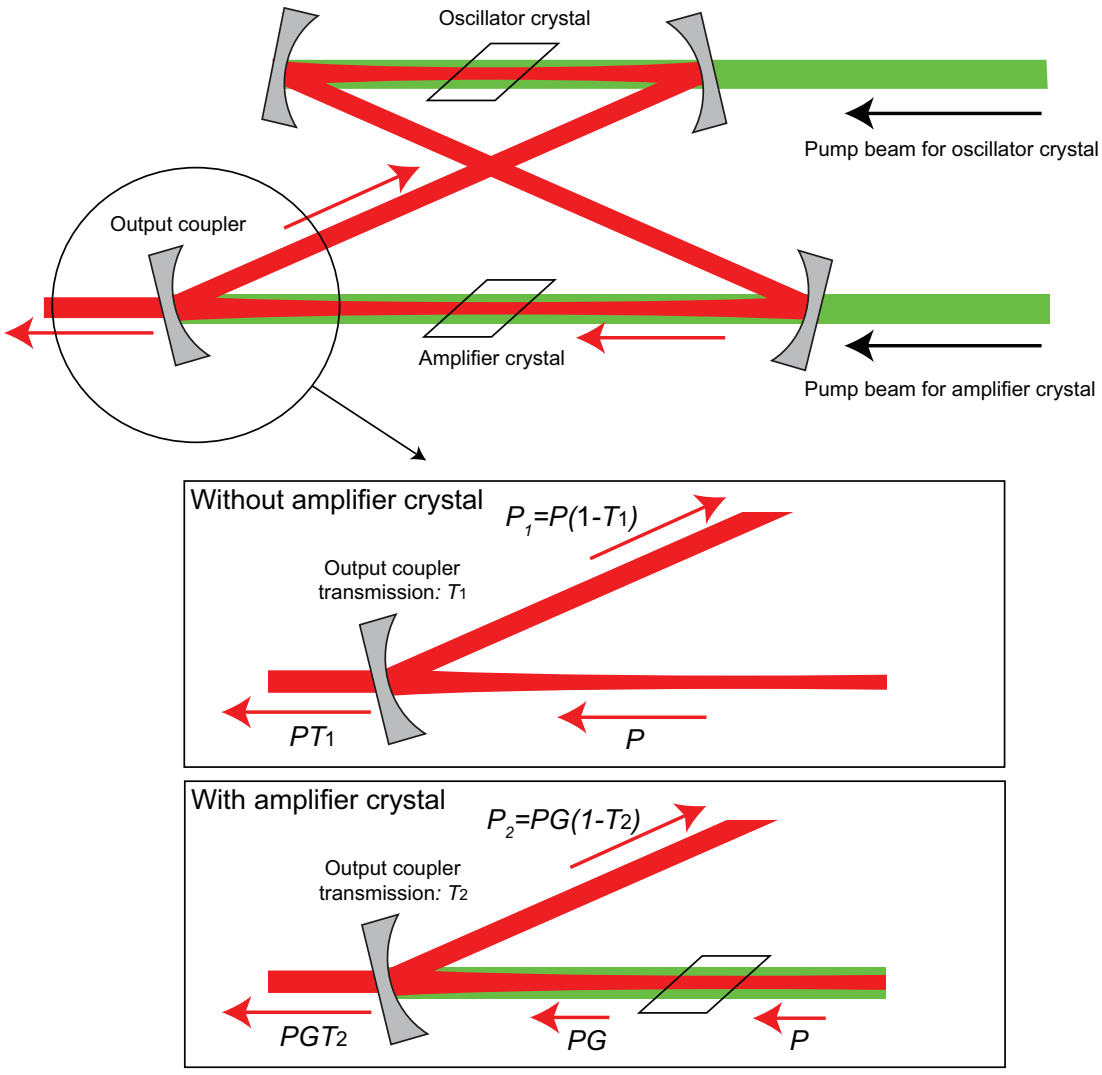

Figure 4.1: *Schematic of the double crystal oscillator. The circulating power at various positions inside the cavity are shown.*

4.1.2 High repetition rate amplifier

In the previous section, recent progress towards high output power oscillators has been discussed. The other strategy to obtain a high average power pulsed beam is to apply external amplification to the oscillator output. With cavity enhanced HHG, the amplifier can be installed in between the oscillator and the enhancement cavity.

The development and investigation of pulse amplifiers is important for laser physics and non-linear optics [144]. For a long time large pulse energies at the mJ to J level could be obtained only by reducing the repetition rate accordingly. In this case the essentially unaffected average power of the pulse train is concentrated in fewer pulses per unit of time. This approach does not work for cavity enhanced HHG. In this case amplification at the full repetition rate of the oscillator, i.e. increased average power is required. In the following, two examples of high repetition rate amplifiers will be discussed.

High repetition rate amplifiers

- Amplification in an external cavity
- Amplification with single or multi-pass configuration

In the first case the amplification is done inside the external cavity. In this method, the amplification crystal is installed at the focus. When the transmittance of the output coupler of that cavity is appropriately chosen, most of the amplified power can be extracted. This method has been proposed and demonstrated by Paul et al. [145]. In this demonstration, 7 W of average power are obtained with 68 fs pulses at a repetition rate of 95 MHz. The amplification cavity can be considered as a second laser which is injection-locked by the seed oscillator. However, the second cavity does not perform mode-locking itself. Thus, the intracavity dispersion of the amplification cavity has to be pre-compensated to support broadband amplification[5]. In addition, the cavity length of the second cavity has to be actively stabilized in order to match the frequency modes of two cavities, which introduces additional experimental complexity.

In this work we use amplification of a high repetition rate pulse train with a single or multi pass amplifier. Single- or double-pass Ti:sapphire amplifiers have been demonstrated before [146–148]. More than 5.5 W of average power has been obtained with 100 fs pulses at 82 MHz [146]. Simple single pass or multi pass amplifiers have several advantages and would be excellent candidates for applications in cavity enhanced HHG. They operate at virtually any repetition rate if the amplifier is pumped with a CW source. In addition, due to the low pulse energy at high repetition rates, a pulse stretcher and compressor is not required like for chirped pulse amplification schemes. Such a setup comes with a moderate experimental effort, which is especially important in combination with an additional enhancement cavity for intra-cavity HHG. Also, the method can be applied to very short. i.e. few-cycle pulses.

The last issue is particularly interesting for applications that aim at investigating non-linear phenomena at the oscillators repetition rate. With ultra-short pulse oscillators optimized for high peak power, together with a special achromatic microscope objective, a peak intensity as high as $5\times10^{13}\,\mathrm{W/cm^2}$ has been generated [149]. Utilizing a single pass amplifier

[5]The injection locking may relax the requirement on the precision of the dispersion compensation.

together with an ultra short-pulse laser rises the hope to explore highly nonlinear phenomena at the full oscillator repetition rate.

For these applications, we have developed a single pass high repetition rate amplifier that works for pulses as short as ∼7 fs [150]. This amplifier has also been tested with rather long pulses (∼ 200 fs) for applications in cavity enhanced HHG. In previous demonstrations [146–148] it was not shown that it is possible to amplify few-cycle pulses with this method, nor was the phase-stability of the amplifier investigated. In our demonstrations, the phase noise before and after the amplifier was compared. This measurement represents an upper limit of the phase noise that is added by the amplifier. In addition, the gain medium of our amplifier is cryogenically cooled. It has been demonstrated that with Ti:sapphire as gain medium cooling to liquid nitrogen (LN2) temperatures is highly advantageous [148, 151, 152]. This is due to the more than one order of magnitude larger heat conductivity and the smaller temperature dependence of the refractive index. This enables fast heat removal from the focus region and mitigates thermal lens effects.

4.2 Experiments and discussions

4.2.1 Cryogenic Amplifier: setup

Fig. 4.2 shows the experimetal setup. A Ti:sapphire crystal is mounted on a liquid nitrogen (LN2) cooled copper block, which is placed in a home-built plexiglass vacuum chamber (Fig. 4.3). The Ti:sapphire crystal is 2.6 mm long, Brewster cut, and highly doped ($\alpha \sim 7\,\mathrm{cm}^{-1}$ at 514 nm). Compensation of the astigmatism turned out to be very critical and needs careful alignment. This was done by first focusing into a dummy sapphire crystal whose input facet was Brewster cut and whose output facet was perpendicular to the beam propagation. The different refraction for the pump and seed beam leads to a less than 1° angle between the incident beams for optimum alignment. After careful alignment the amplifier crystal was put back in place. The vacuum chamber windows are 1 mm thick and carry a broad-band anti-reflective coating. They are mounted 16 mm away from the focal plane in order to prevent damage due to high laser intensity. The LN2 reservoir with a volume of 0.8 l is a home-built stainless steel dewar that sits on top of the crystal mount and serves as a lid for the vacuum vessel. The chamber is connected to a small turbo-molecular pump with 50 l/s pumping speed. The vacuum vessel with the crystal mount is attached to a 2-dimensional translation stage that is mounted on the optical table for precise alignment of the crystal position relative to the laser beams. The pump beam is generated by a low-noise frequency-doubled Nd:YVO_4 laser with up to 18.5 W of output power (Coherent Verdi-18). The first seed beam is generated in a double-chirped mirror dispersion controlled Kerr-lens mode-locked Ti:sapphire oscillator (Nanolayers Venteon, high power version) that is pumped with 6.3 W from another frequency-doubled Nd:YVO_4 laser.

The pump and seed beams are aligned to overlap in the crystal with the help of a dichroic mirror that also serves as focusing mirror for the seed beam ($f = 37.5$ mm). The pump beam is focused with an achromatic doublet with $f = 100$ mm. The spot size ($1/e^2$ intensity radius) of pump and seed are measured to be 10.2 μm and 9.1 μm in the crystal. Too tight focusing of pump and seed reduces the interaction volume within the gain medium. On the other hand, for weaker focusing reduces the intensity and also limits amplification. Optimum focusing can be found by a numerical simulation of the amplification based on rate equations that include focusing. The infrared beam is re-collimated with another curved dichroic mirror, dispersion

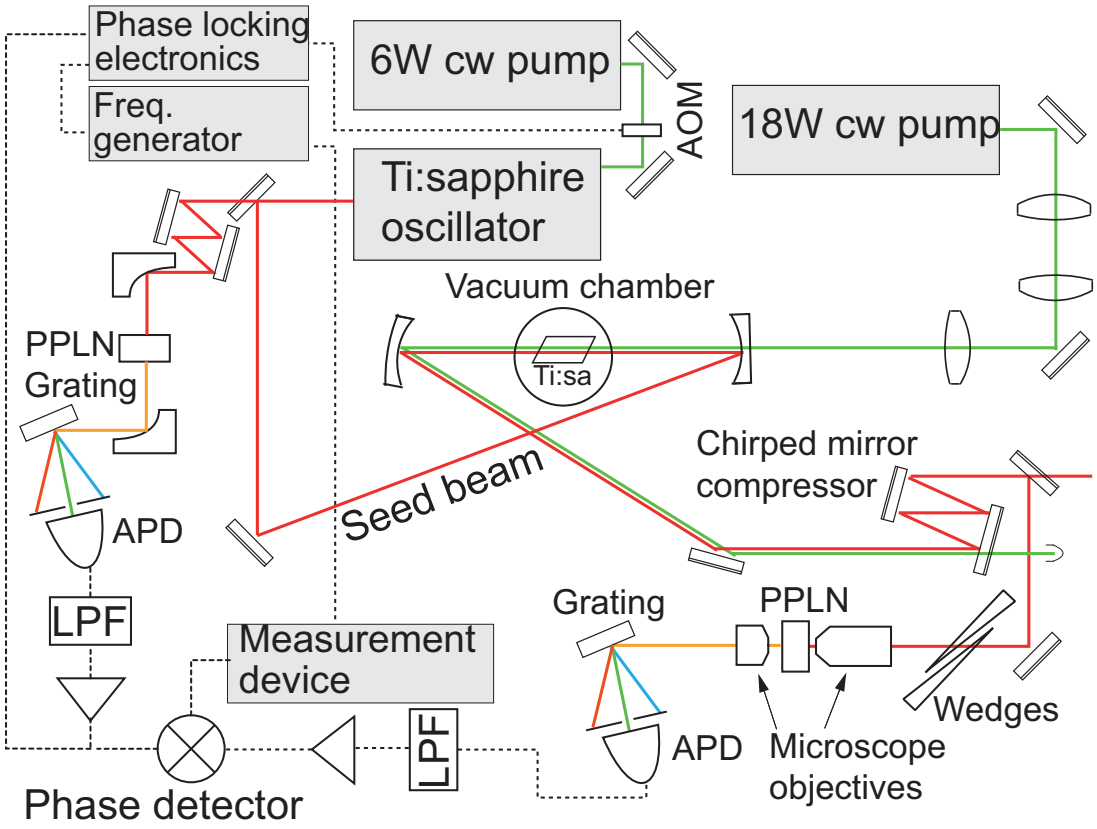

Figure 4.2: *Setup of the experiment. The liquid nitrogen cooled Ti:sapphire crystal is mounted in a small vacuum chamber (an schematic is shown in Fig. 4.3). The 18 W pump beam (green) traverses a telescope that enables adjustment of the pump beam focal spot size. The seed beam (red) is overlapped with the pump beam with a dichroic focusing mirror with the angle of incidence chosen for astigmatic compensation of the crystal's Brewster cut and a re-collimating focusing mirror. LPF: Low pass filter, APD: Avalanche photo diode, AOM: Acousto-optic modulator.*

is compensated with several bounces off chirped mirror pairs, and the amplified beam is sent to a dispersion balanced interferometric autocorrelator, a spectrometer and/or a power meter.

4.2.2 Cryogenic Amplifier: Amplification results

Fig. 4.4 displays the output power of the amplifier after filtering out the remaining pump light. It can be seen that the output power increases monotonically with pump power and reaches up to 1.1 W, which is a gain of 2.1. After careful optimization of the amplification by aligning pump and seed beam, the amplifier runs stably over more than 20 hours without any adjustments. At full pump power the temperature of the crystal mount raises to 96 K.

In a typical operating regime the crystal is far from saturation near the input facet and strongly saturated at the output. The exponential increase of power as a function of propagation length in the unsaturated region is determining the output power. Thus we also expect exponential grow of output power as a function of pump power. The observed conversion efficiency, defined by the ratio of transferred power from the pump to the amplified beam versus total pump power, is 3.1 %. Because gain does decrease with saturation and a well

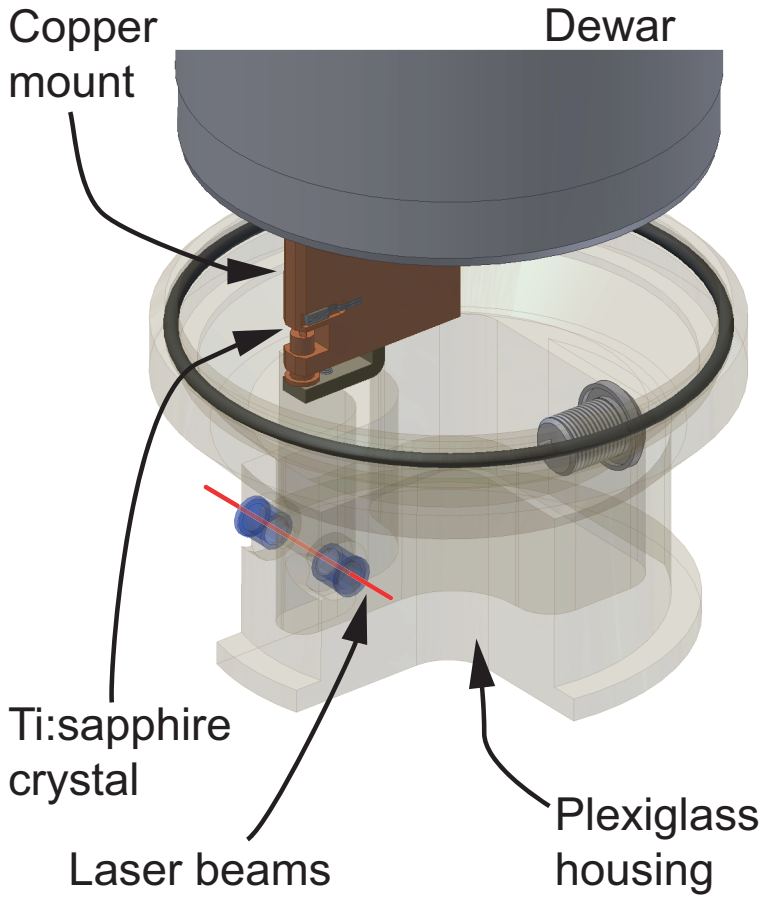

Figure 4.3: *Schematic of the crystal mount.*

optimized amplifier should be strongly saturated we characterize our amplifier in terms of conversion efficiency, i.e. the power that is converted from the pump to the amplified beam. Conversion efficiency increases with seed power while the gain decreases. Numerically we can show that 50 % of the maximum conversion efficiency of about 22 % ($\sim$ 4 W output power at 18.5 W pump power) can be extracted at a seed power of about 2 W. This means that a significant seed power is required for saturation but also that strong laser beams can still be amplified efficiently.

4.2.3 Cryogenic Amplifier: Spectrum and pulse duration

Fig. 4.5 and Fig. 4.6 show the autocorrelation and spectra of the laser before and after the amplifier. The beam is more efficiently amplified at the center of the spectrum compared to both spectral wings. Dividing the curves yields the spectrally dependent gain, as shown in Fig. 4.7. Cooling reduces the optical gain due to a reduction of the occupancy of thermally excited vibrational states. From the initial autocorrelation trace we infer that the laser pulses are less than 6.1 fs long assuming a Gaussian pulse shape; after amplification the pulse duration can be compressed to less than 6.5 fs. The Fourier-limited pulse durations inferred from the spectra are 5.8 fs and 6.3 fs for un-amplified and amplified pulses, respectively. The

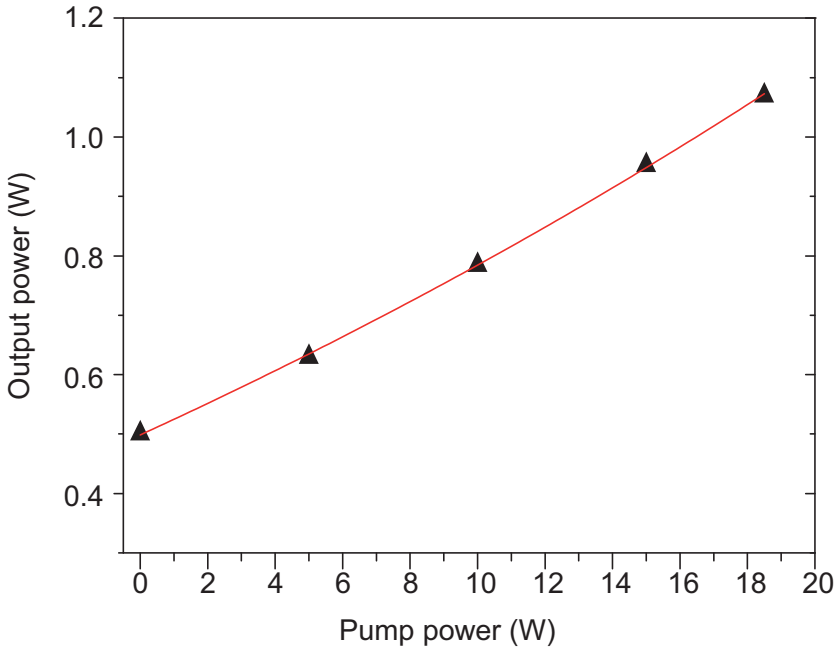

Figure 4.4: *Output power of the amplifier as a function of pump power. Sub-7 fs seed pulses are used for the measurement with a liquid nitrogen cooled crystal. The seed power is given by the output power at 0 W pump power (500 mW). The solid line is an exponential fit to the data.*

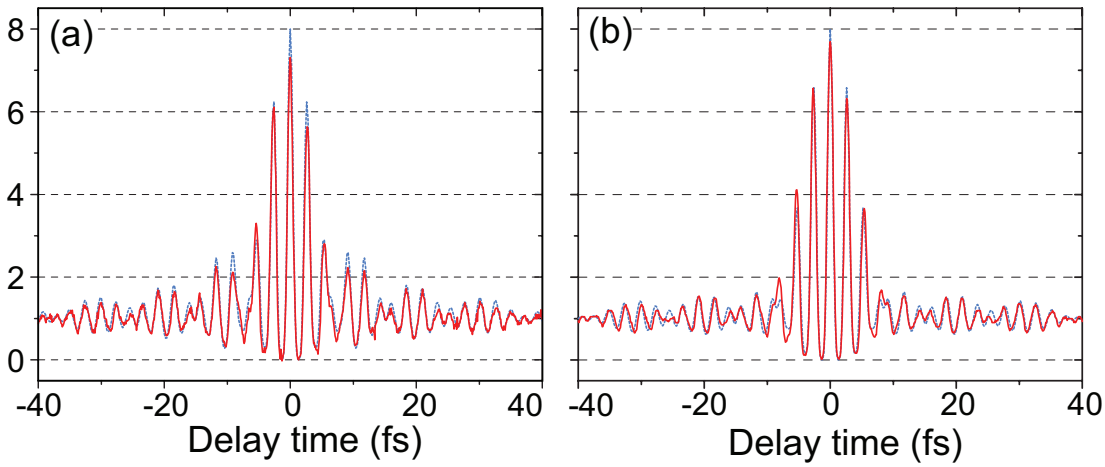

Figure 4.5: *Autocorrelation traces of the ∼ 6 fs laser pulses before (a) and after (b) amplification with 18.5 W of pump power. The full red line shows the measured data, the blue line shows is the Fourier transformation of the measured spectrum which corresponds to the pulse shape in case of a flat spectral phase. We have checked that no satellite pulses are visible in the autocorrelation traces out to ∼ ±100 fs.*

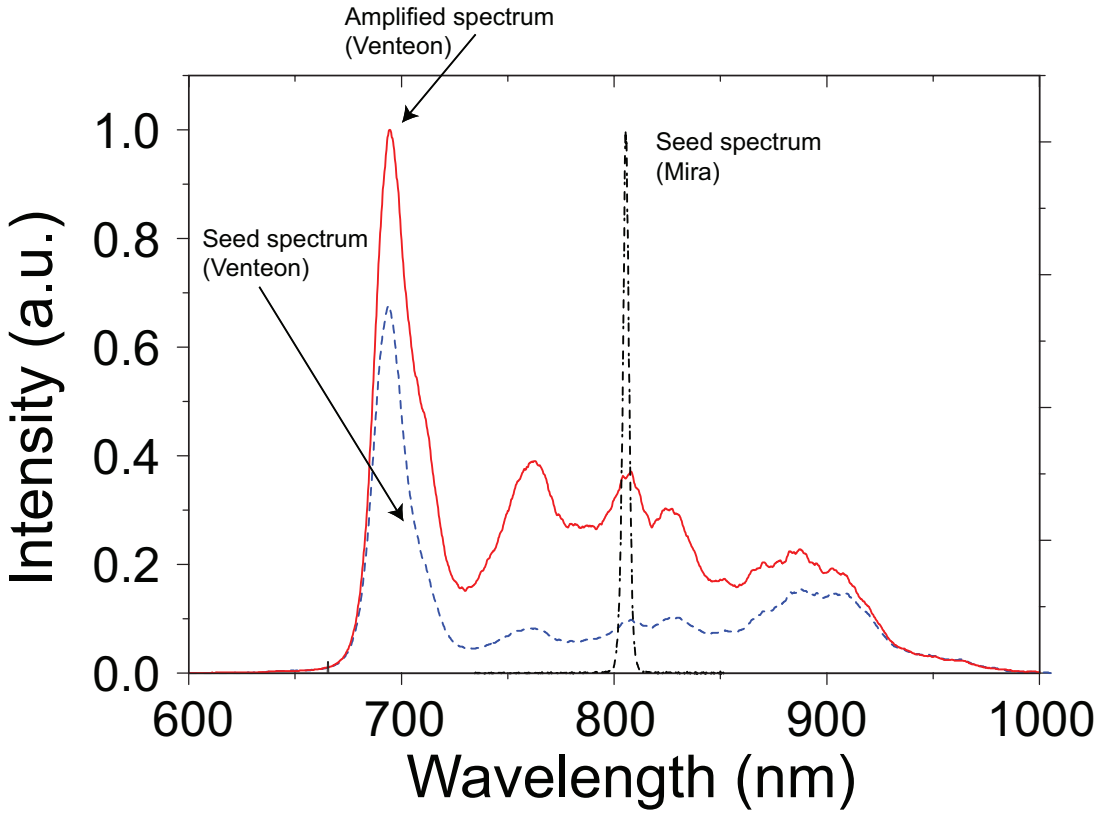

Figure 4.6: *Spectrum of the sub-7 fs laser pulses (Nanolayers Venteon) before and after amplification with a pump power of 18.5 W. In addition the spectrum of 200 fs pulses (Coherent Mira), that have also been used for seeding, is shown (see Sec. 4.2.6).*

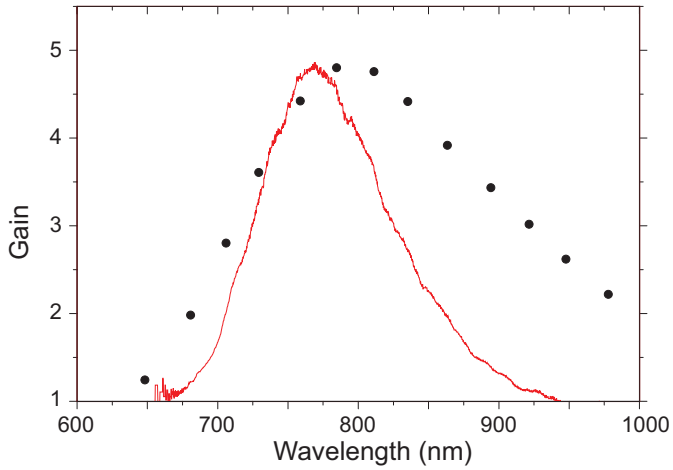

Figure 4.7: *Spectral gain of our cryogenic amplifier determined as the ratio of the amplified and seed spectra (red). The Ti:sapphire gain curve at room temperature published in Ref. [153] is shown for comparison (dots).*

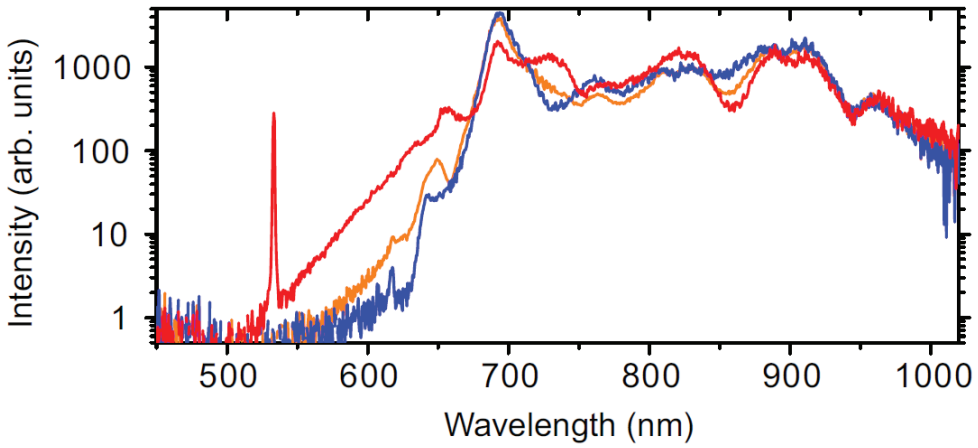

Figure 4.8: *White light generation. The blue curve shows the laser spectrum with the KGW crystal out of focus, the orange one with the crystal in focus and the red one with the crystal in focus and amplification. The broadening is significantly more pronounced with amplified pulses. The peak at 532 nm stems from scattered pump light.*

amplified spectral intensity is more evenly distributed and less structured. This is reflected in the reduced side-lobe structure of the amplified autocorrelation trace.

4.2.4 Cryogenic Amplifier: White light generation in a bulk crystal

To study the possibility of observing highly non-linear processes at high repetition rates, i.e. at the full oscillator repetition rate, we focus the amplified beam tightly. An achromatic triplet objective with $f = 5.8\,\mathrm{mm}$ (CDHC, China) is used for that purpose after pre-compensating the positive chirp introduced by the objective. The pulse duration at the focus is confirmed to be less than 6.5 fs by measuring the autocorrelation trace with a $10\,\mu\mathrm{m}$ thick second-harmonic crystal (BBO) placed at the focus. The focal radius is measured to be $3.4\,\mu\mathrm{m}$ by imaging with an achromatic microscope objective. With this setup the peak intensity at the focus, averaged over optical cycles, is estimated to be $1.0 \times 10^{13}\,\mathrm{W/cm^2}$. By placing a 4 mm thick bulk Potassium Gadolinium Tungstate ($KGd[WO_4]_2$ or KGW) crystal into the focus [154] we observe white light generation including self-trapping, which we infer from the more divergent beam profile (Fig. 4.8). This confirms the high peak power. As opposed to self-phase modulation white light generation scales with power [155] whereas the former scales with intensity.

4.2.5 Cryogenic Amplifier: Phase noise of the carrier-envelope offset frequency after amplification

The carrier-envelope phase (CEP) stability of few-cycle laser pulses is an important issue especially in non-linear processes governed by the optical electric field shape. To investigate possible effects of the amplifier on the CEP stability, two carrier envelope offset frequency detectors have been installed to measure possible additional CEP noise contributions from the amplifier (Fig. 4.2). About 60 % of the Ti:sapphire oscillator output power is picked up from the main beam, pre-chirp compensated by a pair of chirped mirrors and sent into a highly

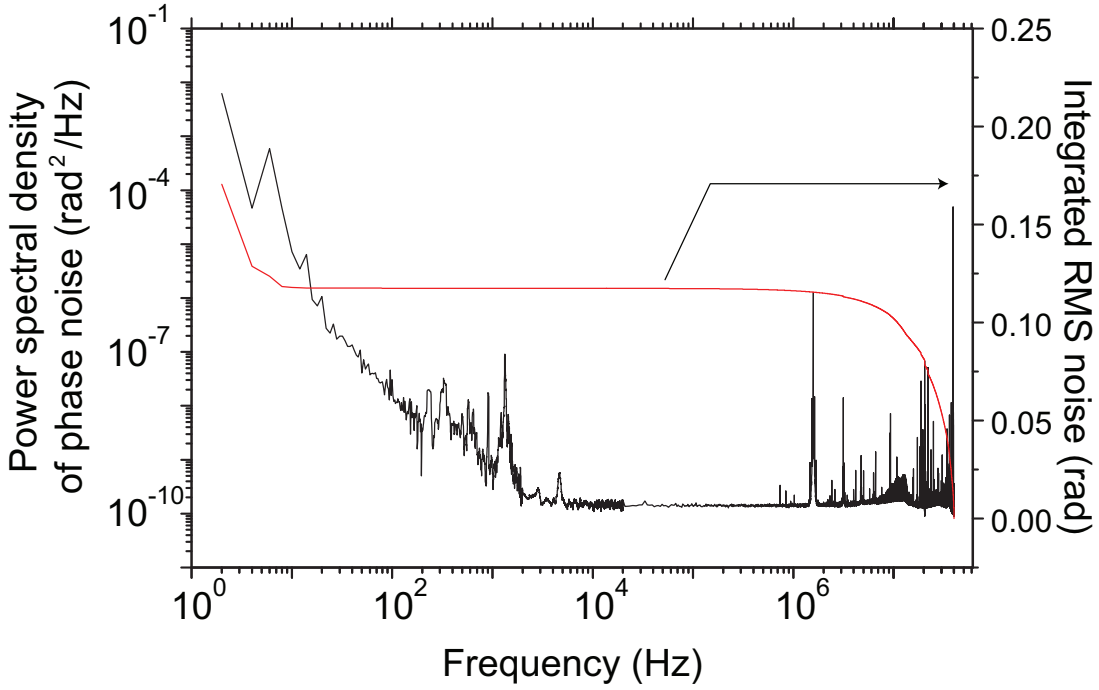

Figure 4.9: *Phase noise power spectral density of the carrier-envelope offset frequency added by the amplifier. The peaks at frequencies above 10 kHz are RF pickups, except for the peaks at 1.58 MHz and 39.2 MHz, which originate from detection artifacts. We have checked that these artifacts originate from RF beatings of the repetition rate frequency and the carrier-envelope offset frequency signals by deliberately changing the carrier-envelope offset frequency and observing a concomitant change of the artifacts. They are presumably generated in the rf-mixer or the photodiodes. We have excluded these two peaks in the integrated phase noise (red curve).*

nonlinear periodically-poled magnesium-oxide-doped lithium niobate (PP-MgO:LN) crystal with a 13.86 μm poling period for CEP locking of the laser [19]. After spectral broadening and frequency doubling in the PP-MgO:LN crystal, the green part of the spectrum is detected with a Si avalanche photodiode (Hamamatsu S5343). This way, we routinely obtain a carrier-envelope beat note with more than 45 dB of signal to noise ratio in a 300 kHz resolution bandwidth. After amplification, we focus the beam with an achromatic triplet lens into another PP-MgO:LN crystal with a 11.21 μm poling period. Dispersion is pre-compensated with chirped mirrors, and 90 mW of laser power suffices to generate a 40 dB S/N signal with a resolution bandwidth of 300 kHz. We mix a part of the output of the in-loop carrier-envelope offset frequency, locked to 20.4 MHz, with the output of the out-of-loop signal, record a 0.5 s long real time trace of this signal with 200 MS/s on a digital oscilloscope (LeCroy WavePro 735Zi) and perform an efficient FFT analysis [128] to obtain the two-sided phase noise spectral density as shown in Fig. 4.9. For the root-mean-square (RMS) phase noise we obtain 171 mrad, integrated from 40 MHz to 2 Hz. This corresponds to 68 as of RMS timing jitter of the CEP. It shows detectable phase noise at frequencies lower than 1 kHz, which can be assigned to mechanical vibrations of the amplifier setup. Above 10 kHz the noise contribution from the amplifier is very small and below the noise floor of our detection system. The integrated RMS noise described above includs this noise floor and thus gives an upper limit of the amplifiers contribution to the carrier-envelop phase noise.

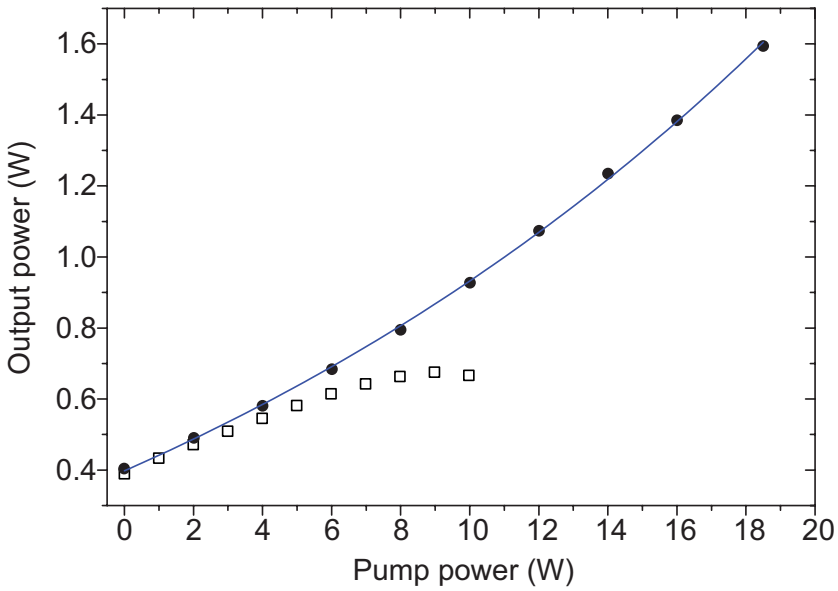

Figure 4.10: *Output power of the amplifier as function of pump power. Seed pulses of ∼200 fs are utilized for this measurement with a liquid nitrogen cooled crystal. The seed power is given by the output power at 0 W pump power (400 mW). The solid line is an exponential fit to the data. The squares show the output power obtained with 200 fs pulses but without cooling the crystal. It can be seen that the output power starts to decrease at ∼9 W of pump power, due to thermal effects. It shows that a liquid nitrogen cryostat is indeed necessary to make full use of the 18.5 W of pump power.*

4.2.6 Cryogenic Amplifier: Amplification of 200 fs pulses

Extremely short pulses require extremely precise intra-cavity dispersion compensation to obtain broadband enhancement. On the other hand, shorter pulse are advantageous due to their high peak intensity. In previous demonstrations of cavity enhanced HHG, a pulse duration in between ∼30 fs and ∼200 fs has been utilized in order to obtain a high peak intensity, without introducing too much trouble in dispersion management. In view of applications of cavity enhanced HHG, we have also amplified the output of a 75 MHz repetition rate ∼200 fs Ti:sapphire oscillator running at 805 nm center wavelength (Coherent Mira) with the same setup as shown in Fig. 4.2. The output power is measured as a function of pump power and shown in Fig. 4.10. With 18.5 W of pump power and 400 mW of input power (5.3 nJ) we obtain 1.6 W of output power (21.3 nJ), i.e. a single-pass gain of 4.0 and a power conversion efficiency of 6.5 %. The gain is higher in this case because of the better spectral overlap with the gain profile of Ti:sapphire as compared to the few-cycle laser case. To the best of our knowledge this is the most efficient cryogenic single-pass amplification demonstrated so far.

Fig. 4.11 shows the output power as function of seed power. From the almost linear dependence we infer that the amplification is mainly in the small signal gain regime. Also, we infer from Fig. 4.7 that the single-pass gain should reach a factor of 5 with a laser running at 780 nm.

4.2.7 Peltier cooled amplifier

The cryogenic cooling method described above requires the crystal to be mounted inside a vacuum chamber for thermal insulation. This in turn necessitates extra windows in the laser

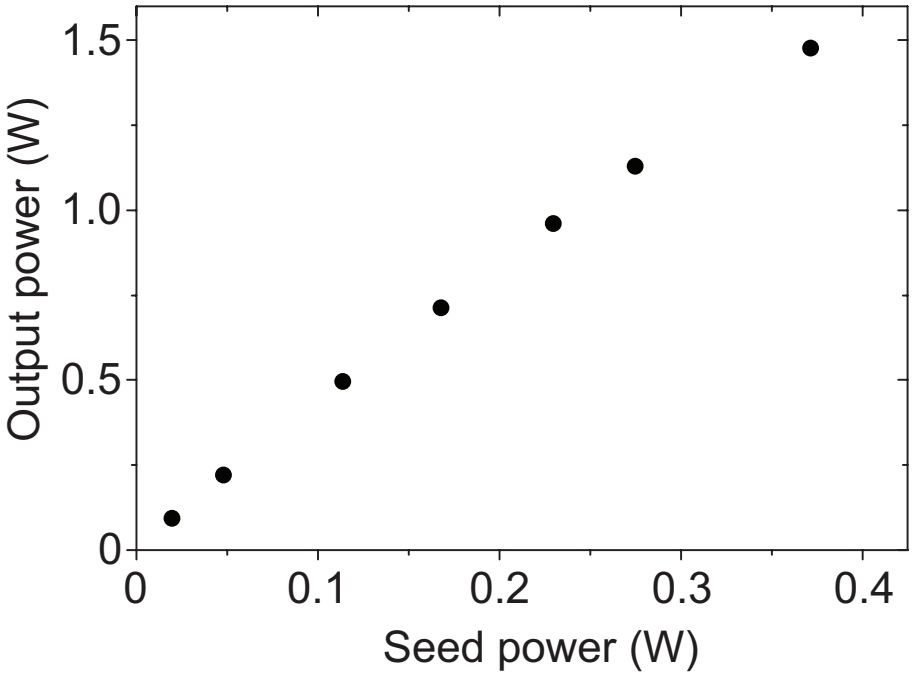

Figure 4.11: *Output power of the amplifier as function of seed power. Seed pulses of ∼200 fs are utilized for this measurement with a liquid nitrogen cooled crystal. The pump power was 18.5 W. From the almost linear dependence it can be seen that the amplifier is working in the small signal gain regime where the effect of saturation is very small.*

beams, which lead to extra dispersion and need to be compensated for if few-cycle laser pulses need to be amplified. Also, boiling LN2 can lead to vibrations of the setup and refills are required every one to two hours. Therefore, we also investigated the possibility of using a double-stack Peltier element for cooling [156]. Fig. 4.12 illustrates the crystal holder with a double-stack Peltier element for cooling.

A highly doped ($\alpha \sim 7\,\mathrm{cm}^{-1}$) 3 mm long, Brewster cut Ti:sapphire crystal is mounted in a copper block with a thin Indium foil to increase thermal conductivity. The copper block is attached to a double stack Peltier element with heat-conductive glue. The Peltier element's specifications are: maximum current of 5.8 A, maximum cooling power of 34 W, maximum temperature difference of 84 K. As usual for Peltier elements, the temperature difference attainable decreases linearly with heat flow until it reaches 0 K for the maximum heat transfer possible. The Peltier element's bottom side in turn was cooled with a water-ethylene glycol mixture to -5 °C. This way, the crystal mount temperature was measured to ∼ -38 °C and ∼ -17 °C for 5 W and 18 W of pump power, respectively. The Peltier current was regulated by means of an electronic feedback circuit using the measured crystal mount temperature. The amplifier crystal is seeded with the Ti:sapphire oscillator with 200 fs pulse duration described in Sec. 4.2.6

The spot sizes ($1/e^2$ intensity radius) inside the crystal have been measured to 11.8 μm for the pump and 11.0 μmm for the seed.

Fig. 4.13 shows the output power as function of pump power. The output power at 0 W corresponds to the seed power, which is 410 mW. It increases almost linearly up to a pump power of ∼ 14 W and an output power of almost 1.1 W with a maximum gain of 2.6. For higher

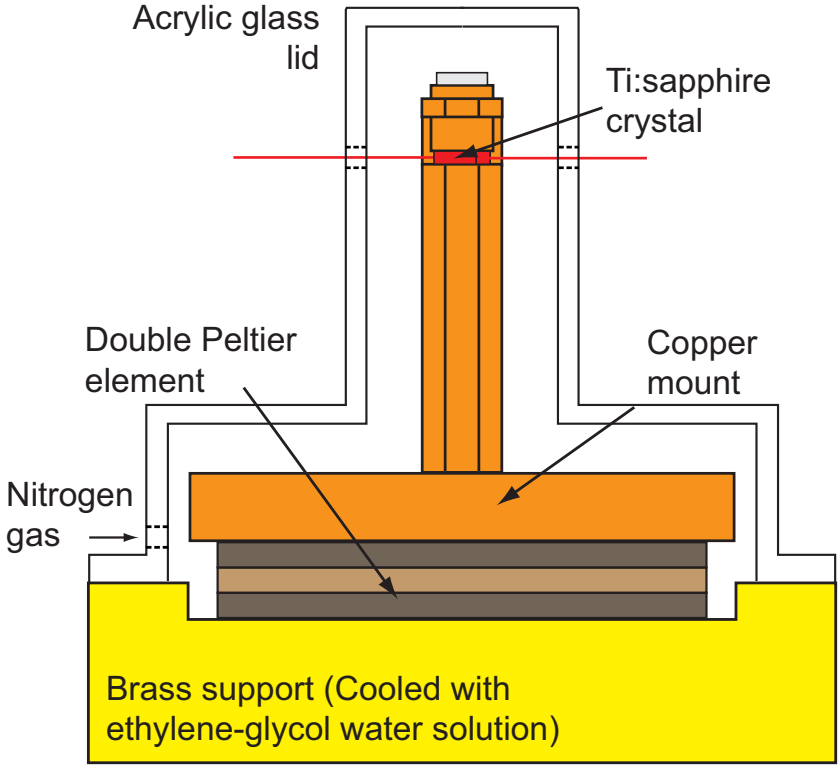

Figure 4.12: *Crystal cooling setup with a Peltier element. The crystal is mounted in a copper mount which is cooled by a double-stack Peltier element. The other side of the Peltier element is cooled by water-ethylene glycol mixture to -5 °C. The crystal mount is covered by a Plexiglas housing, which is flooded with dry nitrogen to prevent water condensation. The laser beams (pump and seed beams) are fed in through 6 mm diameter holes.*

pump power levels the output power drops steeply because thermal lens effects deteriorate the beam profiles (see Fig. 4.14 and Fig. 4.15), reducing the spatial beam overlap.

4.2.8 Beam profiles

The spatial profiles of the amplified and the pump beam after the crystal are shown in Fig. 4.14 and Fig. 4.15, respectively. It can be seen that LN2 cooling is necessary to maintain good beam quality to make use of the full 18.5 W of pump power. When the amplifier is operated without cooling (crystal mount temperature at ∼314 K) the output power starts to decrease with increasing pump power at 9 W of pump power (see Fig. 4.10). This is because the spatial overlap between the pump and seed beam is reduced due to thermal lensing. When the crystal was cooled with a double-stacked Peltier element (∼260 K at crystal mount), strong distortions are somewhat reduced. However, monotonic increase of output power as function of pump power for up to 18.5 W as shown in Fig. 4.10, is only possible with LN2 cooling.

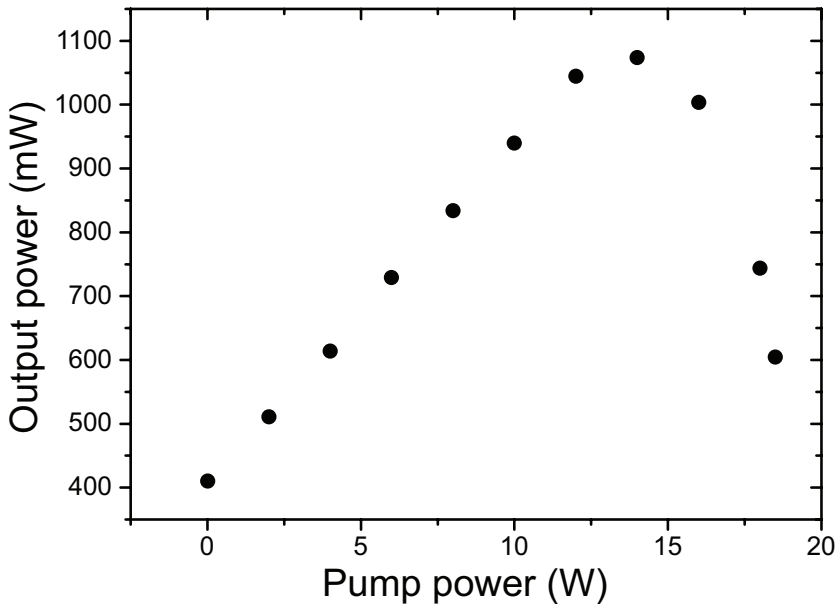

Figure 4.13: *Output power of the amplifier as function of pump power. Seed pulses of ∼200 fs duration are utilized for the measurement with the crystal cooled by a double-stack Peltier element. The seed power is given by the output power at 0 W pump power (410 mW). It can be seen that the output power starts to roll off at 14 W of pump power. This is due to deformation of pump and seed beams by thermal lensing.*

4.3 Conclusions

- Utilizing a high average power seeding laser is a promising option to scale the performance of the enhancement cavity.
- The following methods have been investigated in order to increase the average power of the seed laser.
  - High power mode-locked oscillator
    - High transmission output coupler with high power pumping
    - Chirped pulse oscillator
    - Intra-oscillator amplification (double crystal oscillator)
  - High repetition rate amplifier
    - Amplification with external active cavity
    - Amplification with single or multi-pass configuration
- A cryogenic single pass amplifier was developed and a power gain of 4 was demonstrated with 200 fs pulses at a repetition rate of 80 MHz.
- The amplification of sub-7 fs pulses was demonstrated to yield an average power in excess of 1 W. Utilizing a single pass amplifiers together with ultra-short pulsed-lasers may enable to investigate highly nonlinear processes at the full oscillator repetition rate.

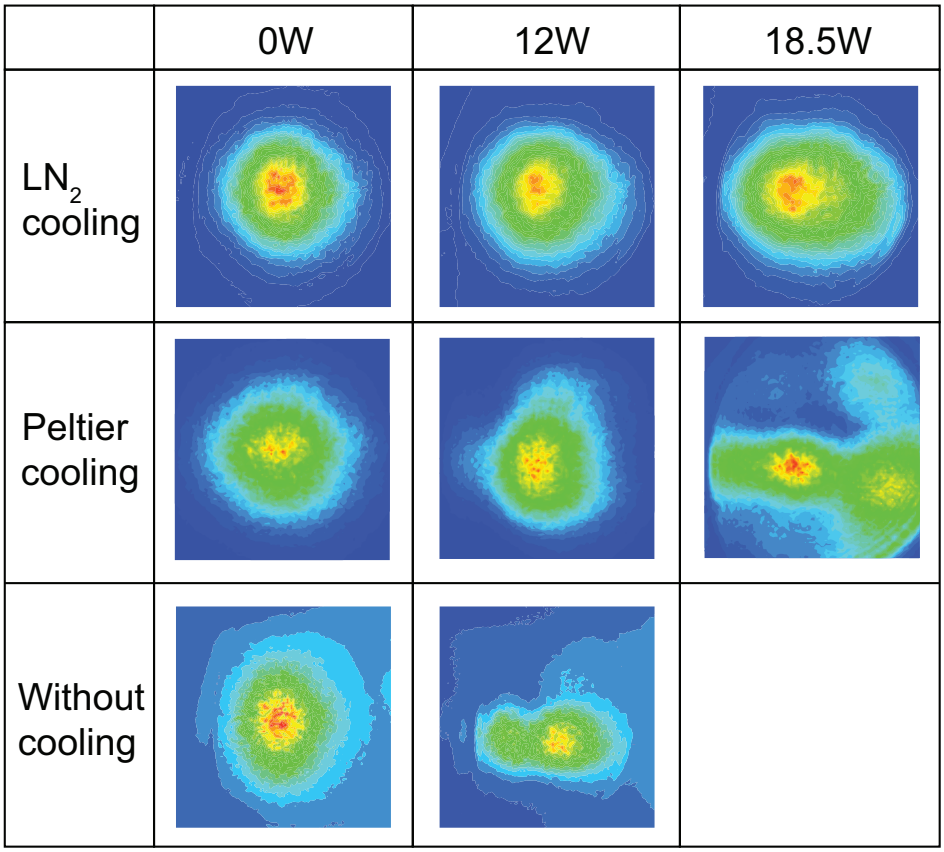

Figure 4.14: *Beam profiles of the amplified infrared beam (200 fs pulses) at various pump power levels. The profiles are measured with three conditions: LN2 cooling, Peltier cooling and without cooling. The beam profile without cooling at full pump power is supposed to lead to even stronger distortion but was not measured to prevent damage to the crystal. Without cooling and a pump power exceeding 12 W the amplified beam can hardly be reshaped with conventional optics, as opposed to the almost perfect beam shape obtained with a cooled crystal.*

- The carrier-envelope RMS phase noise added by amplifier has been characterized and shown to be lower than 171 mrad, integrated from 40 MHz to 2 Hz.
- A model of the pulsed amplification has been developed taking into account the Gaussian beam profile for seed and pump beam as well as gain saturation.
- High repetition rate single pass amplifiers are simple devices and ideal for cavity enhanced HHG applications.

4.4 Future prospects

4.4.1 Multi pass amplifier

As can be seen from Fig. 4.11, the developed amplifier is operated far from gain saturation. For pulses which are not too short, a double-pass geometry can be realized with an optical

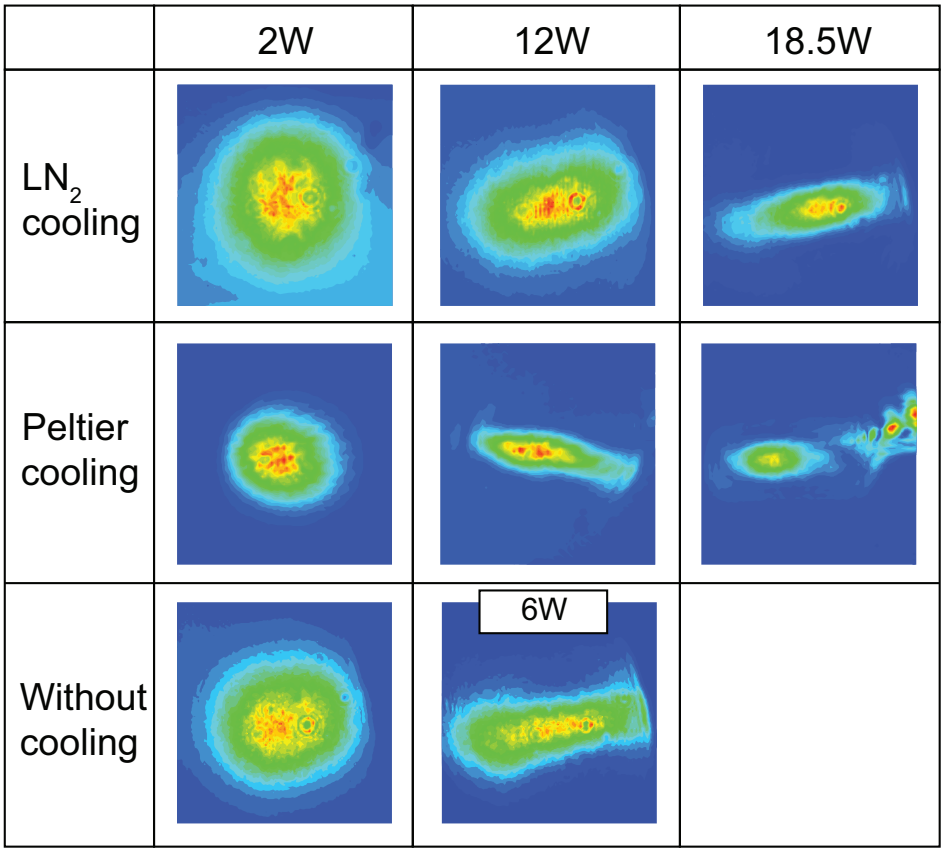

Figure 4.15: *Beam profiles of the pump beam at various pump power levels. The profiles are measured with three conditions: LN2 cooling, Peltier cooling and without cooling. Without cooling, the pump beam profile of 6 W of pump power is shown.*

isolator [147, 148]. This allows to further increase efficiency and full saturation[6]. For ultrashort pulses (for example, as short as sub-7 fs that are used in our demonstration), extra effort will be required to compensate additional dispersion associated with the multi-pass geometry.

4.4.2 High power oscillator combined with high repetition rate amplifier

With the amplification in an external active cavity demonstrated by Paul et al., 7 W of average power was obtained with 68 fs pulse duration and a repetition rate of 95 MHz [145]. A similar result can be expected from a double crystal oscillator scheme proposed in this work. Combining this high power oscillator with a single pass amplifier would significantly improve the efficiency of the amplifier. Here "efficiency" stands for the fraction of pump power that is transferred to the amplified beam. When the single pass amplifier is seeded with 4 W (which is realistic and a conservative value for the double crystal oscillator), the gain of 4 would give 16 W of output power[7]. This would be a factor of 30 more average output power as compared

[6]The mutli-pass geometry may require a special design for sufficient overlap between pump and seed beams.

[7]Saturation, even though desired might eventually be the limit so that larger pump power might be necessary.

with a typical femtosecond mode-locked laser.

4.4.3 Heat dissipation in the enhancement cavity

One of the biggest disadvantages of using a high power seed laser is the heat that is dissipated in the enhancement cavity. Basically, higher seed power result in stronger heating of the cavity. To investigate this in more detail the power budget for the enhancement cavity (without any intra-cavity material other than mirrors) is described as follows:

$$\begin{aligned}(\text{seed power}) &= (\text{power consumption for HHG process}) \\ &+ (\text{reflection from cavity}) \\ &+ (\text{transmission through cavity mirrors}) \\ &+ (\text{absorption and scattering loss by the cavity mirrors}).\end{aligned} \tag{4.4}$$

The first term (power consumed for HHG process) is negligible since the conversion efficiency of the HHG process is on the order of 10^{-4} and lower. The second term (power reflected from the cavity) is dependent on impedance matching, spatial mode-matching, frequency mode-matching, polarization matching, and intra-cavity dispersion compensation. Experimentally, in the demonstration of the 10 MHz enhancement cavity, a total coupling efficiency of more than 50 % could be obtained. This indicates that the rest ($\sim$ 50 %) of the power is taken by the last two terms of Eq. 4.4. The ratio between the contributions from these terms: (power transmitted from cavity mirrors) and (absorption and scattering loss at the mirrors) is determined by the properties of the mirrors. In general, power reflectance R, power transmission T, and power loss L of a mirror satisfy the following energy conservation equation:

$$1 = R + T + L. \tag{4.5}$$

Ideally the loss would be zero ($L = 0$), however, especially for high reflective mirrors ($R \sim 1$), the mirrors are typically loss dominated, i.e. $L \gg T$. In this case, the power loss by absorption or scattering by the cavity mirrors will be a lot larger than the transmitted power. The ratio between the absoprtion and scattering loss is again the properties of mirrors. When the absoption loss is dominant, a significant fraction of incident power will be converted into heat. Since the mirrors are installed in a vacuum environment with poor thermal contact, they may accumulate heat and the surface temperature may increase significantly. The heated mirror may require active cooling to avoid surface deformations and to prevent damage. In the above discussions, the loss from any intra-cavity elements other than the mirrors is neglected. If there are extra components, the heat dissipation there may require additional cooling.

4.4.4 Coupling to the cavity

The enhancement cavity works as a mode filter and only supports spatial eigenmodes. Thus, the coupling efficiency between the laser and the cavity critically depends on how clean the laser mode is. As described in Sec. 4.2.8, the beam profiles of the output from the amplifier are characterized by imaging with a CCD camera. Although the measured beam profiles

look reasonably clean, it should be tested whether the spatial mode is good enough to obtain sufficient mode matching with the enhancement cavity.

Chapter 5

Future Prospects

In this section, possible future extensions of XUV frequency comb generation and related fields will be briefly presented.

5.1 Ytterbium-based systems

Recent developments in laser oscillators and amplifier systems utilizing Ytterbium (Yb) ions as a gain medium enabled the generation of pulse trains with short pulse durations and high repetition rates at very high average power. Yb-based systems typically work in the $1030 \sim 1050\,\mathrm{nm}$ wavelength range. In Yb-doped fiber oscillators, mode-locking is achieved through the saturable-loss effect originating from the non-linear polarization rotation in the fiber. Mode-locking with pulse durations as short as 28 fs has been reported at a repetition rate of 80 MHz [157]. The highest repetition rate that a fiber oscillator can be operated at is limited by the minimum fiber length that is necessary to obtain sufficient gain and nonlinearity for mode-locking. Mode-locking at 200 MHz has been reported [1] [160]. Kerr-lens mode-locking has been demonstrated with an Yb-doped solid-state oscillator. Using a short cavity, mode-locking at a repetition rate of 1 GHz is possible [161]. The output from these mode-locked oscillators can be amplified by Yb-doped disk, bulk or fiber amplifiers. Average output power levels as high as 400 W have been demonstrated [162].

Using a high power Yb laser for cavity-enhanced HHG would be helpful to obtain even higher intracavity powers at high repetition rates [163]. In particular, fiber based oscillators are expected to have a better long-term stability compared with Ti:sapphire systems. In terms of HHG, the cut-off frequency is extended due to the longer driving wavelength of the Yb system. Thus, such a setup might be appropriate for applications that require high harmonic orders. The drawback of using an Yb-based system would be that due to the limited gain bandwidth of Yb, the obtainable pulse duration would be rather long compared with a Ti:sapphire system. The reduced peak intensity has to be compensated for with higher average power, which in turn may cause thermal problems in the enhancement cavity.

[1] Harmonic mode-locking supplies even higher repetition rates [158, 159]

5.2 Cavity-assisted high harmonic generation at shorter fundamental wavelengths

The high harmonic spectrum depends on the peak intensity and the wavelength of the driving beam. Based on the three step model of HHG, the maximum possible energy that an electron can gain from the optical field during acceleration stage decreases according to Eqn. (2.15) for a shorter driving wavelength. Mid-IR optical parametric amplifiers have been developed and used for "high-order high harmonic generation" exploiting the extended cut-off frequency [164, 165]. The time period between ionization and recombination decreases for a driving beam with a shorter wavelength. Therefore, the diffusion of the electron wavepacket between ionization and recombination is reduced. This effect manifests itself in an increased conversion efficiency for below-cut-off high harmonics. Thus, a shorter driving wavelength would be preferable for applications that require high power in a relatively low order of harmonics. This is indeed the case for He^+ 1s-2s spectroscopy, where one would use the 13 th and 17 th order of high harmonics of a Ti:sapphire and Yb-based system, respectively. Therefore, it appears promising to drive cavity-enhanced HHG with shorter wavelengths in order to obtain a high-power XUV frequency comb. However, shorter wavelengths bring about several difficulties for the enhancement cavities:

- Typical coating materials of dielectric mirrors (such as SiO_2 and Ta_2O_5) tend to absorb a higher fraction of light in shorter wavelength regions compared to the IR. When comparing the reflectance of commercially available highly reflective mirrors for different wavelengths, it is found that the reflectance starts to drop at around 400 nm. Thus, an enhancement cavity for a frequency-doubled Ti:sapphire laser will suffer from a low enhancement factor.

- It has been widely observed that the performance of highly reflective mirrors degrades when the mirror are used for high-power beams in the UV wavelength region [166]. This could be one of the limiting factors for the intracavity power when the cavity is driven with shorter wavelengths.

- The requirements on the precision of the locking of the cavity increase for shorter wavelengths. This is because the pulse train from the seeding laser has to be overlapped phase-coherently with the intracavity pulse. A more precise control over the delay and the pulse-to-pulse phase-shift will be required for shorter wavelengths. In the frequency domain, the mode number N of the frequency comb ($\omega_{\mathrm{comb}} = N\omega_{\mathrm{rep}} + \omega_{\mathrm{CEO}}$) becomes larger for shorter wavelengths. Thus, the sensitivity of the comb mode against repetition rate fluctuations increases, requiring a more precise control over the repetition rate.

- So far, there is no mode-locked laser that oscillates at very short wavelengths and can be conveniently operated. Therefore, nonlinear frequency conversion will be required to obtain a seeding beam at short wavelengths. Frequency conversion units, however, deteriorate the beam quality, the pulse duration and the average power.

Considering the above issues, a frequency-doubled Yb laser producing green light at ~520 nm appears to be a promising trade-off for cavity-enhanced, high-average-power XUV frequency comb generation at a relatively low harmonic order. This method is currently under experimental investigation in our laboratory by Birgitta Bernhardt.

5.3 Cavity-assisted high harmonic generation at extremely high repetition rates

Considering the application of XUV frequency comb spectroscopy to the 1s-2s transition in He^+, a repetition rate in the GHz range is preferable because of reasons discussed in Sec. 1.6. In addition, a higher repetition rate has the following advantages: First, it decreases the number of comb lines within a given laser bandwidth. The power contained in a single comb line is proportional to the repetition rate for fixed laser bandwidth and average power. Thus, when the repetition rate is high enough, an XUV frequency comb can be used for some of the applications where a narrow linewidth CW XUV laser is required, such as direct XUV frequency comb spectroscopy with a single comb line [32] or laser cooling in the XUV region [49]. Second, a higher intracavity power is required at higher repetition rates to keep the pulse energy high enough for (cavity-enhanced) HHG. However, as higher repetition rates require a shorter cavity length, an improvement in the enhancement factor can be expected by reducing the number of mirrors used in the cavity. Additionally, a smaller cavity is advantageous in terms of stability.

Combining a high-finesse enhancement cavity with an Yb-based high-power seed laser may yield sufficient intracavity power and pulse energy for XUV frequency comb generation at a repetition rate in the 1 GHz-region.

5.4 Other applications of femtosecond enhancement cavities

Here, I would like to summarize several experiments with femtosecond enhancement cavities in order to give insight into possible applications of those cavities in the future.

- *High-precision dispersion measurement*

  During the development of the 10 MHz enhancement cavity, the intracavity dispersion was measured in order to obtain a precise target dispersion with which chirped mirrors for dispersion compensation could be manufactured (the method is described in Sec. 2.4.5 and elsewhere [102]). This method can be used to precisely measure the dispersion of an optical component when the intracavity dispersion is measured with and without the component. A comparison of these two measurements allows a precise evaluation of the dispersion of the sample. The method also allows measuring the amplitude response and thus enables a simultaneous measurement of phase shift and absorption.

- *High-sensitivity spectroscopy*

  When the sample is installed inside a high-finesse cavity, the response of the cavity changes drastically depending on the loss and the phase shift introduced by the sample. The above mentioned GDD measurement makes use of this effect. Several methods have been proposed and demonstrated to use enhancement cavities to improve the sensitivity and to optimize the measurement time of (molecular) absorption spectroscopy [167,168].

- *Nonlinear processes other than HHG*

  Efficient second harmonic generation with a nonlinear crystal installed inside an enhancement cavity has been demonstrated [45,88,89]. One interesting recent experiment

is the efficient generation of entangled photons by spontaneous intracavity parametric down conversion [169].

Bibliography

[1] S. Cavalieri, R. Eramo, M. Materazzi, C. Corsi, and M. Bellini, *Ramsey-Type Spectroscopy with High-Order Harmonics*. Phys. Rev. Lett. **89**, 133002 (2002).

[2] M. Bellini, A. Bartoli, and T. W. Hänsch, *Two-photon Fourier spectroscopy with femtosecond light pulses*. Optics Lett. **22**, 540 (1997).

[3] S. Witte, R. T. Zinkstok, W. Ubachs, W. Hogervorst, and K. S. E. Eikema, *Deep-Ultraviolet Quantum Interference Metrology with Ultrashort Laser Pulses*. science **307**, 400 (2005).

[4] M. Piche and F. Salin, *Self-mode locking of solid-state lasers without apertures*. Optics Lett. **18**, 1041 (1993).

[5] D. Georgiev, J. Herrmann, and U. Stamm, *Cavity design for optimum nonlinear absorption in Kerr-lens mode-locked solid-state lasers*. Optics Comm. **92**, 368 (1992).

[6] V. P. Kalosha, M. Müller, J. Herrmann, and S. Gatz, *Spatiotemporal model of femtosecond pulse generation in Kerr-lens mode-locked solid-state lasers*. J. Opt. Soc. Am. B **15**, 535 (1998).

[7] T. Brabec, P. F. Curley, C. Spielmann, E. Wintner, and A. J. Schmidt, *Hard-aperture Kerr-lens mode locking*. J. Opt. Soc. Am. B **10**, 1029 (1993).

[8] H. Risken and K. Nummedal, *Self-Pulsing in Lasers*. J. Appl. Phys. **39**, 4662 (1968).

[9] C. Spielmann, P. F. Curley, T. Brabec, and F. Krausz, *Ultrabroadband Femtosecond Lasers*. IEEE J. Quantum Electron. **30**, 1100 (1994).

[10] T. Brabec, C. Spielmann, P. F. Curley, and F. Krausz, *Kerr lens mode locking*. Optics Lett. **17**, 1292 (1992).

[11] T. Fuji, A. Unterhuber, V. Yakovlev, G. Tempea, A. stingl, F. Krausz, and W. Drexler, *Generation of smooth, ultra-broadband spectra directly from a prism-less Ti:sapphire laser*. Appl. Phys. B **77**, 125 (2003).

[12] M. Y. Sander, J. Birge, A. Benedick, H. M. Crespo, and F. X. Kärtner, *Dynamics of dispersion managed octave-spanning titanium:sapphire lasers*. J. Opt. Soc. Am. B **26**, 743 (2009).

[13] V. Pervak, A. Tikhonravov, M. Trubetskov, S. Naumov, F. Krausz, and A. Apolonski, *1.5-octave chirped mirror for pulse compression down to sub-3 fs*. Appl. Phys. B **87**, 5 (2007).

[14] L. Xu, C. Spielmann, A. Poppe, T. Brabec, F. Krausz, and T. W. Hänsch, *Route to phase control of ultrashort light pulses.* Optics Lett. **21**, 2008 (1996).

[15] T. Udem, R. Holzwarth, and T. W. Hänsch, *Optical frequency metrology.* Nature **416**, 233 (2002).

[16] L. Song, C. Zhang, J. Wang, Y. Leng, and R. Li, *Accurate measurement of carrier-envelope phase drift for infrared femtosecond laser pulses.* Optics Express **16**, 21383 (2008).

[17] D. J. Jones, S. A. Diddams, J. K. Ranka, A. Stentz, R. S. Windeler, J. L. Hall, and S. T. Cundiff, *Carrier-Envelope Phase Control of Femtosecond Mode-Locked Lasers and Direct Optical Frequency Synthesis.* Science **288**, 635 (2000).

[18] O. D. Mücke, T. Tritschler, M. Wegener, U. Morgner, and F. X. Kärtner, *Signatures of Carrier-Wave Rabi Flopping in GaAs.* Phys. Rev. Lett. **87**, 057401 (2001).

[19] T. Fuji, J. Rauschenberger, C. Gohle, A. Apolonski, T. Udem, V. S. Yakovlev, G. Tempea, T. W. Hänsch, and F. Krausz, *Attosecond control of optical waveforms.* New J. Phys. **7**, 116 (2005).

[20] R. Holzwarth, T. Udem, T. Hänsch, J. Knight, W. Wadsworth, and P. Russell, *Optical Frequency Synthesizer for Precision Spectroscopy.* Phys. Rev. Lett. **85**, 2264 (2000).

[21] A. Poppe, R. Holzwarth, A. Apolonski, G. Tempea, C. Spielmann, T. Hänsch, and F. Krausz, *Few-cycle optical waveform synthesis.* Appl. Phys. B **72**, 373 (2001).

[22] F. Helbing, G. Steinmeyer, J. Stenger, H. Telle, and U. Keller, *Carrier-envelope-offset dynamics and stabilization of femtosecond pulses.* .

[23] A. Apolonski, A. Poppe, G. Tempea, C. Spielmann, T. Udem, R. Holzwarth, T. Hänsch, and F. Krausz, *Controlling the Phase Evolution of Few-Cycle Light Pulses.* Phys. Rev. Lett. **85**, 740 (2000).

[24] D. Walker, T. Udem, C. Gohle, B. Stein, and T. Hänsch, *Frequency dependence of the fixed point in a fluctuating frequency comb.* Appl. Phys. B **89**, 535 (2007).

[25] T. Udem, A. Huber, B. Gross, J. Reichert, M. Prevedelli, M. Weitz, and T. W. Hänsch, *Phase-Coherent Measurement of the Hydrogen 1S-2S Transition Frequency with an Optical Frequency Interval Divider Chain.* Phys. Rev. Lett. **79**, 2646 (1997).

[26] H. Schnatz, B. Lipphardt, J. Helmcke, F. Riehle, and G. Zinner, *First Phase-Coherent Frequency Measurement of Visible Radiation.* Phys. Rev. Lett. **76**, 18 (1996).

[27] T. Udem, J. Reichert, R. Holzwarth, and T. W. Hänsch, *Absolute Optical Frequency Measurement of the Cesium D1 Line with a Mode-Locked Laser.* Phys. Rev. Lett. **82**, 3568 (1999).

[28] R. Holzwarth, A. Nevsky, M. Zimmermann, T. Udem, T. Hänsch, J. V. Zanthier, H. Walther, J. Knight, W. Wadsworth, P. Russell, M. Skvortsov, and S. bagayev, *Absolute frequency measurement of iodine lines with a femtosecond optical synthesizer.* Appl. Phys. B **73**, 269 (2001).

[29] N. Kolachevsky, M. Fischer, S. Karshenboim, and T. Hänsch, *High-Precision Optical Measurement of the 2S Hyperfine Interval in Atomic Hydrogen*. Phys. Rev. Lett. **92**, 033003 (2004).

[30] M. Niering, R. Holzwarth, J. Reichert, P. Pokasov, T. Udem, M. Weitz, T. Hänsch, P. Lemonde, G. Santarelli, M. Abgrall, P. Laurent, C. Salomon, and A. Clairon, *Measurement of the Hydrogen 1S-2S Transition Frequency by Phase Coherent Comparison with a Microwave Cesium Fountain Clock*. Phys. Rev. Lett. **84**, 5496 (2000).

[31] N. Kolachevsky, A. Matveev, J. Alnis, C. G. Parthey, S. Karshenboim, and T. Hänsch, *Measurement of the 2S Hyperfine Interval in Atomic Hydrogen*. Phys. Rev. Lett. **102**, 213002 (2009).

[32] V. Gerginov, C. E. Tanner, S. A. Diddams, A. Bartels, and L. Hollberg, *High-resolution spectroscopy with a femtosecond laser frequency comb*. Optics Lett. **30**, 1734 (2005).

[33] R. Teets, J. Eckstein, and T. Hänsch, *Coherent Two-Photon Excitation by Multiple Light Pulses*. Phys. Rev. Lett. **38**, 760 (1977).

[34] D. Felinto and C. E. E. Lopez, *Theory for direct frequency-comb spectroscopy*. Phys. Rev. A **80**, 013419 (2009).

[35] P. Fendel, S. D. Bergeson, T. Udem, and T. W. Hänsch, *Two-photon frequency comb spectroscopy of the 6s-8s transition in cesium*. Optics Lett. **32**, 701 (2007).

[36] Y. F. Baklanov and V. P. Chebotayev, *Narrow Resonances of Two-Photon Absorption of Super-Narrow Pulses in a Gas*. Appl. Phys. **12**, 97 (1977).

[37] M. Snadden, A. Bell, E. Riis, and A. Ferguson, *Two-photon spectroscopy of laser-cooled Rb using a mode-locked laser*. Optics Comm. **125**, 70 (1996).

[38] M. Fischer, N. Kolachevsky, M. Zimmermann, R. Holzwarth, T. Udem, T.W.Hänsch, M. Abgrall, J. Grunert, I. Maksimovic, S. Bize, H. Marion, F. P. D. Santos, P. Lemonde, G. Santarelli, P. Laurent, A. Clairon, C. Salomon, M. Haas, U. Jentschura, and C. Keitel, *New Limits on the Drift of Fundamental Constants from Laboratory Measurements*. Phys. Rev. Lett. **92**, 230802 (2004).

[39] A. Huber, T. Udem, B. Gross, J. Reichert, M. Kourogi, K. Pachucki, M. Weitz, and T. W. Hänsch, *Hydrogen-Deuterium 1S-2S Isotope Shift and the Structure of the Deuteron*. Phys. Rev. Lett. **80**, 468 (1998).

[40] S. G. Karshenboim, *Precision physics of simple atoms:QED tests, nuclear structure and fundamental constants*. Phys. Report **422**, 1 (2005).

[41] U. D. Jentschura, *Two-loop Bethe logarithms for non-S levels*. Phys. Rev. A **74**, 062517 (2006).

[42] U. Jentschura and M.Haas, *Two-loop effects and current status of the* $^4He^+$ *Lamb shift*. Can. J. Phys. **85**, 531 (2007).

[43] U. Jentschura, *Extrapolation of the Z* α *-expansion and two-loop bound-state energy shifts*. Phys. Lett. B **564**, 225 (2003).

[44] M. Herrmann, M. Haas, U. D. Jentschura, F. Kottmann, D. Leibfried, G. Saathoff, C. Gohle, A. Ozawa, V. Batteiger, S. Knünz, N. Kolachevsky, H. A. Schüssler, T. W. Hänsch, and T. Udem, *Feasibility of coherent xuv spectroscopy on the 1S-2S transition in singly ionized helium*. Phys. Rev. A **79**, 052505 (2009).

[45] E. Peters, S. A. Diddams, P. Fendel, S. Reinhardt, T. W. Hänsch, and T. Udem, *A deep-UV optical frequency comb at 205 nm*. Optics Express **17**, 9183 (2009).

[46] M. Zimmermann, C. Gohle, R. Holzwarth, T. Udem, and T. Hänsch, *Optical clockwork with an offset-free difference-frequency comb: accuracy of sum- and difference-frequency generation.*. Optics Lett. **29**, 310 (2004).

[47] T. Kanai, T. Kanda, T. Sekikawa, S. Watanabe, T. Togashi, C. Chen, C. Zhang, Z. Xu, and J. Wang, *Generation of vacuum-ultraviolet light below 160 nm in a KBBF crystal by the fifth harmonic of a single-mode Ti:sapphire laser*. J. Opt. Soc. Am. B **21**, 370 (2004).

[48] J. Walz, K. S. E. Eikema, and T. Hänsch, *The first continuous coherent Lyman-α source*. Nucl. Phys. A **692**, 163 (2001).

[49] K. S. E. Eikema, J. Walz, and T. Hänsch, *Continuous Coherent Lyman-a Excitation of Atomic Hydrogen*. Phys. Rev. Lett. **86**, 5679 (2001).

[50] T. Togashi, N. Nabekawa, T. Sekikawa, and S. Watanabe, *Generation of milliwatt narrow-bandwidth vacuum ultraviolet radiation by an all-solid-state tunable high-average-power laser system*. Optics Lett. **26**, 831 (2001).

[51] C. Gohle, T. Udem, M. Herrmann, J. Rauschenberger, R. Holzwarth, H. A. Schuessler, F. Krausz, and T. W. Hänsch, *A frequency comb in the extreme ultraviolet*. Nature **436**, 234 (2005).

[52] R. J. Jones, K. D. Moll, M. J. Thorpe, and J. Ye, *Phase-Coherent Frequency Combs in the Vacuum Ultraviolet via High-Harmonic Generation inside a Femtosecond Enhancement Cavity*. Phys. Rev. Lett. **94**, 193201 (2005).

[53] A. Ozawa, J. Rauschenberger, C. Gohle, M. Herrmann, D. R. Walker, V. Pervak, A. Fernandez, R. Graf, A. Apolonski, R. Holzwarth, F. Krausz, T. Hänsch, and T. Udem, *High Harmonic Frequency Combs for High Resolution Spectroscopy*. Phys. Rev. Lett. **100**, 253901 (2008).

[54] J. Rauschenberger, T. Fuji, M. Hentschel, A.-J. Verhoef, T. Udem, C. Gohle, T. Hänsch, and F. Krausz, *Carrier-envelope phase-stabilized amplifier system*. Laser Phys. Lett. **3**, 37 (2006).

[55] J. Seres, E. Seres, A. J.Verhoef, G. Tempea, C. Streli, P. V. Yakovlev, A. Scrinzi, C. Spielmann, and F. Krausz, *Source of coherent kiloelectronvolt X-rays*. Nature **433**, 596 (2005).

[56] F. Krausz and M. Ivanov, *Attosecond physics*. Rev. Mod. Phys. **81**, 163 (2009).

[57] J. Eden, *High-order harmonic generation and other intense optical field matter interactions: review of recent experimental and theoretical advances.* Prog. in Quant. Electron. **28**, 197 (2004).

[58] J. L. Krause, K. J. Schafer, and K. C. Kulander, *High-order harmonic generation from atoms and ions in the high intensity regime.* Phys. Rev. Lett. **68**, 3535 (1992).

[59] X. F. Li, A. L'Huillier, M. Ferray, L. A. Lompre, and G. Mainfray, *Multiple-harmonic generation in rare gases at high laser intensity.* Phys. Rev. A **39**, 5751 (1989).

[60] A. L'Huillier, P. Balcou, S. Candel, K. J. Schafer, and K. C. Kulander, *Calculations of high-order harmonic-generation processes in xenon at 1064 nm.* Phys. Rev. A **46**, 2778 (1992).

[61] M. Ferray, A. L'Huillier, X. F. Li, L. A. Lompre, G. Mainfray, and C. Manus, *Multiple-harmonic conversion of 1064 nm radiation in rare gases.* J. Phys. B: At. Mol. Opt. Phys. **21**, L31 (1988).

[62] J. Itatani, J. Levesque, D. Zeidler, H. Niikura, H. Pepin, J. C. Kieffer, P. B. Corkum, and D. M. Villeneuve, *Tomographic imaging of molecular orbitals.* Nature **432**, 867 (2003).

[63] P. W. Dooley, I. V. Litvinyuk, K. F. Lee, D. M. Rayner, M. Spanner, D. M. Villeneuve, and P. B. Corkum, *Direct imaging of rotational wave-packet dynamics of diatomic molecules.* Phys. Rev. A **68**, 023406 (2003).

[64] B. K. McFarland, J. P. Farrell, P. H. Bucksbaum, and M. Gühr, *High Harmonic Generation from Multiple Orbitals in N_2.* Science **322**, 1232 (2008).

[65] M. Lewenstein, P. Balcou, M. Y. Ivanov, A. L'Huillier, and P. B. Corkum, *Theory of high-harmonic generation by low-frequency laser fields.* Phys. Rev. A **49**, 2117 (1994).

[66] M. Lewenstein, P. Salieres, and A. L'Huillier, *Phase of the atomic polarization in high-order harmonic generation.* Phys. Rev. A **52**, 4747 (1995).

[67] A. L'Huillier, M. Lewenstein, P. Salieres, P. Balcou, M. Y. Ivanov, J. Larsson, and C. G. Wahlström, *High-order Harmonic-generation cutoff.* Phys. Rev. A **48**, R3433 (1993).

[68] P. B. Corkum, *Plasma perspective on strong field multiphoton ionization.* Phys. Rev. Lett. **71**, 1994 (1993).

[69] T. Morishita, A.-T. Le, Z. Chen, and C. D. Lin, *Accurate Retrieval of Structural Information from Laser-Induced Photoelectron and High-Order Harmonic Spectra by Few-Cycle Laser Pulses.* Phys. Rev. Lett. **100**, 013903 (2008).

[70] A.-T. Le, T. Morishita, and C. D. Lin, *Extraction of the species-dependent dipole amplitude and phase from high-order harmonic spectra in rare-gas atoms.* Phys. Rev. A **78**, 023814 (2008).

[71] Z. Chen, A.-T. Le, T. Morishita, and C. D. Lin, *Quantitative rescattering theory for laser-induced high-energy plateau photoelectron spectra.* Phys. Rev. A **79**, 033409 (2009).

[72] A.-T. Le, R. R. Lucchese, S. Tonzani, T. Morishita, and C. D. Lin, *Quantitative rescattering theory for high-order harmonic generation from molecules*. Phys. Rev. A **80**, 013401 (2009).

[73] X.-M. Tong and S.-I. Chu, *Theoretical study of multiple high-order harmonic generation by intense ultrashort pulsed laser fields: A new generalized pseudospectral time-dependent method*. Chem. Phys. **217**, 119 (1997).

[74] K. C. Kulander, *Multiphoton ionization of hydrogen: A time-dependent theory*. Phys. Rev. A **35**, 445 (1987).

[75] M. D. Feit, J. A. Fleck Jr., and A. Steiger, *Solution of the Schrtidinger Equation by a Spectral Method*. J. Comp. Phys. **47**, 412 (1982).

[76] M. R. Hermann and J. F. Jr., *Split-operator spectral method for solving the time-dependent Schrödinger equation in spherical coordinates*. Phys. Rev. A **38**, 6000 (1988).

[77] J. J. Carrera, S.-K. Son, and S.-I. Chu, *Ab initio theoretical investigation of the frequency comb structure and coherence in the vuv-xuv regimes via high-order harmonic generation*. Phys. Rev. A **77**, 031401 (2008).

[78] T. Ditmire, E. T. Gumbrell, R. A. Smith, J. W. G. Tisch, D. D. Meyerhofer, and M. H. R. Hutchinson, *Spatial Coherence Measurement of Soft X-Ray Radiation Produced by High Order Harmonic Generation*. Phys. Rev. Lett. **77**, 4756 (1996).

[79] R. Zerne, C. Altucci, M. Bellini, M. B. Gaarde, T. W. Hänsch, and A. L'Huillier, *Phase-Locked High-Order Harmonic Sources*. Phys. Rev. Lett. **79**, 1006 (1997).

[80] P. Salieres, L. L. Deroff, T. Auguste, P. Monot, P. d' Oliveira, D. Campo, J.-F. Hergott, H. Merdji, and B. Carre, *Frequency-Domain Interferometry in the XUV with High-Order Harmonics*. Phys. Rev. Lett. **83**, 5483 (1999).

[81] M. Bellini, S. Cavalieri, C. Corsi, and M. Materazzi, *Phase-locked, time-delayed harmonic pulses for high spectral resolution in the extreme ultraviolet*. Optics Lett. **26**, 1010 (2001).

[82] D. Descamps, C. Lynga, J. Norin, A. L'Huillier, C.-G.Wahlström, J.-F.Hergott, H.Merdji, P. Salieres, M. Bellini, and T. W. Hänsch, *Extreme ultraviolet interferometry measurements with high-order harmonics*. Optics Lett. **25**, 135 (2000).

[83] H. Merdji, P. Salieres, L. L. Deroff, J.-F. Hergott, B. Carre, D. Joyeux, D. Descamps, J. Norin, C. Lynga, A. L'Huillier, C.-G. Wahlström, M. Bellini, and S. Huller, *Coherence properties of high-order harmonics: Application to high-density laser-plasma diagnostic*. Laser and Particle Beams **18**, 495 (2000).

[84] M.Bellini, S.Cavalieri, C. Corsi, R. Eramo, and M. Materazzi, *High resolution spectrosocpy in the XUV with pairs of mutually coheren t and time-delayed laser harmonics*. Laser and Particle Beams **22**, 199 (2004).

[85] Y. Nagata, K. Furusawa, Y. Nabekawa, and K. Midorikawa, *Single-shot spatial-coherence measurement of 13 nm high-order harmonic beam by a Young's double-slit measurement*. Optics Lett. **32**, 722 (2007).

[86] M. Bellini, C. Lynga, A. Tozzi, M. B. Gaarde, T. W. Hänsch, A. L'Huillier, and C.-G. Wahlström, *Temporal Coherence of Ultrashort High-Order Harmonic Pulses.* Phys. Rev. Lett. **81**, 297 (1998).

[87] C. Lynga, M. B. Gaarde, C. Delfin, M. Bellini, T. W. Hänsch, A. L'Huillier, and C.-G. Wahlström, *Temporal coherence of high-order harmonics.* Phys. Rev. A **60**, 4823 (1999).

[88] V. Magni, G. Cerullo, S. D. Silvestri, . Svelto, L. J. Qian, and M. Danailovl, *Intracavity frequency doubling of a cw high-power TEM_{00} Nd:YLF laser.* Optics Lett. **18**, 2111 (1993).

[89] R. Smith, *Theory of intracavity optical second-harmonic generation.* IEEE J. Quantum Electron. **6**, 215 (1970).

[90] E. O. Potma, C. Evans, X. S. Xie, R. J. Jones, and J. Ye, *Picosecond-pulse amplification with an external passive optical cavity.* Optics Lett. **28**, 1835 (2003).

[91] R. J. Jones and J. Ye, *High-repetition-rate coherent femtosecond pulse amplification with an external passive optical cavity.* Optics Lett. **29**, 2812 (2004).

[92] A. F. Gonzalez, *Chirped pulse Oscillators: Generating microjoule femtosecond pulses at megahertz repetition rate.* Ph.D. thesis, Ludwig-Maximilians-Universität, München, Germany, 2007.

[93] A. Fernandez, T. Fuji, A. Poppe, A. Fürbach, F. Krausz, and A. Apolonski, *Chirped-pulse oscillators: a route to high-power femtosecond pulses without external amplification.* Optics Lett. **29**, 1366 (2004).

[94] V. L. Kalashnikov and A. Apolonski, *Chirped-pulse oscillators: A unified standpoint.* Phys. Rev. A **79**, 043829 (2009).

[95] H. Kogelnik and T. Li, *Laser Beams and Resonators.* Appl. Opt. **5**, 1550 (1966).

[96] J. Bechhoefer, *Feedback for physicists: A tutorial essay on control.* Rev. Mod. Phys. **77**, 783 (2005).

[97] R. Drever, J. Hall, F. Kowalski, J. Hough, G. Ford, A. Munley, and H. Ward, *Laser Phase and Frequency Stabilization Using an Optical Resonator.* Appl. Phys. B **31**, 97 (1983).

[98] T. Hänsch and B. Couillaud, *Laser frequency stabilization by polarization spectroscopy of a reflecting reference cavity.* Optics Comm. **35**, 441 (1980).

[99] D. Shaddock, M. Gray, and D. McClelland, *Frequency locking a laser to an optical cavity by use of spatial mode interference.* Optics Lett. **24**, 1499 (1999).

[100] R. J. Jones and J.-C. Diels, *Stabilization of Femtosecond Lasers for Optical Frequency Metrology and Direct Optical to Radio Frequency Synthesis.* Phys. Rev. Lett. **86**, 3288 (2001).

[101] E. D. Palik, *Handbook of Optical Constants of Solids I, II* (Academic Press, INC., , 1991).

[102] A. Schliesser, C. Gohle, T. Udem, and T. W. Hänsch, *Complete characterization of a broadband high-finesse cavity using an optical frequency comb.* Optics Express **14**, 5975 (2006).

[103] T. Hammond, A. K. Mills, and D. J. Jones, *Simple method to determine dispersion of high-finesse optical cavities.* Optics Express **17**, 8998 (2009).

[104] M. J. Thorpe, R. J. Jones, K. D. Moll, and J. Ye, *Precise measurements of optical cavity dispersion and mirror coating properties via femtosecond combs.* Optics Express **13**, 882 (2005).

[105] C. Gohle, . Ph.D. thesis, Ludwig-Maximilians-Universität, München, Germany, 2006.

[106] V. Pervak, A. Ozawa, C. Gohle, M. K. Trubetskov, A. V. Tikhonravov, and C. Gohle, *Phase-optimized dielectric multilayer dispersive mirrors. In preparation* .

[107] http://www.optilayer.com.

[108] A. Tikhonravov, M. Trubetskov, and G. DeBell, *Application of the needle optimization technique to the design of optical coatings.* Appl. Opt. **35**, 5493 (1996).

[109] A. Tikhonravov, M. Trubetskov, and G. DeBell, *Optical coating design approaches based on the needle optimization technique.* Appl. Opt. **46**, 704 (2007).

[110] K. D. Moll, R. J. Jones, and J. Ye, *Nonlinear dynamics inside femtosecond enhancement cavities.* Optics Express **13**, 1672 (2005).

[111] K. D. Moll, R. J. Jones, and J. Ye, *Output coupling methods for cavity-based high-harmonic generation.* Optics Express **14**, 8189 (2006).

[112] J. Wu and H. Zeng, *Cavity-enhanced noncollinear high-harmonicgeneration for extreme ultraviolet frequency combs.* Optics Lett. **32**, 3315 (2007).

[113] D. C. Yost, S. R. Schibli, and J. Ye, *Efficient output coupling of intracavity high harmonic generation.* Optics Lett. **33**, 1099 (2008).

[114] A. Ozawa, A. Vernaleken, W. Schneider, I. Gotlibovych, T. Udem, and T. W. Hänsch, *Non-collinear high harmonic generation: a promising outcoupling method for cavity-assisted XUV generation.* Optics Express **16**, 6233 (2008).

[115] Structure Probe Inc., http://www.2spi.com/.

[116] I. Pupeza, private communication, 2009.

[117] S. V. Fomichev, P. Breger, B. Carre, P. Agostini, and D. F. Zaretski, *Non-collinear high harmonic generation.* Laser Phys. **12**, 383 (2002).

[118] W. Run-Hai, J. Hong-Bing, Y. Hong, W. Cheng-Yin, and G. Qi-Huang, *High-Order Harmonic Generation by Two Non-Collinear Femtosecond Laser Pulses in CO.* Chin. Phys. Lett. **22**, 1913 (2005).

[119] A. Bouhal, R. Evans, G. Grillon, A. Mysyrowicz, P. Breger, P. Agostini, R. C. Constantinescu, H. G. Muller, and D. von der Linde, *Cross-correlation measurement of femtosecond noncollinear high-order harmonics.* J. Opt. Soc. Am. B **14**, 950 (1997).

[120] J. J. Carrera and S.-I. Chu, *Extension of high-order harmonic generation cutoff via coherent control of intense few-cycle chirped laser pulses*. Phys. Rev. A **75**, 033807 (2007).

[121] X. Guan, X.-M. Tong, and S.-I. Chu, *Effect of electron correlation on high-order-harmonic generation of helium atoms in intense laser fields: Time-dependent generalized pseudospectral approach in hyperspherical coordinates*. Phys. Rev. A **73**, 023403 (2006).

[122] X.-M. Tong and S.-I. Chu, *Probing the spectral and temporal structures of high-order harmonic generation in intense laser pulses*. Phys. Rev. A **61**, 021802 (2000).

[123] I. A. Ivanov and A. S. Kheifets, *Harmonic generation for atoms in fields of varying ellipticity: Single-active-electron model with Hartree-Fock potential*. Phys. Rev. A **79**, 053827 (2009).

[124] P. P. Szydlik and A. E. S. Green, *Independent-particle-model potentials for ions and neutral atoms with $Z \leq 18$*. Phys. Rev. A **9**, 1885 (1974).

[125] R. H. Garvey, C. H. Jackman, and A. E. S. Green, *Independent-particle-model potentials for atoms and ions with $36 < Z \leq 54$ and a modified Thomas-Fermi atomic energy formula*. Phys. Rev. A **12**, 1144 (1975).

[126] M. B. Gaarde and K. J. Schafer, *Quantum path distributions for high-order harmonics in rare gas atoms*. Phys. Rev. A **65**, 031406 (2002).

[127] L. A. Lompre, A. L'Huillier, M. Ferray, P. Monot, G. Mainfray, and C. Manus, *High-order harmonic generation in xenon: intensity and propagation effects*. J. Opt. Soc. Am. B **7**, 754 (1990).

[128] FFTW library, http://www.fftw.org/.

[129] A. Yariv, *Quantum Electronics* (John Wiley & Sons, , 1988).

[130] A. Fedotov, A. Naumov, V. Silin, S. Uryupin, A. Zheltikov, A. Tarasevitch, and D. von der Linde, *Third-harmonic generation in a laser-pre-excited gas: the role of excited-state neutrals*. Phys. Lett. A **271**, 407 (2000).

[131] K. L. Ishikawa, E. J. Takahashi, and K. Midorikawa, *Wavelength dependence of high-order harmonic generation with independently controlled ionization and ponderomotive energy*. Phys. Rev. A **80**, 011807 (2009).

[132] K. Ishikawa, *Efficient photoemission and ionization of He^+ by a combined fundamental laser and high-order harmonic pulse*. Phys. Rev. A **70**, 013412 (2004).

[133] K. Ishikawa, *Photoemission and Ionization of He^+ under Simultaneous Irradiationof Fundamental Laser and High-Order Harmonic Pulses*. Phys. Rev. Lett. **91**, 043002 (2003).

[134] E. J. Takahashi, T. Kanai, K. L. Ishikawa, Y. Nabekawa, and K. Midorikawa, *Dramatic Enhancement of High-Order Harmonic Generation*. Phys. Rev. Lett. **99**, 053904 (2007).

[135] D. Kane and R. Trebino, *Characterization of arbitrary femtosecond pulses usingfrequency-resolved optical gating*. IEEE J. Quantum Electron. **29**, 571 (1993).

[136] T. Südmeyer, S. V. Marchese, S. Hashimoto, C. R. E. Baer, G. Gingras, B. Witzel, and U. Keller, *Femtosecond laser oscillators for high-field science*. Nature Photon. **2**, 599 (2008).

[137] H. Kitano and S. Kinoshita, *Stable multipulse generation from a self-mode-locked Ti:sapphire laser*. Optics Comm. **157**, 128 (1998).

[138] X. Liu, L. Wang, X. Li, H. Sun, A. Lin, K. Lu, Y. Wang, and W. Zhao, *Multistability evolution and hysteresis phenomena of dissipative solitons in a passively mode-locked fiber laser with large normal cavity dispersion*. Optics Express **17**, 8506 (2009).

[139] B. Proctor, E. Westwig, and F. Wise, *Characterization of a Kerr-lens mode-locked Ti:sapphire laser with positive group-velocity dispersion*. Optics Lett. **18**, 1654 (1993).

[140] P. Curley, C. Spielmann, T. Brabec, F. Krausz, E. Wintner, and A. Schmidt, *Operation of a femtosecond Ti:sapphire solitary laser in the vicinity of zero group-delay dispersion*. Optics Lett. **18**, 54 (1993).

[141] V. Kalashnikov, E. Podivilov, A. Chernykh, S. Naumov, A. Fernandez, R. Graf, and A. Apolonski, *Approaching the microjoule frontier with femtosecond laser oscillators: theory and comparison with experiment*. New J. Phys. **7**, 217 (2005).

[142] S. Naumov, A. Fernandez, R. Graf, P. Dombi, F. Krausz, , and A. Apolonski, *Approaching the microjoule frontier with femtosecond laser oscillators*. New J. Phys. **7**, 216 (2005).

[143] V. Pervak, C. Teisset, A. Sugita, S. Naumov, F. Krausz, and A. Apolonski, *High-dispersive mirrors for femtosecond lasers*. Optics Express **16**, 10220 (2008).

[144] T. Brabec and F. Krausz, *Intense few-cycle laser fields: Frontiers of nonlinear optics*. Rev. Mod. Phys. **72**, 545 (2000).

[145] J. Paul, J. Johnson, J. Lee, and R. J. Jones, *Generation of high-power frequency combs from injection-locked femtosecond amplification cavities*. Optics Lett. **33**, 2482 (2008).

[146] Z. Liu, H. Murakami, T. Kozeki, H. Ohtake, and N. Sarukura, *High-gain, reflection-double pass, Ti:sapphire continuous-wave amplifier delivering 5.77 W average power, 82 MHz repetition rate, femtosecond pulses*. Appl. Phys. Lett. **76**, 3182 (2000).

[147] R. Huber, F. Adler, A. Leitenstorfer, M. Beutter, P. Baum, and E. Riedle, *12-fs pulses from a continuous-wave-pumped 200-nJ Ti:sapphire amplifier at a variable repetition rate as high as 4 MHz*. Optics Lett. **28**, 2118 (2003).

[148] A. Dantan, J. Laurat, A. Ourjoumtsev, R. Tualle-Brouri, and P. Grangier, *Femtosecond Ti:sapphire cryogenic amplifier with high gain and MHz repetition rate*. Optics Express **15**, 8864 (2007).

[149] L. Xu, G. Tempea, C. Spielmann, F. Krausz, A. Stingl, K. Ferencz, and S. Takano, *Continuous-wave mode-locked Ti:sapphire laser focusable to 5 x 10(13) W/cm(2)*. Optics Lett. **23**, 789 (1998).

[150] A. Ozawa, W. Schneider, T. W. Hänsch, T. Udem, and P. Hommelhoff, *Phase-stable single-pass cryogenic amplifier for high repetition rate few-cycle laser pulses.* New J. Phys. **11**, 083029 (2009).

[151] S. Backus, C. Durfee, G. Mourou, H. Kapteyn, and M. Murnane, *0.2-TW laser system at 1 kHz.* Optics Lett. **15**, 1256 (1997).

[152] M. Zavelani-Rossi, F. Lindner, C. Le Blanc, G. Cheriaux, and J. P. Chambaret, *Control of thermal effects for high-intensity Ti:sapphire laser chains.* Appl. Phys. B **70**, S193 (2000).

[153] P. F. Moulton, *Spectroscopic and Laser Characteristics of Ti-Al2O3.* Journal of the Optical Society of America B-optical Physics **3**, 125 (1986).

[154] M. Bradler, P. Baum, and E. Riedle, *Femtosecond continuum generation in laser host materials.* Accepted to Appl. Phys. B (2009).

[155] R. W. Boyd, *Nonlinear Optics, 2nd edition* (Academic Press, , 2003).

[156] A. Ozawa, W. Schneider, F. Najafi, T. W. Hänsch, T. Udem, and P. Hommelhoff, *A Peltier cooled single pass amplifier for Titanium:Sapphire laser pulses.* submitted to Laser Phys. (2009).

[157] X. Zhou, D. Yoshitomi, Y. Kobayashi, and K. Torizuka, *Generation of 28-fs pulses from a mode-locked ytterbium fiber oscillator.* Optics Express **16**, 7055 (2008).

[158] S. Zhou, D. G. Ouzounov, and F. W. Wise, *Passive harmonic mode-locking of a soliton Yb fiber laser at repetition rates to 1.5 GHz.* Optics Express **30**, 1734 (2005).

[159] N. G. Usechak, G. P. Agrawal, and J. D. Zuegel, *Tunable, high-repetition-rate, harmonically mode-locked ytterbium fiber laser.* Optics Lett. **29**, 1360 (2004).

[160] F. Ilday, J. Chen, and F. Kärtner, *Generation of sub-100-fs pulses at up to 200 MHz repetition rate from a passively mode-locked Yb-doped fiber laser.* Optics Express **13**, 2716 (2005).

[161] P. Wasylczyk, P. Wnuk, and C. Radzewicz, *Passively modelocked, diode-pumped Yb:KYW femtosecond oscillator with 1 GHz repetition rate.* Optics Express **17**, 5630 (2009).

[162] P. Russbueldt, T. Mans, G. Rotarius, J. Weitenberg, H. Hoffmann, and R. Poprawe, *400 W Yb:YAG Innoslab fs-amplifier.* Optics Express **17**, 12230 (2009).

[163] I. Hartl, T. R. Schibli, A. Marcinkevicius, D. C. Yost, D. D. Hudson, M. E. Fermann, and J. Ye, *Cavity-enhanced similariton Yb-fiber laser frequency comb:* 3×10^{14} *W/cm*^{2} *peak intensity at 136 MHz.* Optics Lett. **32**, 2870 (2007).

[164] T. Fuji, N. Ishii, C. Teisset, X.Gu, T. Metzger, A. Baltuska, N. Forget, D. Kaplan, A. Galvanauskas, and F. Krausz, *Parametric amplification of few-cycle carrierenvelope phase-stable pulses at 2.1 μm.* Optics Lett. **31**, 1103 (2006).

[165] C. Vozzi, F. Calegari, F. Frassetto, L. Poletto, G. Sansone, P. Villoresi, M. Nisoli, S. D. Silvestri, and S. Stagira, *Coherent continuum generation above 100 eV driven by an ir parametric source in a two-color scheme*. Phys. Rev. A **79**, 033842 (2009).

[166] K. Yamada, T. Yamazaki, N. Sei, R. Suzuki, T. Ohdaira, T. Shimizu, M. Kawai, M. Yokoyama, T. Mikado, T. Noguchi, S. Sugiyama, and H. Ohgaki, *Saturation of cavity-mirror degradation in the UV FEL*. Nucl. Inst. and Meth. for Phys. Res. A **393**, 44 (1997).

[167] C. Gohle, B. Stein, A. Schliesser, T. Udem, and T. W. Hänsch, *Frequency Comb Vernier Spectroscopy for Broadband, High-Resolution, High-Sensitivity Absorption and Dispersion Spectra*. Phys. Rev. Lett. **99**, 263902 (2007).

[168] M. J. Thorpe, D. Balslev-Clausen, M. S. Kirchner, and J. Ye, *Cavity-enhanced optical frequency comb spectroscopy: application to human breath analysis*. Optics Express **16**, 2387 (2008).

[169] W. Wieczorek, R. Krischek, N. Kiesel, P. Michelberger, G. Toth, and H. Weinfurter, *Experimental Entanglement of a Six-Photon Symmetric Dicke State*. Phys. Rev. Lett. **103**, 020504 (2009).

Acknowledgements

First of all, I would like to thank Prof. Theodor W. Hänsch for giving me the opportunity to work on fantastic topics in the excellent research environment of his group .

I wish to thank Thomas Udem. He kindly supervised and supported me with exciting discussions and advice. His detailed and comprehensive instructions based on his experiences always helped me to learn many new things in the most efficient way. Additionally, he enriched my life in Germany by introducing me to many fun activities, like hiking, climbing, cycling etc.

I am grateful to Christoph Gohle, who assisted me in the cavity-enhanced HHG experiment. It was a great pleasure and highly instructive to see his expertise in the lab and to try to learn how an outstanding physicist thinks.

I'm indebted to Peter Hommelhoff for his significant contributions and advice in the high repetition rate amplifier experiments. His experiences in ultrashort pulsed lasers helped me to work with 6 fs oscillators. I also thank him for reading and correcting the manuscript of this thesis.

I would like to thank Andreas Vernaleken with whom I spent the most time together in the lab. I enjoyed to work with him listening to his jokes and to discuss the problems in the experiments. I appreciate his great contributions in writing our papers in an extremely rapid way. Especially, this thesis could not have been completed without his careful, detailed and speedy reading of the manuscript.

I would like to acknowledge Ronald Holzwarth who assisted me in organizing and preparing the experiment that I was working on. Especially I thank him for his kind help in planning and realizing Yb-based systems for the enhancement cavity.

I wish to thank Maximilian Herrmann. His multi-discipline expertise, knowledge and investigations always helped me a lot to lead me into the right direction, even when discussing detailed problems in my work.

I highly appreciate the contribution of Igor Gotlibovych in simulating HHG. Valuable discussions with him helped me to better understand the NCHHG processes.

I would like to acknowledge Wolfgang Simon, Karl Linner and Helmut Brückner, who always tried to satisfy my requests in the fastest possible way. The experiment with high repetition rate amplifier would not have been possible without Wolfgang's skilled hands designing and building an efficient cryostat. I appreciate Charly's efforts to construct a vacuum chamber for 30 m of cavity. Helmut always kindly explained all the details of feed-back circuits to me.

I appreciate the help from Jens Rauschenberger. He planned the 10 MHz cavity experiment before I joined the project and supplied me with necessary equipment.

Many thanks to Birgitta Bernhardt. I enjoyed working with her on her impressive green cavity and the neat Yb-amplifier system. I appreciate her and Katharina Predehl's contribu-

tion to the Christmas movies, in which I participated with lots of fun.

I wish to thank Waldemar Schneider who worked together with me in the lab and shared my office. He also boosted my experiments by helping me in preparing the equipment with his precise machining.

I would like to acknowledge Tilo Steinmetz and Tobias Wilken for supplying us with an excellent Yb-oscillator and amplifier. They patiently answered plenty of my basic questions about fiber optics.

Many thanks to Tobias Nebel whom I spent quite some time with as an office-mate, and also I enjoyed to play with Elias, his great son. Tobias kindly helped me to start up my life in Germany by translating the German documents and offering his help when I moved to my apartment.

I shared a lab with Sebastian Knünz and Valentin Batteiger. I would like to thank them for their kind instructions to their experiments and valuable discussions about He experiments. Also it was nice to talk with Sebastian in our office when I was annoyed by experiments in the lab.

I wish to thank Masaki Hori who gave me the precious opportunity to enjoy speaking Japanese. His latest news and his experiences in Japan helped me to think about my future.

I am grateful to Janis Alnis, Arthur Matveev, and David Walker. It was great to always have dinner together in the MPQ cafeteria chatting with them.

I appreciate the cooperations with Ioachim Pupeza, Vladimir Pervak, Roswitha Graf, Alma Fernandez, and Alexander Apolonskiy in the cavity-enhanced HHG experiments.

I thank Ingrid Hermann and Gabriele Gschwendtner for their kind administrative help. Rosemarie Lechner assisted me to complete the administrative work to start my PhD here.

I would like to express my appreciation to the rest of the group members that I could not mention here.

Finally, I would like to thank my family for supporting my life in Germany and welcoming me with excellent dining during my winter vacations at home.

Curriculum Vitae

Akira Ozawa

Born	October 3rd, 1981
	Ibaraki, Japan
Nationality	Japanese

Max-Planck-Institut für Quantenoptik
Hans-Kopfermann-Strasse 1
85748 Garching
Germany

Telephone	+49 89 32905 261
e-mail	akira.ozawa@mpq.mpg.de

Education

Feb. 2006 – today	PhD candidate *"Frequency combs in the extreme ultraviolet"* Max-Planck-Institute of Quantum Optics, Germany Laser Spectroscopy group (Prof. Hänsch)
Apr. 2004 – Mar. 2006	Master of Science in Physics Department of Physics, Graduate School of Science, The University of Tokyo, Japan
Apr. 2000 – Mar. 2004	Bachelor of Science in Physics Department of Physics The University of Tokyo, Japan

Publications

Efficient 494 mW sum-frequency generation of sodium resonance radiation at 589 nm by using a periodically poled Zn:LiNbO3 ridge waveguide
T. Nishikawa, A. Ozawa, Y. Nishida, M. Asobe, F.L. Hong, T.W. Hänsch
Opt. Express **17** 17792 (2009)

Phase-stable single-pass cryogenic amplifier for high repetition rate few-cycle laser pulses
A. Ozawa, W. Schneider, T.W. Hänsch, Th. Udem, P. Hommelhoff
New J. Phys. **11** 083029 (2009)

Puzzling spectral structures of molecular vibration observed in ultrafast pump–probe experiment of transparent material
A. Ozawa, T. Kobayashi
Chem. Phys. Lett. **477** 281 (2009)

Feasibility of coherent xuv spectroscopy on the 1S-2S transition in singly ionized helium
M. Herrmann, M. Haas, U.D. Jentschura, F. Kottmann, D. Leibfried, G. Saathoff, C. Gohle, A. Ozawa, V. Batteiger, S. Knünz, N. Kolachevsky, H.A. Schüssler, T.W. Hänsch, Th. Udem
Phys. Rev. A **79** 052505 (2009)

Non-collinear high harmonic generation:
A promising outcoupling method for cavity-assisted XUV generation
A. Ozawa, A. Vernaleken, W. Schneider, I. Gotlibovych, Th. Udem, T.W. Hänsch
Opt. Express **16** 6233 (2008)

High harmonic frequency combs for high resolution spectroscopy
A. Ozawa, J. Rauschenberger, Ch. Gohle, M. Herrmann, D.R. Walker, V. Pervak, A. Fernandez, R. Graf, A. Apolonski, R. Holzwarth, F. Krausz, T.W. Hänsch, Th. Udem
Phys. Rev. Lett. **100** 253901 (2008)
Selected for Virtual Journal of Ultrafast Science, Volume 7, Issue 7

Time resolution of chirped lattice vibrations in a mixed-valence metal-halogen complex system
F. Araoka, A. Ozawa, D. Kawakami, S. Takaishi, M. Yamashita, T. Kobayashi
Phys. Rev. B **75** 224304 (2007)

Sub-5 fs time-resolved dynamic Franck-Condon overlaps associated with the S_1 -> S_0 stimulated transition in oligothiophene 13-mer
A. Ozawa, K. Takimiya, T. Otsubo, T. Kobayashi
Chem. Phys. Lett. **409** 224 (2005)

Conference contributions

Current Progress in XUV frequency combs (invited talk)
2nd International Conference on Attosecond Physics, Manhattan, KS, USA (2009)

Amplification of ultrashort pulses with a single-pass cryogenic Ti:sapphire Amplifier at 80MHz Repetition Rate (talk)
CLEO Europe, Munich, Germany (2009)

High Harmonic Frequency Combs for High Resolution Spectroscopy (talk)
16th International Conference on Ultrafast Phenomena, Stresa, Italy (2008)

Dynamics of one-dimensional exciton in porphyrin J aggregates by sub-5fs transient absorption experiment (poster)
15th International Conference on Ultrafast Phenomena, Pacific Grove, CA, USA (2006)